CRANFIELD UNIVERSITY

RAINER KRAFFT

ELECTROMAGNETIC FLOWMETERS IN MULTIPHASE FLOWS

SCHOOL OF MECHANICAL ENGINEERING
DEPARTMENT OF FLUID ENGINEERING AND INSTRUMENTATION

PhD THESIS

Acknowledgements

I would like to thank everybody who helped me with my project.

Many thanks to my supervisors Prof Sanderson and John Hemp who guided me through the project with their ideas and encouragement. John provided invaluable help in all mathematical questions and he showed a never ending interest in my work.

For all the advice and help in electronic designs I want to thank Duncan Macleod. Thanks also to Gary Oddie for many useful discussions and support in all technical matters. Also a big thank you to Alex Guilbert for sharing his expertise in computing.

Last but not least I would like to thank everybody who helped me to find life easier at Cranfield.

CRANFIELD UNIVERSITY

SCHOOL OF MECHANICAL ENGINEERING
DEPARTMENT OF FLUID ENGINEERING AND INSTRUMENTATION

Phd THESIS

Academic Year 1992-93

Rainer Krafft

Electromagnetic flowmeters in multiphase flows

Supervisor: M L Sanderson
JHemp

September 1993

Abstract

The response of an Electromagnetic Flowmeter to a secondary, nonconducting phase in a continuous conducting phase is investigated. Experiments are carried out on a commercial 2" Foxboro flowmeter with sinusoidal mains field excitation and point electrodes. The main aspects which are looked for are the change in flow signal and transformer signal. A mathematical model is developed to simulate the effect of the nonconducting phase in the form of single spherical particles. The model also allows one to alter the electrode geometry. A second flowmeter is designed to incorporate an improved electrode and coil geometry as well as a newly designed signal processing unit. In a series of experiments, the predictions of the theoretical model have been mostly verified.

Contents

List of Figures

Notation

The following notation is used unless otherwise stated:

θ	Angle to a point in the pipe cross section
$\overline{W}$	Mean value of weight function in specified area
ΔU	Potential difference between electrodes
θ_1,θ_2	Angles from x-axis through centre of radially directed dipole to current source or -sink
φ	Angle to centre of dipole
ΔU_{rel}	Relative potential difference between electrodes
α	Volumetric ratio of nonconducting phase to mixture (for a no-slip condition this is equal to the area ratio of void to pipe area)
δ	Half the distance between current source and -sink
ε	Electromotive forces in generator theory (chapter 3)
ε	Non-uniformity of weight function
μ_0	Relative permeability
σ	Conductivity of fluid
τ	Flow tube volume used for integration
ω	Angular frequency
a	Inner flow tube radius
b	Radius to centre of dipole
B	Magnetic field strength
c	Radius of gas core in annular flow
c	Radius of nonconducting sphere (chapter 3)
d	Inner flowtube diameter
I	Current
j	Virtual current density
j_0	Current density of circulating current (chapter 3)
j_0	Undisturbed eddy current density
j_n	Component of circulating current, perpendicular to the pipe wall

j'	Current density of dipole current source
l	Distance between current source and -sink
Q	Volumetric flow rate
Q_g	Gas flow rate
Q_l	Liquid flow rate
r	Radius to a point in the pipe cross section
r_1,r_2,r_3	Radii to current sinks and sources
U_0	Potential difference between electrodes in virtual current theory
U_{0EE}	Potential difference without nonconducting sphere
U_1	Potential distribution for $\|z\|>\delta$
U_2	Potential distribution for $\|z\|<\delta$
U'	Change of U_0 due to nonconducting sphere
U'_{EE}	Potential difference due to nonconducting sphere
v	Local liquid velocity
v_m	Mean fluid velocity
W	Weight vector

Chapter 1

1.1 General Introduction

In this thesis the performance of Electromagnetic Flowmeters in multiphase flows is investigated.

Electromagnetic Flowmeters have been in use for 30 years or more in various parts of industry. Their basic principle is to measure the voltage which is generated when a conducting fluid passes through a magnetic field. The volumetric flow is directly proportional to the voltage. The major advantage of E.M.flowmeters over any other kinds of mechanical flowmeter is, that they are not intrusive. They don't cause an additional pressure drop because of some obstruction in the flow and they are not easily damaged by solid particles in the flow. Moreover, their accuracy has been proved to be as good as 0.2% if they are installed properly. Traditionally, Electromagnetic Flowmeters as well as almost all other types of flowmeters are used for measuring single phase flows only. In practice however, there are many applications where multiphase flows have to be measured. One example is the oil industry, where oil wells can produce a mixture of water, gas and oil. Although E.M.flowmeters can often be used for multiphase flows, there is always an uncertainty regarding the effects of a nonconducting second or third phase. Some experimental data is available on tests with two phase flows and the results indicate a limited applicability. However, the causes of variations of the output signal do not seem to be understood thoroughly.

1.2 Objectives

In previous studies, E.M.flowmeters have been optimised to eliminate the effects of a nonconducting phase.
In this project the opposite view is taken. The usual output of the flowmeter is of minor interest and the work concentrates on and tries to utilize effects on signal due to the nonconducting phase. In the theory and experiments the following aspects are covered:

Theoretical work

a) Prediction of the effect of gas bubbles or oil droplets on the flow signal
   - using the virtual current(Weight Function) theory
   - using the Generator theory

b) Investigation of the effect of a second, nonconducting phase on the transformer signal

Experiments.
Firstly, a conventional EM-flowmeter with 2" diameter flowtube and point electrodes is used to measure

- the flow signal
- the transformer signal
- electrode noise picked up on the electrodes without a magnetic field

Based on the theoretical and experimental results, an E.M.flowmeter is designed, which uses additional information due to the nonconducting phase. It is attempted to measure the velocity of air bubbles using the transformer signal power spectrum. Finally, the new meter is tested in order to verify the predictions.

1.3 Literature review

The method of metering the flowrate of a liquid using a magnetic field has been known for a long time. In the early days, Faraday tried (in 1832) to measure the flow of the Thames by inserting two electrodes at each side of the river and using the magnetic field of the earth. For various reasons he did not succeed but the idea was born.

In 1962, Shercliff was one of the first who investigated the performance of an electromagnetic flowmeter theoretically. He allowed for conducting and non-conducting flowtube walls, circular and rectangular cross sections and point and area electrodes at various positions on the pipe wall or in the centre of the meter. One of his major achievements is the definition of a weighting function which describes the sensitivity of the signal from the electrodes to velocity at points in the cross-section. He showed that for a flowmeter with uniform magnetic field and point electrodes this weighting function is such that any axissymmetric rectilinear flow profile with the mean flow velocity v_m gives rise to the signal $\Delta U = v_m B d$. Due to this fact, electromagnetic flowmeters were often described as ideal flowmeters which under all conditions, independent of the velocity profile, measure the mean velocity.

The idea of the weighting function was then used by Bevir(1970) when he developed the powerful concept of the virtual current **j**, and introduced the weighting vector **W=Bxj**. The virtual current is the imaginary current which would flow when a unit current enters through electrode 1 and leaves through electrode 2. The distribution of **j** for a flowmeter with point electrodes and insulating walls is shown in **Fig.1.1.** Bevir showed that the condition for an ideal flowmeter with an incompressible fluid is $\nabla \times W = 0$. In that case, the signal at the electrodes will be proportional to the flow rate irrespective of the velocity distribution. One type of ideal flowmeter is one with a rectangular cross section and insulating walls. Its strip electrodes are parallel to the uniform field (**Fig.1.2**).

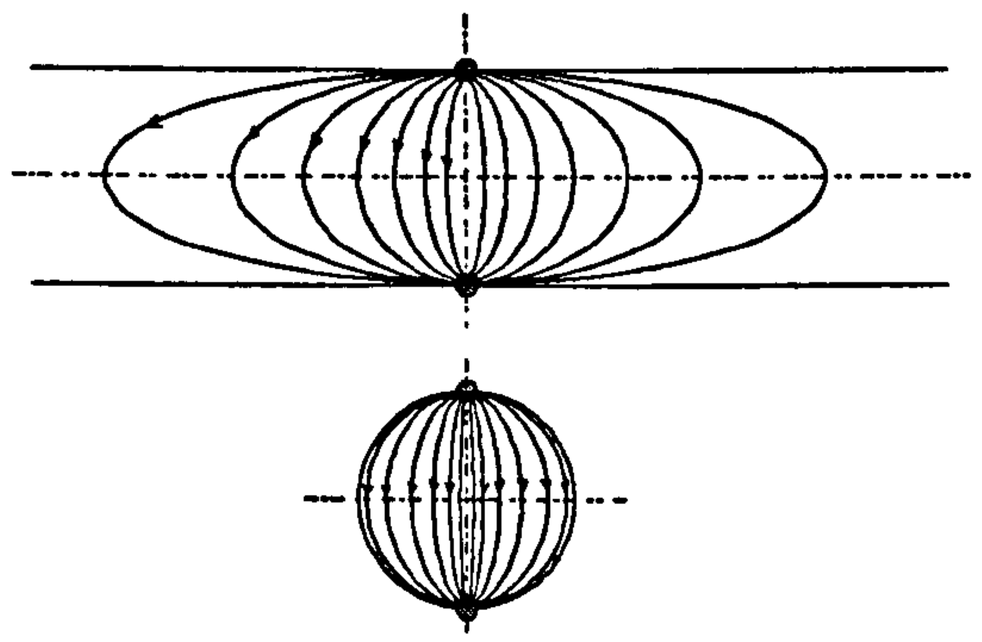

Fig.1.1 Virtual current distribution in E.M.flowmeter with point electrodes and insulating pipe walls.

Bevir also proved that the conditions for an ideal E.M.flowmeter cannot be met by the above shown circular flowtube with point electrodes.

By using the virtual current theory, many weight functions were theoretically investigated since then, altering the electrode shape and size and modelling the magnetic field as well. It was mainly tried to make the weighting function as uniform as possible. A uniform weighting function would mean that a velocity jet(tube of flow parallel to the axis) causes always the same flow

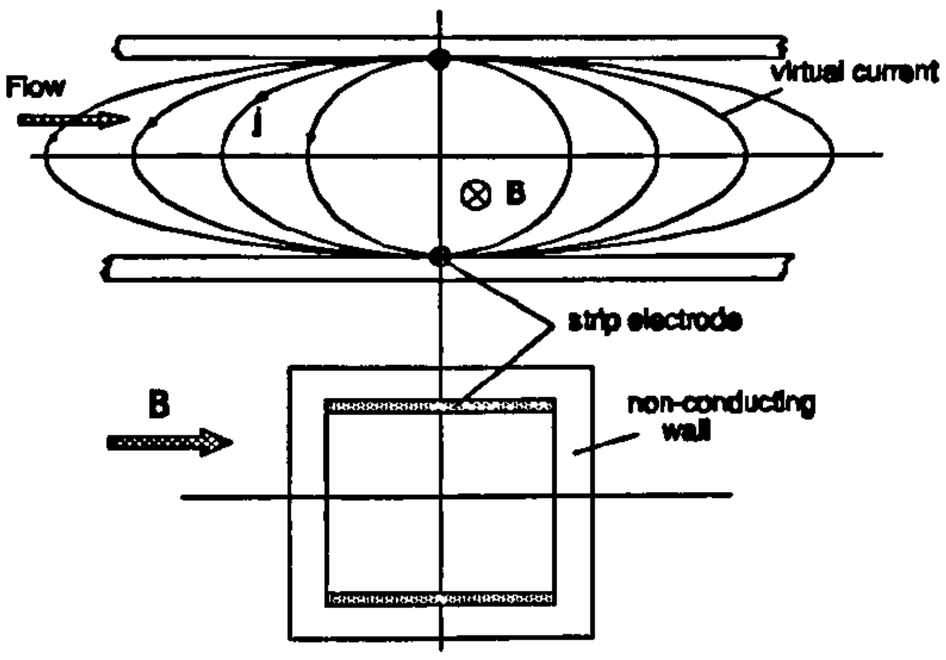

Fig.1.2 Type of ideal E.M.flowmeter with square channel and strip electrodes

signal independent of its position in the pipe cross section. In order to compare the non-uniformity ε of a weight function, the following definition can be used (Wyatt 1972):
ε is the root mean square deviation of the rectilinear weight function $W(r,\theta)$ from the mean value $\bar{W}$ within a circle of radius r_0, normalised to $\bar{W}$.

$$\varepsilon=\frac{1}{\bar{W}(r_0)}\left(\frac{1}{\pi r_0^2}\int_0^{r_0}\int_0^{2\pi}[W(r,\theta)-\bar{W}(r_0)]^2 r\,dr\,d\theta\right)^{1/2}$$

$$\bar{W}(r_0)=\frac{1}{\pi r_0^2}\int_0^{r_0}\int_0^{2\pi}W(r,\theta)\,r\,dr\,d\theta$$

The radius r_0, at which ε is calculated is taken with r_0=0.9a(Wyatt) or r_0=0.95a(Hemp,1975).
An ideal flowmeter as in **Fig.1.2** is described by Wyatt(1977). The flowtube had a 1in square cross section with contacting strip electrodes. A long, uniform magnetic field was achieved by using a magnet of about 5in length. An 1/8 in diameter water jet was then situated 2.5in upstream from the electrodes and the jet could be rotated on a circle of 3/8in radius. The variation of the signal, with the jet either positioned towards the electrodes or towards the wall, was only 2%. Another flowmeter with 1in diameter and point electrodes showed variations of 100% under the same conditions. Although the ideal type flowmeter performed very well as far as the response to velocity peaks was concerned, it is not build as a commercial meter. One reason may be that a square flowtube, combined with the very long magnet are impractical. A more serious problem however is the high sensitivity of the meter to any deposits on the electrodes. Because the electrodes were in contact with the fluid, a variation in contact impedance will alter the virtual current and hence destroy the ideal performance of the flowmeter. The signal output for example varied in an experiment by about 15% after the electrodes were washed with a detergent surfactant and the experiment repeated. Generally, point electrodes are the most velocity profile prone kind of electrodes with a weighting factor of ∞ at the electrodes and 0.5 at the pipe wall away from the electrodes, when a uniform magnetic field is applied.
A three dimensional magnetic field optimization has been solved by Hemp(1975). He defined the non-uniformity of the weight function W as

$$\varepsilon=\frac{1}{\bar{W}}\left(\frac{1}{45}\sum_{i=1}^{45}(W_i-\bar{W})^2\right)^{\frac{1}{2}}$$

Here, $W_1..W_{45}$ are values of W at 45 points in a quadrant of the flowmeter cross section. $\bar{W}$ was averaged over a circle of radius r=0,95a. The resultant shape of the coils was very complex (**Fig.1.3**). The axissymmetric weight function was almost unity

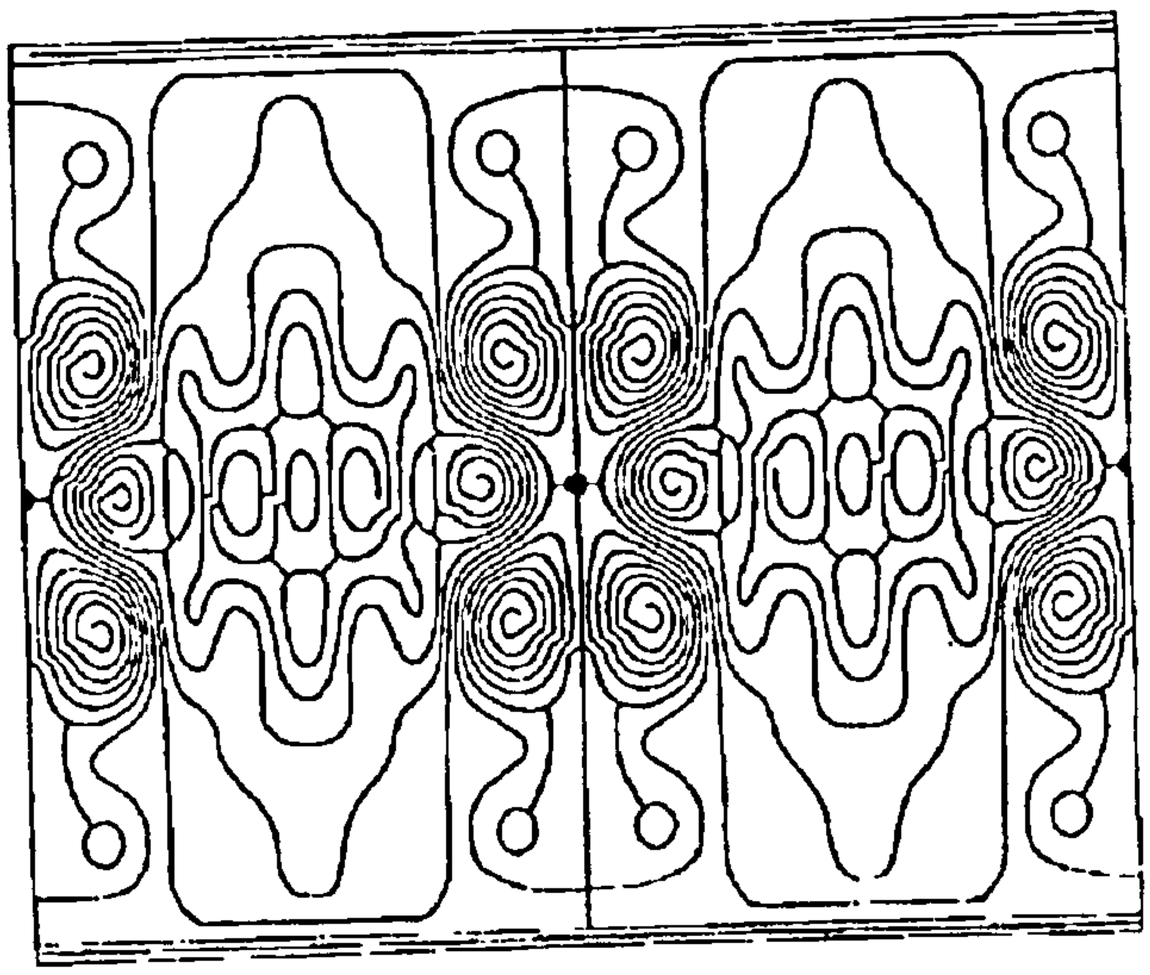

Fig1.3 Optimised coil shape for E.M.flowmeter with point electrodes

up to a radius of 0.9a. A 20mm diameter flowmeter with point electrodes was build on which the coils were etched onto a copper foil.
Although the design was again very good regarding the uniformity of the weight function, there is a drawback: The magnet is 2.5D long and therefore impractical for small medical flowmeters as well as for large meters of several inches diameter. Secondly, the efficiency is 25 times lower than for an ordinary point electrode flowmeter and hence it would consume too much power in larger sizes.

Wyatt and O'Sullivan(1983) derived a method to compute the signal in an E.M.flowmeter for any rectilinear velocity distribution. If the flowmeter signal is given by $U=\int_{\tau} W v \, d\tau$ and $\mathbf{W}=\mathbf{B}\times\mathbf{j}$, the magnetic field vector **B** was obtained from a series of measurements and the virtual current density **j** was determined by mathematical analyses of the pipe/electrode configuration. Beside the two-point electrode configuration, multiple contacting and noncontacting point electrodes and large area electrodes were investigated. The large area electrodes were simulated by an array of noncontacting point electrodes.
Considering the non uniform weight function of an E.M.Flowmeter with point electrodes, O'Sullivan(1983) then designed and tested an arrangement with 6 point electrodes. These were placed in three pairs on a flowtube with radius a=10mm. The magnet was only 10mm long and it was designed to generate a uniform field. It was energised with a current of 0.96A RMS at 240 Hz, producing a maximum field strength of 15 Gauss. Due to the short field and the associated field fringing however, the field strength reached only 68% in the centre of the pipe. The computed weight function with six electrodes showed still area of high sensitivity at each electrode but it was overall more uniform than a conventional 2 point electrode weight function. This result was verified with following experiments. A jet through an orifice plate 38mm upstream of the electrodes was rotated at radii of r=0, 0.5a and 1a. The flowrate was 1.5l/min which is equivalent to a mean velocity of v_m=0.08m/s. As a result it was found that the variation of the flow signal reduced by a factor of 2 compared to a meter with two point electrodes.
Al-Khazraji and Baker (1979) analyzed the performance of a flowmeter with large area, contacting electrodes. Three different arrangements were used for the coils; with or without yoke or the windings embedded into the flowtube. The weight functions were computed for all-contacting electrodes and it was shown that these weight functions were all more uniform than for point electrodes and for the previously

described six electrodes. Partially fouled electrodes were investigated as well. When part of the electrode is fouled, a quadrature signal is generated due to the loop which is formed with the electrode leads and the remaining conducting path in the liquid between the electrodes. For the case that the whole electrode was fouled except one edge, at a mean velocity of 1m/s, the transformer signal is a factor of 10 larger than the actual flow signal.

In order to overcome the disadvantage of the fouling of the large contacting electrodes, Wyatt and Cox (1983) designed a small E.M.Flowmeter with noncontacting large electrodes. The flowtube had 20mm diameter so that it was small enough to be used in medical applications. The electrodes were embedded into the flowtube and coated with a thin film of plastic to seal them off the liquid. To the rear, the electrodes were shielded with an active driven screen. The coils were operated at a 480Hz sinusoidal excitation. The high frequency allowed to use the meter in a pulsed flow up to 80Hz. Like in the experiment described above, a rotating jet through an orifice plate, 2mm off the pipe wall was used to investigate the sensitivity of the meter to non-axissymmetric flow. The result was such that the large electrodes reduced the sensitivity to the jet by a factor of 14 compared to point electrodes. This also shows a considerable increase in performance with regard to the 6-electrodes flowmeter.

Hussain and Baker(1985) optimised a noncontact large area electrode E.M.flowmeter. They considered a meter body with a magnetic field based on a commercial design. By using a finite difference method they optimised the insulation thickness between electrode and fluid in order to obtain a more uniform weight function W. For the computation, point electrodes were grouped in longitudinal arrays as 8 strip electrodes per quadrant. As a result, The insulation thickness increased from 1.5mm on the x-axis to 10.9mm on the y-axis (**Fig.1.4**). The non-uniformity ε of the weight function hereby reduced to 0.92% compared to 47.8% for the point electrode flowmeter. In a series of experiments a 76mm diameter flowtube was tested. Its electrodes were 76mm long with a subtended angle of 180°. An orifice plate with 38mm bore was placed 2.5D and 5.5D upstream of the centre of the electrodes; the bore was either in centre or midway between pipe axis and wall. The results showed only a 2% change in signal for the peak velocity at 90° to the electrodes and the orifice at 2.5D upstream. The effect of electrode fouling was simulated by smearing the electrode area with grease. The maximum change in sensitivity was only 0.17% which is small compared to a 1.8% change for large contacting electrodes(Al-Khazraji,Baker 1979).

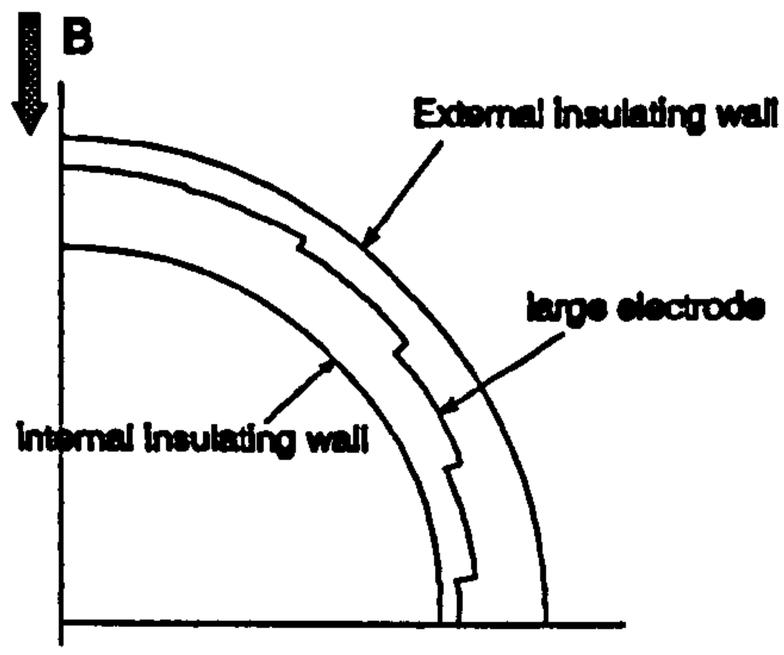

Fig.1.4 Optimised thickness of insulating layer in E.M.flowmeter with large area electrodes

Most of the optimizations have been made in order to make the weighting function as uniform as possible, whether for point-, strip- or large area electrodes. In the case of the large contacting area electrodes, the problem of electrode fouling was investigated and as a result, noncotacting, capacitively coupled electrodes seem to be the only way to realize them. As far as the fluid is considered, there was generally a single phase liquid assumed. Growing interest in multiphase flow however lead to the

investigation of the performance of E.M.flowmeters in various multiphase flow regimes.

1966, Masao Hori, Tetsuo Kobori and Yoshihirio Ouchi did a series of experiments with Electromagnetic Flowmeters in two phase flows.
As continuous phase they used mercury and water, the second phase were plastic rods. Two flowmeters were set in series, of which into flowmeter II the rods were inserted to simulate a void (**Fig.1.5**).
By inserting the rods of various sizes into the 1' flowtube they simulated an annular flow at flow rates between 0.15-1.5 m/s with a void fraction up to 75%. Beside the diameter of the rods they also varied its position in the cross section of the pipe and its number.
Because the flowrate of the continuous phase was the same in flowmeter I and II, the void fraction could be calculated from **eqn.1.1**, where E_I and E_{II} are the outputs of flowmeter I and II respectively.

$$\alpha = 1 - (E_I / E_{II}) \qquad \textbf{(1.1)}$$

Comparing the calculated void fraction with the measured one they could not find a clear dependency of the measured voltage on the factors above.

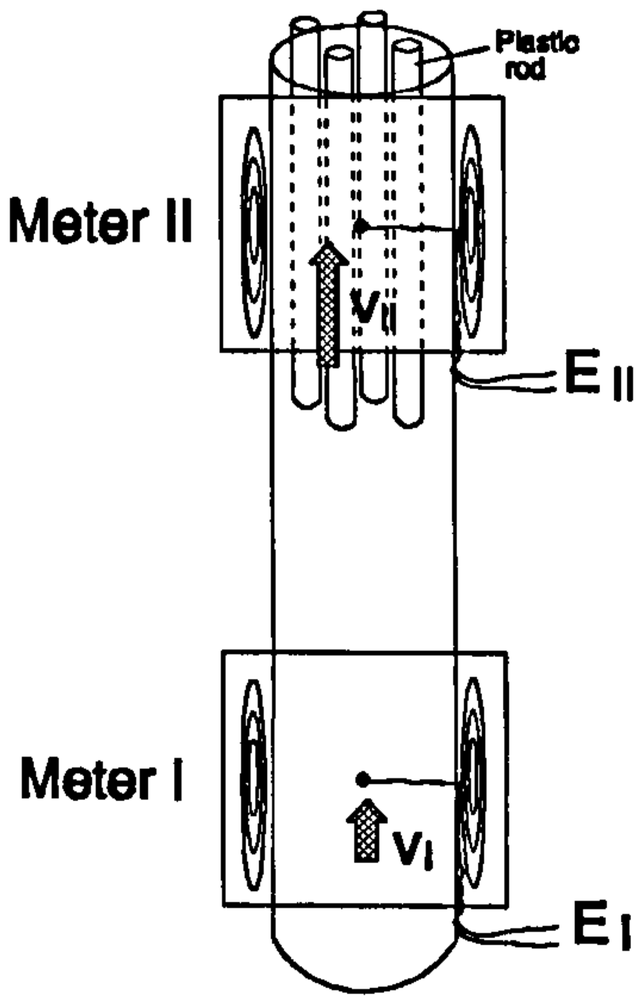

Fig.1.5 simulated void calibration

The measured void fractions were generally slightly lower than those calculated from the ratio of the pipe area and the cross section of the rod(s). It can be assumed that at high flow rates with an almost flat velocity profile the discrepancies vanish.
In 1982 Bernier and Brennan investigated the use of Electromagnetic flowmeters in two phase flows. For a single phase flow the potential difference between two opposite electrodes is $\Delta\phi = \frac{2BQ}{\pi b}$, where Q is the volume flow rate, B the magnetic field strength and b the radius of the pipe. They concluded that a well dispersed nonconducting second phase which has no relative motion to the main flow will give rise to a PD of $\Delta\phi = \frac{2BQ_l}{\pi b(1-\alpha)}$ **(1.2)** . Here, Q_l is the volume flow rate of the continuous water flow and α is the void fraction of the second, nonconducting phase. However this simple relation does only seem to be valid for the above mentioned well dispersed flow in which the main phase is continuous. In practice it is difficult to decide whether a flow is well enough dispersed or not. It is also still necessary to determine the void fraction separately in order to evaluate the volumetric flowrate of the continuous phase.

The second special case of a two phase flow, investigated by Bernier(1981) was the annular flow with a concentric gas core in the middle of the pipe.

The exact solution for the PD was then $\Delta\phi=\frac{2Bb}{\pi(b^2-c^2)}\int_c^b 2\pi r u(r)\,dr$, where c is the radius of the gas core. When substituting the void fraction $\alpha=c^2/b^2$ into the equation above, it is the same as the one for a fine dispersed flow. This result was also verified by D.Wyatt in 1986. For a flow with many long cylindrical voids Bernier(1981) calculated the PD with $\Delta\phi=\frac{2B}{\pi b}(1+\alpha)Q_l$, which is identical to **eqn.1.2** for low void fractions.

In order to verify their predictions, Bernier and Brennen tested a 4in Foxboro Flowmeter in a vertical pipe section. The flowmeters magnets were energised at a frequency of 380Hz. Flowrates were measured up to 1.14m/s superficial velocity and void fractions up to 20%. The results agreed very well with their predictions; a deviation of ±2% was recorded. Additionally it was found that the flow noise was almost independent of void content and flow rate.

The case of an annular flow with an insulating core was extended to the consideration of a core flow (Wyatt, 1986). The core flow was defined as a flow with a poorly conducting outer ring and a well conducting liquid core of radius c. The void fraction α is then $\alpha=\frac{(b^2-c^2)}{b^2}$, where b is again the inner radius of the pipe. If the ratio of the conductivities between conducting core and outer insulating ring yields infinity, then the potential difference between two point electrodes is given by

$$U=2\frac{B}{\pi b}\frac{Q_l}{1-\frac{\alpha}{2}}\ .$$

Wyatt also investigated uniform isotropic dispersed flows, where the nonconducting phase consists of thin rods or thin disks, parallel to the flow. In either case the result was the same as by Bernier and Brennen for the well dispersed flow with small spherical particles. He explains that, microscopically, the reduced volume of liquid between the nonconducting particles causes an increase in local virtual current density. This is balanced by the reduced volume of liquid and when integration the volume integral $U=\int_\tau \underline{B}\times\underline{j}\cdot\underline{v}\,d\tau$, U remains unchanged. If the two-phase flow becomes non uniform and non isotropic, further dependencies arise. Bevir(1971) showed that in this case the signal is a function of the conductivity distribution and the velocity profile.

In 1983, Deacon and Baker tested a commercial E.M.flowmeter with point electrodes and 50Hz mains excitation in a two phase air-water flow.. The meter was installed in a vertical pipe with a multihole plate inserted 25D upstream. The flow rate was between 7.5m^3/h and 15.3m^3/h, which is equivalent to a mean velocity of 0.26m/s and 0.52m/s respectively. The void fraction ranged from 0 to 14%. As a reference, the

water- and gas flow rates were measured separately and the actual flow rate was calculated, using the relation $Q=Q_l+Q_g'\frac{P_i}{P_t}$. Here, Q_l is the liquid flow rate, Q'_g the volumetric gas flow rate in the airline and P_i and P_t are measured pressures in the airline and the test section respectively. The readings of the E.M.flowmeter showed a maximum error of +0.5%,-3%, where the over reading was for 2% void fraction and the under reading at 14% void fraction.

A different approach to the multiphase flow was taken by I.D.Velt et al(1982). They considered the eddy currents due to the alternating magnetic field. When a nonconducting particle passes through the current field, it will unbalance the eddy currents and therefore produce a signal at the electrodes. This signal will vary along z as shown in **Fig.1.6**. The distance between the peaks is only determined by the geometry of the flowmeter, its magnetic field and the electrode design. It is independent of the flowrate since the eddy currents itself are present even without flow. By correlating the maxima of this signal in two cross sections of the pipe, it was possible to determine the flowrate, provided the particles had no relative velocity to the main flow.

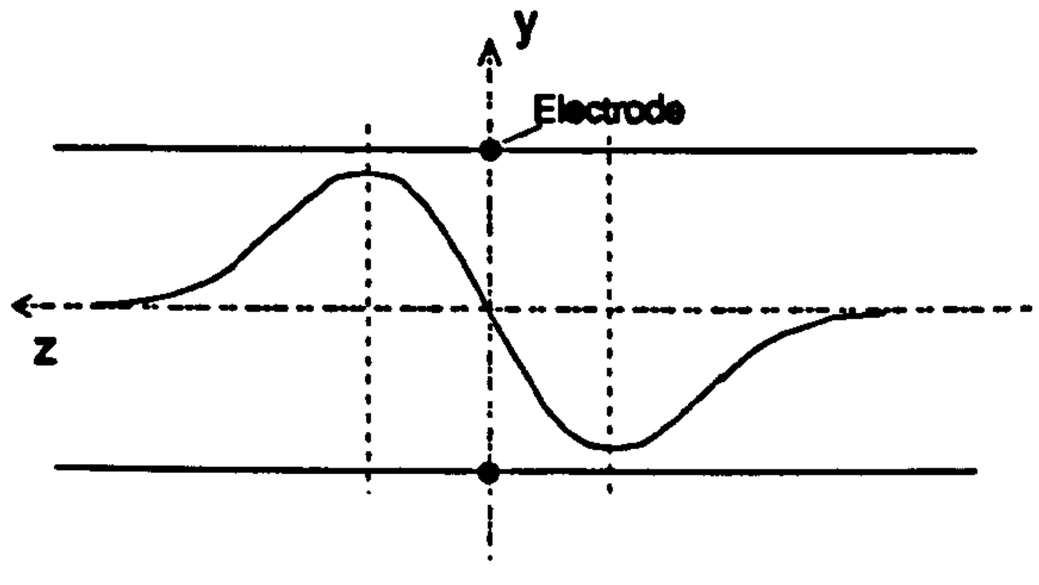

Fig.1.6 Transformer signal of a single spherical particle

Chapter 2

Noise signal without magnetic field

2.1 Experimental setup

At the beginning of a series of experiments with the 2" flowmeter, the noise signal from the electrodes was measured. It was not intended to investigate in every detail the causes of this noise but it had to be investigated whether a second phase causes a signal even in the absence of a magnetic field.
The flowmeter was mounted in the centre of a 2m long vertical pipe section. A straight length of 20 pipe diameters before and after the flow-meter ensured a well developed flow profile.
With the coils on the flow-meter switched off, the noise signal was recorded. Hereby, two signals were measured, one, which would be in phase with the flow signal and a second, which would have a phase shift of $\pi/2$ and is therefore in phase with the transformer signal. The noise was first measured in a single phase flow and then compared with that measured in a two phase flow. The second phase consisted in one case of plastic balls of 8mm diameter, released into the flow and in another case of air injected into the pipe. The real time signal was too low to show any obvious effects, therefore the noise spectrum was studied. None of the graphs show a significant noise signal increase due to a second phase. **Fig.2.1** and **Fig.2.2** show the noise spectra of the flow signal with and without balls being injected. The experiment has been carried out on various flow rates on upward and downward flow. The result is always the same.

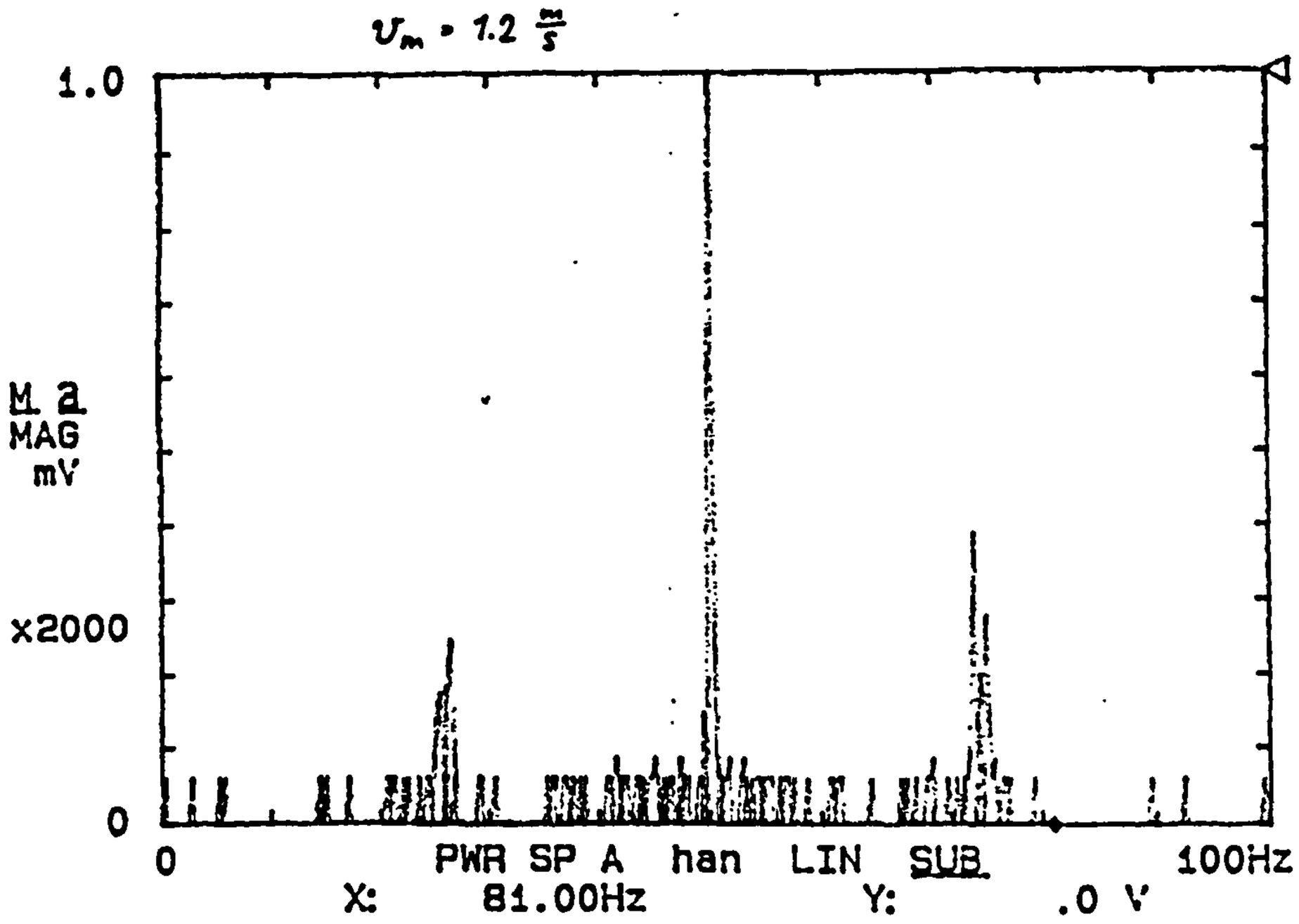

Fig.2.1 Measured noise signal without magnetic field in 2" flowmeter with point electrodes, water flow only

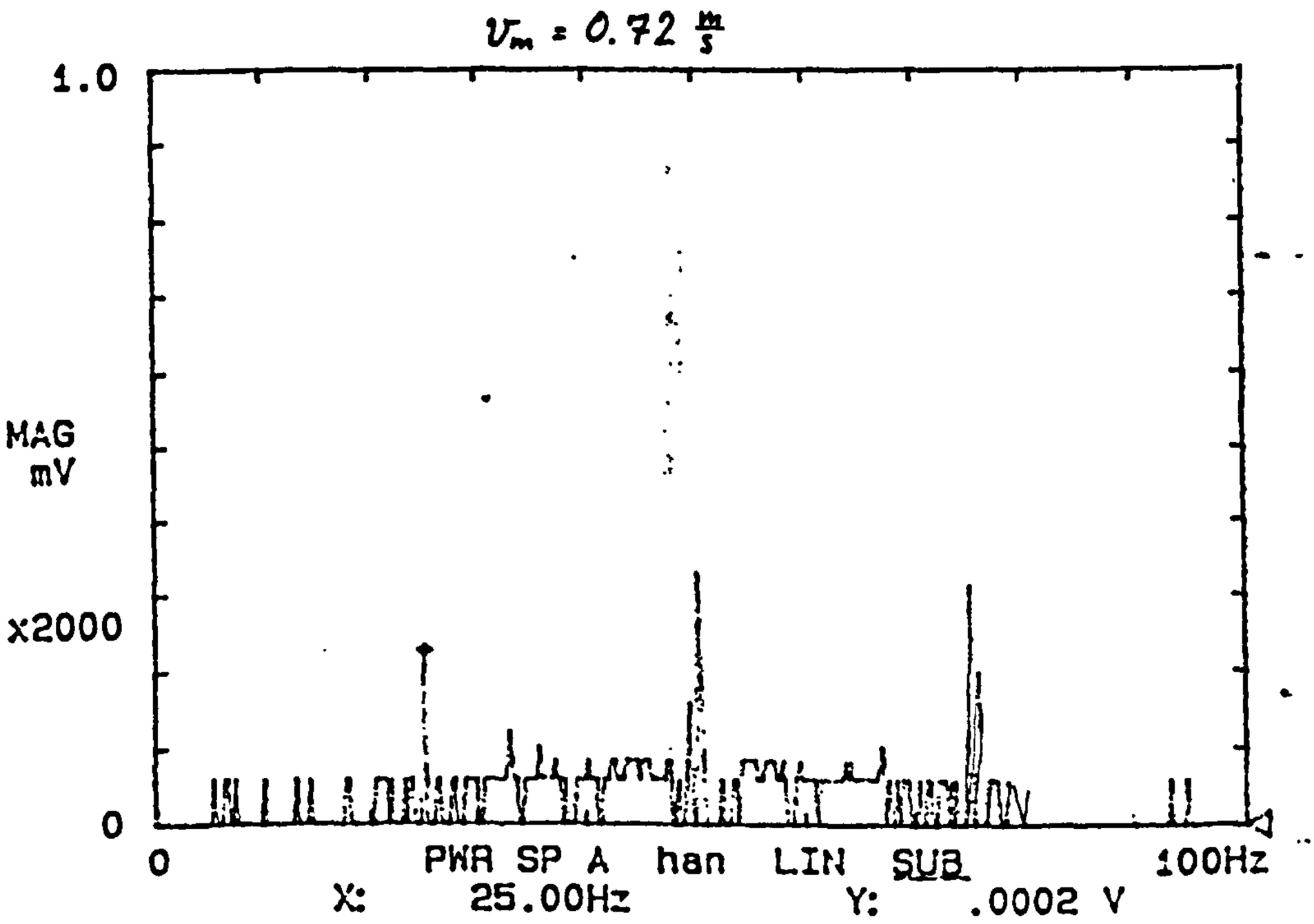

Fig.2.2 Measured noise signal without magnetic field in 2" flowmeter with point electrodes; plastic balls injected into water flow

Chapter 3

Flow Signal

A conductor of length l, moving through a static and uniform magnetic field induces at its ends a potential difference of $\Delta U = vBl$. This law applied to a conducting liquid flowing through a pipe still holds.The potential difference between two opposite electrodes for any axisymmetric, rectilinear flow is $\Delta U = v_m Bd$, where v_m is the mean velocity of the flow, B the magnetic field strength and d the diameter of the pipe. In order to investigate the influence of a second, nonconducting phase, the problem is simplified by regarding a single nonconducting sphere first. Two approaches are in principle possible:

3.1 Virtual current approach

The virtual current $\underline{j}$ is the imaginary current density in the fluid due to a unit current driven into one electrode and extracted from the opposite electrode. The potential difference between the electrodes is equal to the volume integral $U_0 = \int_{vol} \underline{v} \cdot \underline{W} d\upsilon$, where $\underline{W}$ is the weight vector $\underline{B} \times \underline{j}$. In the presence of a nonconducting particle the virtual current is altered by the amount of $\underline{j}'$ and hence the output signal is changed by $U' = \int_{vol} \underline{v} \cdot \underline{W}' d\upsilon$ with $\underline{W}' = \underline{B} \times \underline{j}'$. The total virtual current has to satisfy the boundary condition that its normal component is zero at all insulating surfaces i.e. at the pipe wall and the bubble surface.

3.2 Generator approach

The liquid passing through the meter can be imagined to consist of an infinite number of small cylindrical shaped voltage generators, each one contributing to the output signal by producing an electromotive force $d\varepsilon = \underline{v} \times \underline{B} \cdot \underline{\hat{u}} dl$, where dl is the length of the element and $\underline{\hat{u}}$ is the unit vector in direction of $\underline{v} \times \underline{B}$. Since the velocity of the fluid is not uniform across the pipe section the electromotive forces $d\varepsilon$ are not uniform either. As a result, the larger central e.m.f drives a current back against the weaker e.m.f close to the pipe wall and currents start circulating. The presence of an

airbubble will distort these currents and hence change the signal at the electrodes. The calculation of this signal change is done in two steps:

1. The circulating current j_0 is determined in the absence of a bubble (**Fig.3.1**)

2. A dipole current source j', opposing the circulating current, is inserted at the position of the bubble (**Fig.3.2**).

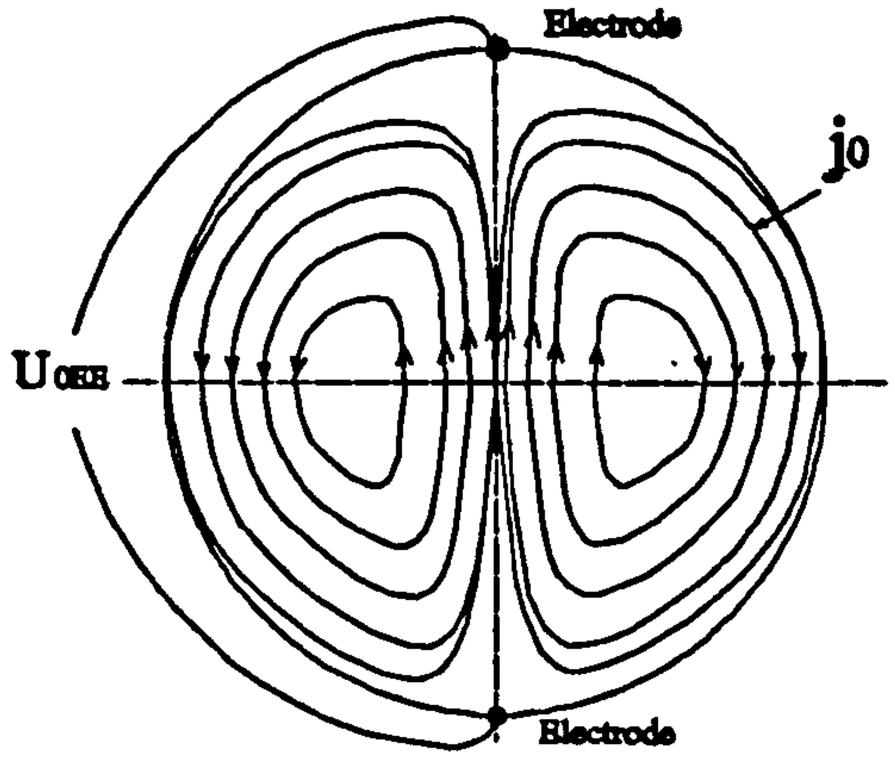

Fig.3.1 Circulating currents within an insulating pipe

Together, j_0 and j' have to satisfy the condition that the normal component j_n of the current is zero at all insulating surfaces. The relative change of the signal is then

$\Delta U_{rel}=U'_{EE}/U_{0EE}$, where U'_{EE} is the signal due to the bubble alone and U0EE is the signal without the bubble.

The first obvious result is that in a flow with a uniform velocity distribution no circulating currents exist, provided the magnetic field is uniform and infinitely long. In this case a bubble has no effect and the output is directly related to the velocity of the main flow.

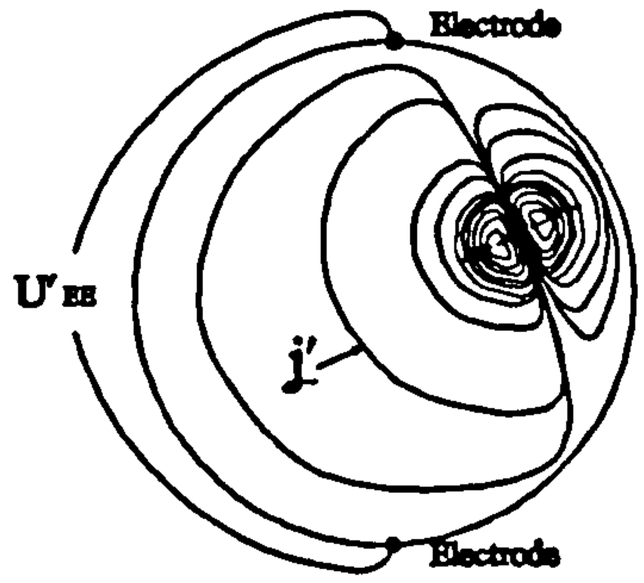

Fig.3.2 Dipole source within an insulating pipe

In the following attempt to predict the influence of a nonconducting second phase the generator approach is used. First of all some idealisations are made:

- the flowmeter has point electrodes
- the magnetic field is uniform, infinitely long and perpendicular to the flow
- the fluid flow is axisymmetric and rectilinear with a parabolic flow profile
- the undisturbed circulating current is uniform at the position of the bubble
- the size of the bubble is small compared with the pipe diameter

3.2.1 Circulating currents in a pipe section with a parabolic flow profile

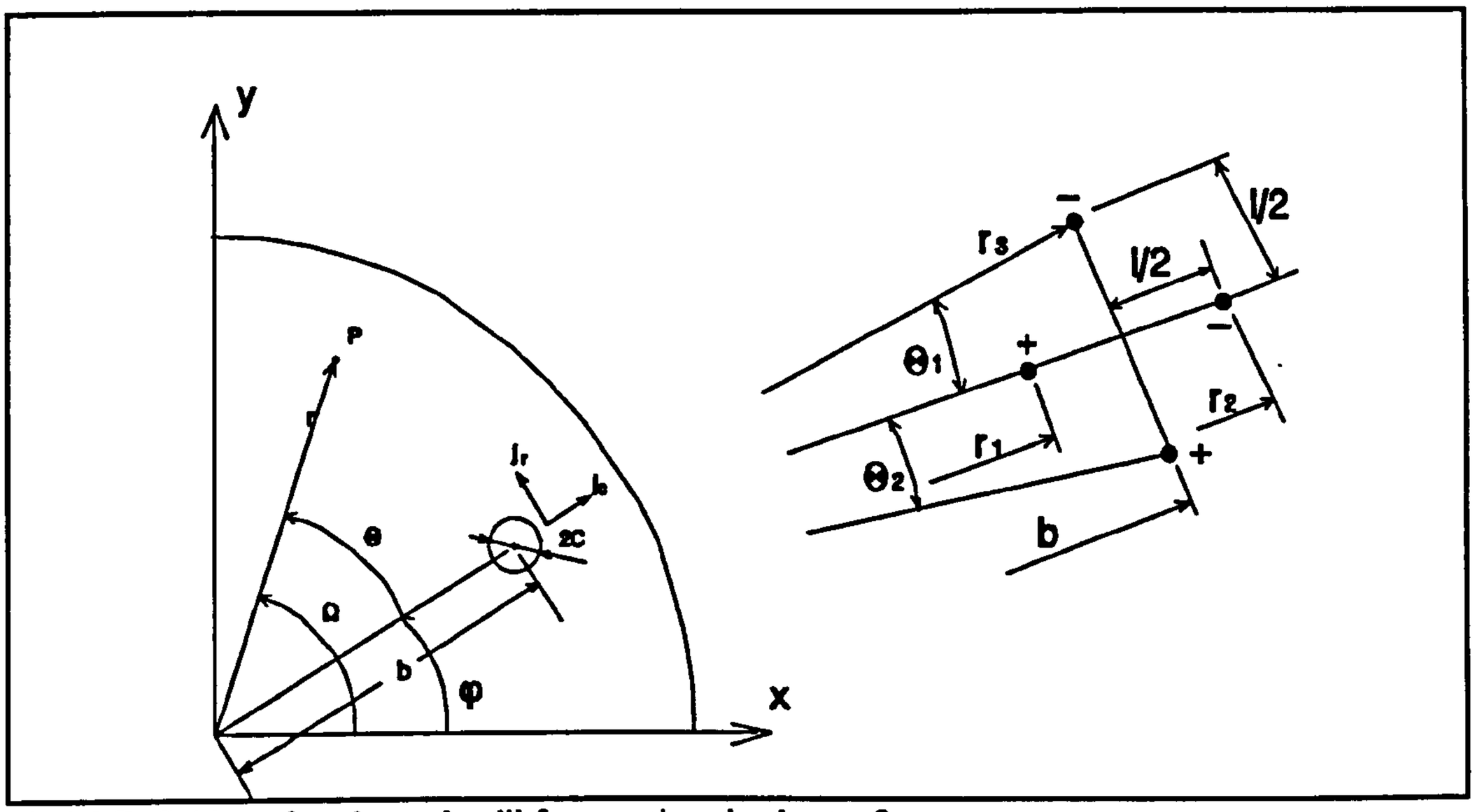

Fig.3.3 Definition of angles and radii for equations in chapter 3

The flow at any point in the cross section of the pipe is assumed to have the profile shown in **Fig.3.4.**

$$v_z(r)=2v_m\left(\frac{r^2}{a^2}-1\right) \tag{3.1}$$

where v_m is the mean velocity of the flow

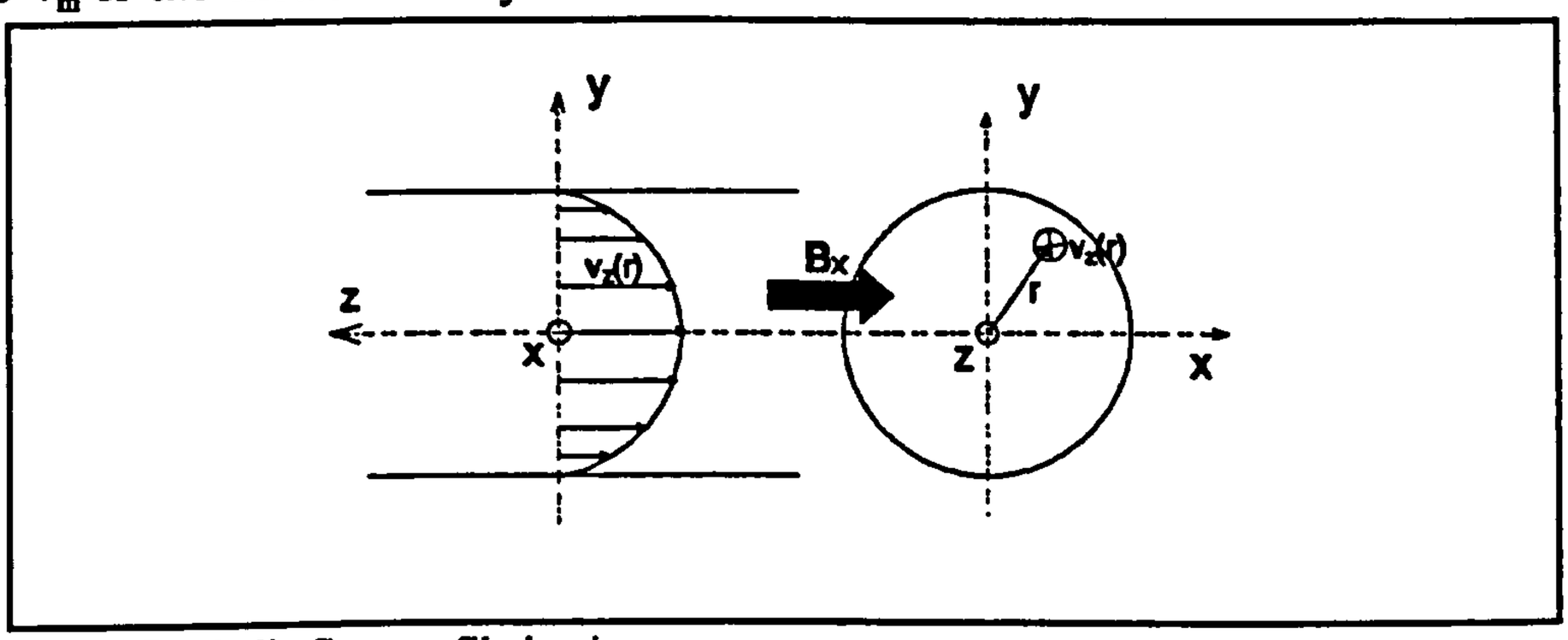

Fig.3.4 Parabolic flow profile in pipe

To find the current due to this velocity profile, the equations to be satisfied are

$$\underline{j}=\sigma(\underline{E}+\underline{v}\times\underline{B})$$

$$\nabla\times\underline{E}=0$$

$$\nabla\cdot\underline{j}=0$$

$j_n=0$ at the pipe wall i.e. at r=a

With $E=-\nabla U$, we can write j as

$$\underline{j}=\sigma(\underline{E}+\underline{v}\times\underline{B})=\sigma(-\nabla U+\underline{v}\times\underline{B})$$

$$\nabla\cdot\underline{j}=0\Rightarrow\frac{\partial j_x}{\partial x}+\frac{\partial j_y}{\partial y}+\frac{\partial j_z}{\partial z}=0$$

Because the radial component of j is zero at the pipe wall, we find

$$\underline{j}_n\Big|_{r=a}=0\Rightarrow\frac{j_n}{\sigma}=(-\nabla U+\underline{v}\times\underline{B})_n=0$$

$$\therefore\nabla U=v\times B$$

By definition, $\nabla^2=\nabla\cdot\nabla U$

$$\therefore\nabla^2U=\nabla\cdot(\underline{v}\times\underline{B})=\underline{B}\cdot\nabla\times\underline{v}$$

Expanding the expression above and writing it in polar coordinates yields

$$\nabla^2U=\frac{1}{r}\frac{\partial}{\partial r}(r\frac{\partial U}{\partial r})+\frac{1}{r^2}\frac{\partial^2U}{\partial\varphi^2}+\frac{\partial^2U}{\partial z^2}=\underline{B}\cdot\nabla\times\underline{v}$$

$$\frac{\partial^2U}{\partial r^2}+\frac{1}{r}\frac{\partial U}{\partial r}+\frac{1}{r^2}\frac{\partial^2U}{\partial\varphi^2}+\frac{\partial^2U}{\partial z^2}=$$

$$(B_r\underline{a}_r+B_\varphi\underline{a}_\varphi+B_z\underline{a}_z)[(\frac{1}{r}\frac{\partial v_z}{\partial\varphi}-\frac{\partial v_\varphi}{\partial z})\underline{a}_r+(\frac{\partial v_r}{\partial z}-\frac{\partial v_z}{\partial r})\underline{a}_\varphi+\frac{1}{r}(\frac{\partial}{\partial r}(r-v_\varphi)-\frac{\partial v_r}{\partial\varphi})\underline{a}_z]$$

$$\frac{\partial^2U}{\partial r^2}+\frac{1}{r}\frac{\partial U}{\partial r}+\frac{1}{r^2}\frac{\partial^2U}{\partial\varphi^2}=\frac{1}{r}B_r\frac{\partial v_z}{\partial\varphi}-B_\varphi\frac{\partial v_z}{\partial r}$$

with $B_r=B_x\cos\varphi+B_y\sin\varphi$; $B_\varphi=B_y\cos\varphi-B_x\sin\varphi$

$$\frac{\partial^2U}{\partial r^2}+\frac{1}{r}\frac{\partial U}{\partial r}+\frac{1}{r^2}\frac{\partial^2U}{\partial\varphi^2}=\frac{1}{r}(B_x\cos\varphi+B_y\sin\varphi)\frac{\partial v_z}{\partial\varphi}-(B_y\cos\varphi-B_x\sin\varphi)\frac{\partial v_Z}{\partial r}$$

if $v_Z(r)=2v_m(\frac{r^2}{a^2}-1)$, *then* $\frac{\partial v_Z}{\partial r}=2v_m2\frac{r}{a^2}=4v_m\frac{r}{a^2}$; $\frac{\partial v_z}{\partial\varphi}=0$

$$\therefore\frac{\partial^2U}{\partial r^2}+\frac{1}{r}\frac{\partial U}{\partial r}+\frac{1}{r^2}\frac{\partial^2U}{\partial\varphi^2}=4B_X\sin\varphi\,v_m\frac{r}{a^2}$$

A solution for this equation can be found by guessing a solution (U^*) first without considering the boundary condition that $\frac{\partial U}{\partial n}\Big|_{r=a}=0$.

Then another potential U′ is determined, satisfying Laplace's equation $\nabla^2U'=0$ and the condition $\frac{\partial U'}{\partial n}\Big|_{r=a}=-\frac{\partial U^*}{\partial n}\Big|_{r=a}$

Superimposing U′ and U* then yields U=U′+U*, with

$$\nabla^2 U = 4B_x \sin\varphi \, v_m \frac{r}{a^2} \; ; \qquad \frac{\partial U}{\partial n}\Big|_{r=a} = 0$$

First, a solution is guessed for U* :

$$U^* = \frac{1}{2} B_x v_m \sin\varphi \frac{r^3}{a^2} \tag{3.2}$$

Its derivatives are

$$\frac{\partial U^*}{\partial r} = \frac{3}{2} B_x v_m \sin\varphi \, \frac{r^2}{a^2}$$

$$\frac{\partial^2 U^*}{\partial r^2} = \frac{6}{2} B_x v_m \sin\varphi \, \frac{r}{a^2}$$

$$\frac{\partial U^*}{\partial \varphi} = \frac{1}{2} B_x v_m \cos\varphi \, \frac{r^3}{a^2}$$

$$\frac{\partial^2 U^*}{\partial \varphi^2} = -\frac{1}{2} v_m \sin\varphi \, \frac{r^3}{a^2}$$

$$\frac{\partial U^*}{\partial r}\Big|_{r=a} = \frac{3}{2} B_x v_m \sin\varphi \Rightarrow \frac{\partial U'}{\partial r} = -\frac{3}{2} B_x v_m \sin\varphi$$

$$\nabla^2 U' = \frac{\partial^2 U'}{\partial r^2} + \frac{1}{r}\frac{\partial U'}{\partial r} + \frac{1}{r^2}\frac{\partial^2 U'}{\partial \varphi^2} = 0$$

By means of separation of variables the solution for U′ is found. The result is

$$U' = -\frac{3}{2} B_x v_m r \sin\varphi \tag{3.3}$$

Now, U_0 can be determined by adding U* and U′ **(eqn.3.2, 3.3)**

$$U_0 = \frac{1}{2} B_x v_m \sin\varphi \left(\frac{r^3}{a^2} - 3r\right) \tag{3.4}$$

Having obtained U_0, $\underline{E}_0$ and $\underline{j}_0$ can be evaluated:

$$\underline{E}_0 = -\nabla U_0 = -\left(\frac{\partial U_0}{\partial r}\underline{a}_r + \frac{1}{r}\frac{\partial U_0}{\partial \varphi}\underline{a}_\varphi + \frac{\partial U_0}{\partial z}\underline{a}_z\right)$$

$$\underline{E}_0=-[\frac{1}{2}B_x v_m \sin\varphi(3\frac{r^2}{a^2}-3)\underline{a}_r+\frac{1}{2r}B_x v_m \cos\varphi(\frac{r^3}{a^2}-3r)\underline{a}_\varphi]$$

Since $v_z(r)=2v_m(\frac{r^2}{a^2}-1)$; $\underline{B}=B_r\underline{a}_r+B_\varphi\underline{a}_\varphi$,

$$\underline{v}\times\underline{B}=\begin{vmatrix}\underline{a}_r & \underline{a}_\varphi & \underline{a}_Z\\ 0 & 0 & 2v_m(\frac{r^2}{a^2}-1)\\ B_r & B_\varphi & 0\end{vmatrix}=-B_\varphi 2v_m(\frac{r^2}{a^2}-1)\underline{a}_r+B_r 2v_m(\frac{r^2}{a^2}-1)\underline{a}_\varphi$$

$$\underline{v}\times\underline{B}=2v_m(\frac{r^2}{a^2}-1)[(B_x\sin\varphi-B_y\cos\varphi)\underline{a}_r+(B_x\cos\varphi+B_y\sin\varphi)\underline{a}_\varphi]$$

$$\underline{v}\times\underline{B}=2v_m(\frac{r^2}{a^2}-1)B_x(\sin\varphi\underline{a}_r+\cos\varphi\underline{a}_\varphi)$$

$$\underline{j}_0=\sigma(-\nabla\underline{U}+\underline{v}\times\underline{B})$$

$$\underline{j}_0=\frac{\sigma}{2}B_x v_m[(3-3\frac{r^2}{a^2}+4\frac{r^2}{a^2}-4)\sin\varphi\underline{a}_r+(-\frac{r^2}{a^2}+4\frac{r^2}{a^2}-1)\cos\varphi\underline{a}_\varphi]$$

$$\boxed{\underline{j}_0=\frac{1}{2}\sigma B_x v_m[(\frac{r^2}{a^2}-1)\sin\varphi\underline{a}_r+(3\frac{r^2}{a^2}-1)\cos\varphi\underline{a}_\varphi]} \qquad (3.5)$$

This is the circulating current due to a parabolic flow profile in a pipe with insulating walls and uniform magnetic field.

In order to plot the current in vector form it is more convenient to write $\underline{j}_0$ in cartesian coordinates:

$$\boxed{\underline{j}_0=\frac{1}{2}\sigma B_x v_m[(-2\frac{xy}{a^2})\underline{a}_x+(\frac{3x^2+y^2}{a^2}-1)\underline{a}_y]} \qquad (3.5a)$$

$$\boxed{|\underline{j}_0|=\frac{1}{2}\sigma B_x v_m\sqrt{(-2\frac{xy}{a^2})^2+(\frac{3x^2+y^2}{a^2}-1)^2}} \qquad (3.5b)$$

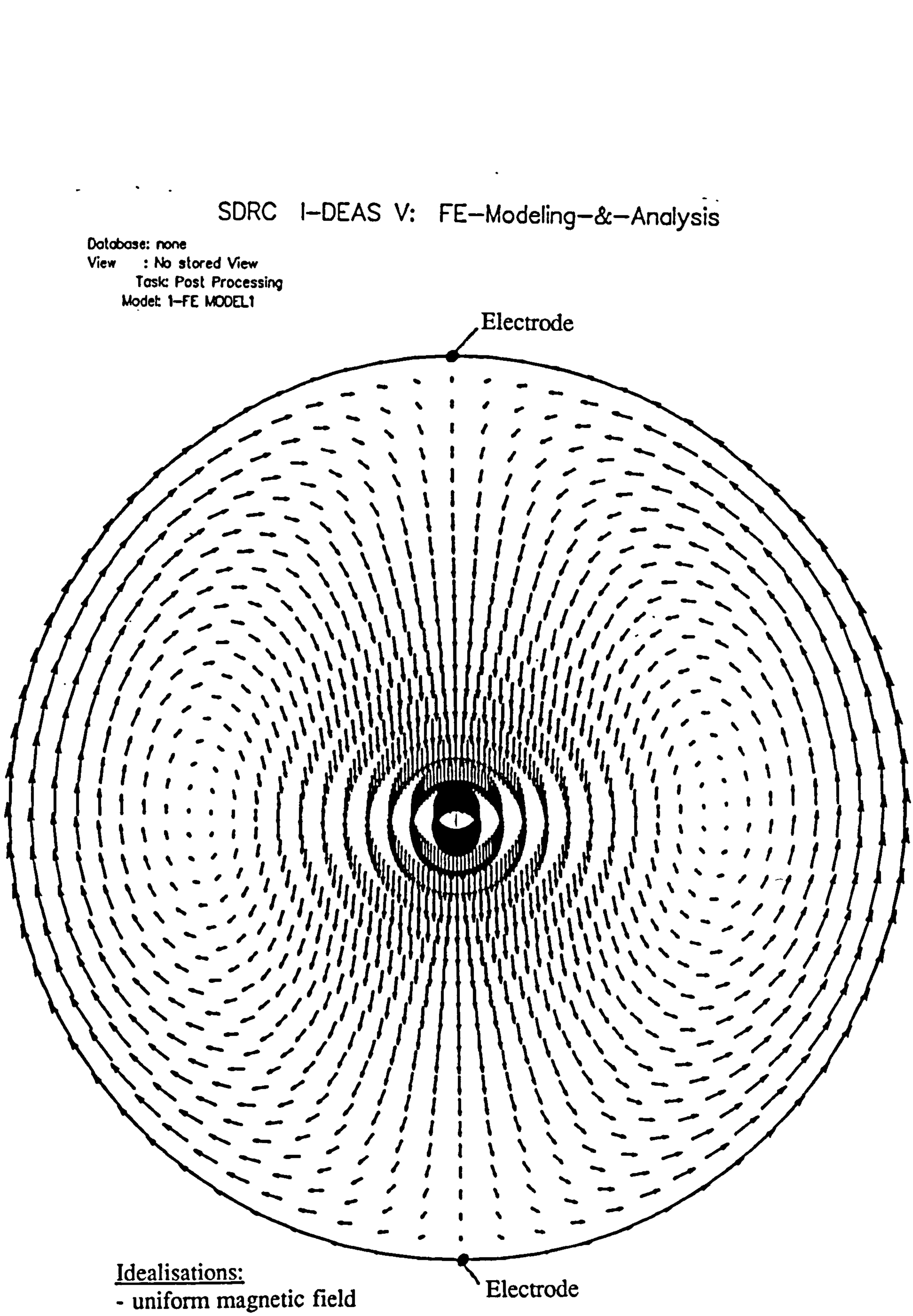

Idealisations:
- uniform magnetic field
- parabolic flow profile
- 2 point electrodes

Fig.3.5 Computed circulating currents in insulated pipe with uniform magnetic field, parabolic flow profile and 2 point electrodes

3.2.2 Dipole current source and potential difference between point electrodes

The basic equations for a conducting liquid flowing through a magnetic field are

$$\underline{j}=\sigma(\underline{E}+\underline{v}\times\underline{B})$$

$$\nabla\times\underline{E}=0$$

$$\nabla\cdot\underline{j}=0$$

$j_n=0$ at all insulating surfaces i.e
at the pipe wall and on the bubble surface.

These conditions have been so far satisfied with **eqn.3.5** except the condition that the current on the bubble surface $j_{0n}=0$. Thus another current $\underline{j}'$ has to be added, so that $j_n=j_{0n}+j'_n=0$, i.e $j'_n=(-j_0)_n$ on the bubble surface. Conditions for the new current distribution therefore are:

$$\underline{j'}=\sigma\cdot\underline{E'}$$

$$\nabla\times\underline{E'}=0$$

$$\nabla\cdot\underline{j'}=0$$

$j'_n=(-j_0)_n$ on bubble surface
$j'_n=0$ at the pipe wall

Without regard to the boundary conditions on the pipe wall and considering the condition of $j_n=0$ on the bubble surface only, a solution (outside the bubble) can be found by imposing a dipole source of appropriate
strength onto the uniform current j_0 **(Fig.3.6)**

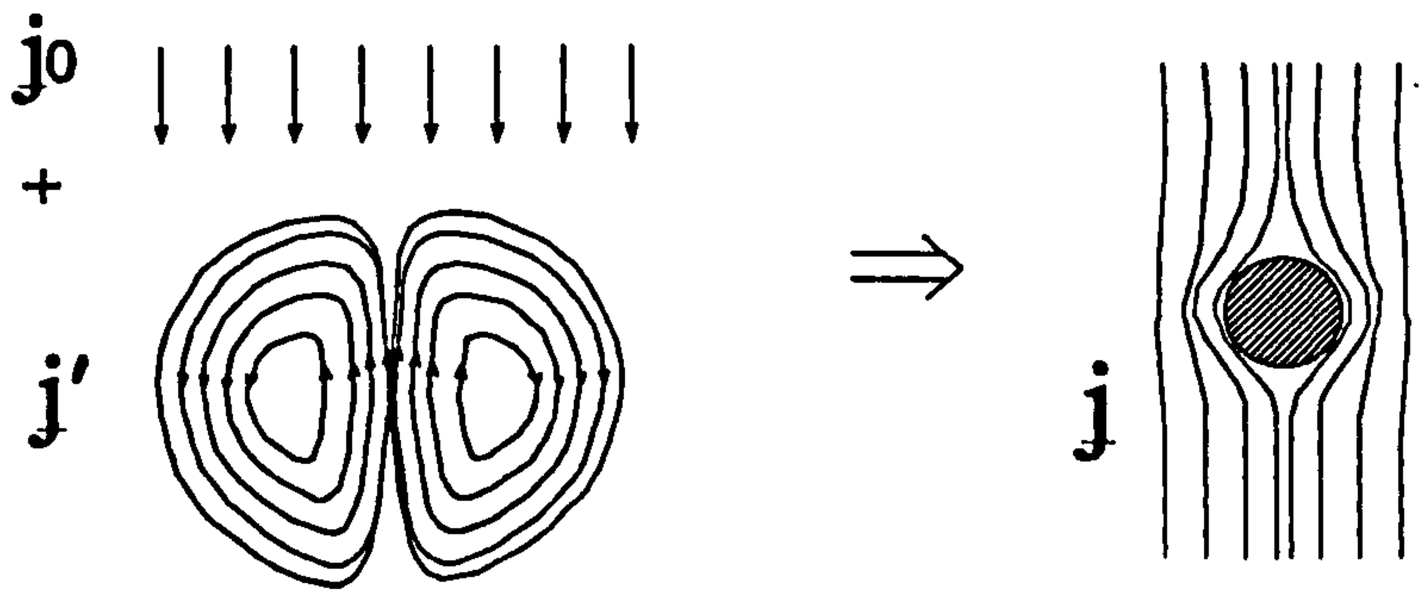

Fig.3.6 Current dipole inserted into a uniform current

Provided the bubble diameter is small compared to the pipe size, the current j_0 can be treated as uniform in the region of the bubble. The distortion of the current dipole by the pipe wall is negligible if the bubble is not too close to it. In this case the wall boundary condition $j'_n=0$ can be neglected because of the rapid decaying of a dipoles potential. Therefore it has to be a dipole current distribution found as a function $f(r,\theta,z)$.

Any function $f(r,\theta)$ $0\le r\le a$; $-\pi\le\theta\le\pi$ *with* $\frac{\partial f}{\partial r}\Big|_{r=a}=0$ **(Fig.3.7)** can be written as a Fourier -Bessel series

$$f(r,\theta)=\sum_{m=-\infty}^{\infty}\sum_{n=1}^{\infty}f_{n,m}e^{im\theta}J_{|m|}(j'_{|m|n}\frac{r}{a}) \qquad (3.6)$$

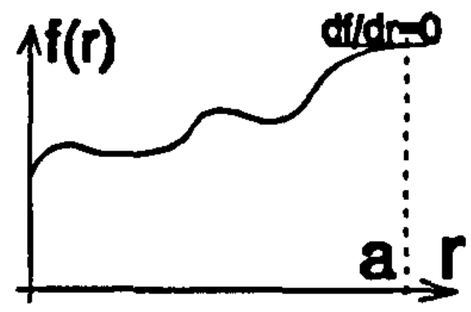

Fig.3.7 Function written as Fourier-Bessel series

Here $J_m(x)$ is the Bessel function of order 'm'(m=0;1;2;3;...) and j'_{mn} is the n_{th} zero of $\frac{\partial(J_m(x))}{\partial x}$ *i.e.* $\frac{\partial(J_m(x))}{\partial x}\Big|_{x=j'_{mn}}=0$ (n=1;2;3;...)

Thus the eqn. $\nabla^2U'=0$ with $\frac{\partial U'}{\partial r}\Big|_{r=a}=0$ can be written as a double series where U′ is a function of r, θ and z.

$$U'(r,\theta,z)=\sum_{m=-\infty}^{\infty}\sum_{n=1}^{\infty}U'_{n,m}e^{im\theta}J_{|m|}(j'_{|m|n}\frac{r}{a}) \qquad (3.7)$$

where $U'_{nm}=U'_{nm}(z)$

Substituting $U'_{nm}(z)$ into ∇^2U' :

$$\frac{\partial^2U'}{\partial r^2}+\frac{1}{r}\frac{\partial U'}{\partial r}+\frac{1}{r^2}\frac{\partial^2U'}{\partial\theta^2}+\frac{\partial^2U'}{\partial z^2}=0 \;\; yields \;\; \frac{\partial^2U'_{nm}}{\partial z^2}-(\frac{j'_{|m|n}}{a})^2U'_{nm}=0$$

with the general solution

$$U'_{nm}=a_{nm}e^{\pm\frac{j'_{|m|n}}{a}z}\;, \; where \;\; a_{nm} \; are \; constants$$

Substituting U'_{nm} now into **eqn.3.7** yields

$$U'=\sum_{m=-\infty}^{\infty}\sum_{n=1}^{\infty}a_{nm}e^{im\theta}J_{|m|}(j'_{|m|n}\frac{r}{a})\,e^{-\frac{j'_{|m|n}}{a}z} \qquad (3.8)$$

The $e^{+\frac{j'_{|m|n}}{a}z}$ is omitted (for z>0) because U′ has to decay for $z\to\infty$.

So far only a general solution for $\nabla^2U'=0$ has been obtained without considering the current dipole. Placing a unit current source and a unit current sink at two points on the x-axis, we can find the distribution of U′ by using **eqn.3.8** with $|z|$ instead of z.

The coefficients a_{nm} have to be chosen so as to satisfy

$$-\frac{\partial U'}{\partial z}\Big|_{0+}+\frac{\partial U'}{\partial z}\Big|_{0-}=\frac{1}{r}\delta(\theta)[\delta(r-r_1)-\delta(r-r_2)] \qquad \textbf{(3.9)}$$

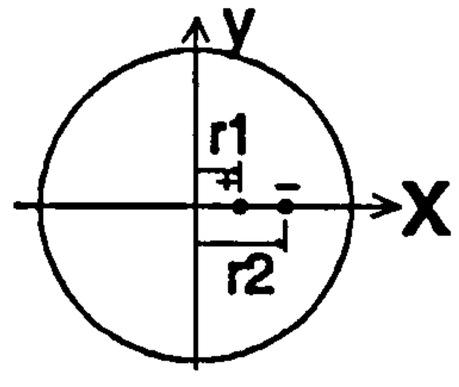

Fig.3.8 Definition of radii to current source and -sink

differentiating **eqn.3.8**, we then obtain

$$-\frac{\partial U'}{\partial z}\Big|_{0+}+\frac{\partial U'}{\partial z}\Big|_{0-}=-2\frac{\partial U'}{\partial z}\Big|_{0+}$$

$$=-2\sum\sum a_{nm}e^{im\theta}J_{|m|}(j'_{|m|n}\frac{r}{a})(-\frac{j'_{|m|n}}{a})e^{-\frac{j'_{|m|n}}{a}|z|} \qquad \textbf{(3.10)}$$

A basic property of the delta-function is, that
a)it is ∞ at its origin and 0 elsewhere

b) $\int_b \delta(r)\,dr=1$

c) $\int_a f(x)\,\delta(x-x_0)\,dx=f(x_0)\,1$

hence $$\iint\frac{1}{r}\delta(\theta)\,\delta(r-r_1)\,r\,dr\,d\theta=\int\delta(\theta)d\theta\int\delta(r-r_1)dr=1 \qquad \textbf{3.(11)}$$

when combining **eqn.3.9** and **eqn.3.10** one obtains

$$\frac{1}{r}\delta(\theta)[\delta(r-r_1)-\delta(r-r_2)]=2\sum_m\sum_n a_{nm}e^{im\theta}J_{|m|}(j'_{|m|n}\frac{r}{a})\frac{j'_{|m|n}}{a} \qquad \textbf{(3.12)}$$

The general solution for the coefficients f_{nm} as in **eqn.3.6** is

$$f_{nm}=\frac{\int_{-\pi}^{\pi}\int_0^a f(r,\theta)\,e^{-im\theta}J_{|m|}(j'_{|m|n}\frac{r}{a})\,r\,dr\,d\theta}{\frac{\pi a^2}{j'^2_{|m|n}}(j'^2_{|m|n}-m^2)(J_{|m|}(j'_{|m|n}))^2} \qquad \text{(see Appendix A)} \qquad \textbf{(3.13)}$$

The left hand side of **eqn.3.12** is a function $f(r,\theta)$ and on the right hand side the terms $2a_{n,m}\frac{j'_{|m|n}}{a}$ make up the coefficients f_{nm}.

Inserting these expressions into **eqn.3.13** yields

$$2a_{nm}\frac{j'_{|m|n}}{a}=\frac{\int_{-\pi}^{\pi}\int_0^a\frac{1}{r}\delta(\theta)(\delta(r-r_1)-\delta(r-r_2))\,e^{-im\theta}J_{|m|}(j'_{|m|n}\frac{r}{a})\,r\,dr\,d\theta}{\frac{\pi a^2}{j'^2_{|m|n}}(j'^2_{|m|n}-m^2)(J_{|m|}(j'_{|m|n}))^2}$$

Splitting up the numerator into the sum of two integrals and using **eqn.3.11** we obtain the coefficients a_{nm} of **eqn.3.8.**

$$a_{nm}=\frac{j'_{|m|n}}{2\pi a}\frac{J_{|m|}(j'_{|m|n}\frac{r_1}{a})-J_{|m|}(j'_{|m|n}\frac{r_2}{a})}{(j'^2_{|m|n}-m^2)(J_{|m|}(j'_{|m|n}))^2} \tag{3.14}$$

Since it is easier and faster to carry out the computation with real numbers rather than with complex ones, **eqn.3.8** is rearranged:

$$U'_1=\sum_{m=0}^{\infty}\sum_{n=1}^{\infty}[a_{n,-m}e^{-im\theta}J_{|m|}(j'_{|m|n}\frac{r}{a})e^{-\frac{j'_{|m|n}}{a}|z|}$$
$$+a_{n,m}e^{im\theta}J_{|m|}(j'_{|m|n}\frac{r}{a})e^{-\frac{j'_{|m|n}}{a}|z|}(1-\frac{1}{2}\delta_{m0})]$$

$$U'_1=\sum_{m=0}^{\infty}\sum_{n=1}^{\infty}(a_{n-m}e^{-im\theta}+a_{nm}e^{im\theta})J_{|m|}(j'_{|m|n}\frac{r}{a})e^{-\frac{j'_{|m|n}}{a}|z|}(1-\frac{1}{2}\delta_{m0}) \tag{3.15}$$

The last term $(1-\frac{1}{2}\delta_{m0})$ provides that every term in the series is multiplied by 1 for $m\neq 0$ and by 1/2 for m=0. By inspecting **eqn.3.13** it can be seen that $a_{nm}=a_{n,-m}$. Rewriting **eqn.3.15** therefore gives

$$U'_1=\sum_{m=0}^{\infty}\sum_{n=1}^{\infty}a_{nm}(e^{-im\theta}+e^{im\theta})J_{|m|}(j'_{|m|n}\frac{r}{a})e^{-\frac{j'_{|m|n}}{a}|z|}(1-\frac{1}{2}\delta_{m0}) \tag{3.16}$$

but $(e^{-im\theta}+e^{im\theta})=2\cosh(im\theta)=2\cos(m\theta)$

hence **eqn.3.16** can finally be written as:

$$U'_1=\sum_{m=0}^{\infty}\sum_{n=1}^{\infty}a_{nm}\frac{\cos(m\theta)}{\pi a}C(1-\frac{1}{2}\delta_{m0}) \tag{3.17}$$

potential distribution of a radially directed dipole, in a cylinder with insulating walls.

$$a_{nm}=j'_{|m|n}\frac{J_{|m|}(j'_{|m|n}\frac{r_1}{a})-J_{|m|}(j'_{|m|n}\frac{r_2}{a})}{(j'^2_{|m|n}-m^2)(J_{|m|}(j'_{|m|n}))^2} \tag{3.18}$$

$$C=J_{|m|}(j'_{|m|n}\frac{r}{a})e^{-\frac{j'_{|m|n}}{a}|z|} \tag{3.19}$$

Note:For m=0;n=1, all terms $e^{i0\theta}$; $J_{|0|}(j'_{|0|1})$; $e^{-j'_{|0|1}\frac{|z|}{a}}$ in **eqn.3.17** are 1. Therefore, $a_{1,0}$ has to be zero to satisfy $U'_1=0$ for $z\to\infty$.
In the following **Fig.3.9, 3.11 & 3.14,** z and b are shown as fraction of the pipe radius.

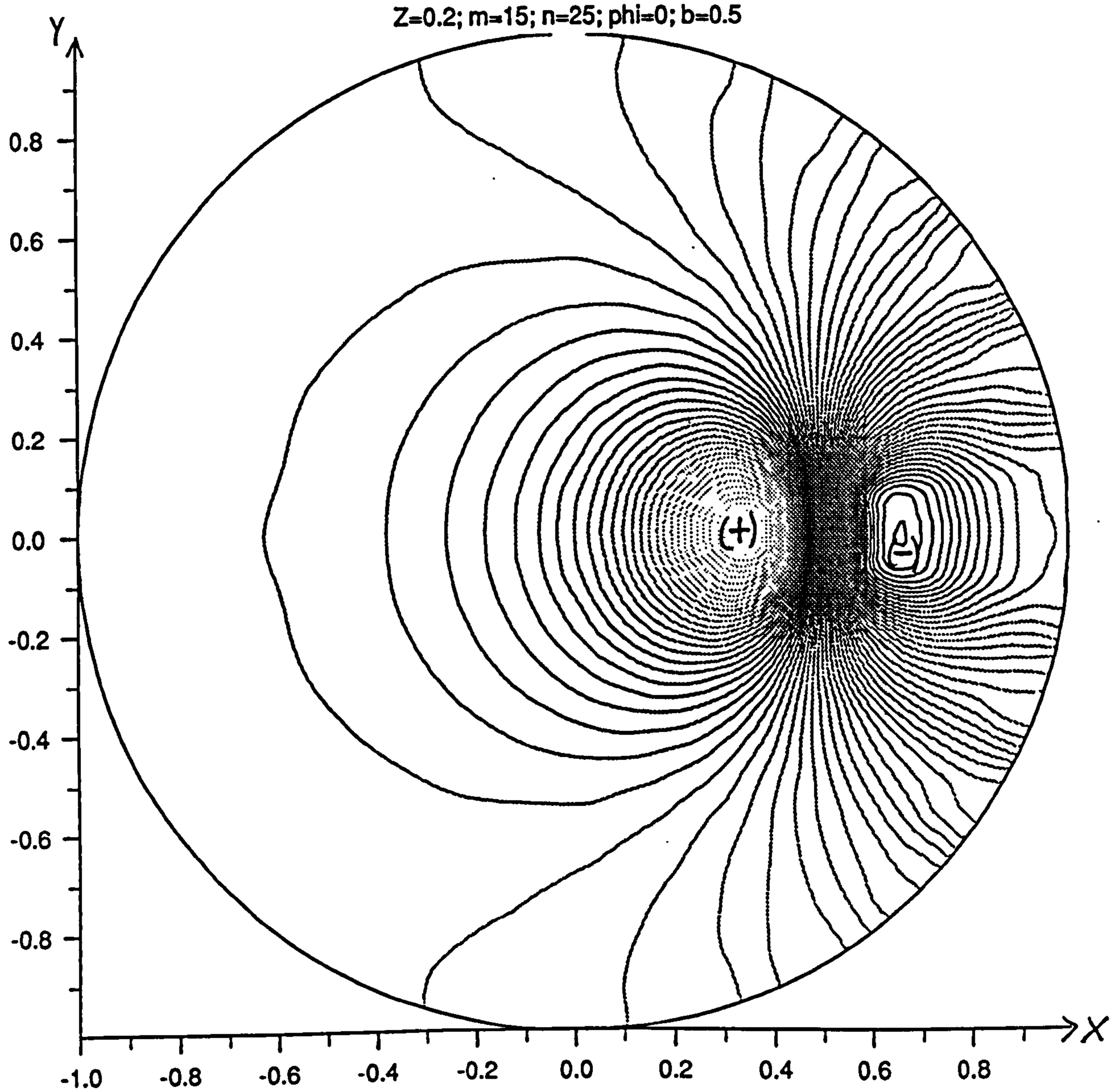

Fig.3.9 Potential lines of a radially directed dipole in an insulating pipe

The expression for U'_2, representing the potential of a vertical dipole, ie one positioned on the x-axis and pointing in the y-direction (**Fig.3.10**)is derived in a way similar to **eqn.3.17.**

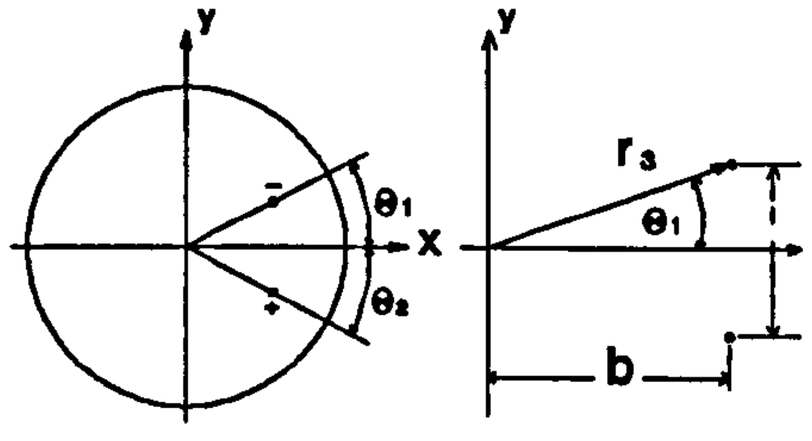

Fig.3.10 Definition of angle and radii to current source and -sink

The coefficients a_{nm} of **eqn.3.8** now have to satisfy the condition

$$-\frac{\partial U_2'}{\partial z}\Big|_{0+}+\frac{\partial U_2'}{\partial z}\Big|_{0-}=\frac{1}{r}\delta(r-r_3)[\delta(\theta-\theta_1)-\delta(\theta-\theta_2)] \qquad \textbf{(3.20)}$$

Combining **eqn.3.10** and **eqn.3.20** then yields the following equation, where on the left hand side we again have a function $f(r,\theta)$ and on the right hand side the terms $2b_{nm}\frac{j'_{|m|n}}{a}$ make up the coefficients f_{nm}.

$$\frac{1}{r}\delta(r-r_3)(\delta(\theta-\theta_1)-\delta(\theta-\theta_2))=2\sum_m\sum_n b_{nm}e^{im\theta}J_{|m|}(j'_{|m|n}\frac{r}{a})\frac{j'_{|m|n}}{a}$$

Using again the general expression for the coefficients f_{nm} from **eqn.3.13**, we can write b_{nm} as:

$$b_{nm}=\frac{j'_{|m|n}}{2\pi a}\frac{\int_{-\pi}^{\pi}\int_0^a\frac{1}{r}\delta(r-r_3)(\delta(\theta-\theta_1)-\delta(\theta-\theta_2))e^{-im\theta}J_{|m|}(j'_{|m|n}\frac{r}{a})\,r\,dr\,d\theta}{(j'^2_{|m|n}-m^2)(J_{|m|}(j'_{|m|n}))^2}$$

With the properties of the δ -functions in mind, the integrals in the numerator can be determined:

$$\int_0^a\delta(r-r_3)J_{|m|}(j'_{|m|n}\frac{r}{a})\,dr=J_{|m|}(j'_{|m|n}\frac{r_3}{a})$$

$$\int_{-\pi}^{\pi}(\delta(\theta-\theta_1)-\delta(\theta-\theta_2))e^{-im\theta}J_{|m|}(j'_{|m|n}\frac{r_3}{a})\,d\theta$$

$$=[\int_{-\pi}^{\pi}\delta(\theta-\theta_1)e^{-im\theta}d\theta-\int_{-\pi}^{\pi}\delta(\theta-\theta_2)e^{-im\theta}d\theta]J_{|m|}(j'_{|m|n}\frac{r_3}{a})$$

$$=J_{|m|}(j'_{|m|n}\frac{r_3}{a})(e^{-im\theta_1}-e^{-im\theta_2})$$

Since $\theta_1=-\theta_2$,

$$\therefore\ J_{|m|}(j'_{|m|n}\frac{r_3}{a})(e^{im\theta_2}-e^{-im\theta_2})=J_{|m|}(j'_{|m|n}\frac{r_3}{a})2\sinh(im\theta_2)$$

Inserting the integrals above into the expression for b_{mn} then yields

$$b_{nm}=\frac{j'_{|m|n}}{\pi a}\frac{J_{|m|}(j'_{|m|n}\frac{r_3}{a})i\sin(m\theta_2)}{(j'^2_{|m|n}-m^2)(J_{|m|}(j'_{|m|n}))^2} \qquad (3.21)$$

with $\sin(-m\theta)=-\sin(m\theta)$,$b_{n,-m}=-b_{n,m}$ and hence we can write U'_2 as a series with $m\geq 0$,ie

$$U'_2=\sum_{m=0}^{\infty}\sum_{n=1}^{\infty}b_{nm}(e^{im\theta}-e^{-im\theta})J_{|m|}(j'_{|m|n}\frac{r_3}{a})e^{-\frac{j'_{|m|n}}{a}|z|}(1-\frac{1}{2}\delta_{m0})$$

$$U'_2=\sum_{m=0}^{\infty}\sum_{n=1}^{\infty}2b_{nm}i\sin(m\theta)J_{|m|}(j'_{|m|n}\frac{r_3}{a})e^{-\frac{j'_{|m|n}}{a}|z|}(1-\frac{1}{2}\delta_{m0}) \qquad (3.22)$$

In order to shorten the computation, all terms with m=0 can be omitted since for these $\sin(m\theta)=0$. Combining the complex numbers from **eqn.3.21** and **eqn.3.22** gives a real expression for U'_2:

$$U'_2=-\frac{2}{\pi a}\sum_{m=1}^{\infty}\sum_{n=1}^{\infty}b_{nm}\sin(m\theta)D \qquad (3.23)$$

potential distribution of a circumferentially directed dipole, in a cylinder with insulating walls.

$$b_{nm}=j'_{|m|n}\frac{J_{|m|}(j'_{|m|n}\frac{r_3}{a})\sin(m\theta_2)}{(j'^2_{|m|n}-m^2)(J_{|m|}(j'_{|m|n}))^2} \qquad (3.24)$$

$$D=J_{|m|}(j'_{|m|n}\frac{r_3}{a})e^{-\frac{j'_{|m|n}}{a}|z|} \qquad (3.25)$$

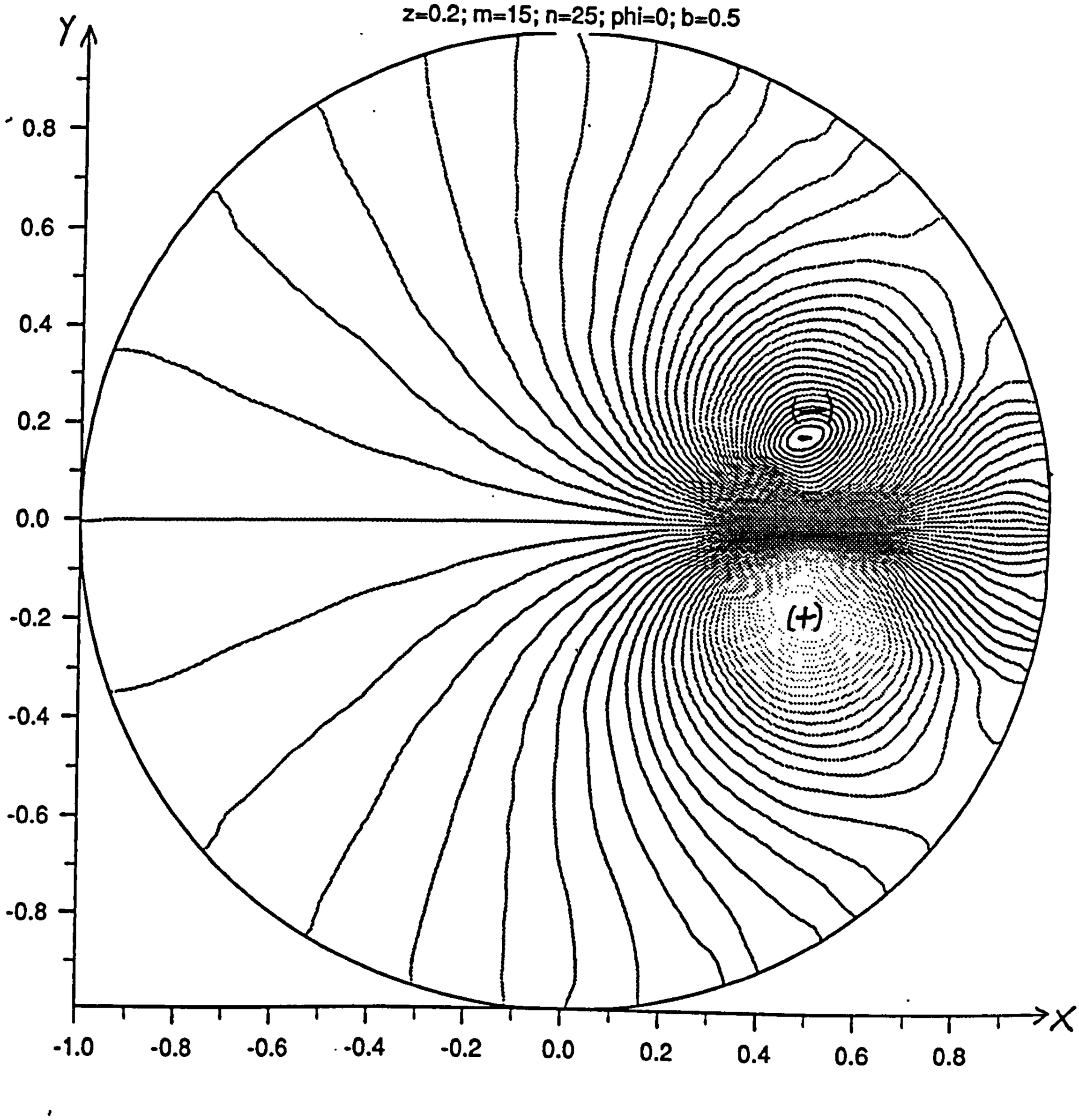

Fig3.11 Potential lines of a circumferentially directed dipole in an insulating pipe

Having derived equations **3.17** and **3.23,** the potential distribution of any arbitrarily positioned dipole can be evaluated. For example adding U'_1 and U'_2 results in a dipole potential with its zero potential line at 45 degrees to the x-axis.

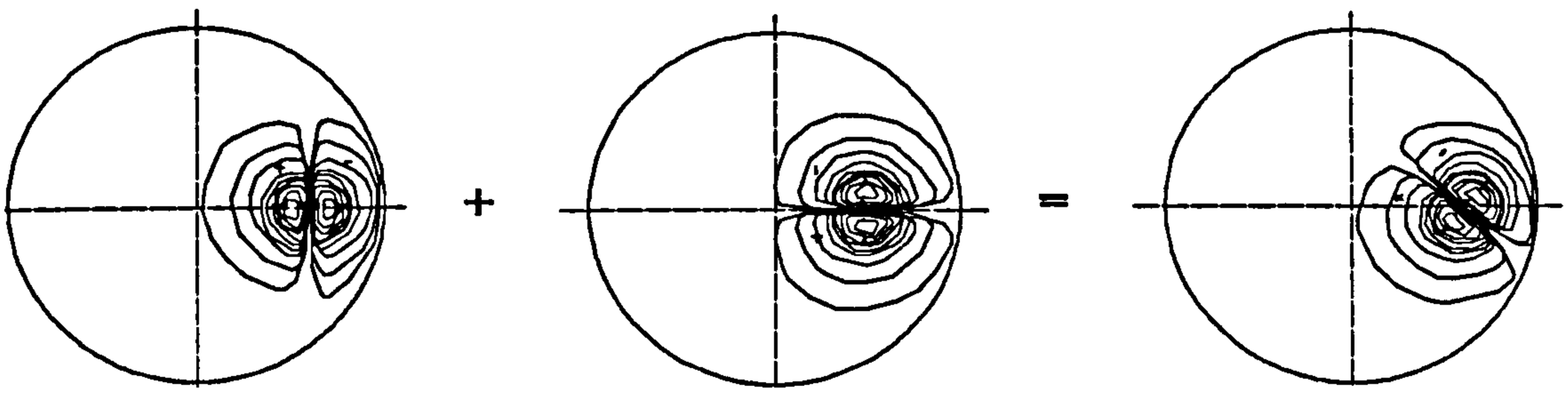

Fig.3.12 Summation of a horizontal and a vertical dipole of the same strength

By scaling the values of U'_1 and U'_2 different angles can be achieved. U'_1 and U'_2 should be scaled in a way dependent on the direction and length of the current vector j_0, so that the axis of the dipole is parallel to j_0 and its direction opposes j_0.

The size of the bubble is assumed to be small and the current j_0 to be uniform in the region where the bubble is placed. Then the scaling factor of $U'_{1,2}$ can be found by considering a similar problem:

For a spherical insulator in a uniform field $\underline{E}_0$, the potential at every point outside the sphere is given by **[1]** with:

$$\phi = E_0 r\cos\theta\left(1+\left(\frac{c}{2r}\right)^3\right) = E_0 z + E_0 z\frac{1}{2}\left(\frac{c}{r}\right)^3 \qquad (3.26)$$

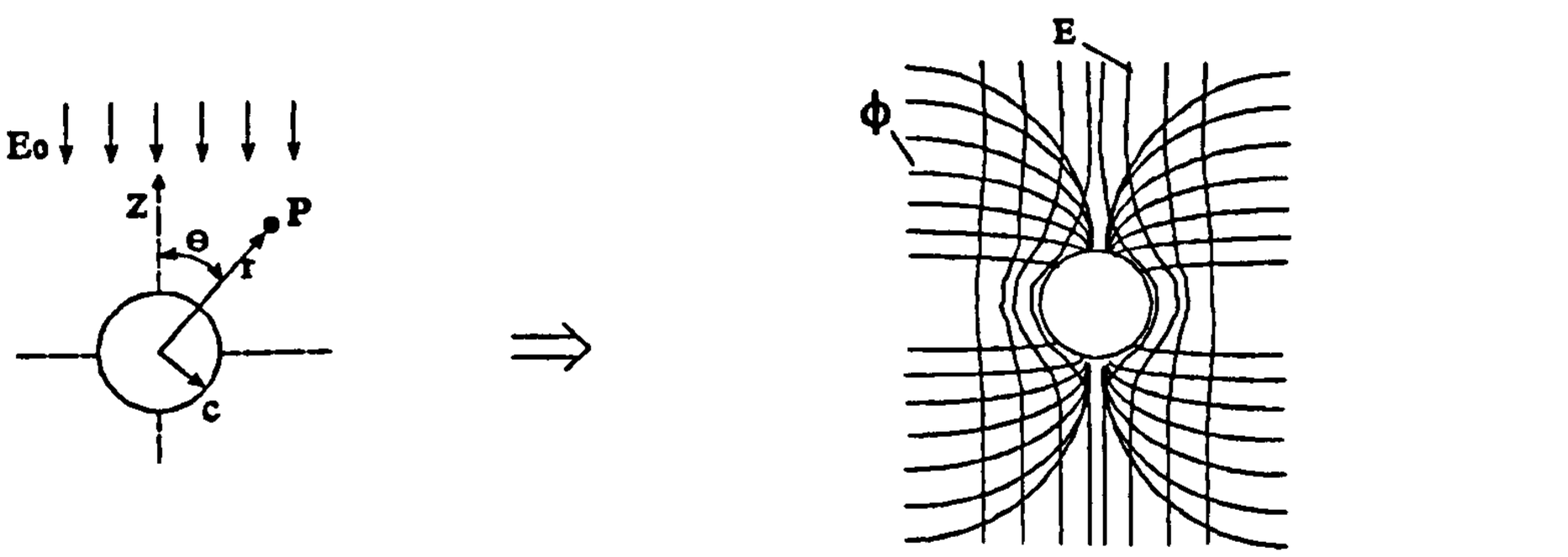

Fig.3.13 Potential around insulating sphere in a uniform field E_0

The change of potential due to the insulator is expressed in the second part of the right hand side, $E_0 z\frac{1}{2}\left(\frac{c}{r}\right)^3$. This change $\Delta\phi$ is equivalent to the potential of a dipole.

The equation for a dipole potential only is $\phi = \frac{Ql}{4\pi\varepsilon_0}\frac{\cos(\theta)}{r^2}$.

Comparing the potential of the dipole with the change $\Delta\phi = E_0 z \frac{1}{2}(\frac{c}{r})^3$ gives the required dipole strength.

$$E_0 z \frac{1}{2}\frac{c^3}{r^3} = \frac{Ql}{4\pi\varepsilon_0}\frac{\cos(\theta)}{r^2}\frac{r}{r} = \frac{Ql}{4\pi\varepsilon_0}\frac{z}{r^3}$$

$$\therefore Q = \frac{2\pi}{l}c^3 E_0 = \frac{2\pi c^3}{l\sigma} j_0 \qquad (3.27)$$

here, ε_0 was omitted since it was not used in **eqn.3.26.**

In the initial calculation the dipole was modelled with a unit current source and a unit current sink. Thus $U'_{1,2}$ has to be multiplied by the factor of **eqn.3.27.** Next, the current j_0 has to be resolved into its radial and circumferential components j_{0r} and j_{0c} respectively.
Then the correctly scaled components U'_1 and U'_2 are:

$$U'_1 = U'_{1\,(eqn.3.17)}\frac{2\pi c^3}{\sigma l} j_{0r} = U'_{1\,(eqn.3.17)}\frac{2\pi c^3}{\sigma l}\frac{\sigma}{2} B_x v_m \sin(\varphi)(\frac{b^2}{a^2} - 1)$$

$$U'_1 = \frac{\pi c^3 B_x v_m \sin(\varphi)}{l}(\frac{b^2}{a^2} - 1)\sum_{m=0}^{\infty}\sum_{n=1}^{\infty} a_{nm}\frac{\cos(m\theta)}{\pi a} C(1 - \tfrac{1}{2}\delta_{m0})$$

$$\boxed{U'_1 = B_x v_m \sin(\varphi)(\frac{b^2 - a^2}{a^3})\frac{c^3}{l}\sum_{m=0}^{\infty}\sum_{n=1}^{\infty} a_{nm}\frac{\cos(m\theta)}{a} C(1 - \tfrac{1}{2}\delta_{m0})} \qquad (3.28)$$

Potential of a radially directed dipole positioned in an insulating cylinder at a radius b and an angle φ .

$$U'_2 = U'_{2\,(eqn.3.23)}\frac{2\pi c^3}{\sigma l} j_{0c} = U'_{2\,(eqn.3.23)}\frac{2\pi c^3}{\sigma l}\frac{1}{2}\sigma B_x v_m (3\frac{b^2}{a^2} - 1)\cos(\varphi)$$

$$\boxed{U'_2 = -B_x v_m \cos(\varphi)(\frac{3b^2 - a^2}{a^3})\cos(\varphi)\frac{2c^3}{l}\sum_{m=1}^{\infty}\sum_{n=1}^{\infty} b_{nm}\sin(m\theta) D} \qquad (3.29)$$

Potential of a circumferentially directed dipole, positioned in an insulating cylinder at a radius b and an angle φ .

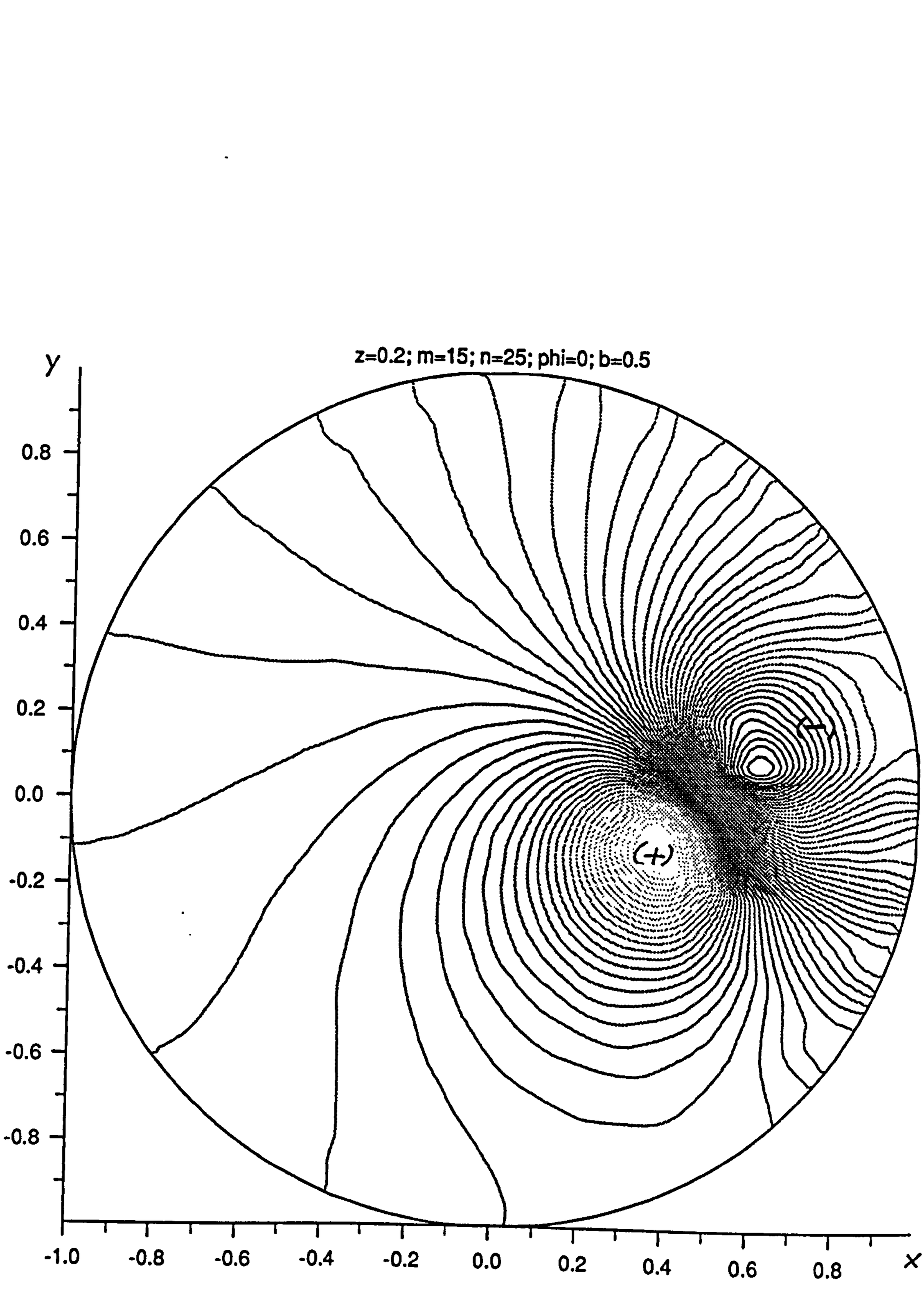

Fig.3.14 Computed potential lines of two perpendicular dipoles of equal strength

The potential of the dipole at any point in the cylinder is then the sum of U'_1 and U'_2: $U'=U'_1+U'_2$

The total potential at any point in the pipe is therefore given as the sum $U=U_{ref}+U'$, where U_{ref} is the reference potential without a bubble. U_{ref} is given by

$U_{ref}=\frac{1}{2}B_x v_m \sin(\varphi)(-3r+\frac{r^3}{a^2})$ for any point in a pipe with insulating walls.

$$\therefore U=\frac{1}{2}B_x v_m \sin(\varphi)(-3r+\frac{r^3}{a^2})+(U'_1+U'_2) \qquad (3.30)$$

Total potential at any point in a pipe in the presence of a nonconducting sphere

More important than the total potential is the relative change of the signal compared with the signal obtained without a bubble. Assuming two point electrodes at opposite sides of the pipe, the potential difference between them is $\Delta U_{ref}=B_x v_m 2a$ without the bubble.

The change in signal between the electrodes is

$$\Delta U'=(U'_1+U'_2)_{(\Omega=\frac{\pi}{2})}-(U'_1+U'_2)_{(\Omega=-\frac{\pi}{2})}$$

Dividing through by the reference signal finally yields the required relative change in the signal.

$$\Delta U_{rel}=\frac{\Delta U'}{\Delta U_{ref}} \qquad (3.31)$$

Relative potential difference between two opposite point electrodes due to a single insulating sphere with radius c.

Numerical aspects

In order to compute U′, the values of J_m and j'_{mn} have to be determined. The zeros of the derivative J'_m are calculated using the following asymptotic equation from [2]:

$$\left.\begin{aligned} j'_{mn} &= \beta' - \frac{\mu+3}{8\beta'} - \frac{4(7\mu^2+82\mu-9)}{3(8\beta')^3} - \frac{32(83\mu^3+2075\mu^2-3039\mu+3537)}{15(8\beta')^5} \\ &\quad - \frac{64(6949\mu^4+296492\mu^3-1248002\mu^2+7414380\mu-5853627)}{105(8\beta')^7} \\ \beta' &= (n+\frac{1}{2}m-\frac{3}{4})\pi \quad ; \quad \mu=4m^2 \end{aligned}\right\} \qquad (3.32)$$

The equation above is only valid for $n>m$. Since the equation for U′also requires zeros for which $n\leq m$, **eqn.3.32** was only used as a first approximation with the following iteration to the correct value.

The iteration works backwards, starting at a large n and using the fact that the distances between the n_{th} and $(n-1)_{th}$ zeros increase only slowly. Hence the previous distance could always be used as the first iterative step.

The values of J_m were calculated using three methods in order to keep the computational time as low as possible. A direct computation with power series **(eqn.3.33)** was only possible for small values of m.

$$J_m = \sum_{p=0}^{\infty} (-1)^p \frac{\left(\frac{x}{2}\right)^{2p+m}}{p!\,(m+p)!} \qquad (3.33)$$

High values of m require a computation in quadruple precision, which is very time consuming. However, that can be speeded up by using the factorials in tabulated form. The minimum number of terms for a given accuracy varies with x and m. By plotting the number of terms versus x and m, an almost linear relation is found. For a chosen maximum of 50 terms and an accuracy of10^{-8} a function f(x,m) was worked out, describing the minimum number of terms. Empirically, the equation was found to be:

$$n_{\min(x,m)} = 1.44x - 0.06m - 0.01124mx + 6 \qquad \begin{matrix} 0\leq x\leq 50 \\ 0\leq m\leq 50 \end{matrix} \qquad (3.34)$$

A large order Bessel function therefore needs (for small x) less than 10 terms for an accuracy of 10^{-8}.

For x,m outside the range of the power series, two other formulae are used.

The forward recurrence equation **3.35** can be used for m<x. If m>>x, the rounding errors dominate and the method becomes unstable.

$$J_{m+1} = \frac{2m}{x} J_m - J_{m-1} \qquad (3.35)$$

The inverted recurrence equation **3.36** works using the same equation as above but starts with $J_m = 0$.

$$J_{m-1} = \frac{2m}{x} J_m - J_{m+1} \qquad (3.36)$$

The order of m to start with depends on the required accuracy. For a high accuracy one has to start with a large m. How large m has to be, can only be guessed. A description of this method is found in [2], page 385. This method always works but it is unnecessarily time consuming for $m < x$.
In the computation of $J_m(x)$, each of the equations described above covers the range shown below.

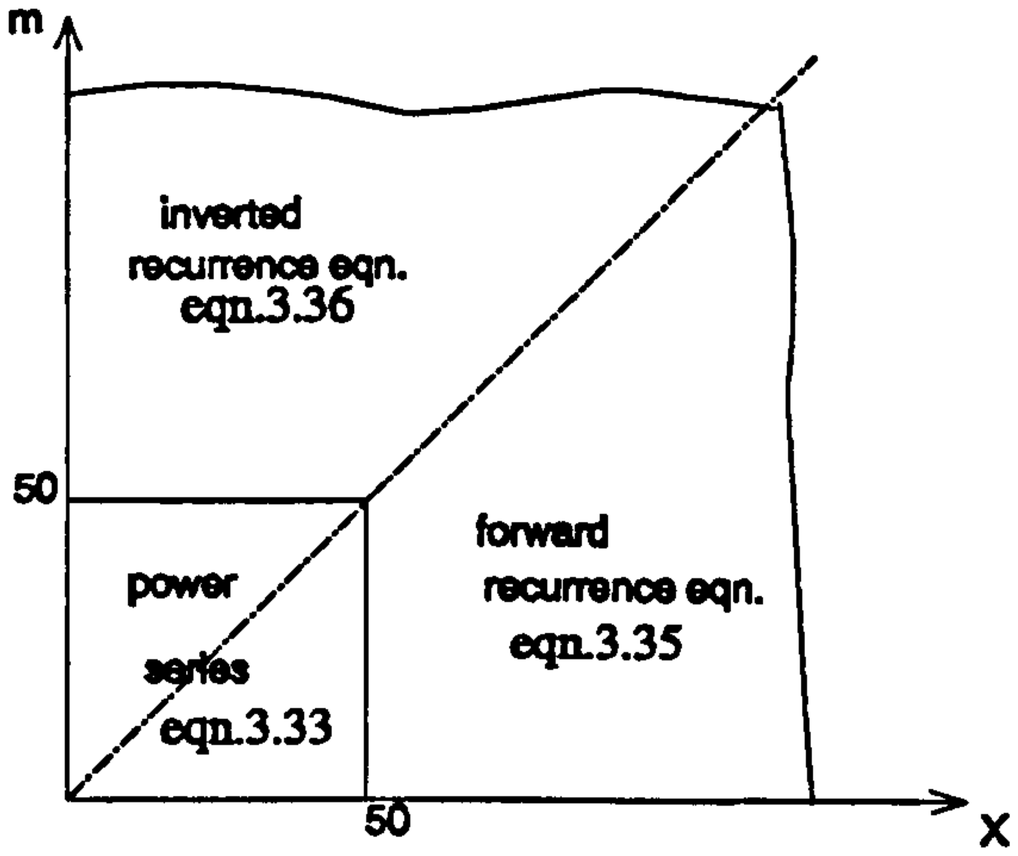

Fig.3.15 Computation of the Bessel function using three methods.

3.3 Theoretical values of flow signal

With the derivation of **eqn.3.30** and **eqn.3.31** it is now possible to compute the effect of a single insulating sphere on the flow signal, on the basis of the idealisations made at the beginning of chapter 3.
Three types of electrode geometries are investigated:

- Point electrodes
- Strip electrodes
- Large area electrodes.

For each electrode type, the effects of two parameters are investigated, namely

- the position of the bubble
- the bubble size.

In the following computations and figures all dimensions ie axial position 'z', radius to bubble 'b' and bubble radius 'br' are expressed as a fraction of the flow tube radius 'a'.

3.3.1 Flow signal with point electrodes

As we see from the equation for U', the potential difference depends exponentially on z, therefore the calculations are only carried out in a range of z=±1 radius. Considering two extreme cases, where the bubble is placed along the x-axis and the y-axis, we see that large variations in the signal occur. Moving along the x-axis, ie (φ=0°), the current j_0 changes its sign at the radius b=0.578. Therefore the relative potential difference is zero at that position (**Fig.3.16**). If the bubble moves along the y-axis(φ=90°) towards one electrode the output increases rapidly and close to the electrode it is one order of magnitude higher than average (**Fig.3.16**).
The following graphs (**Fig.3.17** to **Fig.3.19**) show the computed results of relative potential changes between point electrodes at different positions when the bubble moves along the z-axis with the same speed as the main flow. The maximum change always occurs in the z_0-plane and the signal change is symmetric about z. These maxima are shown in **Fig.3.20** for the bubble at every point in the cross section at z = 0.

Equations **3.28** and **3.29** show that the output is proportional to the cube of the size of the bubble. This is reflected in **Fig.3.21**. An increase in size has again its largest effect in the y-z plane. A doubling in size means an 8 fold increase in the signal. However, one should keep in mind that too great an increase in bubble size reduces the validity of the idealisations stated at the beginning of the chapter.

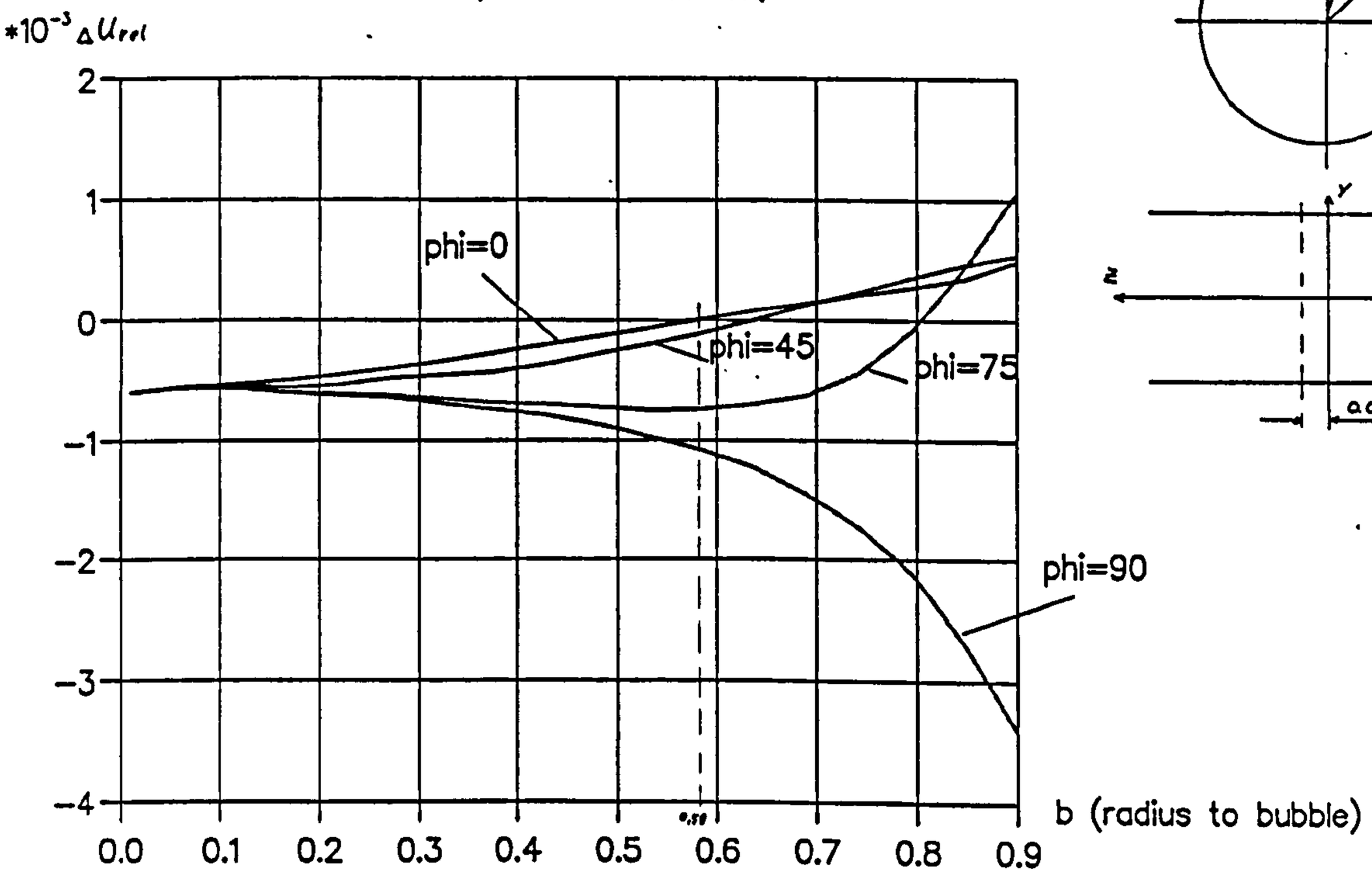

Fig.3.16 Relative potential difference between point electrodes

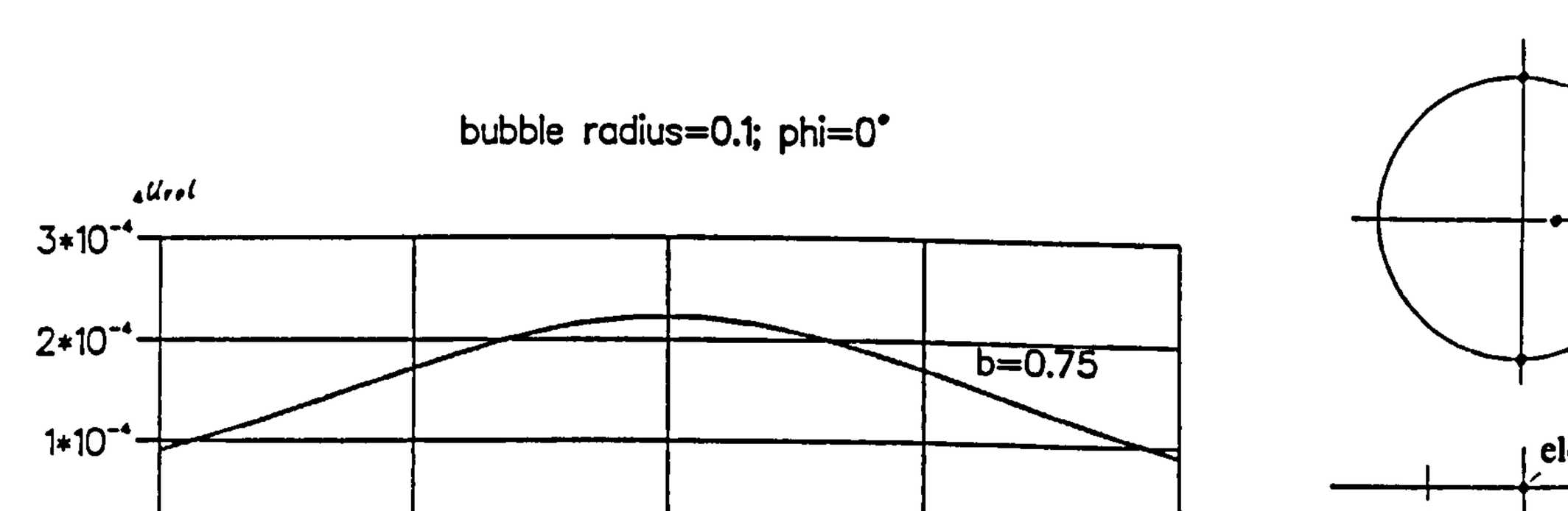

Fig.3.17 Relative potential difference between point electrodes

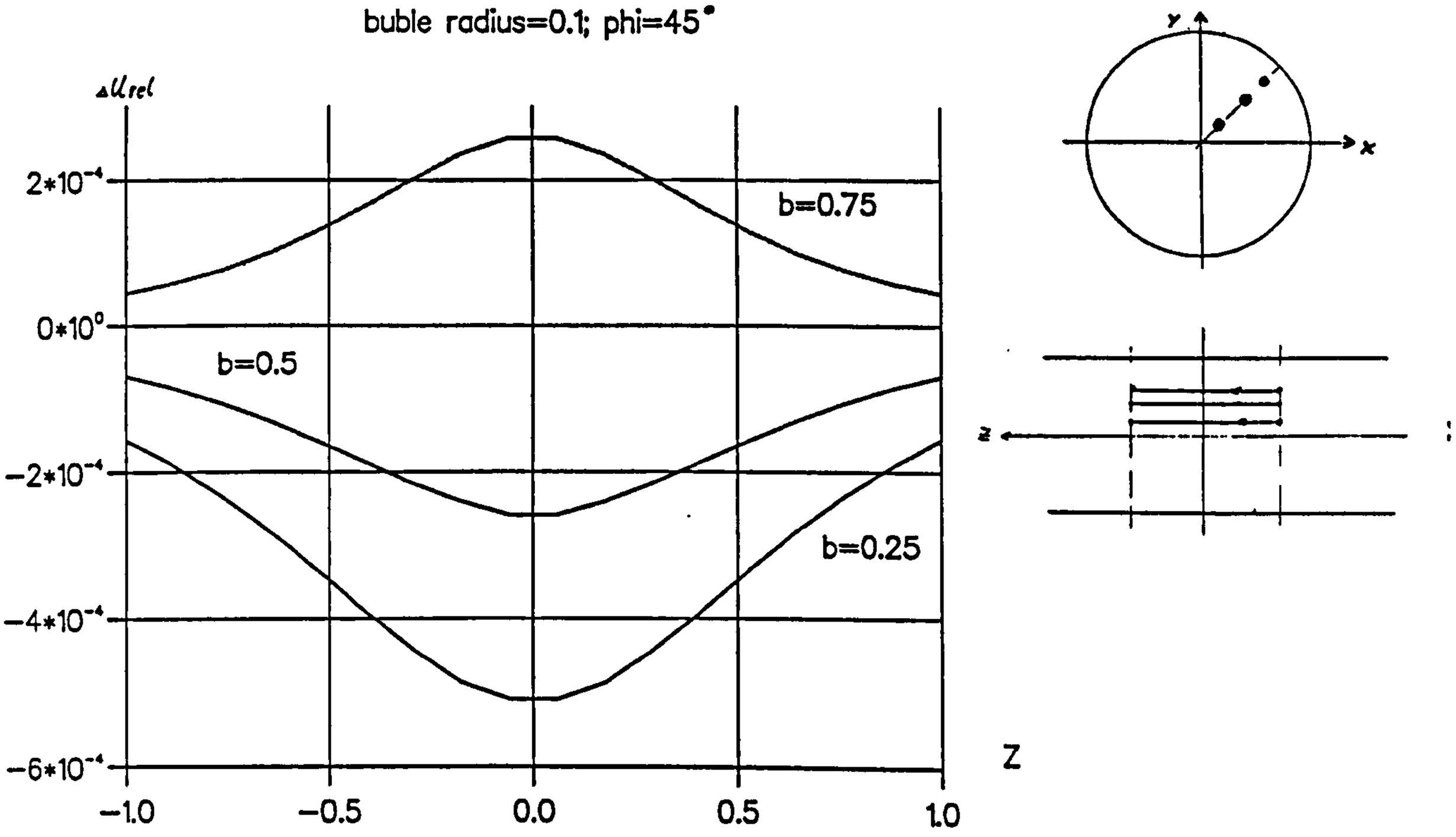

Fig.3.18 Relative potential difference between point electrodes

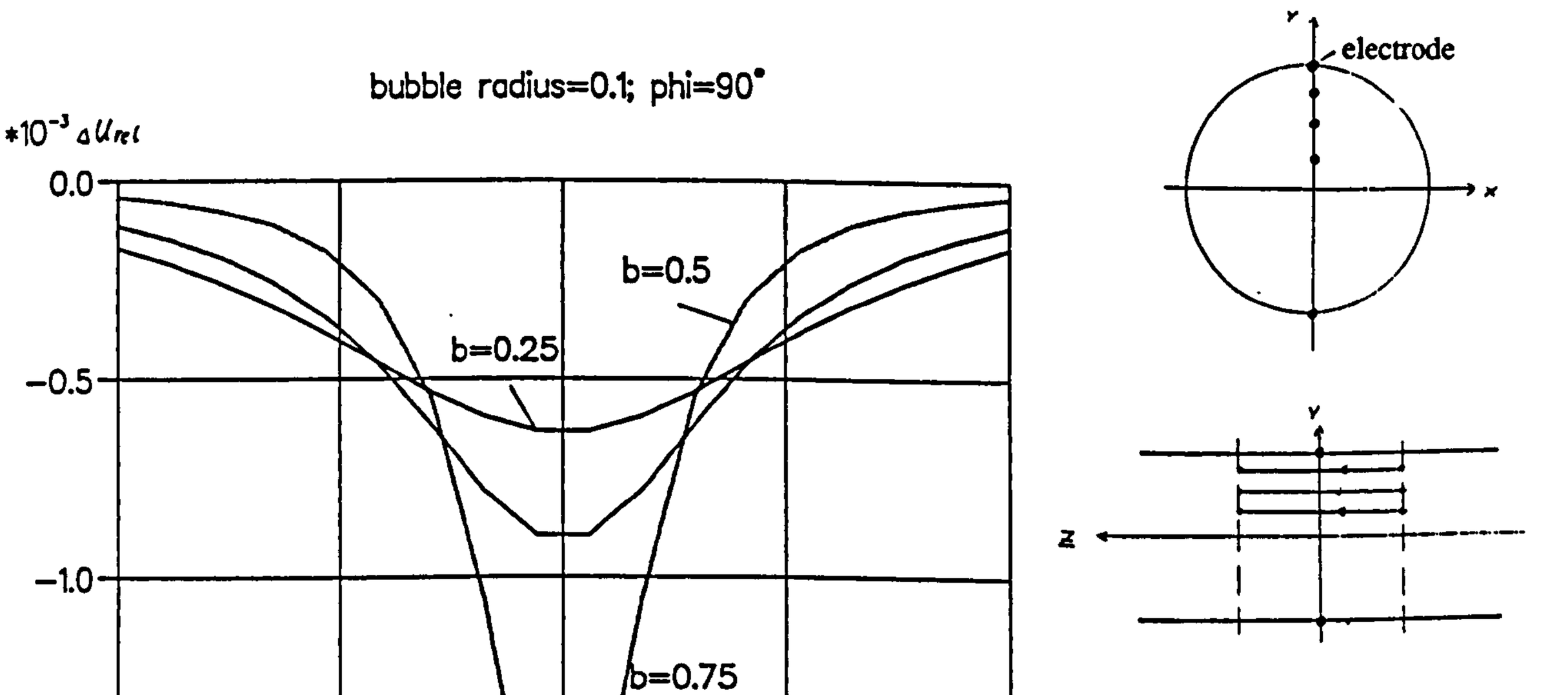

Fig.3.19 Relative potential difference between point electrodes

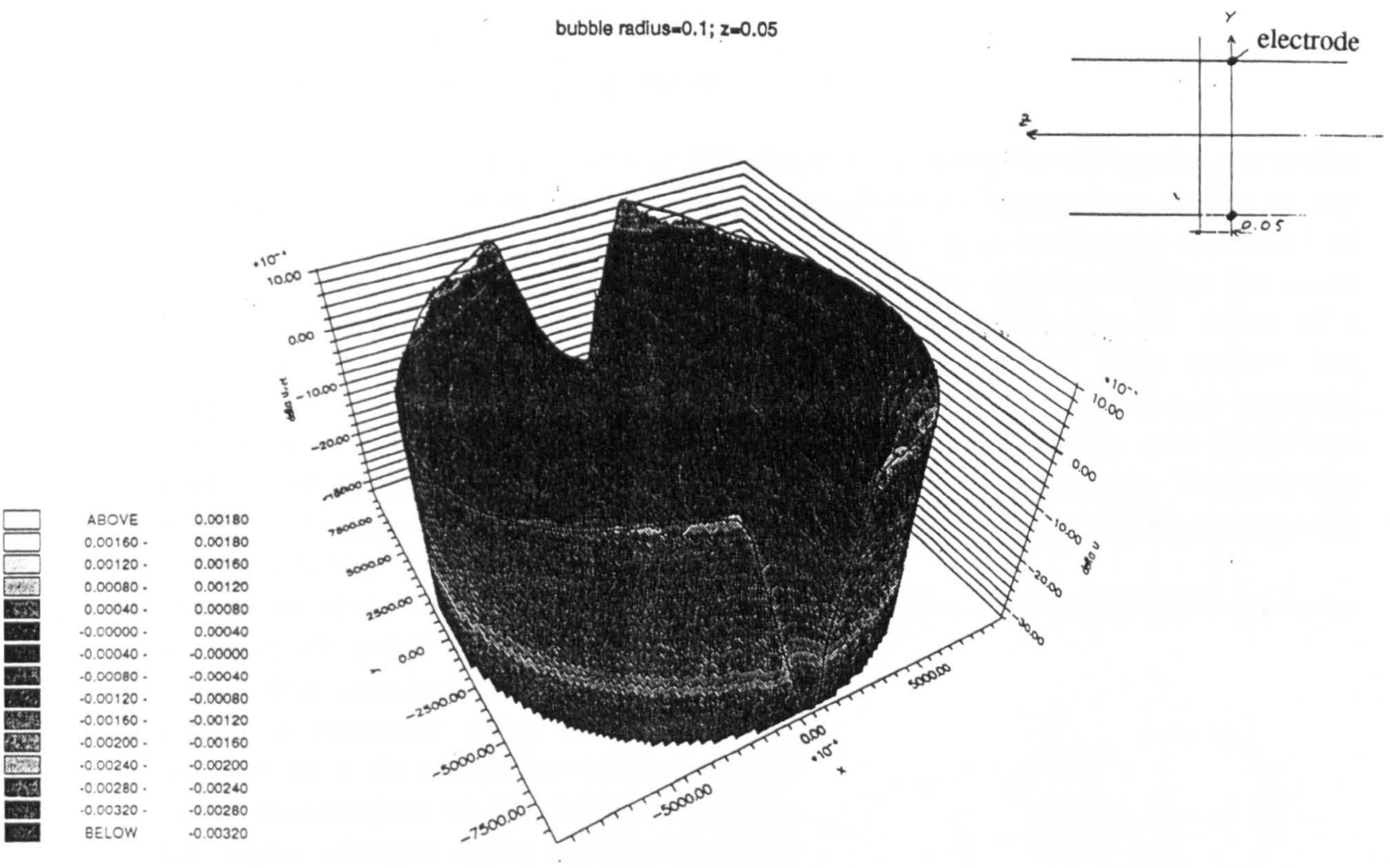

Fig.3.20 Maximum relative potential difference between point electrodes

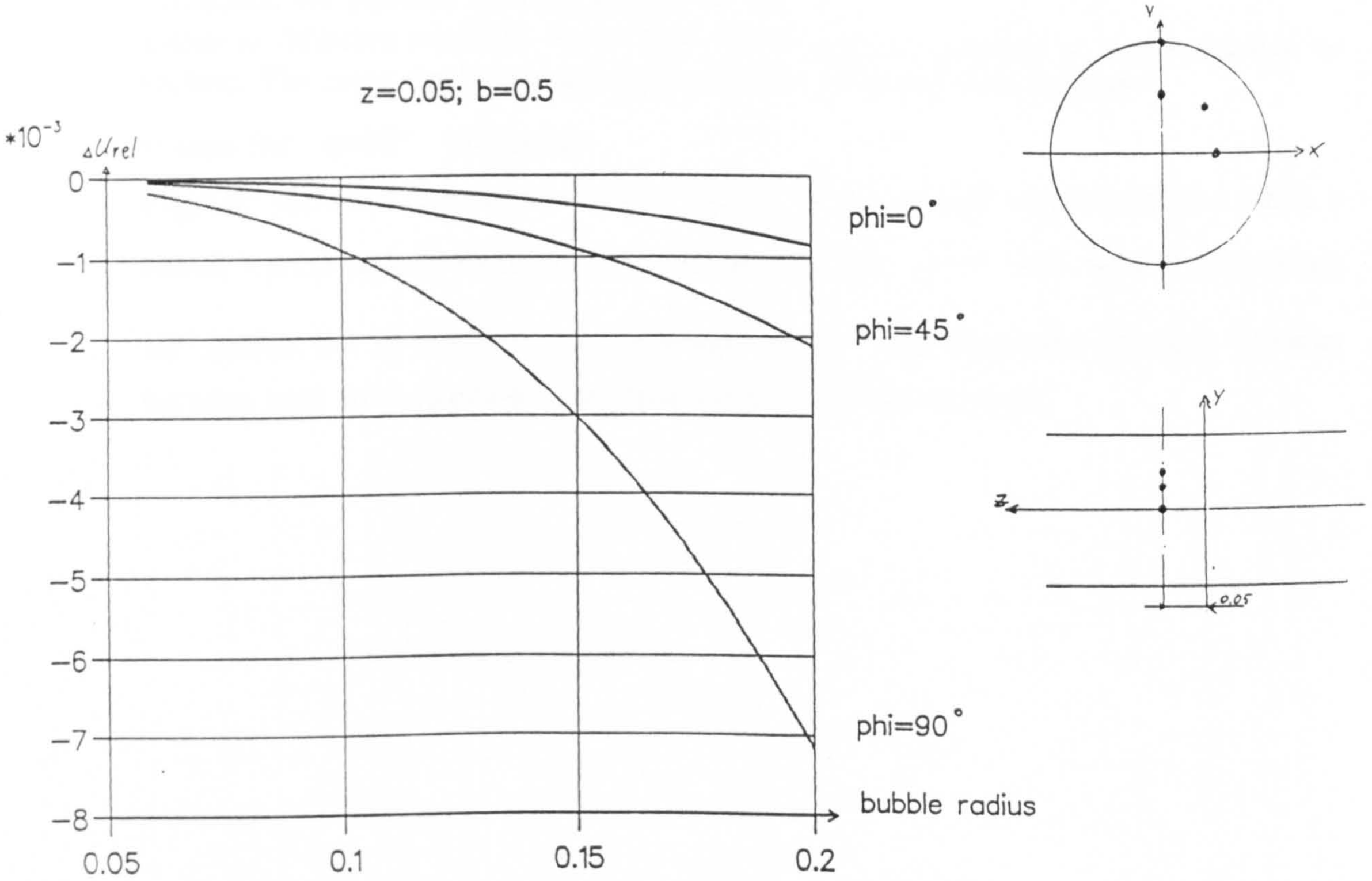

Fig.3.21 Relative potential difference between point electrodes

3.3.2 Flow signal with strip electrodes

After calculating the relative potential difference for a flowmeter with point electrodes it is of interest to consider whether larger electrodes may improve the output in any way. It is known that large non-contacting electrodes tend to average the effect of vortices or sharp changes in the velocity profile and they therefore reduce the noise level of the readings due to turbulence. It could be possible that the effect of a nonconducting sphere is also averaged out and hence becomes even smaller. For computing the relative potential difference between strip electrodes it was assumed that the electrodes are contactless. Due to their high input impedance it is possible to model them by using a large number of point electrodes along an arc. The potential difference between all point electrodes is then averaged and related to the average PD without a bubble **[15,19,20]**.

The results of the new computations show that the peaks are reduced while the order of magnitude is still the same. The flowmeter is now less sensitive to the position of the bubble, in particular along the y-axis where the position of the maximum signal change is almost independent of the radius **(Fig.3.23)**. The signal changes for a bubble, at points along the x-axis, is nearly the same as it was with point electrodes **(Fig.3.23)**. In **Fig.3.24** to **Fig.3.26** the relative potential difference was calculated for bubbles moving parallel to the z-axis at different positions in the pipe cross section. The most significant averaging effect is seen for $\varphi=90°$ **(Fig.3.26)**.

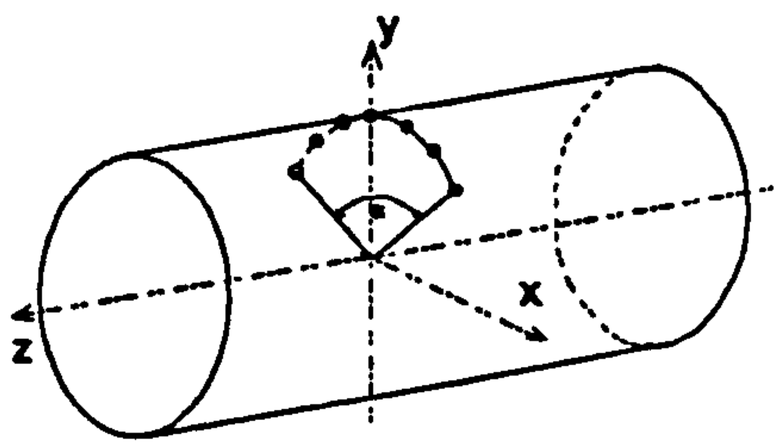

Fig.3.22 modelling of a strip electrode by using many point electrodes

Fig.3.27 shows a comparison of the signals of point- and strip electrodes when a bubble moves radially from the centre to the wall. For $\varphi=0°$ and $\varphi=45°$ the values are similar but at $\varphi=90°$ the advantage of the strip electrode becomes obvious because with strip electrodes the flow signal is almost constant.

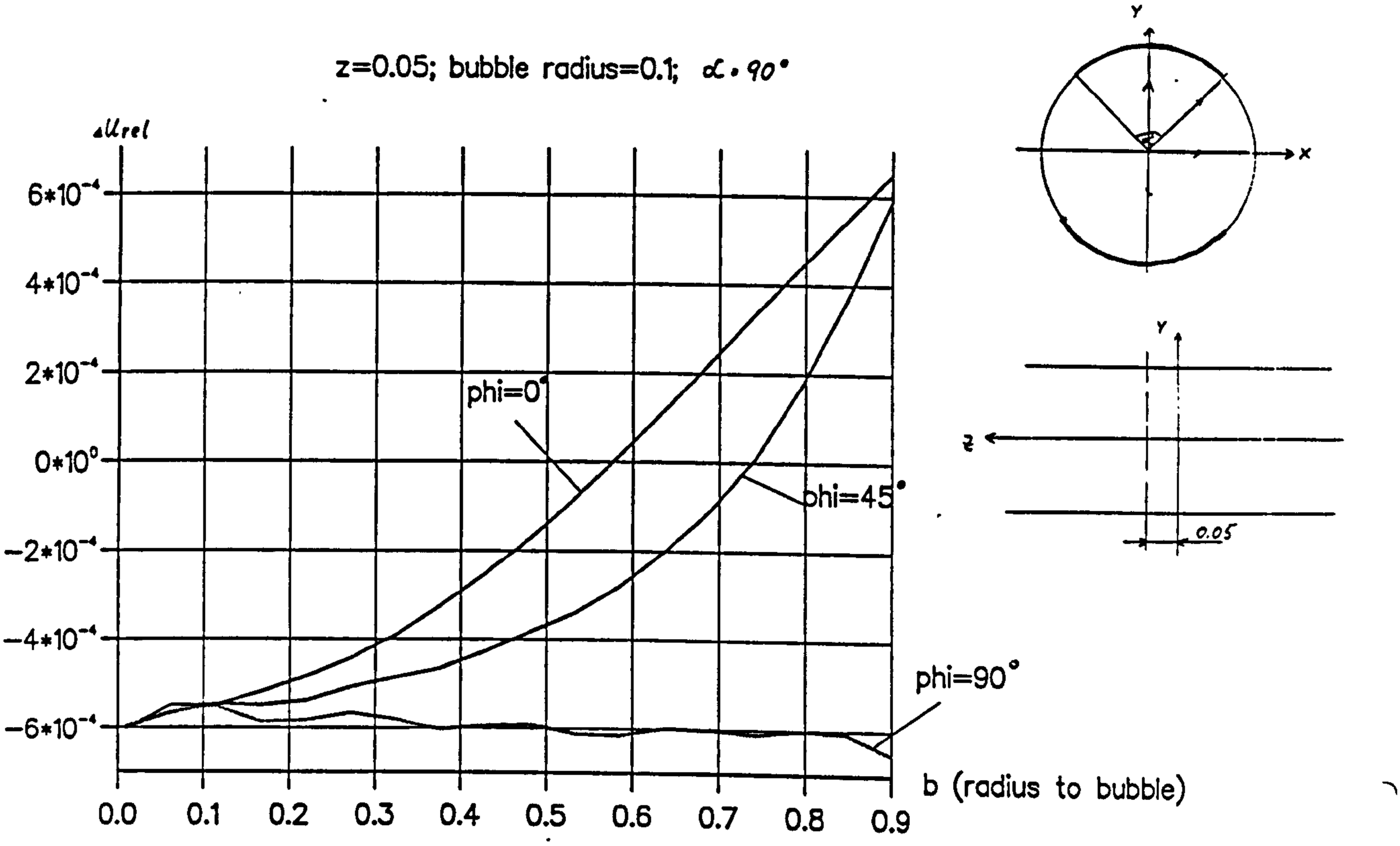

Fig.3.23 Relative potential difference between strip electrodes

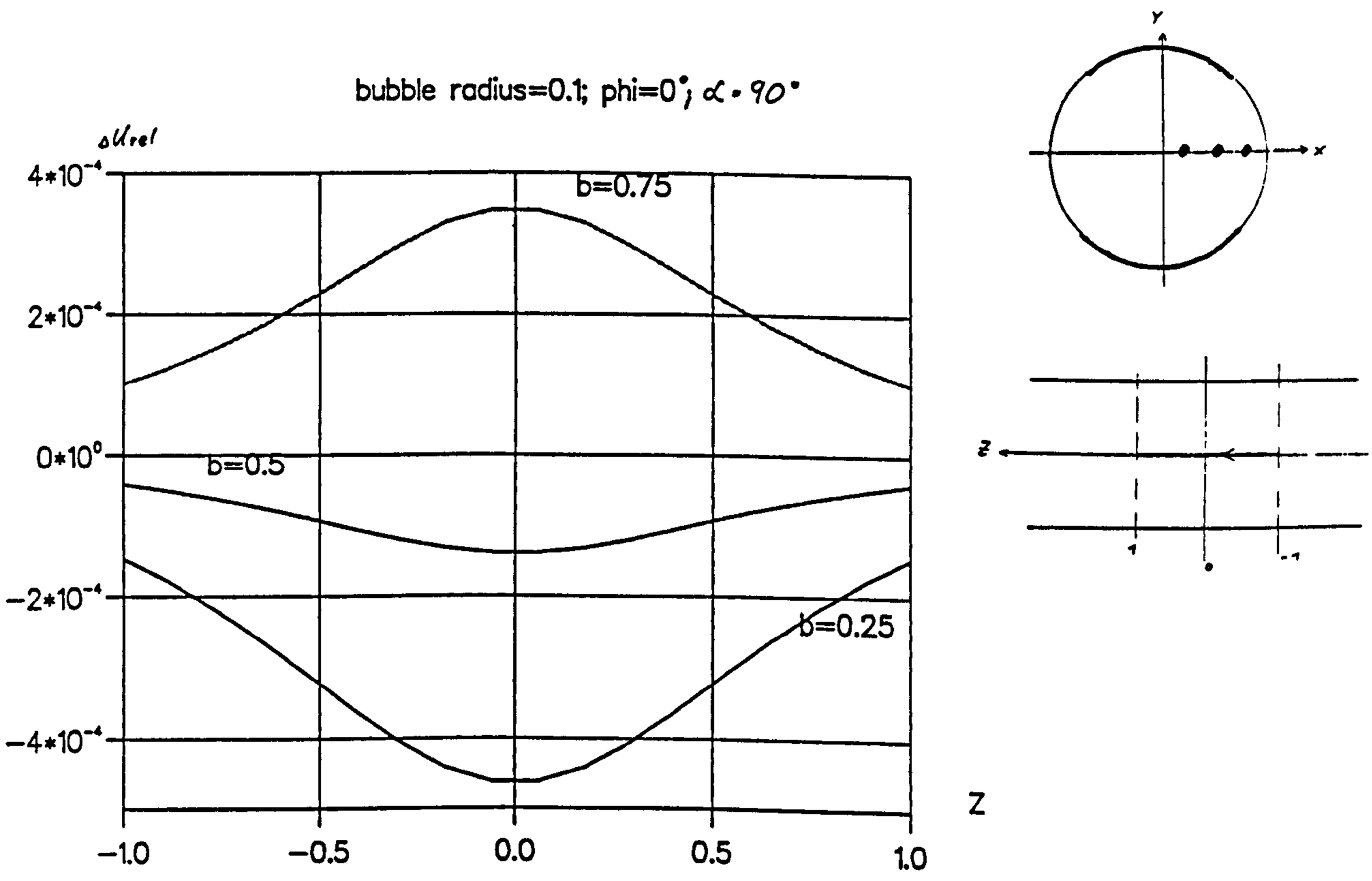

Fig.3.24 Relative potential difference between strip electrodes

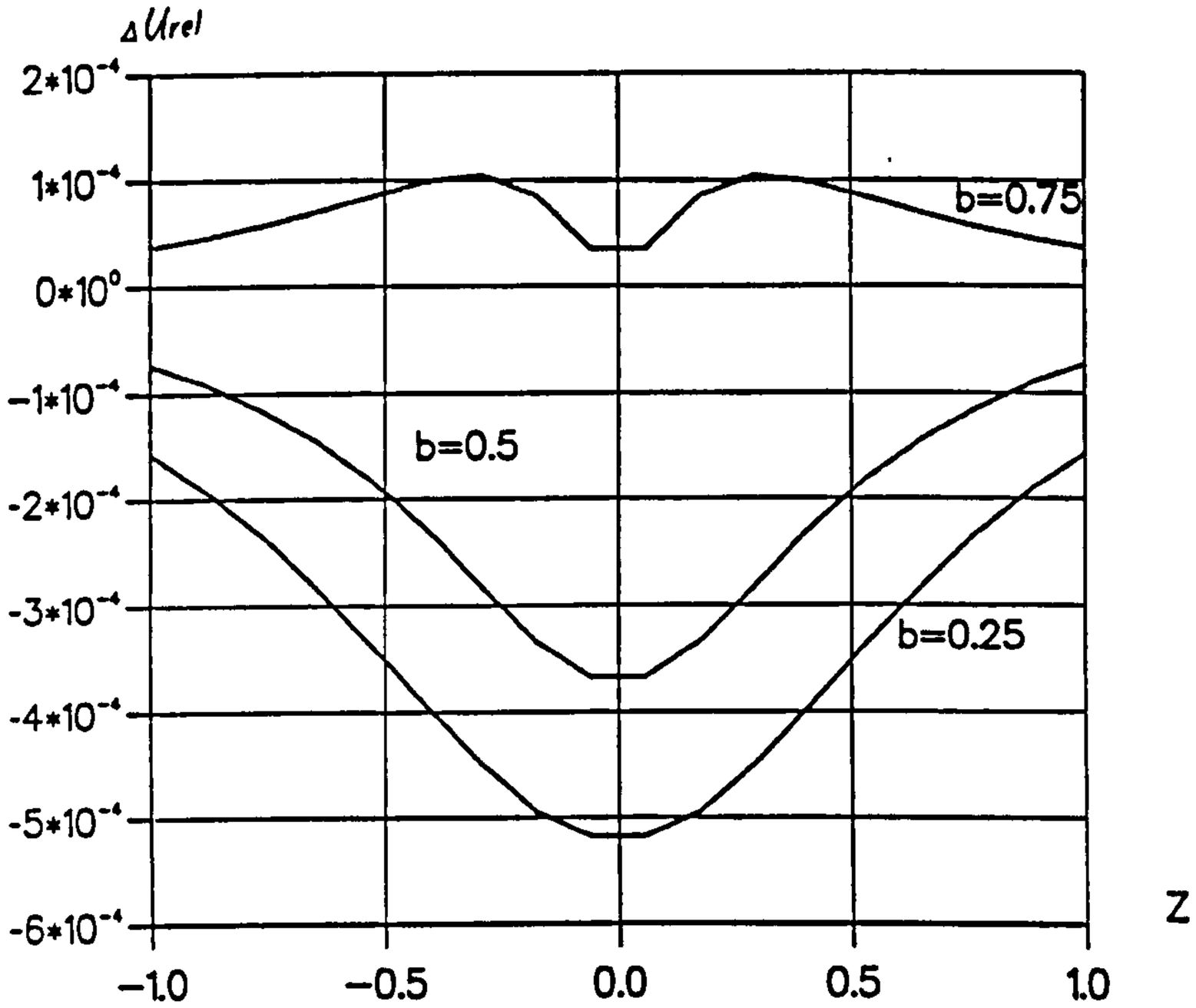

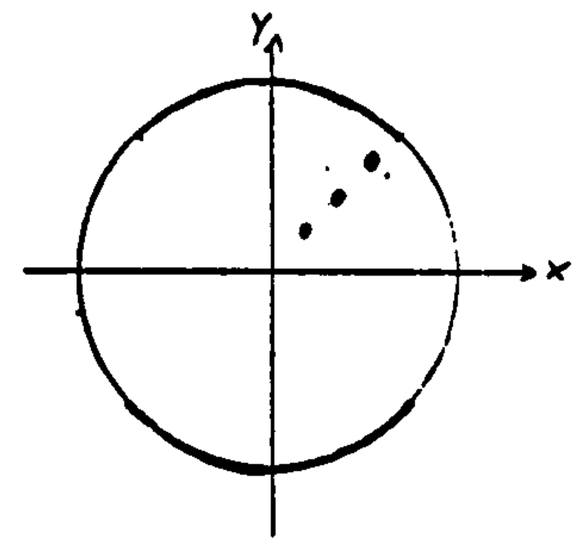

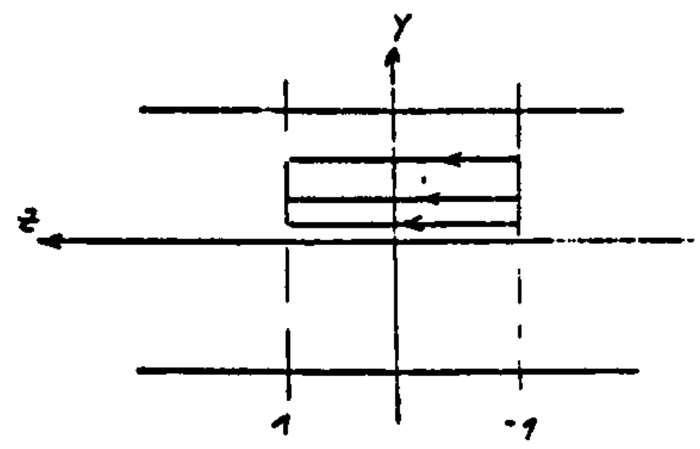

Fig.3.25 Relative potential difference between strip electrodes

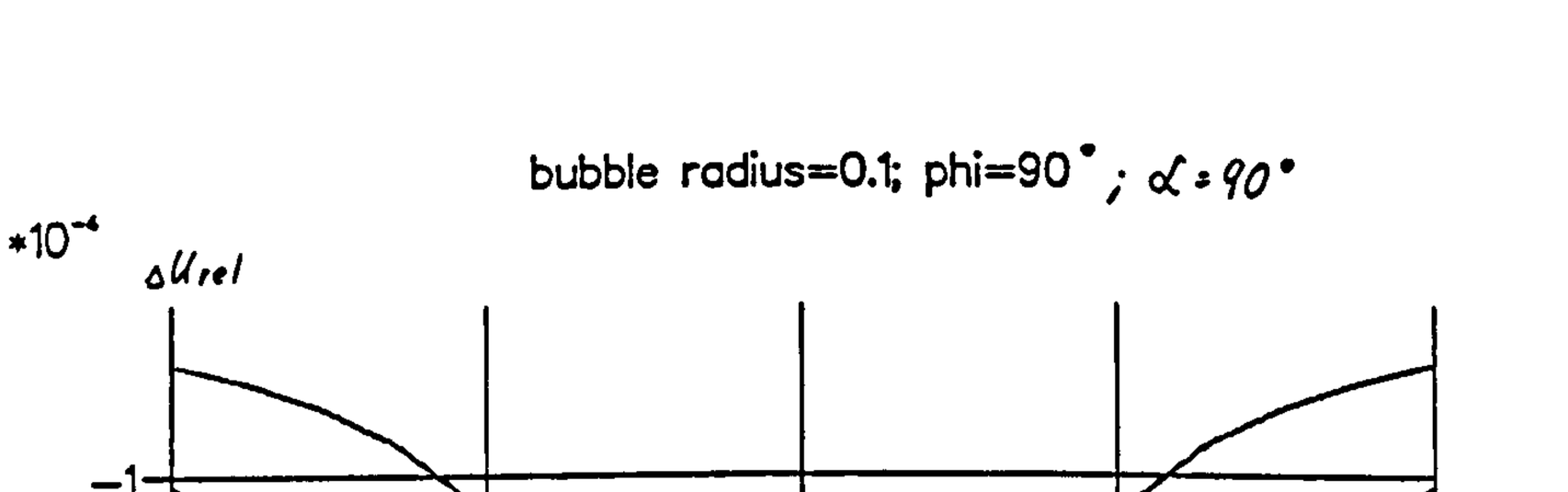

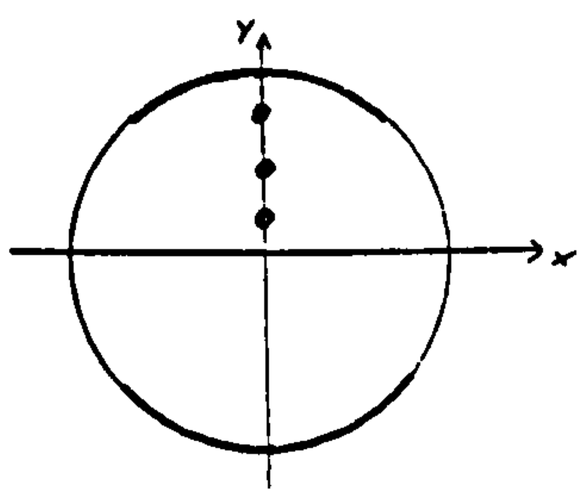

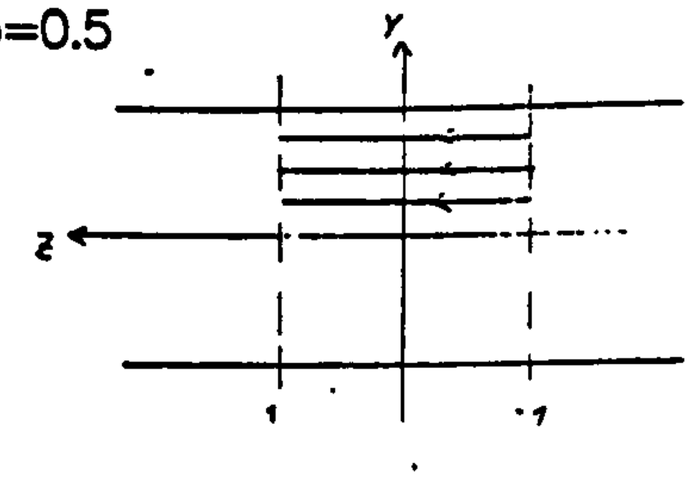

Fig.3.26 Relative potential difference between strip electrodes

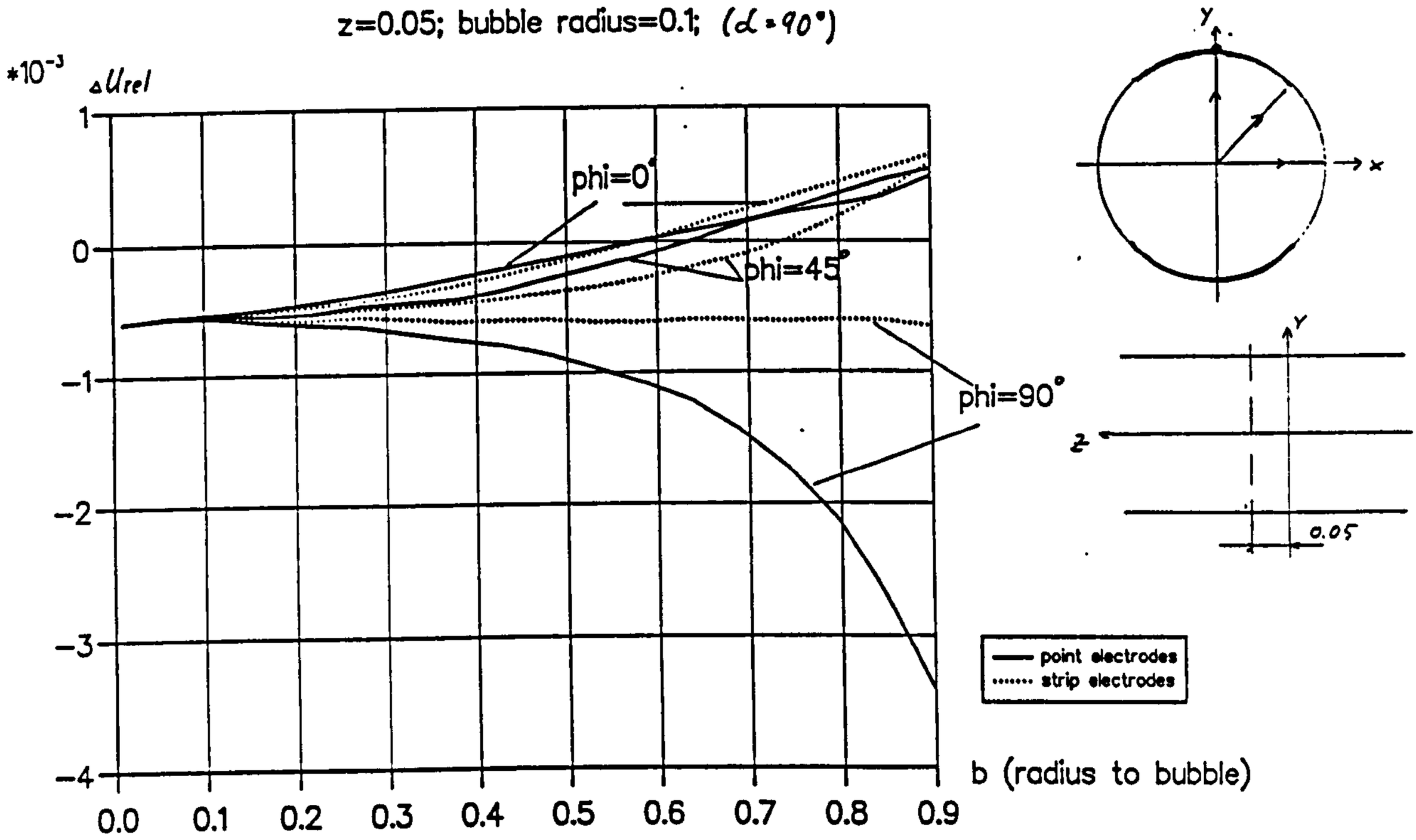

Fig.3.27 Relative potential difference between point- and strip electrodes

3.3.3 Flow signal with large area electrodes

As for the strip electrodes, relative potential differences are computed for large area electrodes. Here a whole mesh of point electrodes is generated instead of just an arc and then the PD is averaged again. The results show only a slight variation from those for the strip electrodes in that the peaks are more flattened (**Fig.3.29** to **Fig.3.31**). The order of magnitude is the same as with point electrodes and strip electrodes except for bubbles very close to the electrodes. In **Fig.3.32** and **Fig.3.33** the results are directly compared for all three types of electrodes at two radii. Here, the point electrodes can produce a relative signal up to 5 times larger than that with area electrodes but the comparison between point electrodes and area electrodes depends very much on the position of the bubble in the pipe.

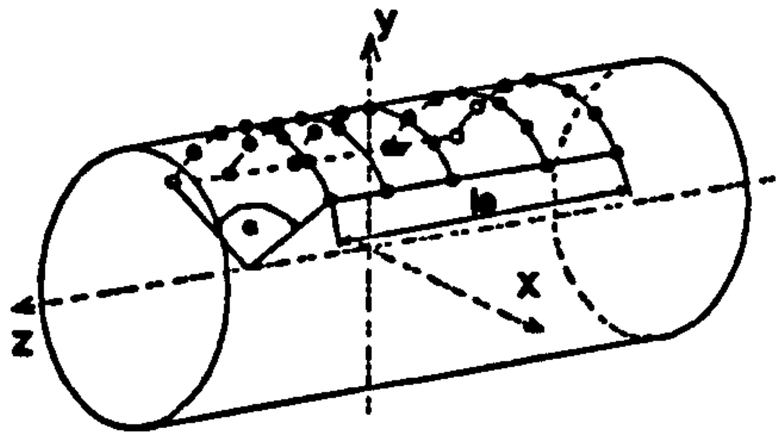

Fig.3.28 Modelling of a noncontacting area electrode with point electrodes

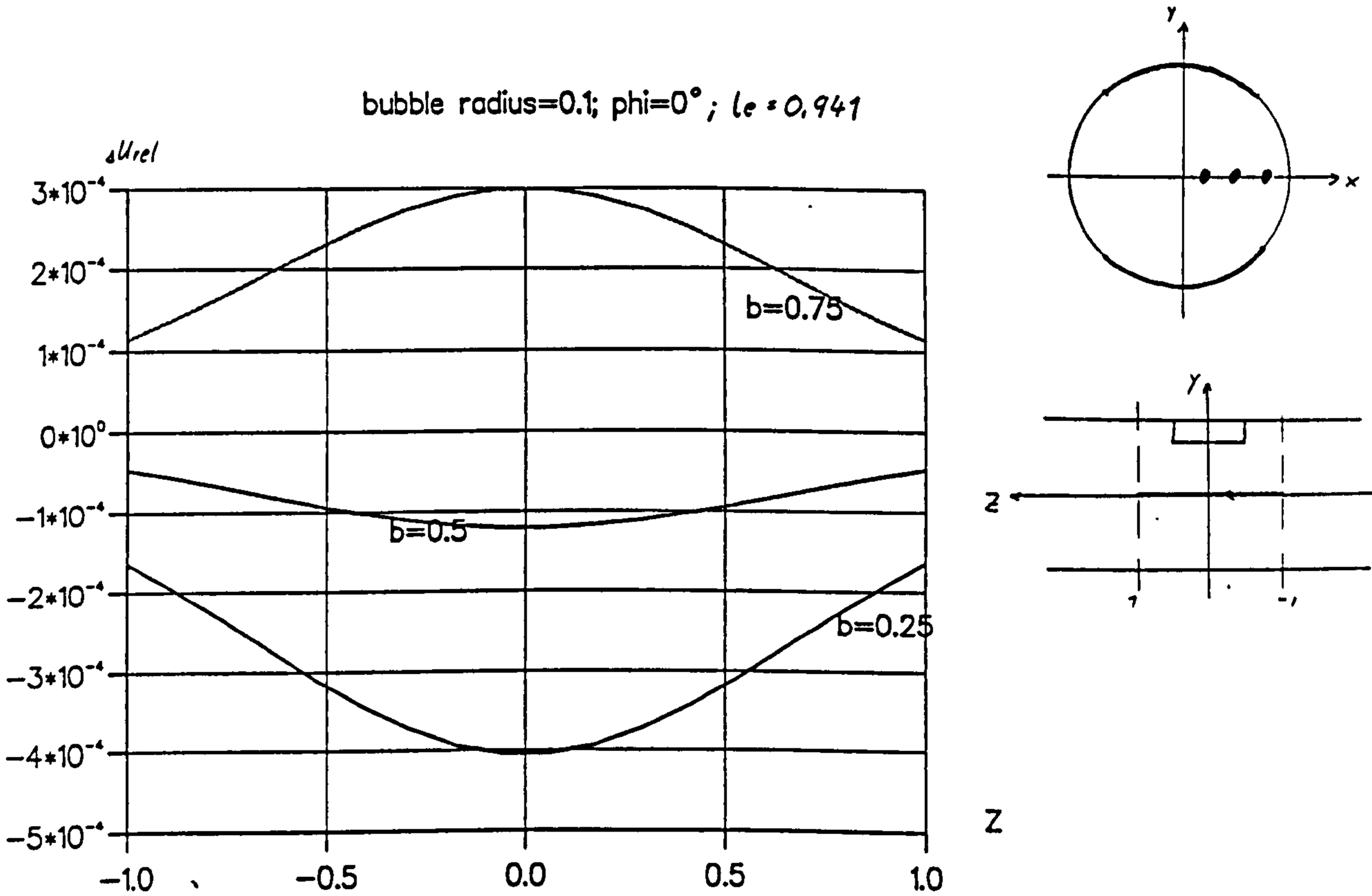

Fig.3.29 Relative potential difference between area electrodes

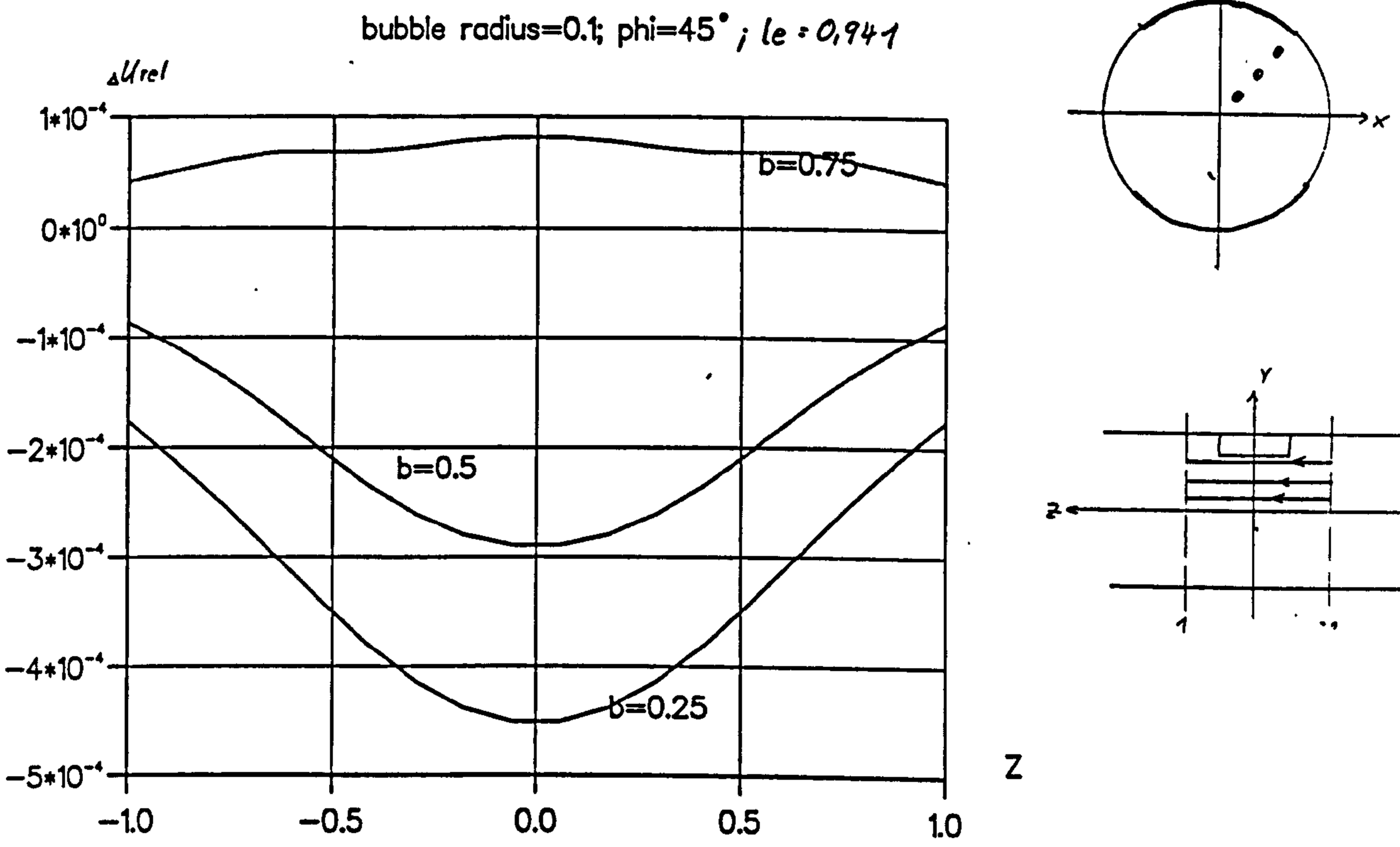

Fig.3.30 Relative potential difference between area electrodes

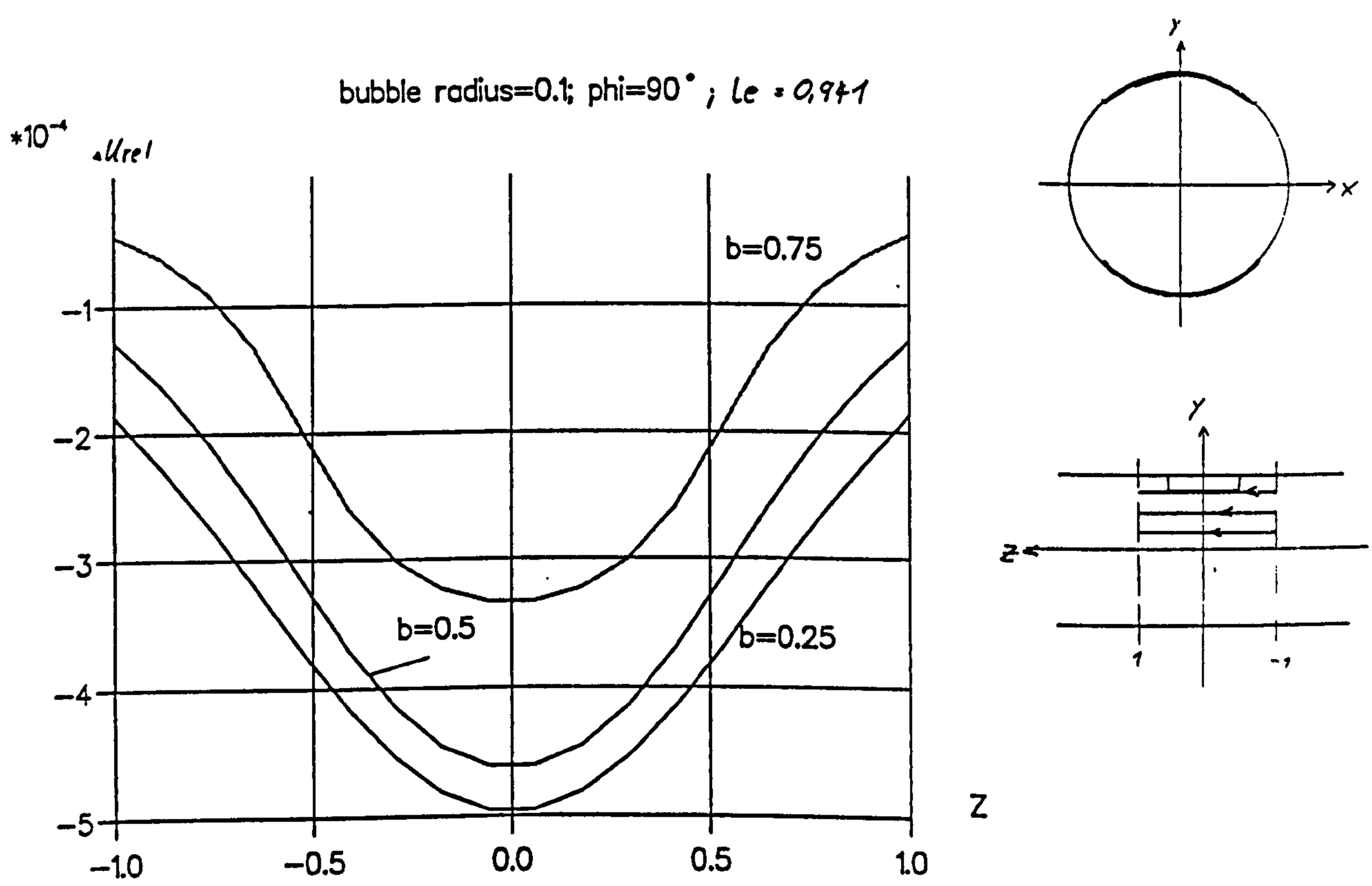

Fig.3.31 Relative potential difference between area electrodes

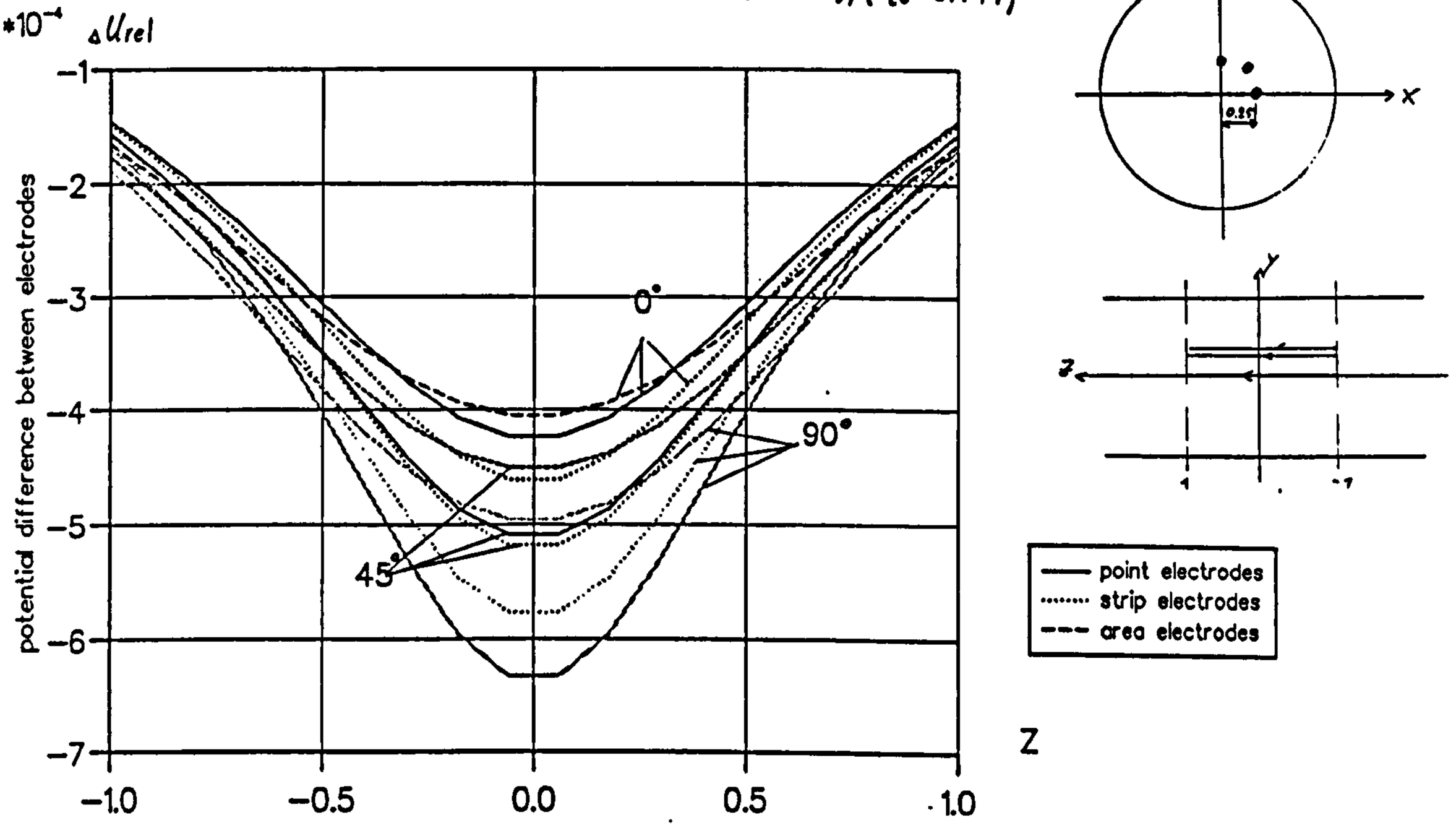

Fig.3.32 Comparison of relative potential difference between point-, strip- and area electrodes

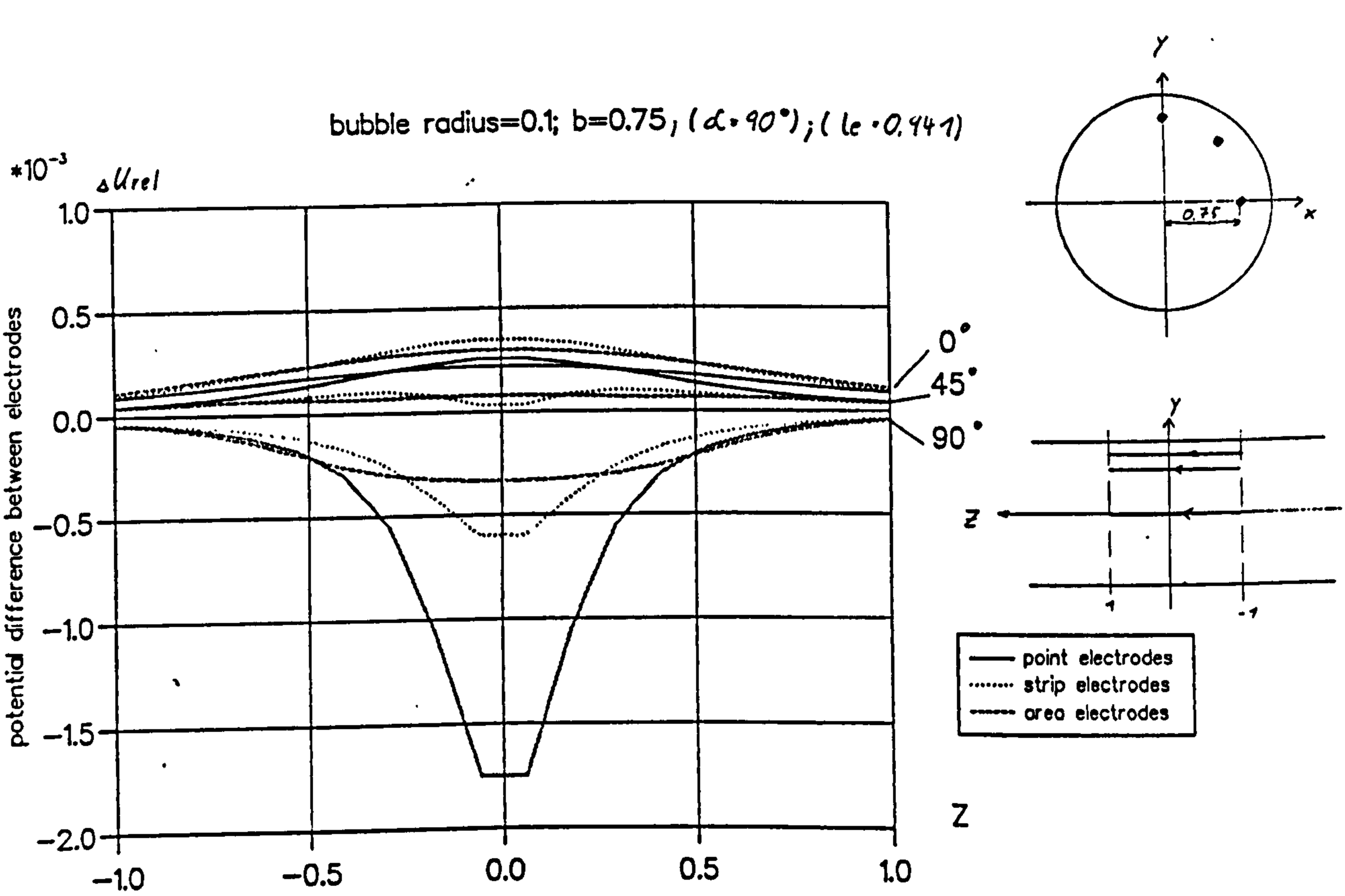

Fig.3.33 Comparison of relative potential difference between point-, strip- and area electrodes

3.4 Experimental measurement of the flow signal

Setting up the experiment

The 2" flow rig comprises a horizontal and a vertical section. The flow in the vertical section can be either way. This allows the generation of a large range of flow regimes. Gas and oil can be injected into the water to create a two and three component flow.
For symmetry reasons, all experiments are carried out with the flowmeter installed in the vertical section of the rig.
To prove the validity of the theoretical results, a device was designed which was able to inject balls of ca. 8mm diameter at a constant time interval into the pipe (**Fig.3.34**). The hollow plastic balls were filled with oil-solvent mixture in order to achieve an almost neutral buoyancy with respect to water. This was necessary to satisfy the idealisation of no slip velocity between the balls and the water flow. It is expected that a frequent change in the amplitude of the flow signal will be seen whenever a ball is passing the electrodes. This change should also be visible in the frequency spectrum analysis.
In the first experiment the flow signal was recorded on an oscilloscope with

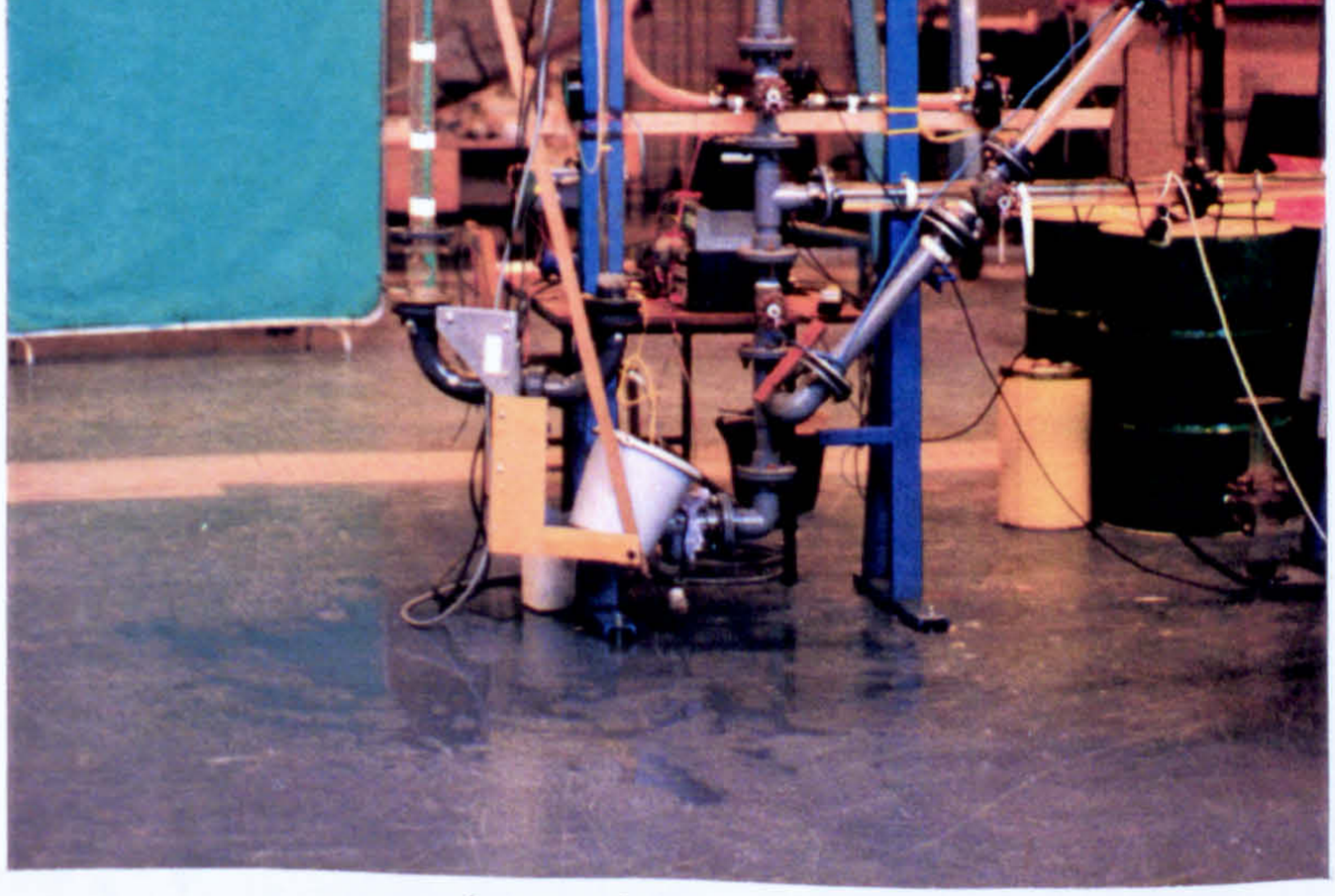

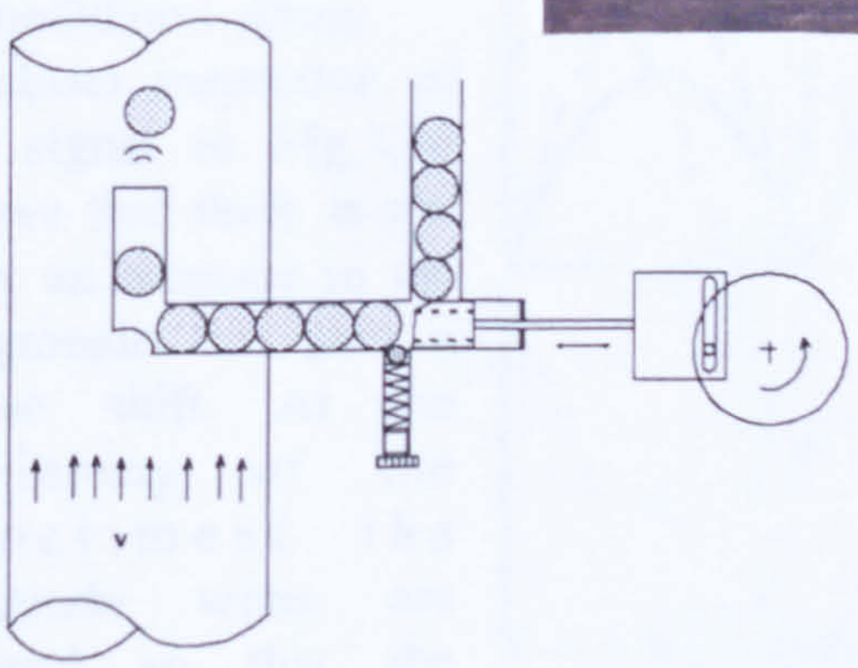

Fig.3.34 Device for injecting balls into the pipe

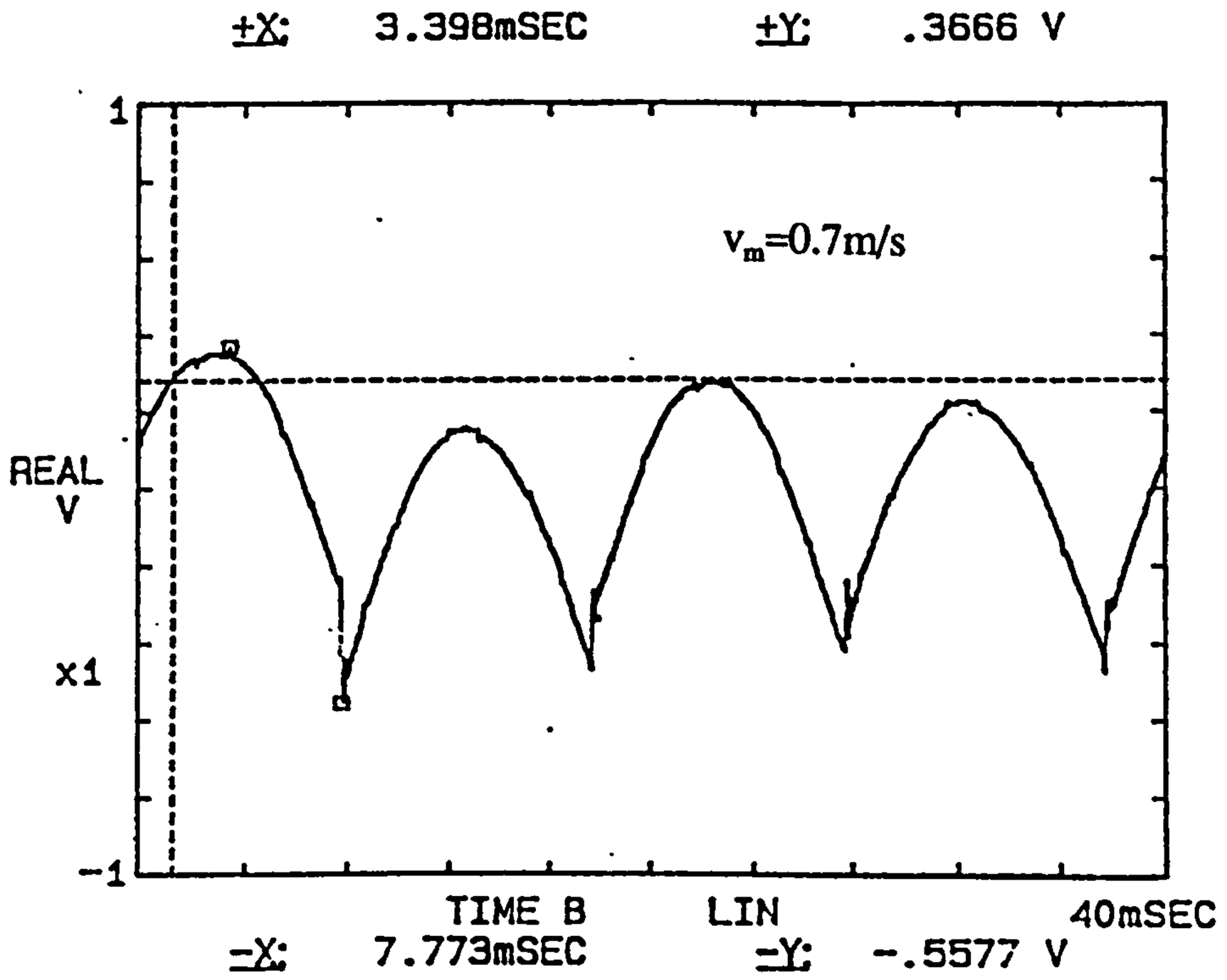

Fig.3.35 Measured flow signal with airbubbles

and without balls passed through the meter. The change in the time signal was hardly visible. However, when air was injected and bubbles of 20 mm or more passed through the flowmeter a change in the signal's amplitude could be seen (**Fig.3.35**). Due to the nature of the flow induced signal it is difficult to say at this stage whether the measured signal was caused by the predicted change in flow signal or whether it is a transformer effect. A flow meter with a low frequency sinusoidal magnetic field cannot suppress quickly changing transformer signals. After demodulation, the flow signal has the form of a fully rectified sine wave (**Fig.3.36**,graph1). An alteration in flowrate changes the amplitude and therefore the dc-level of the demodulated signal.

A closer inspection of the signal in **Fig.3.35** shows that there is not only an increase in the magnitude but also a phase shift. At the beginning of the experiment the electrode wires are aligned so that the transformer signal is minimised. If the increase in signal was

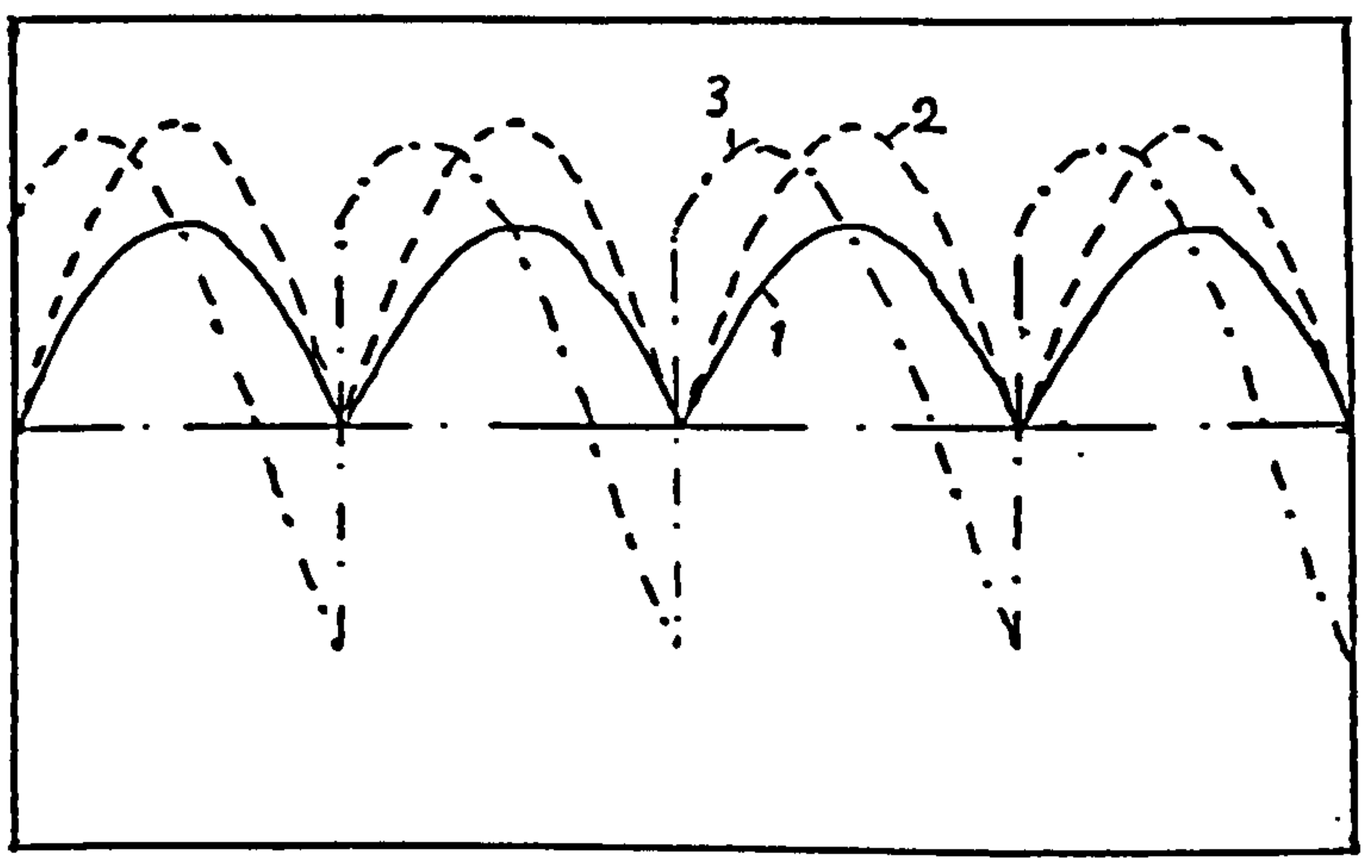

Fig.3.36 Rectified flow signal with additional transformer signal.

purely due to the previously described effect of the bubbles on the flow signal, then the new signal would only show an increase in magnitude (**Fig.3.36**,graph2). Only if the transformer signal, which has a phase shift of 90°, has increased as well can the resultant signal (the sum of transformer- and flowsignal) be phase shifted (**Fig.3.36**,graph3). A direct measurement of the effect of a bubble on the flow signal is only possible with a constant magnetic field. This could be done either with a DC-driven coil or with a coil driven by a trapezoidal function where the sampling of the flow signal is taken at the end of the flat section.

In the following experiment, the power spectrum of the flow signal is recorded. A comparison of the power spectra with and without balls shows a definite increase in the signal when the balls are injected. With changing flowrate, the frequency at which the envelope of the power spectrum has a maximum, varies. This indicates that the signal depends either on the flowrate or on the velocity of the balls.

These first experiments are followed by a series of more systematic experiments, altering the parameters

- flowrate
- density of the balls

The aim is to determine whether the change in the signal depends on the velocity of the nonconducting phase or on that of the continuous conducting phase.

The Fourier series expansion of the rectified sinusoidal flow signal f(t) can be written as the product of a sine wave and a square wave:

$$f(t)=v\frac{4}{\pi}[\frac{1}{2}-\frac{1}{3}\cos(2\omega t)-\frac{1}{15}\cos(4\omega t)-\frac{1}{35}\cos(6\omega t)-...]$$

In a spectrum analysis one would therefore expect a dc-component and components at multiple frequencies of 2ωt. Thus a 50 Hz driven magnet creates a dc-voltage $2\frac{v}{\pi}$ and decreasing signals at 100 Hz, 200Hz ....

Fig.3.37 shows the recorded power spectrum of the flow signal. In all graphs, v_m is the mean superficial water velocity and v_{baver} is the average velocity of the balls in the water flow. Because a turbine meter is used as a reference water meter, the water velocity is often expressed in terms of the counter frequency. Calibration curves for the turbine meters used are given in Appendix D. The measured frequency spectrum shows additionally low frequency noise which is generated by vortices in the turbulent flow. Due to poor filtering in the electronics, the power spectrum also shows spikes at the mains frequency and multiples of it, i.e at 50Hz, 150Hz.. .Because these are also present when the coils were turned off, we ignore it in the further discussions of the flow- and transformer signal. In **Fig.3.38** to **Fig.3.44** the power spectra obtained with balls injected at different water flow rates is shown. The maximum of the signal change moves with the flowrate. The multiple traces on each graphic are due to several readings made under the same conditions.

The lower the flowrate the closer is the maximum to 100Hz. This was to be expected because of the demodulation effect. A modulating 5Hz signal will (after demodulation) be shown at 100±5Hz. A higher flowrate and therefore faster ball speed will modulate at say 10Hz which after demodulation will be shown at 100±10Hz. To show that the position of the signal maximum depends on the speed of the balls only, empty and

hence less dense balls are used in the next experiment. The flowrate is then changed until the rising velocity of the empty balls matches the rising velocity of the balls in the previous experiment. Comparing **Fig.3.39** and **Fig.3.41** with **Fig.3.42** and **Fig.3.43**, the maxima are seen to be at the same position for equal ball speeds v_{baver}, independent of the flowrate. The use of empty and filled plastic balls allows us to alter their density by only a small amount. This results in an even more limited alteration in the speed of the balls. However, it can be shown that the change of the velocity of the conducting phase does not influence the position of the peak of the power spectrum.

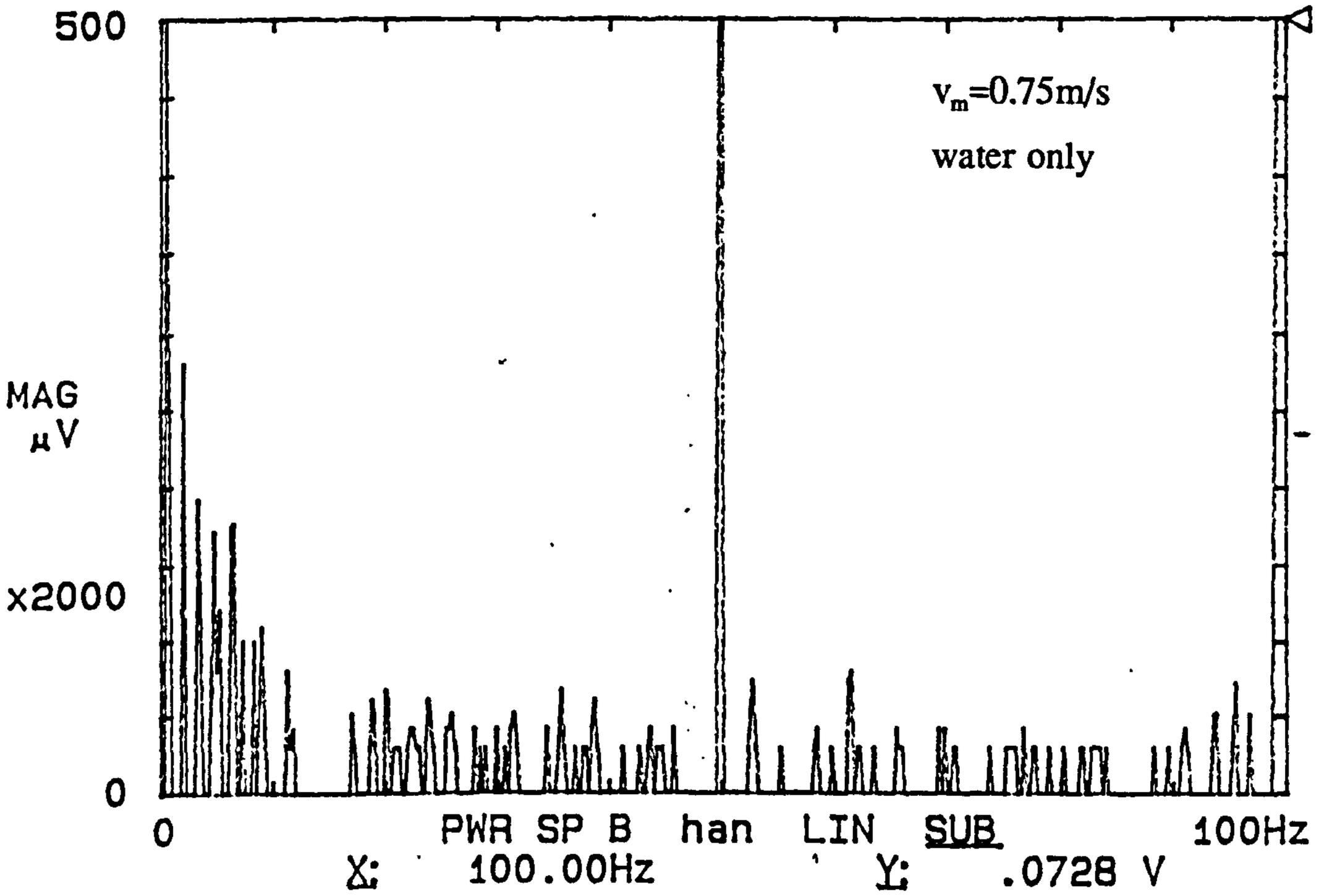

Fig.3.37 Measured power spectrum of flow signal for a single phase water flow

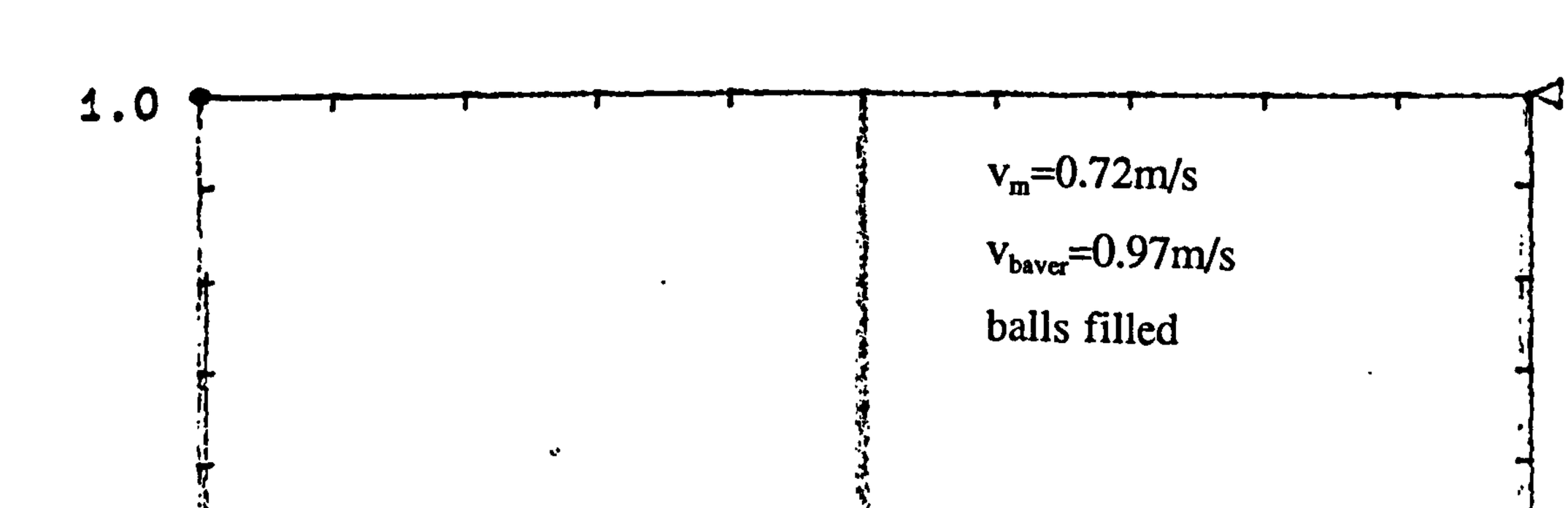

Fig.3.38 Measured power spectrum of flow signal with balls injected

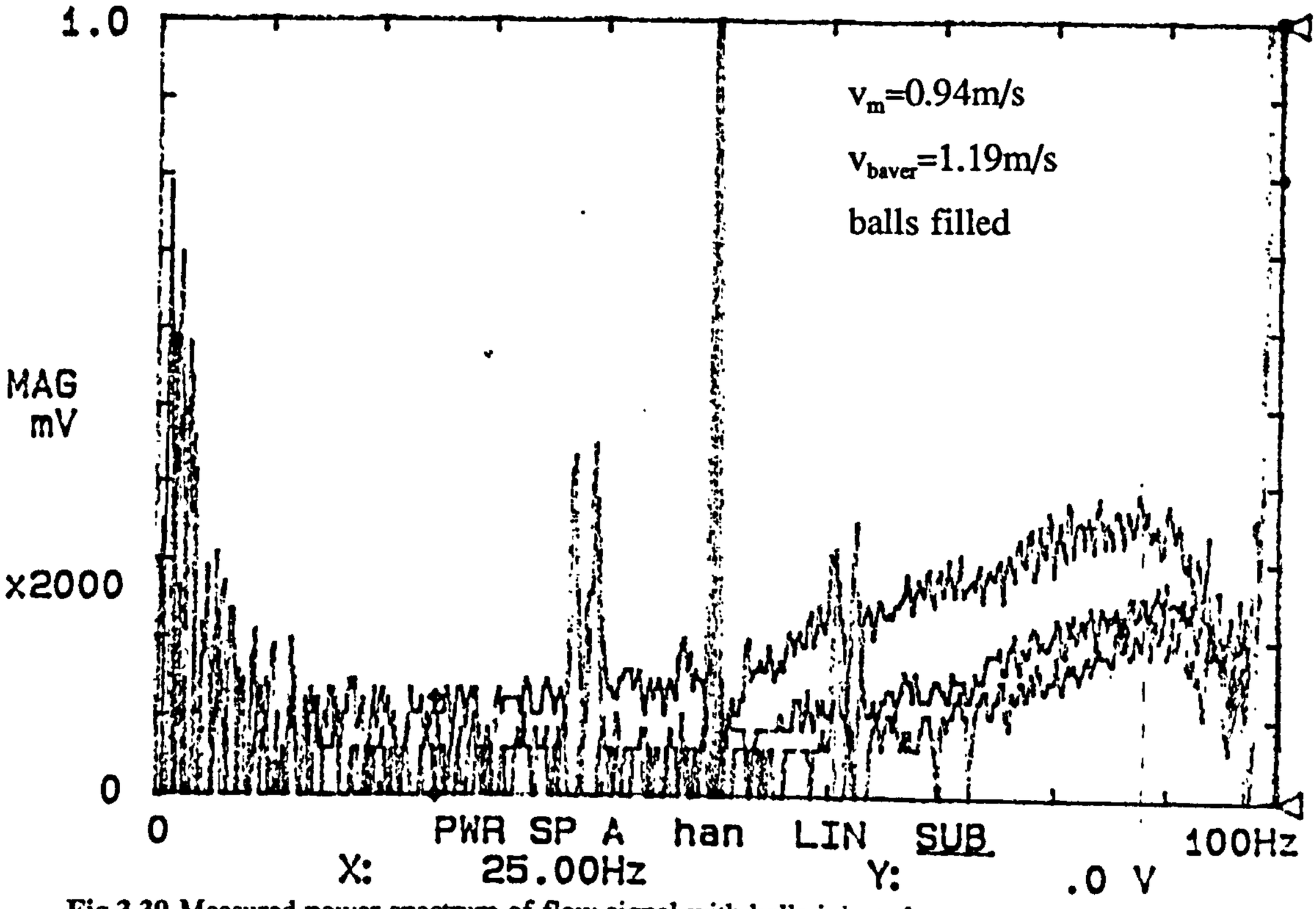

Fig.3.39 Measured power spectrum of flow signal with balls injected

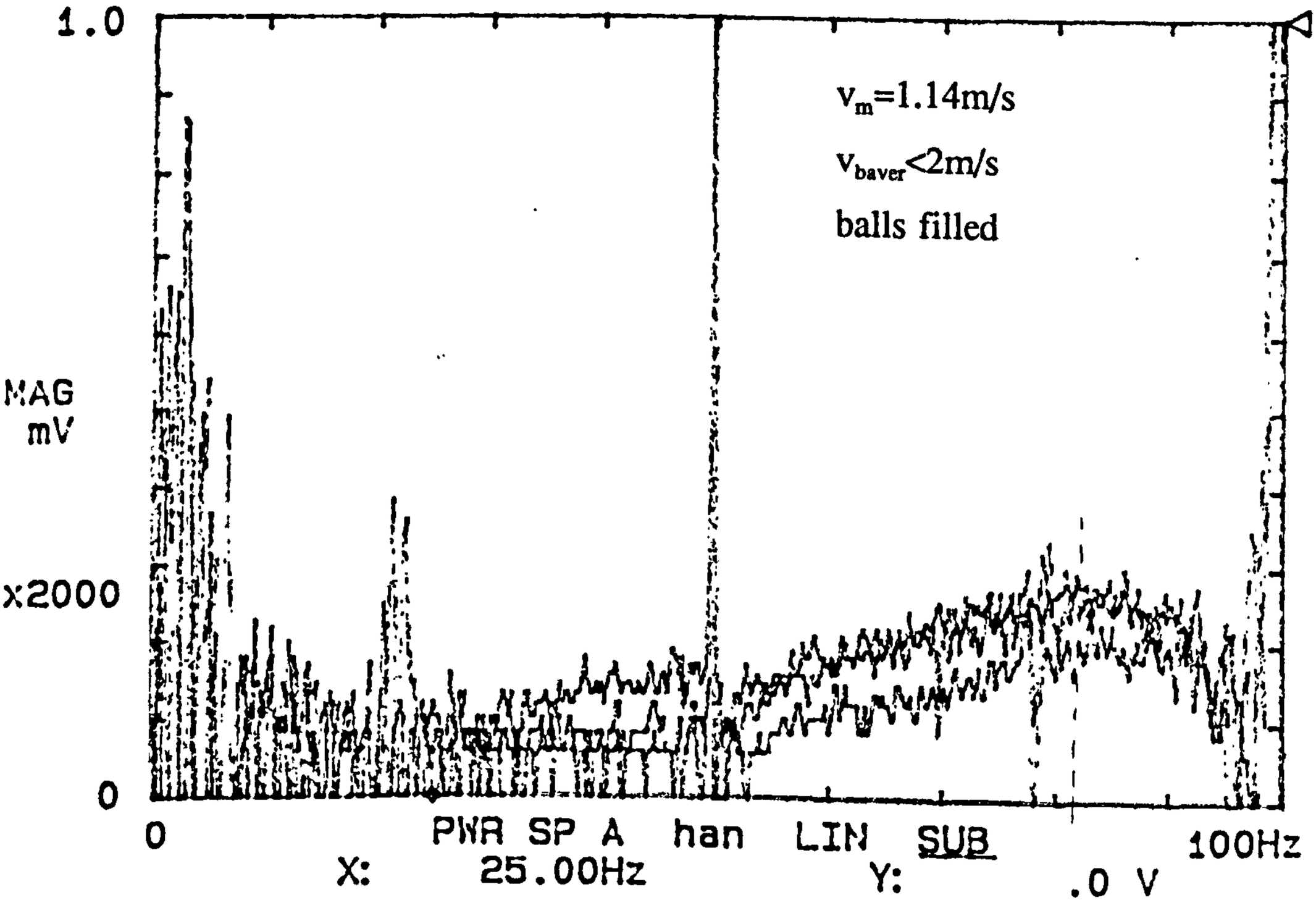

Fig.3.40 Measured power spectrum of flow signal with balls injected

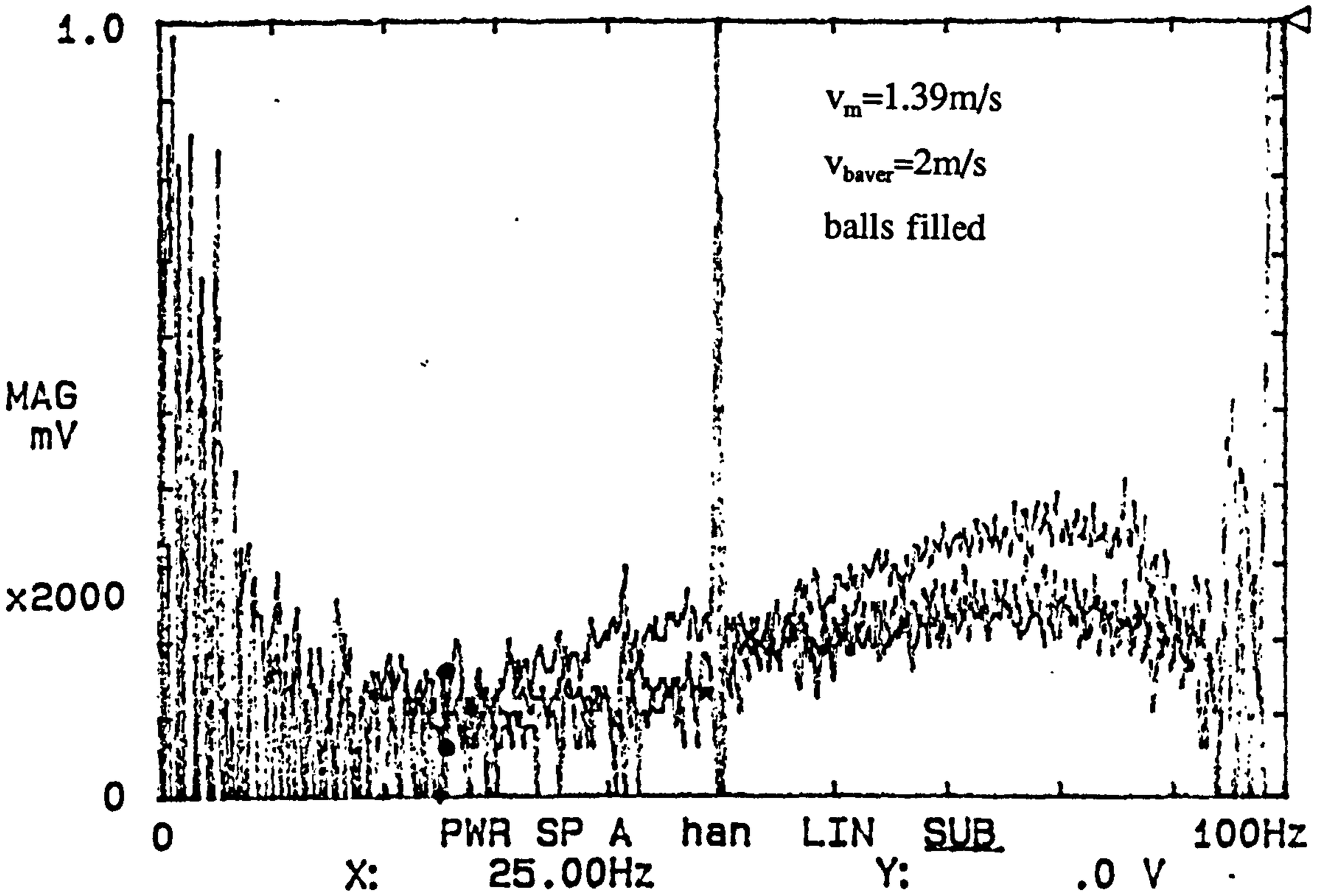

Fig.3.41 Measured power spectrum of flow signal with balls injected

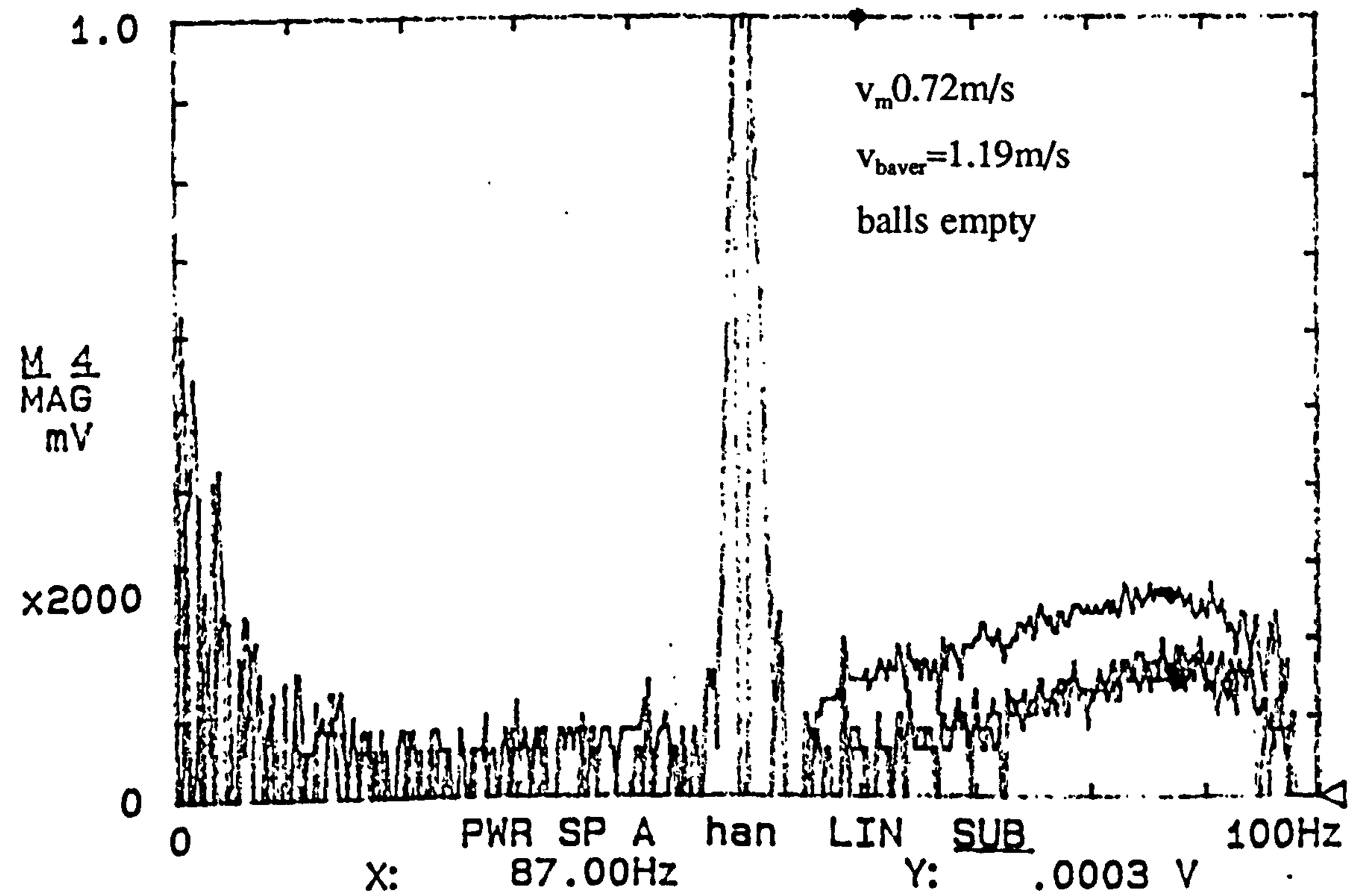

Fig.3.42 Measured power spectrum of flow signal with balls injected

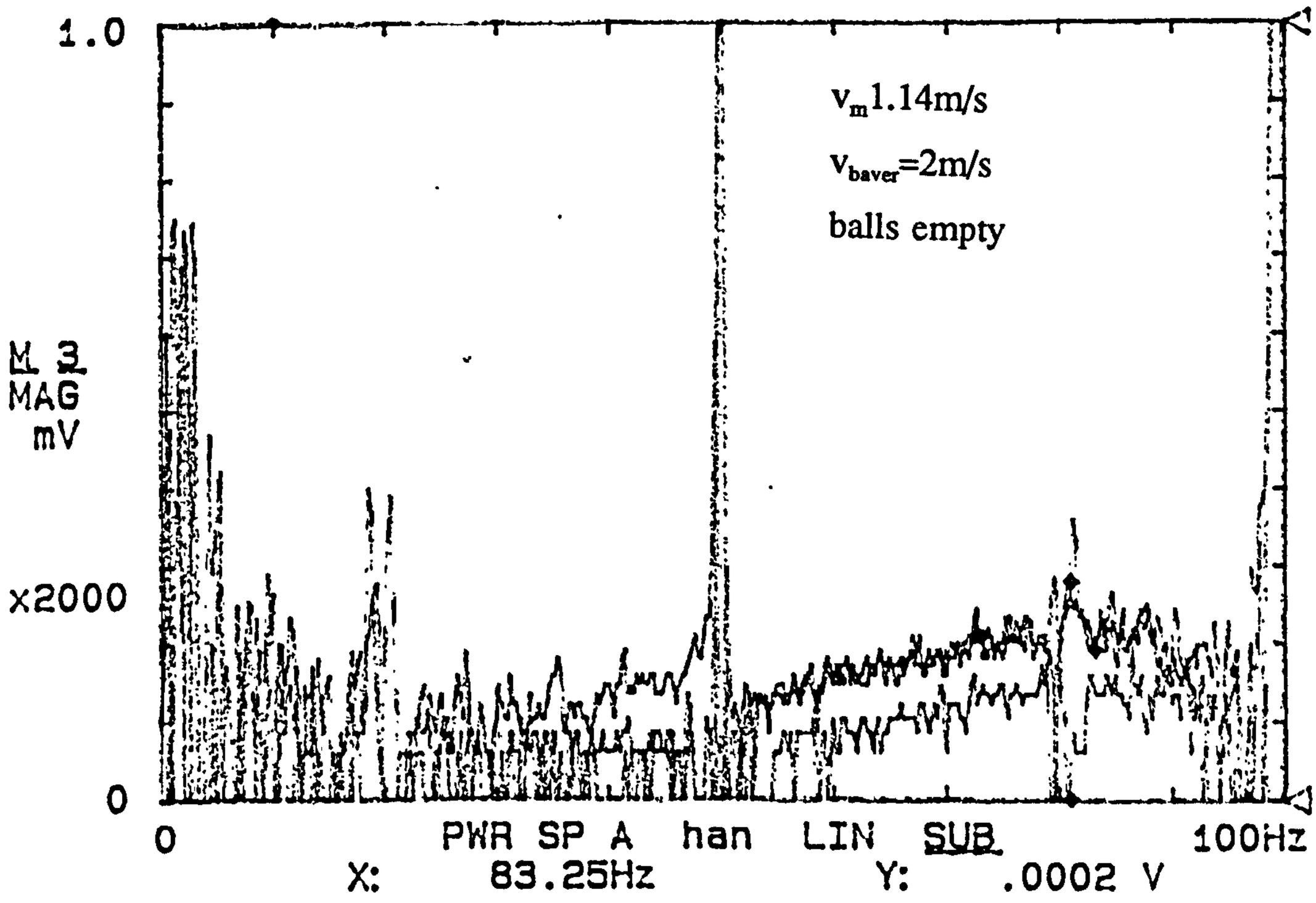

Fig.3.43 Measured power spectrum of flow signal with balls injected

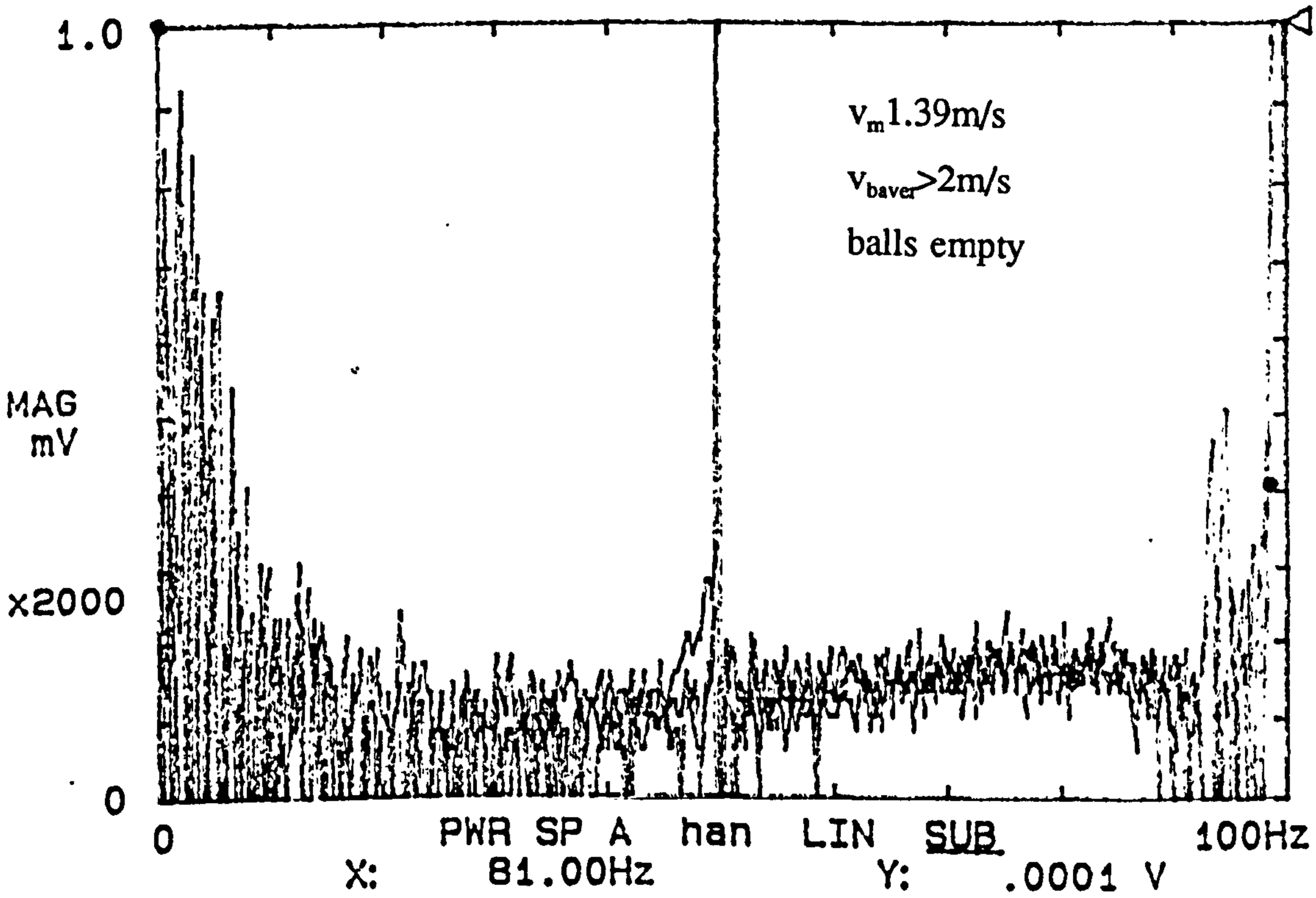

Fig.3.44 Measured power spectrum of flow signal with balls injected

CHAPTER 4

Transformer signal

In the previous chapter, it was shown that a nonconducting second phase does have an effect on the readings of an E.M-flowmeter. However, two questions are still open; what effect has been measured and on what parameters does it depend?
As said before, it could either be an effect on the flow signal or on the transformer signal. In order to predict the effect of a nonconducting second phase on transformer signal, a theoretical model has to be developed which can simulate a single ball or multiple balls. In addition it should allow an investigation of the effect of different electrode shapes.

4.1 Modelling a dipole in z-direction

In this section, a theoretical method is developed to predict the transformer signal in an E.M-flowmeter. In order to simplify the analysis, only a single sphere is considered. The analysis is based on the same idea used previously for the flow signal. A current dipole is imposed in a locally uniform current and the potential of this dipole is measured on the electrodes. The strength of the dipole is proportional to the strength of the current, its direction is opposite to the current.
The calculation is divided into four steps:

1). Evaluation of the eddy currents in a single conducting phase. Hereby a simplified model is used with an infinitely long magnetic field. In this case, the eddy currents are parallel to the pipe wall and are only a function of y. The end short effects are not considered.

2). Calculation of the field of a general dipole directed in the z-direction. The boundary conditions are again that no current is flowing into the pipe wall, i.e $j_n=0$.

3). Scaling the dipole to the strength of the eddy current and size of the sphere.

4.1.1 Eddy currents in an E.M-flowmeter

Considering again an infinitely long magnetic field, applied to the flowmeter with point electrodes, the equations describing the E-field in the liquid are [3]:

$$\nabla \times \underline{E} = -i\omega \underline{B}$$
$$\nabla \times \underline{B} = 0$$
$$\nabla \cdot \underline{B} = 0$$
$$\nabla \cdot \underline{j} = 0$$

In an infinitely long magnetic field, the eddy currents will be aligned parallel to the z-axis, turning round at infinity (**Fig.4.1**).

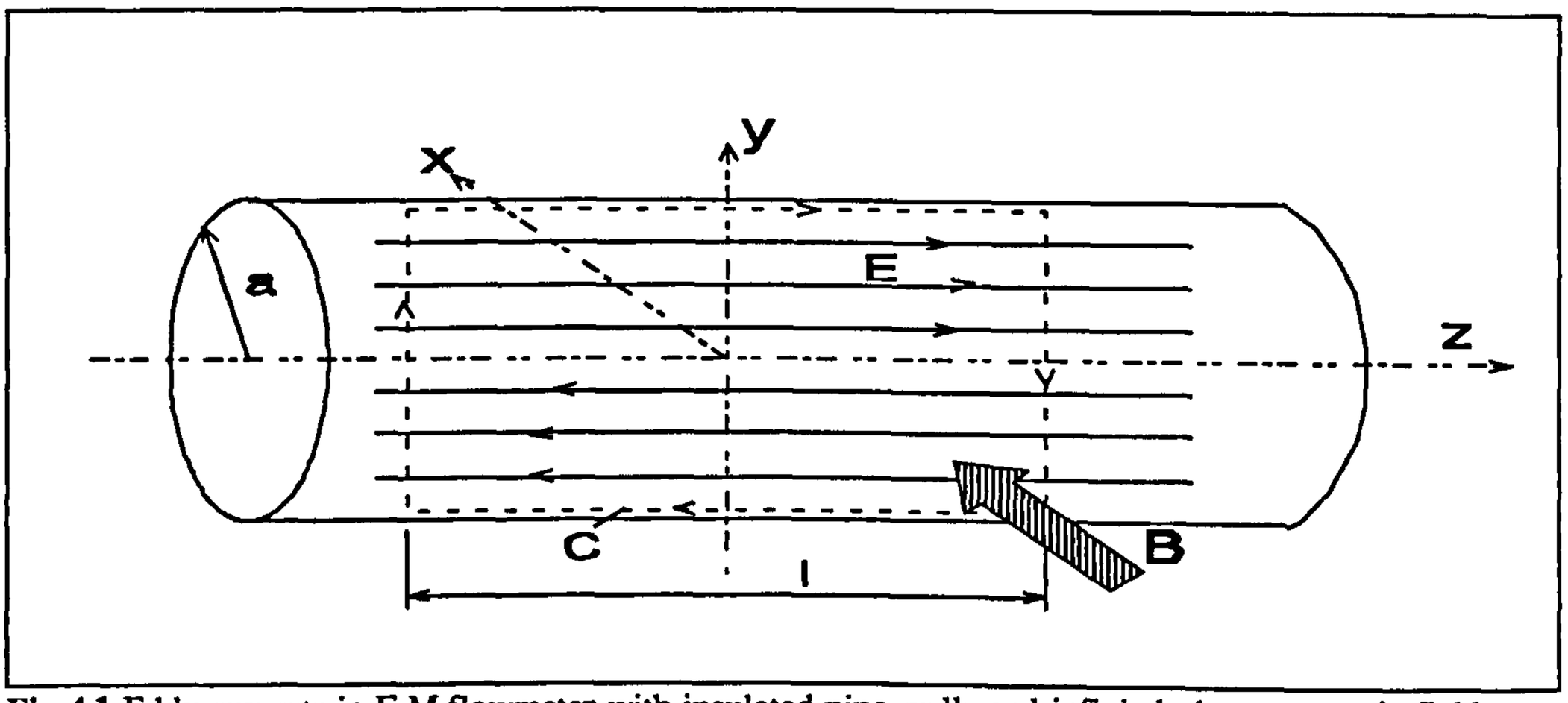

Fig.4.1 Eddy currents in E.M.flowmeter with insulated pipe walls and infinitely long magnetic field

When applying Faraday's law to this E-field, the maximum magnitude can easily be determined:

Faraday's law $\oint_c \underline{E}\,d\underline{l} = -i\omega \int_s \underline{B} \cdot d\underline{S}$.

Here, C is a closed contour, bounding the area S.
Equating both sides of the equation above yields

$$2El = -i\omega l 2yB$$
$$E = -i\omega By$$

with the current written as $j = \sigma E$, we find

$$\boxed{j = -\sigma i\omega By} \qquad \textbf{(4.1)}$$

4.1.2 Dipole in z-direction in a pipe with insulating walls.

The calculation of the field of a dipole in z-direction is similar to that for a dipole in a radial or circumferential direction.
A source and a sink are placed on the z-y-plane, a distance δ away from the y-axis and at height y (**Fig.4.2**)

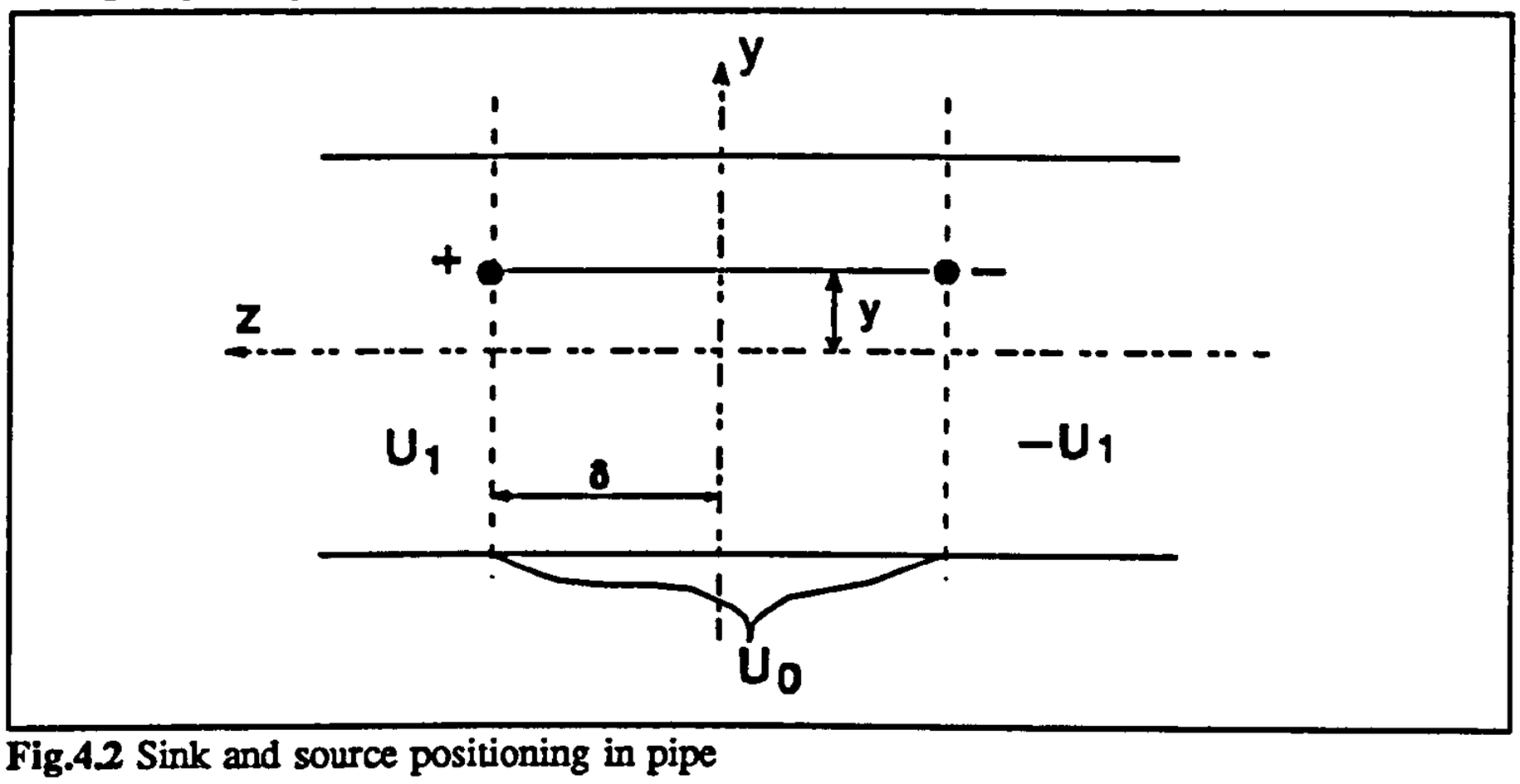

Fig.4.2 Sink and source positioning in pipe

The potential for $|z|>\delta$ is denoted $\pm U_1$, the potential for $|z|<\delta$ is U_0.

The equations for U_1 and U_0 are again Fourier-Bessel series'.

$$U_1=\sum_{m=-\infty}^{\infty}\sum_{n=1}^{\infty} a_{nm}e^{im\theta}J_{|m|}(j'_{|m|n}\frac{r}{a})e^{-\frac{j'_{|m|n}}{a}z}+a_{10} \qquad z>\delta \tag{4.2}$$

$$U_0=\sum_{m=-\infty}^{\infty}\sum_{n=1}^{\infty} b_{nm}e^{im\theta}J_{|m|}(j'_{|m|n}\frac{r}{a})\sinh(\frac{j'_{|m|n}}{a}z)+b_{10}z \qquad |z|<\delta \tag{4.3}$$

In both of these series', the term with m=0, n=1 is initially separated.
The conditions for U_1 and U_0 are continuity of potential and current at $z=\delta$.

$$U_1=U_0 \quad at\ z=\delta \tag{4.4}$$

$$-\left.\frac{\partial U_1}{\partial z}\right|_{z=\delta+}+\left.\frac{\partial U_0}{\partial z}\right|_{z=\delta-}=\frac{1}{r}\delta(\theta-\tfrac{\pi}{2})\delta(r-y) \tag{4.5}$$

From equation **4.4** we can relate the coefficients a_{nm} in terms of b_{nm}.

$$\sum_{m=-\infty}^{\infty}\sum_{n=1}^{\infty} a_{nm} e^{im\theta} J_{|m|}(j'_{|m|n}\frac{r}{a}) e^{-\frac{j'_{|m|n}}{a}\delta} + a_{10}$$
$$= \sum_{m=-\infty}^{\infty}\sum_{n=1}^{\infty} b_{nm} e^{im\theta} J_{|m|}(j'_{|m|n}\frac{r}{a}) \sinh(\frac{j'_{|m|n}}{a}\delta) + b_{10}\delta$$

Because the Fourier series and the Bessel series are unique, the expressions on both sides can only be equal if their coefficients are equal.

$$\therefore \quad \begin{aligned} a_{10} &= b_{10}\delta \\ a_{nm} &= b_{nm}\sinh(j'_{|m|n}\frac{\delta}{a}) e^{j'_{|m|n}\frac{\delta}{a}} \end{aligned} \qquad (4.6)$$

Differentiating U_1 and U_0 with respect to z yields

$$-\frac{\partial U_1}{\partial z} = \sum_{m=-\infty}^{\infty}\sum_{n=1}^{\infty} a_{nm} e^{im\theta} J_{|m|}(j'_{|m|n}\frac{r}{a}) e^{-\frac{j'_{|m|n}}{a}z} (\frac{j'_{|m|n}}{a})$$

$$\frac{\partial U_0}{\partial z} = \sum_{m=-\infty}^{\infty}\sum_{n=1}^{\infty} b_{nm} e^{im\theta} J_{|m|}(j'_{|m|n}\frac{r}{a}) \cosh(\frac{j'_{|m|n}}{a}z) \frac{j'_{|m|n}}{a} + b_{10}$$

Combining both equations with $z=\delta$ and substituting the coefficients a_{nm} from **eqn.4.6** yields

$$\left.\frac{-\partial U_1}{\partial z}\right|_{z=\delta} + \left.\frac{\partial U_0}{\partial z}\right|_{z=\delta} = \sum_{m=-\infty}^{\infty}\sum_{n=1}^{\infty} b_{nm}\frac{j'_{|m|n}}{a} e^{j'_{|m|n}\frac{\delta}{a}} e^{im\theta} J_{|m|}(j'_{|m|n}\frac{r}{a}) + b_{10}$$

We can write the product $b_{nm}\frac{j'_{|m|n}}{a}$ as c_{nm}, for $n,m \neq 1,0$. Also, $b_{10}=c_{10}$. This is because b_{10} is of course an element of the series and $j'_{|0|1}=0$, $J_{|0|}(0)=1$, $e^0=1$. The expression above can now be substituted into **eqn.4.5**:

$$\sum_{m=-\infty}^{\infty}\sum_{n=1}^{\infty} c_{nm} e^{j'_{|m|n}\frac{b}{a}} e^{im\theta} J_{|m|}(j'_{|m|n}\frac{r}{a}) = \frac{1}{r}\delta(\theta-\frac{\pi}{2})\,\delta(r-y) \qquad (4.7)$$

The coefficients c_{nm} are now determined by inverting **eqn.4.7.** With the right side of the equation above being a function $f(r,\theta)$ and the left side a series $\sum\sum f_{nm} e^{im\theta} J_{|m|}(x)$, we have the general expression for f_{nm} :

$$f_{nm} = \frac{j'^{2}_{|m|n}}{\pi a^{2}} \frac{\int_{-\pi}^{\pi}\int_{0}^{a} f(r,\theta)\, e^{-im\theta} J_{|m|}(j'_{|m|n}\frac{r}{a})\, r\,dr\,d\theta}{\left(j'^{2}_{|m|n}-m^{2}\right)\left(J_{|m|}(j'_{|m|n})\right)^{2}} \qquad (4.8)$$

Therefore

$$c_{nm} e^{j'_{|m|n}\frac{b}{a}} = \frac{j'^{2}_{|m|n}}{\pi a^{2}} \frac{\int_{-\pi}^{\pi}\delta(\theta-\frac{\pi}{2})\, e^{-im\theta} d\theta \int_{0}^{a}\frac{1}{r}\delta(r-y) J_{|m|}(j'_{|m|n}\frac{r}{a})\, r\,dr}{\left(j'^{2}_{|m|n}-m^{2}\right)\left(J_{|m|}(j'_{|m|n})\right)^{2}}$$

giving

$$\left.\begin{aligned} c_{nm} &= \frac{j'^{2}_{|m|n}}{\pi a^{2}} \frac{e^{-im\frac{\pi}{2}} J_{|m|}(j'_{|m|n}\frac{y}{a})\, e^{-j'_{|m|n}\frac{b}{a}}}{\left(j'^{2}_{|m|n}-m^{2}\right)\left(J_{|m|}(j'_{|m|n})\right)^{2}} \\ c_{10} &= \frac{1}{\pi a^{2}} \frac{e^{-i0\frac{\pi}{2}} J_{|0|}(j'_{|0|1}\frac{y}{a})\, e^{-j'_{|0|1}\frac{b}{a}}}{\left(J_{|0|}(j'_{|0|1})\right)^{2}} = \frac{1}{\pi a^{2}} \end{aligned}\right\} \qquad (4.9)$$

$$\therefore \quad \textit{with} \qquad b_{10}=c_{10} \;\Rightarrow\; b_{10}=\frac{1}{\pi a^{2}} \qquad (4.10)$$

Because $b_{nm}=\frac{c_{nm}a}{j'_{|m|n}}$, we find b_{nm} from **eqn.4.9:**

$$b_{nm}=\frac{j'_{|m|n}}{\pi a}\frac{e^{-im\frac{\pi}{2}}J_{|m|}(j'_{|m|n}\frac{y}{a})e^{-j'_{|m|n}\frac{\delta}{a}}}{\left(j'^{2}_{|m|n}-m^{2}\right)\left(J_{|m|}(j'_{|m|n})\right)^{2}} \tag{4.11}$$

For simplicity, we write from now on

$$G_{nm}=\frac{J_{|m|}(j'_{|m|n}\frac{y}{a})}{\left(j'^{2}_{|m|n}-m^{2}\right)\left(J_{|m|}(j'_{|m|n})\right)^{2}} \tag{4.12}$$

Inserting b_{10} and b_{nm} into **eqn.4.6**, we also find a_{10} and a_{nm} respectively:

$$a_{10}=\frac{\delta}{\pi a^{2}} \tag{4.13}$$

with

$$a_{nm}=\frac{j'_{|m|n}}{\pi a}e^{-im\frac{\pi}{2}}e^{-j'_{|m|n}\frac{\delta}{a}}G_{nm}\sinh(j'_{|m|n}\frac{\delta}{a})e^{j'_{|m|n}\frac{\delta}{a}}$$

$$\therefore \qquad a_{nm}=\frac{j'_{|m|n}}{\pi a}e^{-im\frac{\pi}{2}}\sinh(j'_{|m|n}\frac{\delta}{a})G_{nm} \tag{4.14}$$

Having determined expressions for the coefficients a_{nm} and b_{nm}, it is now possible to calculate U_1 and U_0. In order to reduce computational time later on, the series is rewritten with m starting at 0 instead at $-\infty$. We now have

$$U_1=\sum_{m=0}^{\infty}\sum_{n=1}^{\infty}\left(a_{n-m}e^{-im\theta}+a_{nm}e^{im\theta}\right)J_{|m|}(j'_{|m|n}\frac{r}{a})e^{-\frac{j'_{|m|n}}{a}z}(1-\frac{1}{2}\delta_{m0})+a_{10}$$

The term $(1-\frac{1}{2}\delta_{m0})$ ensures that all terms with m=0 are counted once only. Substituting for the a_{nm} using **(4.14)** we find

$$\left(a_{n-m}e^{-im\theta}+a_{nm}e^{im\theta}\right)=\left(e^{im\frac{\pi}{2}}e^{-im\frac{\pi}{2}}+e^{-im\frac{\pi}{2}}e^{im\theta}\right)\frac{j'_{|m|n}}{\pi a}\sinh(j'_{|m|n}\frac{\delta}{a})G_{nm}$$

$$\left(a_{n-m}e^{-im\theta}+a_{nm}e^{im\theta}\right)=\left(e^{im(\frac{\pi}{2}-\theta)}+e^{-im(\frac{\pi}{2}-\theta)}\right)\frac{j'_{|m|n}}{\pi a}\sinh(j'_{|m|n}\frac{\delta}{a})G_{nm}$$

$$\left(a_{n-m}e^{-im\theta}+a_{nm}e^{im\theta}\right)=2\cosh\left((-im(-\frac{\pi}{2}+\theta)\right)\frac{j'_{|m|n}}{\pi a}\sinh(j'_{|m|n}\frac{\delta}{a})G_{nm}$$

$$\left(a_{n-m}e^{-im\theta}+a_{nm}e^{im\theta}\right)=2\cos\left((m(\theta-\frac{\pi}{2})\right)\frac{j'_{|m|n}}{\pi a}\sinh(j'_{|m|n}\frac{\delta}{a})G_{nm}$$

Inserting the expression above in U_1 and substituting a_{10} from **(4.13)** yields

$$U_1=\sum_{m=0}^{\infty}\sum_{n=1}^{\infty}2\frac{j'_{|m|n}}{\pi a}\cos\left((m(\theta-\frac{\pi}{2})\right)J_{|m|}(j'_{|m|n}\frac{r}{a})\frac{\sinh(\frac{j'_{|m|n}}{a}\delta)}{e^{j'_{|m|n}\frac{\delta}{a}}}G_{nm}(1-\frac{1}{2}\delta_{m0})+\frac{\delta}{\pi a^2} \qquad \textbf{(4.15)}$$

This is the potential distribution of the current source and -sink in the pipe with insulating walls for $|z|>\delta$

In the same way we can rewrite U_0 as

$$U_0=\sum_{m=0}^{\infty}\sum_{n=1}^{\infty}(b_{n-m}e^{-im\theta}+b_{nm}e^{im\theta})J_{|m|}(j'_{|m|n}\frac{r}{a})\sinh(\frac{j'_{|m|n}}{a}z)(1-\frac{1}{2}\delta_{m0})+b_{10}z$$

$$\left(b_{n-m}e^{-im\theta}+b_{nm}e^{im\theta}\right)=\left(e^{im\frac{\pi}{2}}e^{-im\theta}+e^{-im\frac{\pi}{2}}e^{im\theta}\right)\frac{j'_{|m|n}}{\pi a}e^{-j'_{|m|n}\frac{\delta}{a}}G_{nm}$$

$$\left(b_{n-m}e^{-im\theta}+b_{nm}e^{im\theta}\right)=\left(e^{-im(\theta-\frac{\pi}{2})}+e^{im(\theta-\frac{\pi}{2})}\right)\frac{j'_{|m|n}}{\pi a}e^{-j'_{|m|n}\frac{\delta}{a}}G_{nm}$$

$$\left(b_{n-m}e^{-im\theta}+b_{nm}e^{im\theta}\right)=2\cos\left(m(\theta-\frac{\pi}{2})\right)\frac{j'_{|m|n}}{\pi a}e^{-j'_{|m|n}\frac{\delta}{a}}G_{nm}$$

$$U_0=\sum_{m=0}^{\infty}\sum_{n=1}^{\infty}2\frac{j'_{|m|n}}{\pi a}\cos\left(m(\theta-\frac{\pi}{2})\right)J_{|m|}(j'_{|m|n}\frac{r}{a})\frac{\sinh(\frac{j'_{|m|n}}{a}z)}{e^{j'_{|m|n}\frac{\delta}{a}}}G_{nm}(1-\frac{1}{2}\delta_{m0})+b_{10}z \qquad \textbf{(4.16)}$$

This is the potential distribution of a current source and -sink in a pipe with insulating walls for $|z|<\delta$.

So far we have considered a source and sink of unit strength at a distance 2δ away from each other. If we take the limit of $U_1\frac{K}{2\delta}$ for $\delta\rightarrow 0$, we obtain the expression for a point dipole of unit strength $K=Q\cdot l$ in z-direction.

$$\lim_{\delta\rightarrow 0} U_1\frac{K}{2\delta}=$$

$$\lim_{\delta\rightarrow 0}\left[\sum_{m=0}^{\infty}\sum_{n=1}^{\infty} 2\frac{j'_{|m|n}}{\pi a}\cos\left((m(\theta-\tfrac{\pi}{2})\right)J_{|m|}(j'_{|m|n}\tfrac{r}{a})\frac{\sinh(\frac{j'_{|m|n}}{a}\delta)}{e^{j'_{|m|n}\frac{z}{a}}}G_{nm}(1-\tfrac{1}{2}\delta_{m0})+\frac{\delta}{\pi a^2}\right]\frac{K}{2\delta}$$

because $\lim_{\delta\rightarrow 0}\left[\sinh\left(j'_{|m|n}\frac{\delta}{a}\right)\right]=j'_{|m|n}\frac{\delta}{a}$, *we find*

$$\lim_{\delta\rightarrow 0} U_1\frac{K}{2\delta}=$$

$$K\left[\sum_{m=0}^{\infty}\sum_{n=1}^{\infty}\frac{j'^2_{|m|n}}{\pi a^2}\cos\left((m(\theta-\tfrac{\pi}{2})\right)J_{|m|}(j'_{|m|n}\tfrac{r}{a})e^{-j'_{|m|n}\frac{z}{a}}G_{nm}(1-\tfrac{1}{2}\delta_{m0})+\frac{1}{\pi a^2}\right] \qquad (4.17)$$

This is the potential distribution of a dipole in z-direction in a pipe with insulating walls.(valid for z>0)

4.1.3 Scaling the dipole to the strength of the eddy current.

In order to obtain the final equation for U_1, we have to scale the strength of the dipole according to the strength of the eddy current and the size of the sphere. Here we can use the same factor as in the previous calculation of the flow signal (chapter3.2.2, eqn.3.27). For a sphere of radius c, the dipole strength K has to be:

$$K=2\pi\frac{c^3}{\sigma}j_0 \qquad (4.18)$$

where σ is the conductivity of the fluid and j_0 is the undisturbed eddy current from equation **4.1**.

4.2 Computed results for flowmeter with point electrodes

Fig.4.3 and **Fig.4.4** illustrate the potential distribution of a dipole in a pipe with insulating walls.

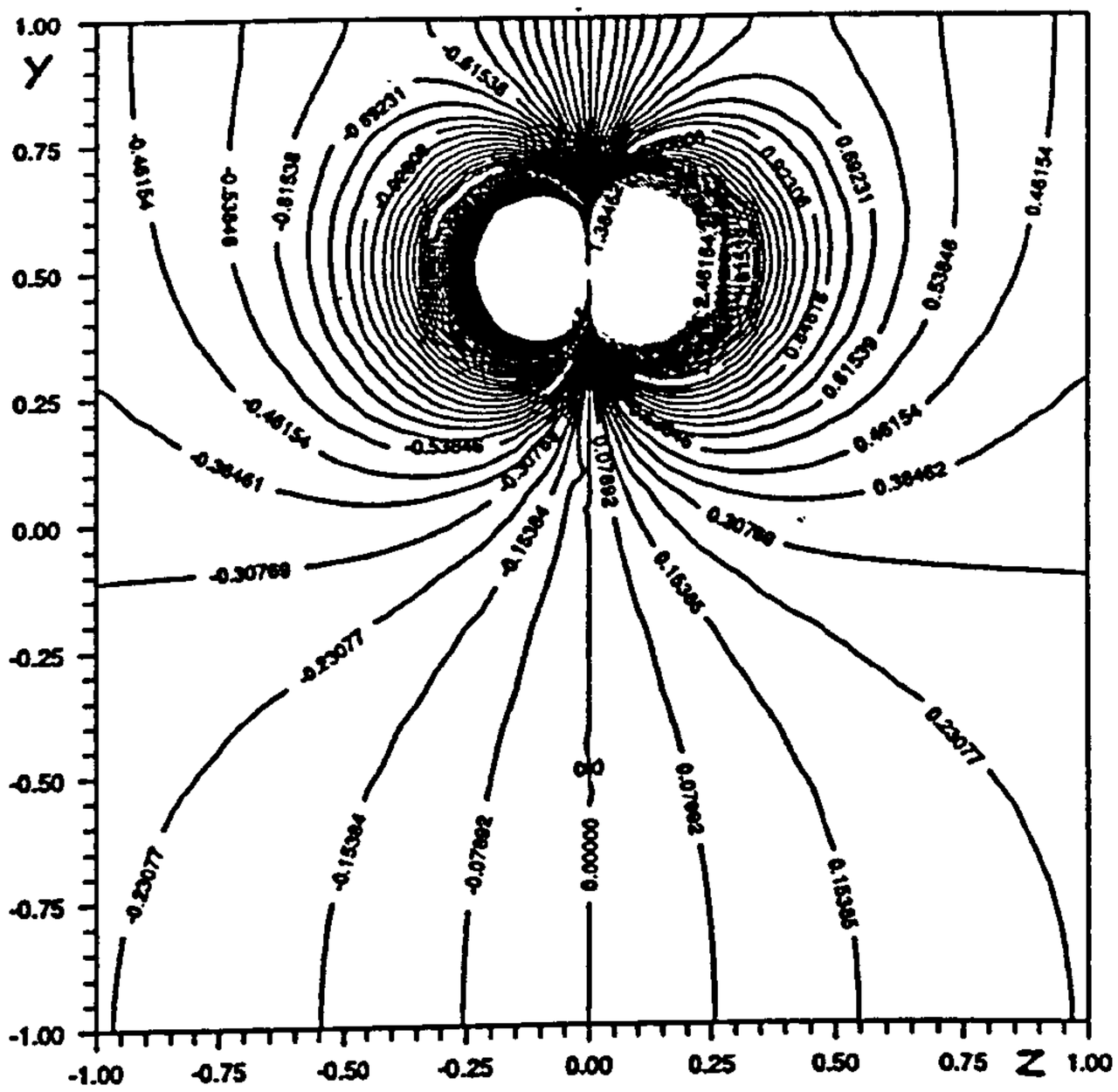

Fig.4.3 Potential lines in the y-z plane of a dipole in a pipe with insulated walls

The potential lines are perpendicular to the wall, therefore the normal component of the current is zero at the wall.
Based on this potential distribution, the voltage difference is calculated between opposite points on the pipe wall, where the electrodes are located. For larger electrodes, the potential difference is computed at a grid of points and then averaged.

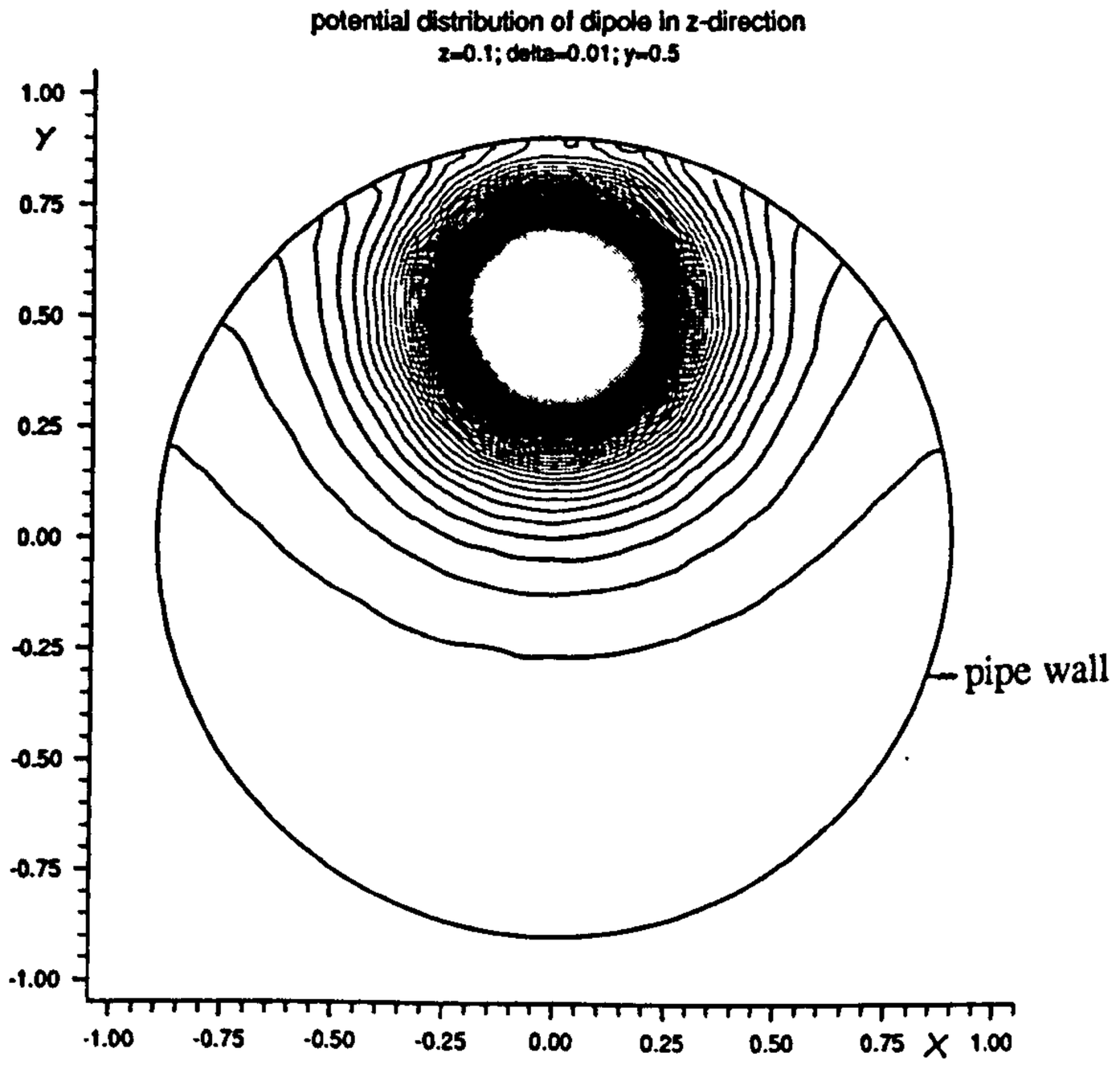

Fig.4.4 Potential lines in the x-y plane of a dipole in a pipe with insulated walls

Fig.4.5 shows the rectified transformer signal, generated by a ball with a diameter of 1/10 of the pipe diameter. It moves along the pipe axis in the y-z plane. The computed curve decays exponentially to almost zero after three times the radius. At z=0.5 to each side of the electrode plane, the transformer signal reaches a peak and in the electrode plane it crosses through zero, changing its sign. When the signal has reached its maximum value, it then quickly decays. At a distance of twice the pipe radius it is already decreased to 20% of its maximum value. In all the following graphs (unless otherwise stated), the transformer signal is computed for a pipe of unit radius and a magnetic field strength of 1. The frequency of the magnetic field is 50Hz.

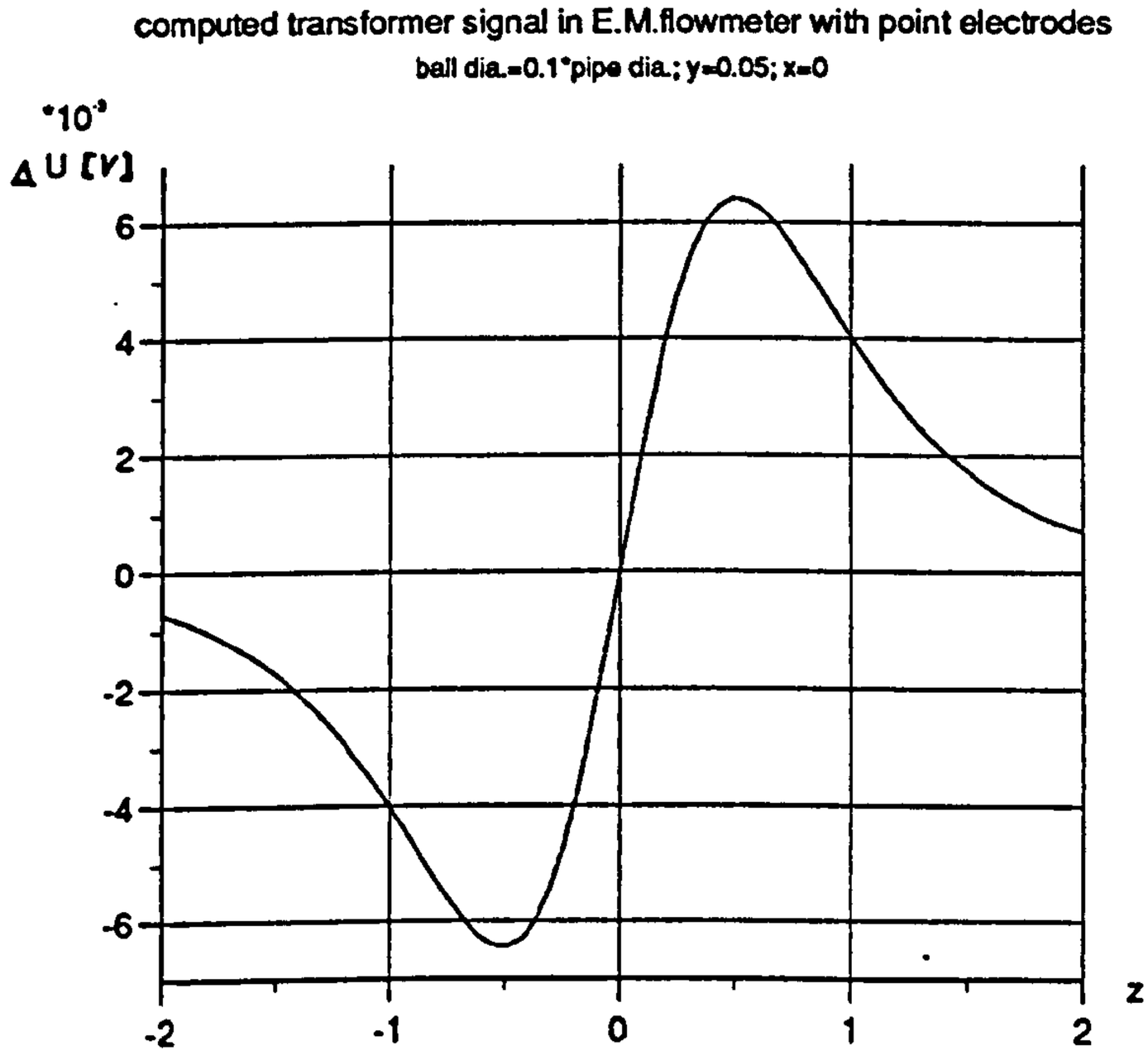

Fig.4.5 Computed rectified transformer signal due to a single nonconducting sphere.

Fig.4.6 shows again the computed transformer signals for a single ball in the y-z-plane. The radius of the ball is 10% of the pipe radius. The position of the ball in the cross section of the pipe is kept constant while it passes through the meter.
The shape of the transformer signal curves are similar but the absolute value increases as the path of the ball is moved closer to the pipe wall. Also, the distance between the maximum and minimum of the signal decreases considerably from approximately 25mm to half the ball size when the ball passes closest to the electrodes.

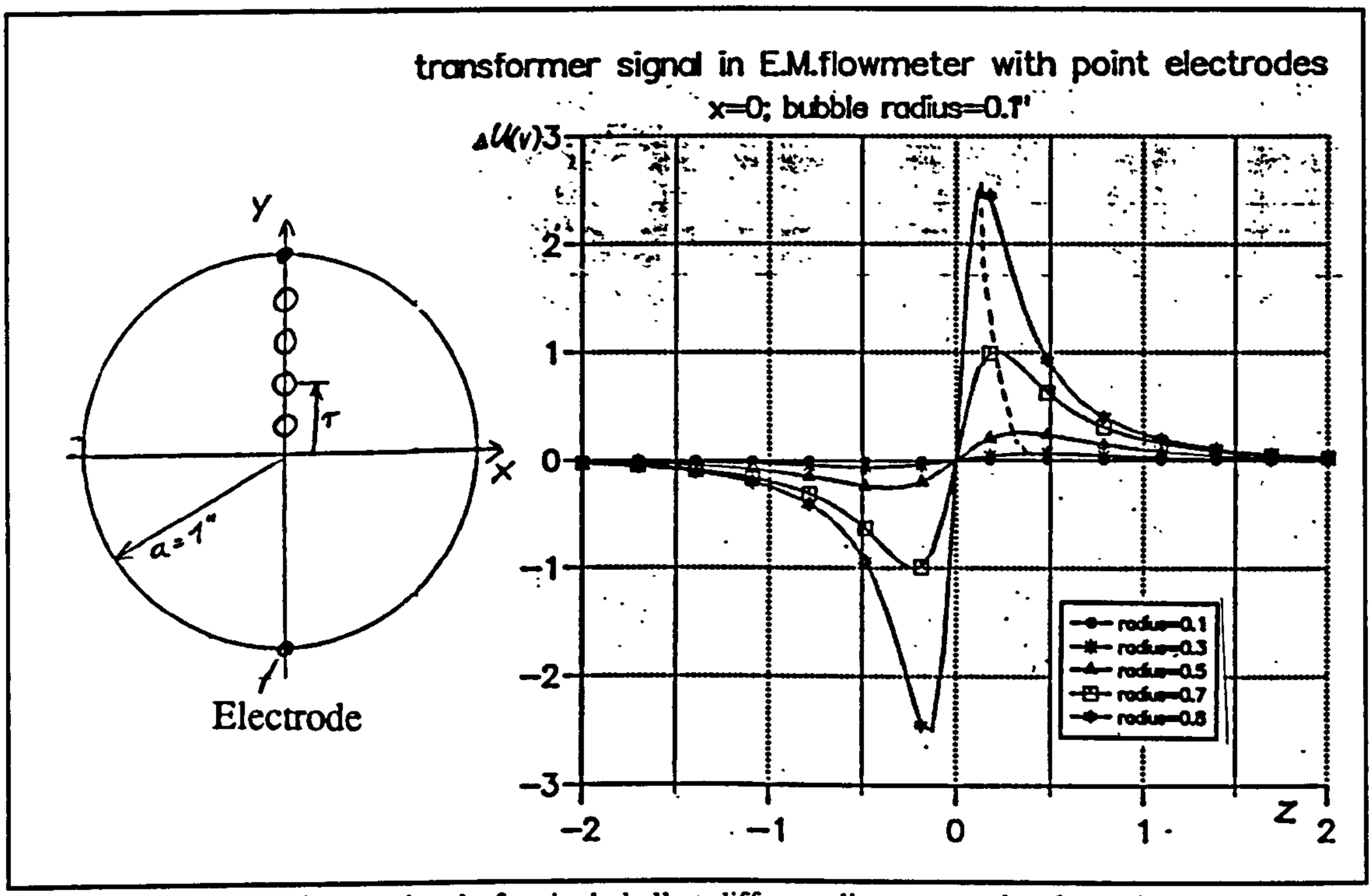

Fig.4.6 Rectified transformer signal of a single ball at different distances to the electrodes.

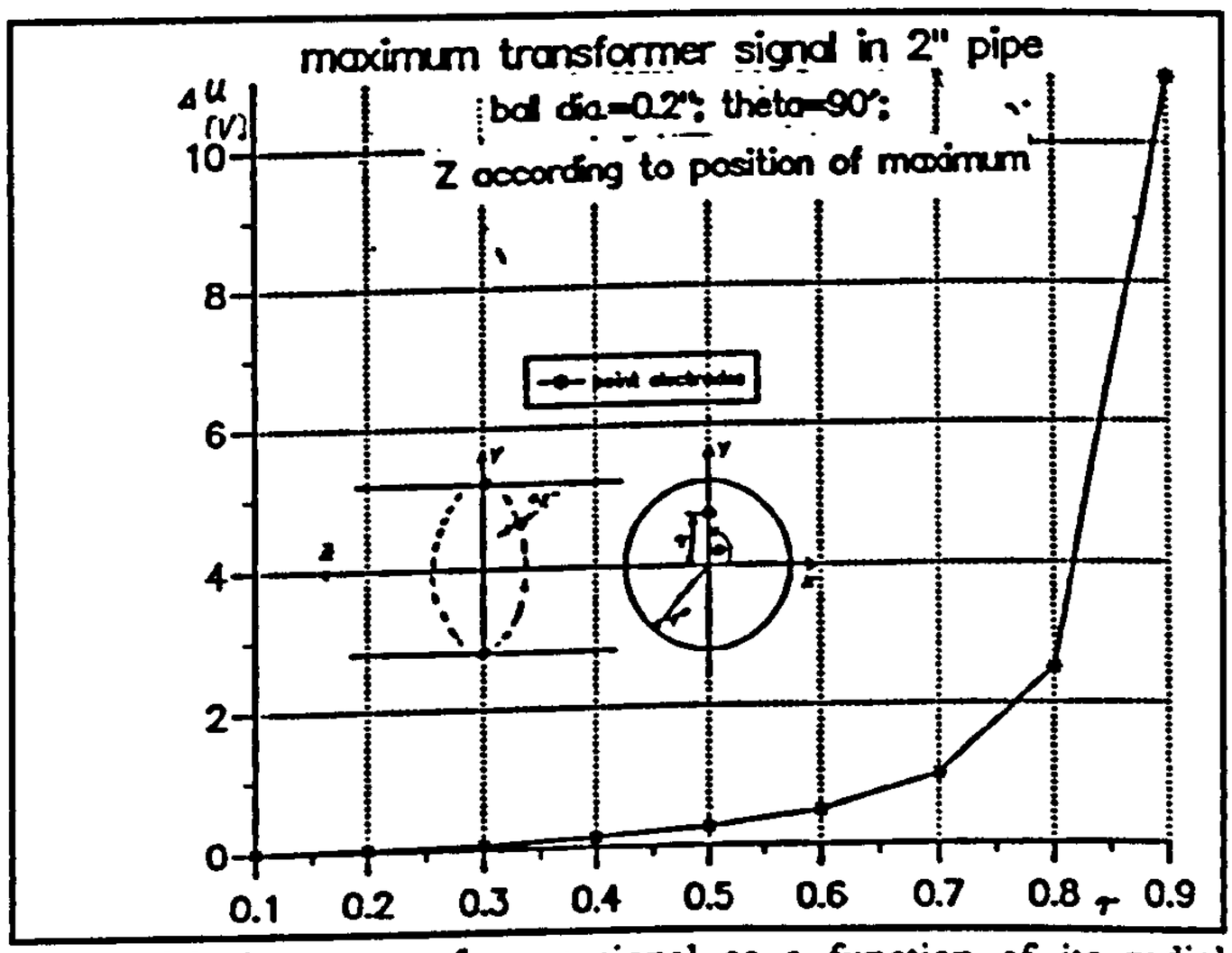

Fig.4.7 Maximum transformer signal as a function of its radial position in the pipe

In **Fig.4.7**, the maximum transformer signal is plotted as a function of its radial position in the pipe. The magnitude of the signal increases exponential like with the radius. Although the graph refers only to the signal change for motion in the y-z plane, the shape of the curve will be similar for other paths parallel to the tube axis.
It is important to notice that the maximum of the transformer signal does not occur at a constant z-value.

The rate of change depends on the angular position in the pipe as well. This is shown in **Fig.4.8** for a radial position of r=0.9.
Again, the magnitude of the signal increases almost exponentially on approaching one electrode.

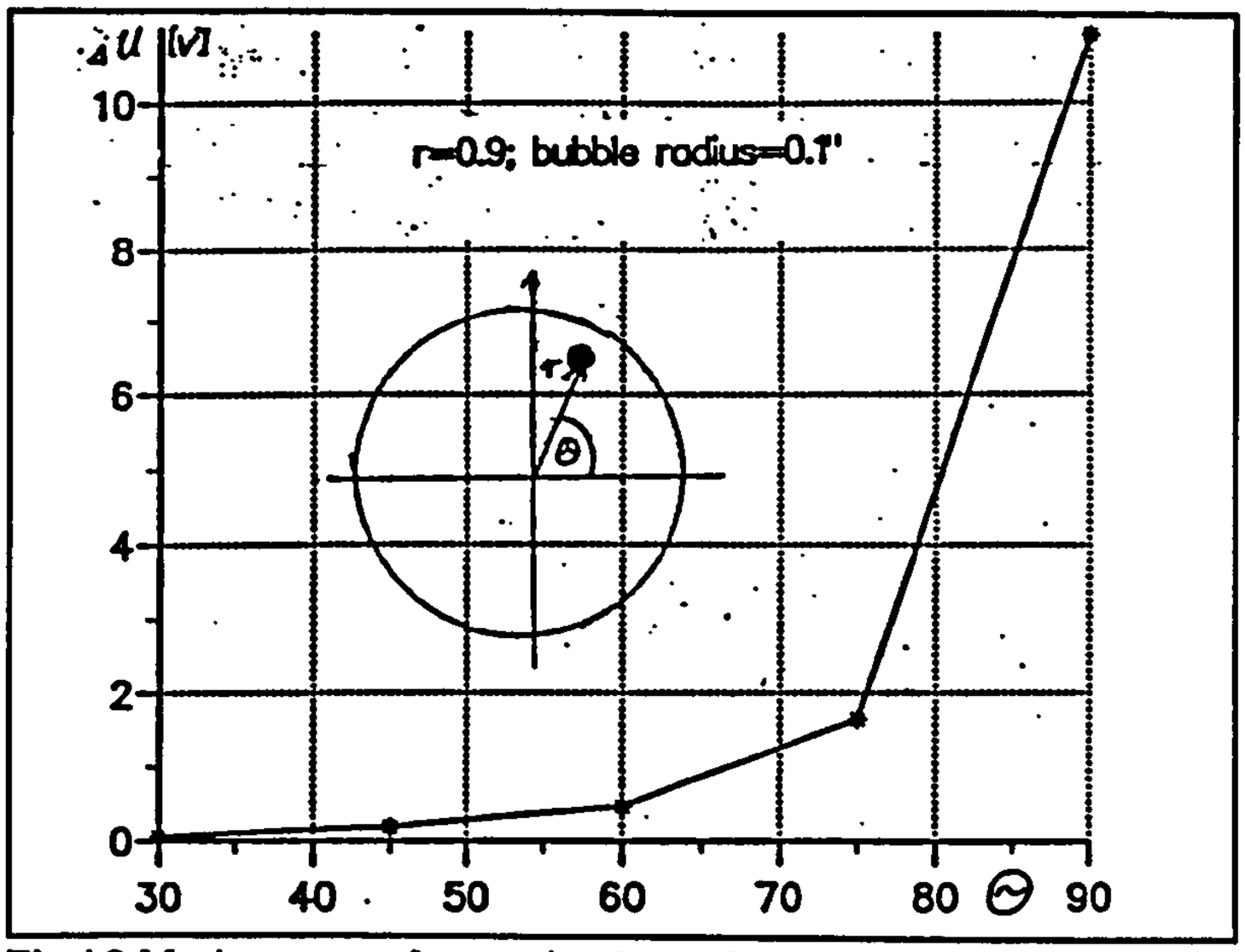

Fig.4.8 Maximum transformer signal as a function of the circumferential position of the ball.

Fig.4.9 illustrates the previously mentioned curves of the maximum transformer signal for different angular positions. For angles of less than 45 degrees, the curve is almost a straight line or even curved slightly outwards. At larger angles however, the path is more and more curved with its maximum curvature in the y-z plane. As a consequence, it takes a bubble in the y-z-plane almost five times longer to travel the distance between the points of maximum and minimum transformer signal when it is in the centre of the pipe as if it is near on an electrode. In other words, bubbles could generate frequencies in the power spectrum which vary by a factor of five, even though their velocities are equal.

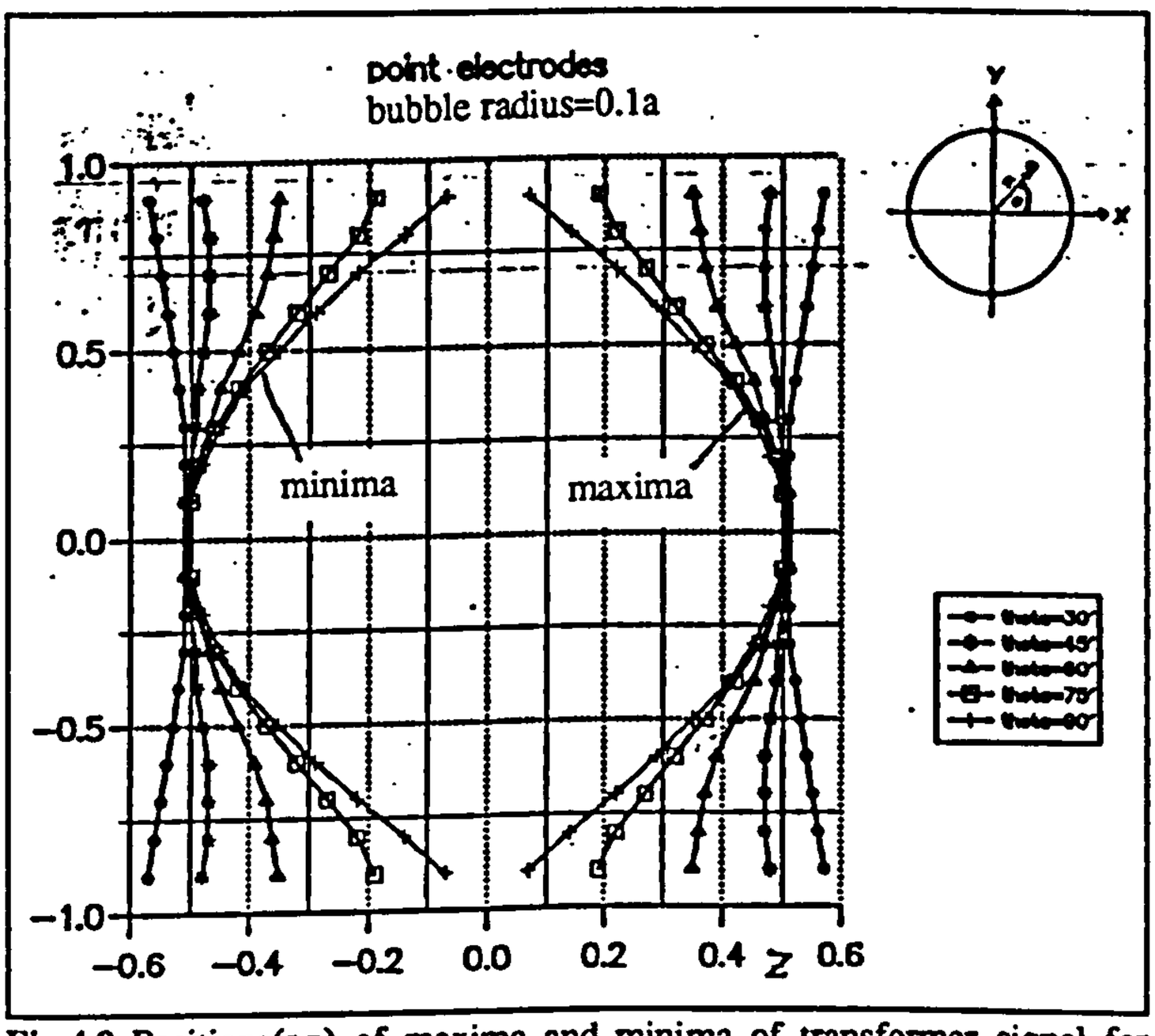

Fig.4.9 Positions(r,z) of maxima and minima of transformer signal for paths at certain angles in an E.M-flowmeter with point electrodes

Fig.4.10 shows the locus of maximum transformer signal as a three dimensional shape. The z-value in the plot is the distance between the maximum transformer signal and the electrode plane.
It becomes apparent that point electrodes are not ideal for relating the transformer signal to bubble velocity because the position of the bubble influences the magnitude of the signal and its shape.

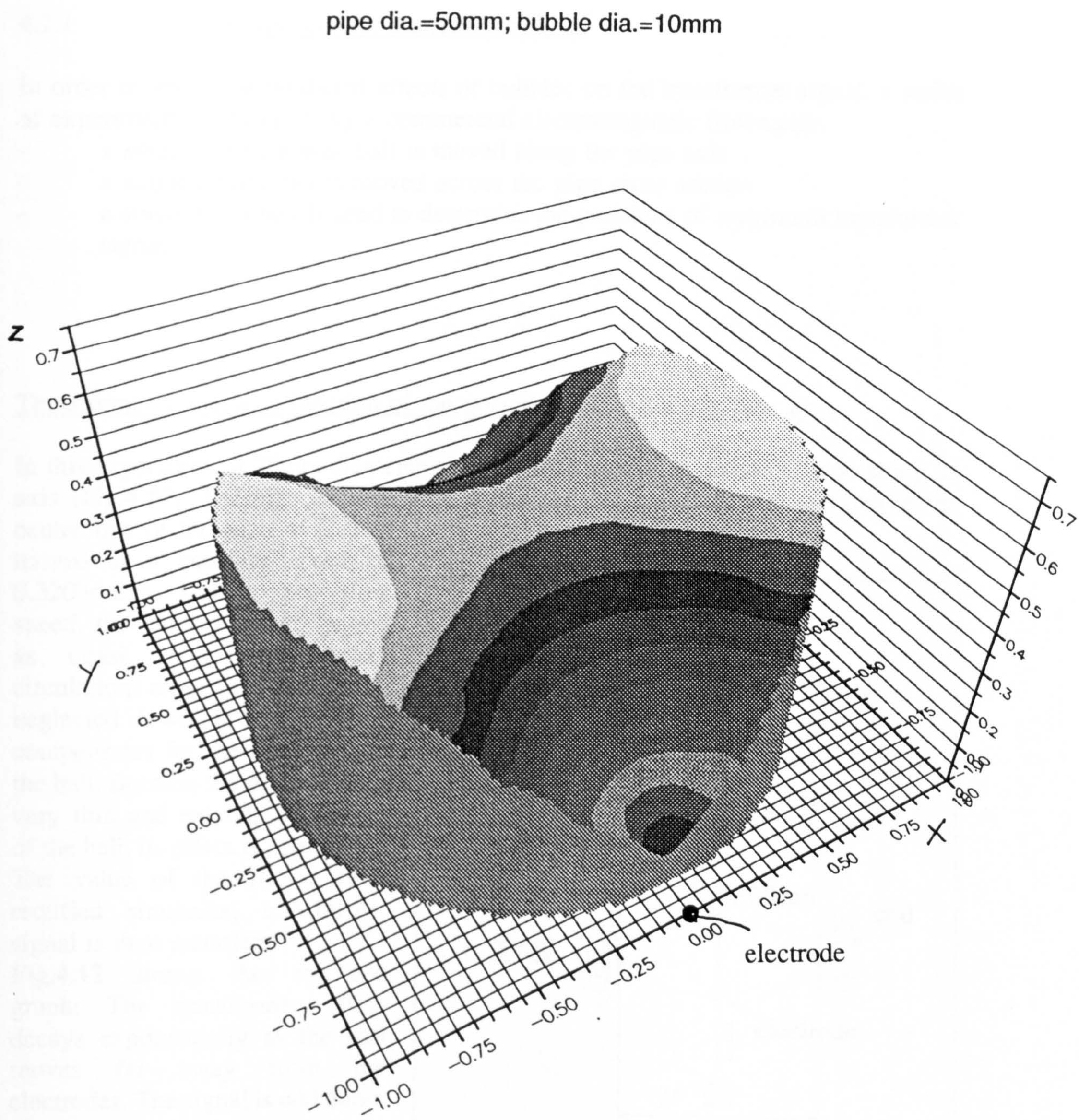

Fig.4.10 Surface of maximum transformer signal due to a small bubble in an E.M-flowmeter with point electrodes and uniform magnetic field.

4.2.1 Experiments with transformer signal

In order to verify the predicted effects of bubbles on the transformer signal, a series of experiments is set up using a commercial electromagnetic flowmeter.

- a single 25mm plastic ball is moved along the pipe axis
- a single 25mm ball is moved across the pipe cross section
- a single 8mm ball is used to determine the positions of maximum transformer signal.

Transformer signal as a function of the position of a ball along tube axis

In this experiment, a 25mm diameter plastic ball is moved in a vertical pipe along its axis (**Fig.4.11**). The pipe is filled with water and the ball is first positioned in the centre line of the pipe. It is then moved at a constant speed of 0.3203mm/s. Due to the slow speed, the motion can be treated as quasi static. Any water circulations around the ball can be neglected. A weight on a long line compensates for the buoyancy of the ball. Because the plastic line is very thin and extends both sides of the ball, its effect is negligible. The value of the 100Hz fully rectified sinusoidal transformer signal is then recorded.

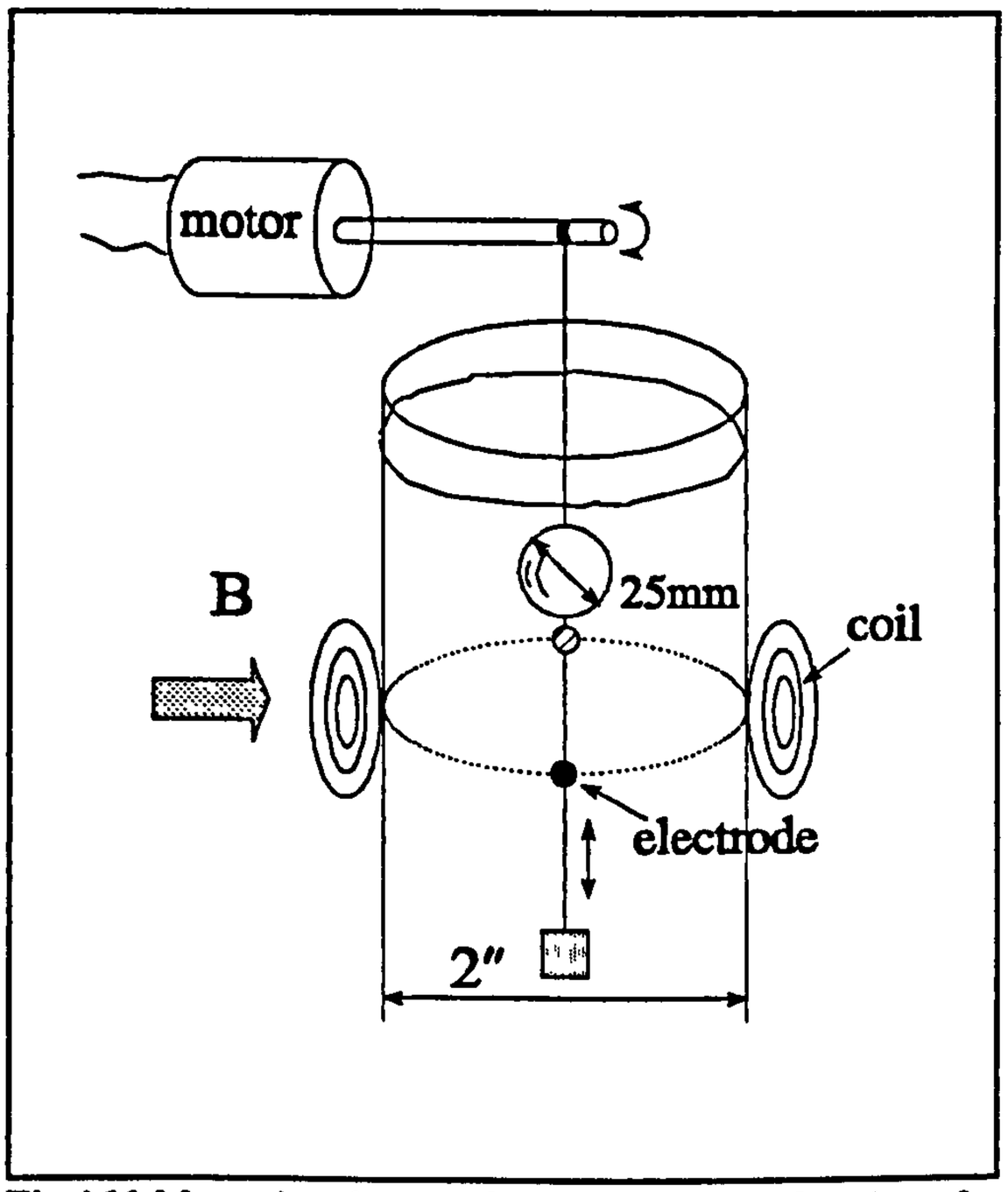

Fig.4.11 Measuring the transformer signal as a function of z

Fig.4.12 shows the recorded graph: The transformer effect decays exponentially as the ball moves far away from the electrodes. The signal is odd about the electrode plane and zero in the electrode plane, as expected for an E-field shown in **Fig.4.1.** The maximum and minimum are 73.44 seconds apart from each other
which is equivalent to 23.52mm.
When comparing the measured transformer signal in **Fig.4.12** with the computed signal shown below (**Fig.4.12a**), a good agreement is found.
The computed curve has decayed after 75mm whereas the measured signal has decayed after 60mm. This difference can be explained with the fact that the theoretical model assumes an infinitely long magnetic field and therefore the bubble goes on generating a transformer signal at a longer distance away from the electrodes.
The distance between maximum and minimum transformer signal is 23.5mm in the

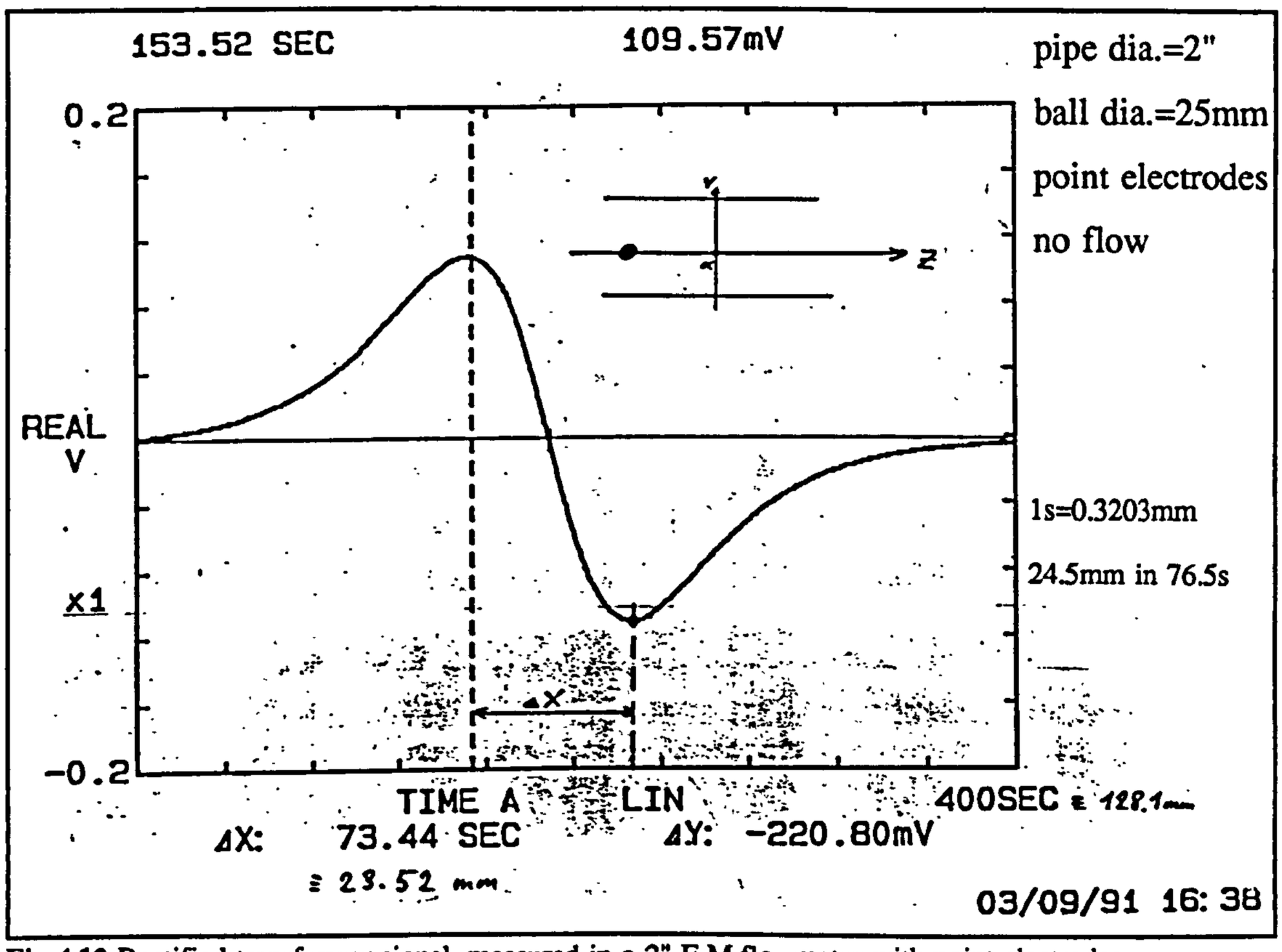

Fig.4.12 Rectified transformer signal, measured in a 2" E.M.flowmeter with point electrodes.

experiment compared to 25.9mm computed. An explanation for this discrepancy could be again that the eddy currents were assumed to be parallel and only a function of y, whereas in reality the magnetic field is relatively short and end shorting currents exist. In addition the theory only holds for small bubbles and not really for one of 1" diameter in a 2" pipe.

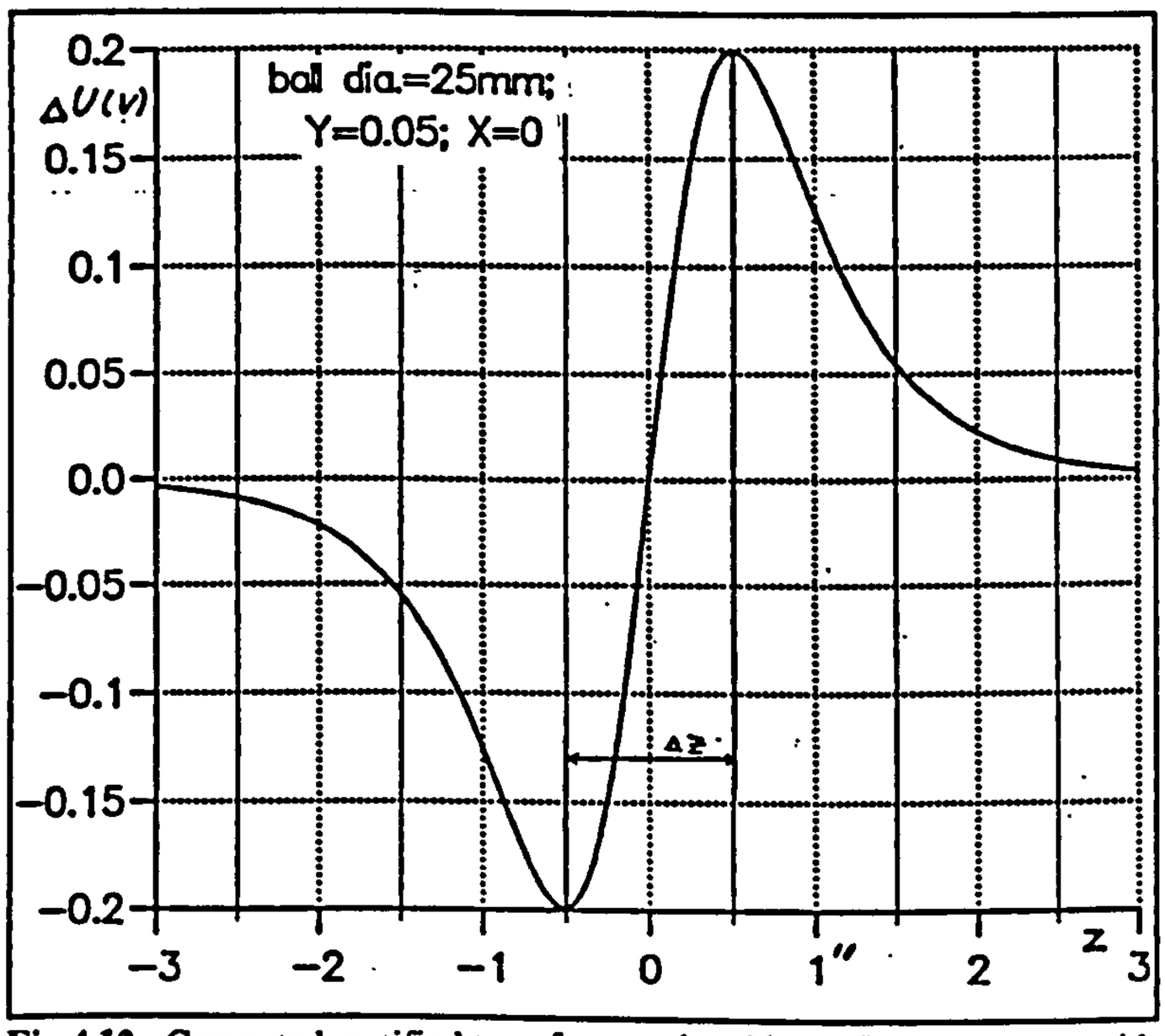

Fig.4.12a Computed rectified transformer signal in an E.M.flowmeter with point electrodes. Bubble size =0.5*pipe diameter

Transformer signal as a function of position of ball in pipe cross section

In the following experiment, the dependance of the transformer signal on the position of the ball in the pipe cross section is investigated. **Fig.4.13** shows the setup of the experiment. The 25mm ball is attached to a thin fishing line. The upper end of the line is fixed to a traverse which is itself mounted on an indexed brass ring. In order to map the cross section of the pipe, the angle is manually set in increments of 10°. The traverse is moved with a motorised micrometer in steps of 1mm. The height of the ball is then adjusted to 12.5 mm above the electrode plane. A weight at the bottom end of the nylon string compensates again for the buoyancy of the ball. Again, the amplitude of the transformer signal is recorded.

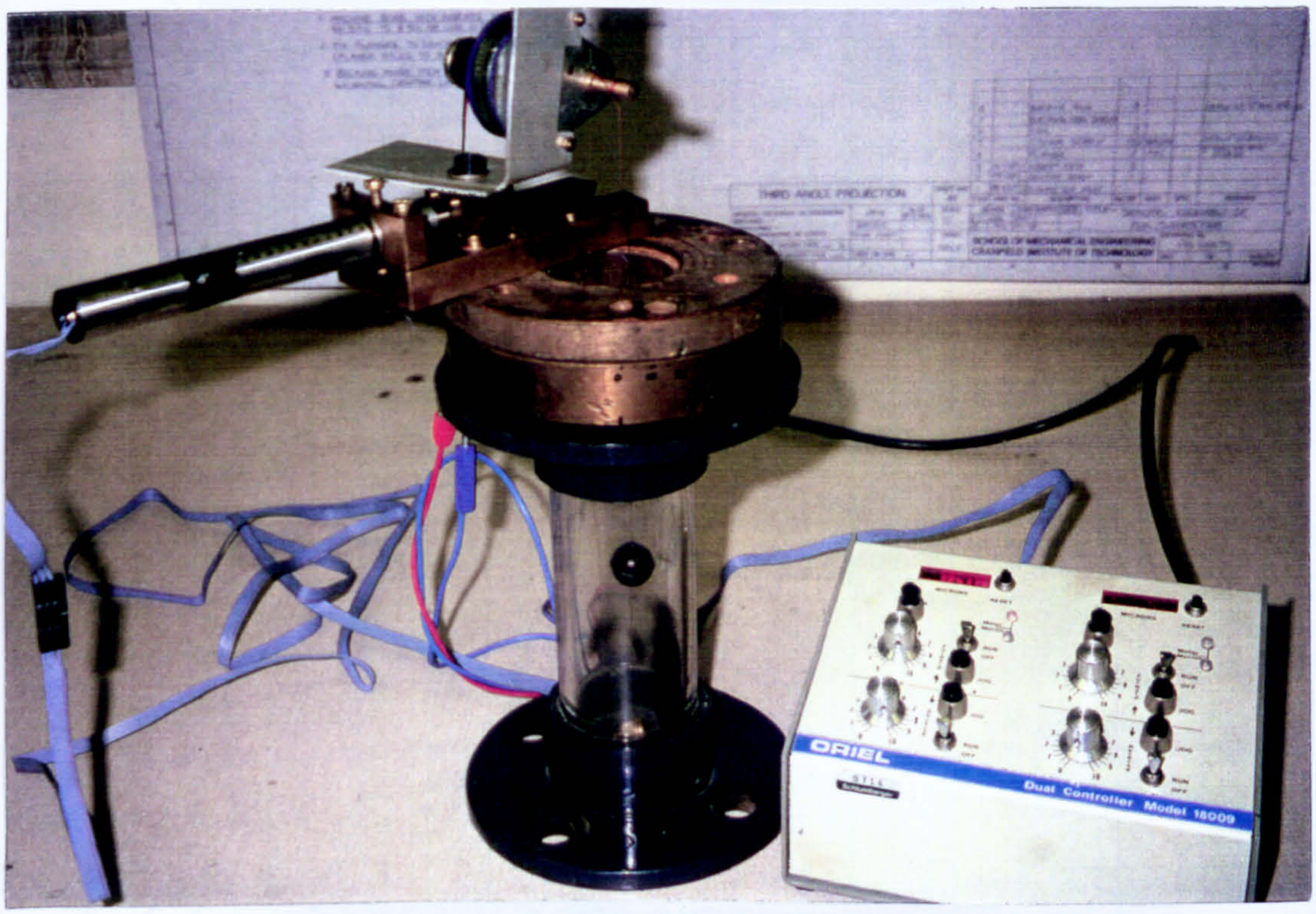

Fig.4.13

Fig.4.14 shows the high degree of sensitivity of the meter to the position of the ball. Here, the z-value in the diagram is equivalent to the magnitude of the signal.
In close proximity to the electrode, the ball generates a transformer signal 5 times as high as it does in the middle of the pipe. If the experiment is repeated with the ball moved on the saddle shaped surface (as in Fig.4.10) in order to record the maximum transformer signal, this ratio would be even higher. Due to this variable weighting it is obvious that the magnitude of the transformer signal cannot indicate the void fraction.
The above experimental result is compared with the computed transformer signal in **Fig.4.15**. Both graphs agree extremely well in symmetry and shape despite the fact that the theory strictly holds for small bubble sizes only.

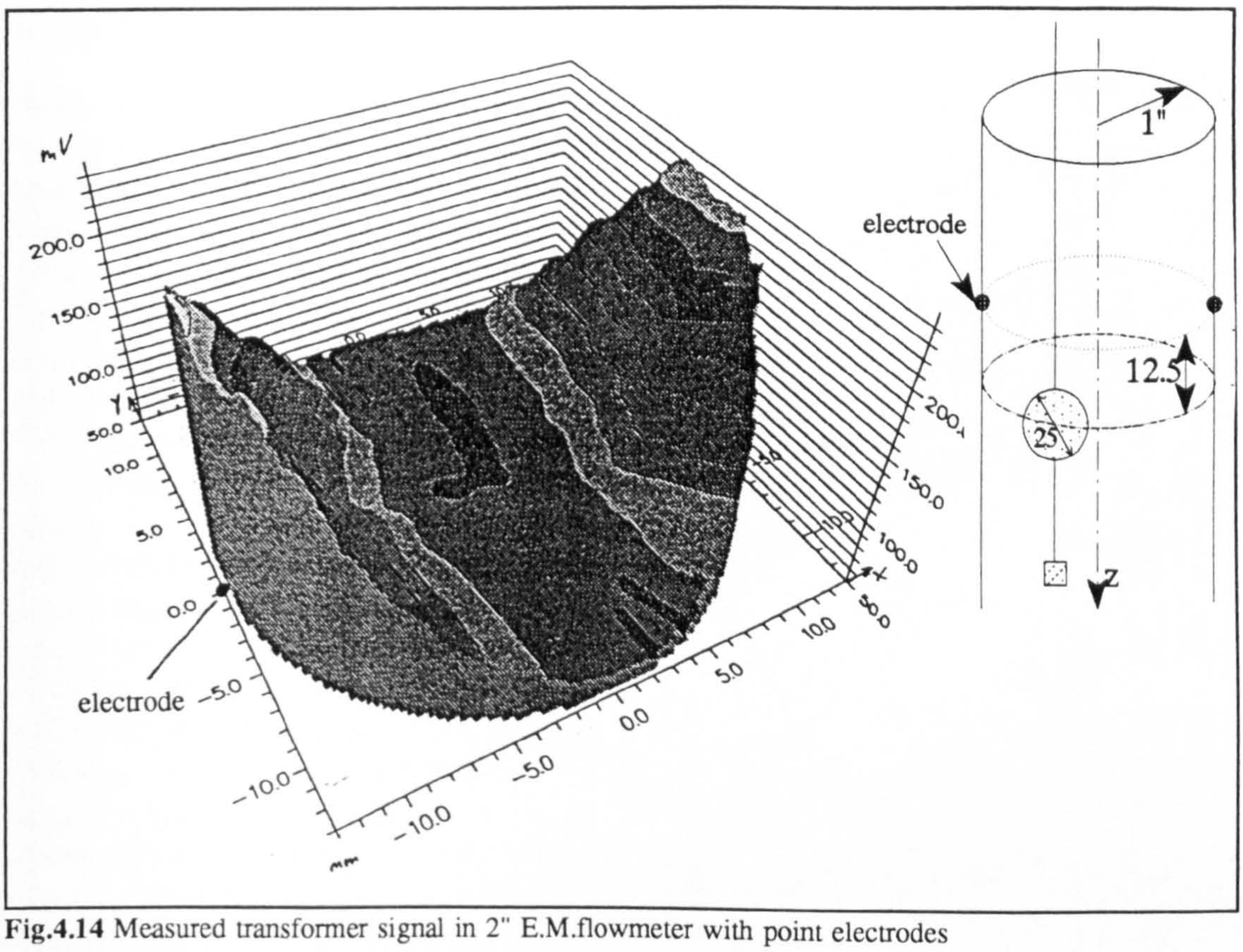

Fig.4.14 Measured transformer signal in 2" E.M.flowmeter with point electrodes

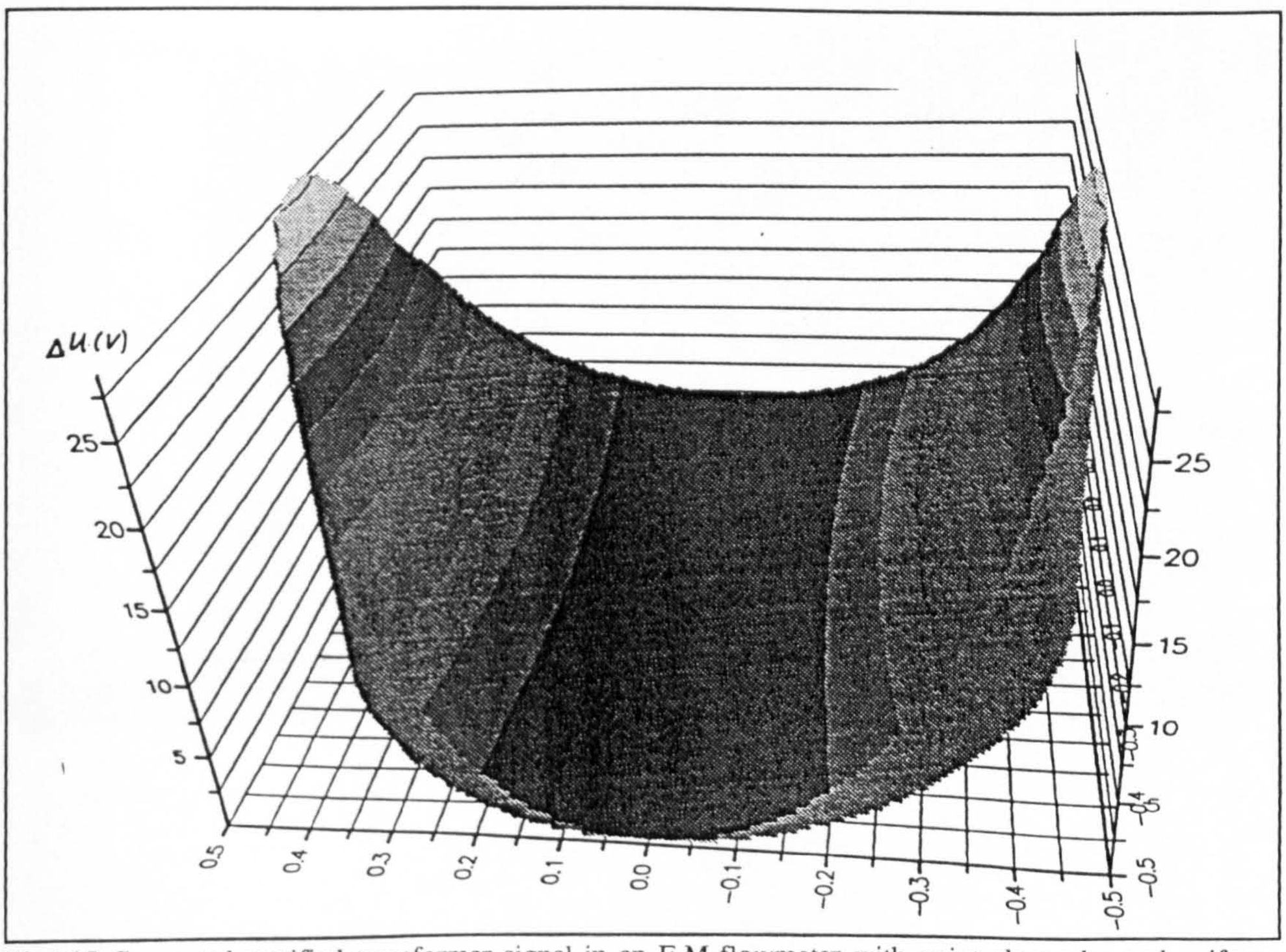

Fig4.15 Computed rectified transformer signal in an E.M-flowmeter with point electrodes and uniform, infinitely long magnetic field.
Pipe dia.=2; Ball dia.=1; z=1

Lines of maximum and minimum transformer signal

With the experimental result shown in **Fig.4.12** and the corresponding theoretical result in **Fig.4.5**, the variation of the amplitude of the transformer signal was determined as a function of z. If a row of single balls passes the electrodes at irregular intervals, there will be one characteristic frequency in the power spectrum which all passing balls have in common. If the balls travel faster, this frequency will rise, if they slow down, it will fall. This characteristic frequency is independent of the position of the ball in the pipe cross section as long as the distance between the maximum and minimum of the transformer signal is constant throughout the cross section of the pipe. The computational result shown in **Fig.4.9** has already indicated that for an E.M-flowmeter with point electrodes the maximum or minimum transformer effect does not occur at a single value of z. In the following experiment a single plastic ball of 8mm dia. is used to verify this prediction. The experiment is only carried out in the y-z-plane because here the variation is the largest. **Fig.4.16** shows the measured lines. these are curved towards the electrodes with the distance from maximum to minimum varying between 26mm and 8mm. In the theoretical result the maximum distance was 25.9mm and the minimum distance only ca.3mm. This discrepancy of the minimum distance is due to the fact that the point electrodes in the flowmeter are in fact 10mm large in diameter whereas the theory assumes point electrodes.
From this experiment it is finally clear that we will not find a single frequency in the power spectrum when a large number of balls randomly distributed over the cross section passes through the meter all at the same speed.

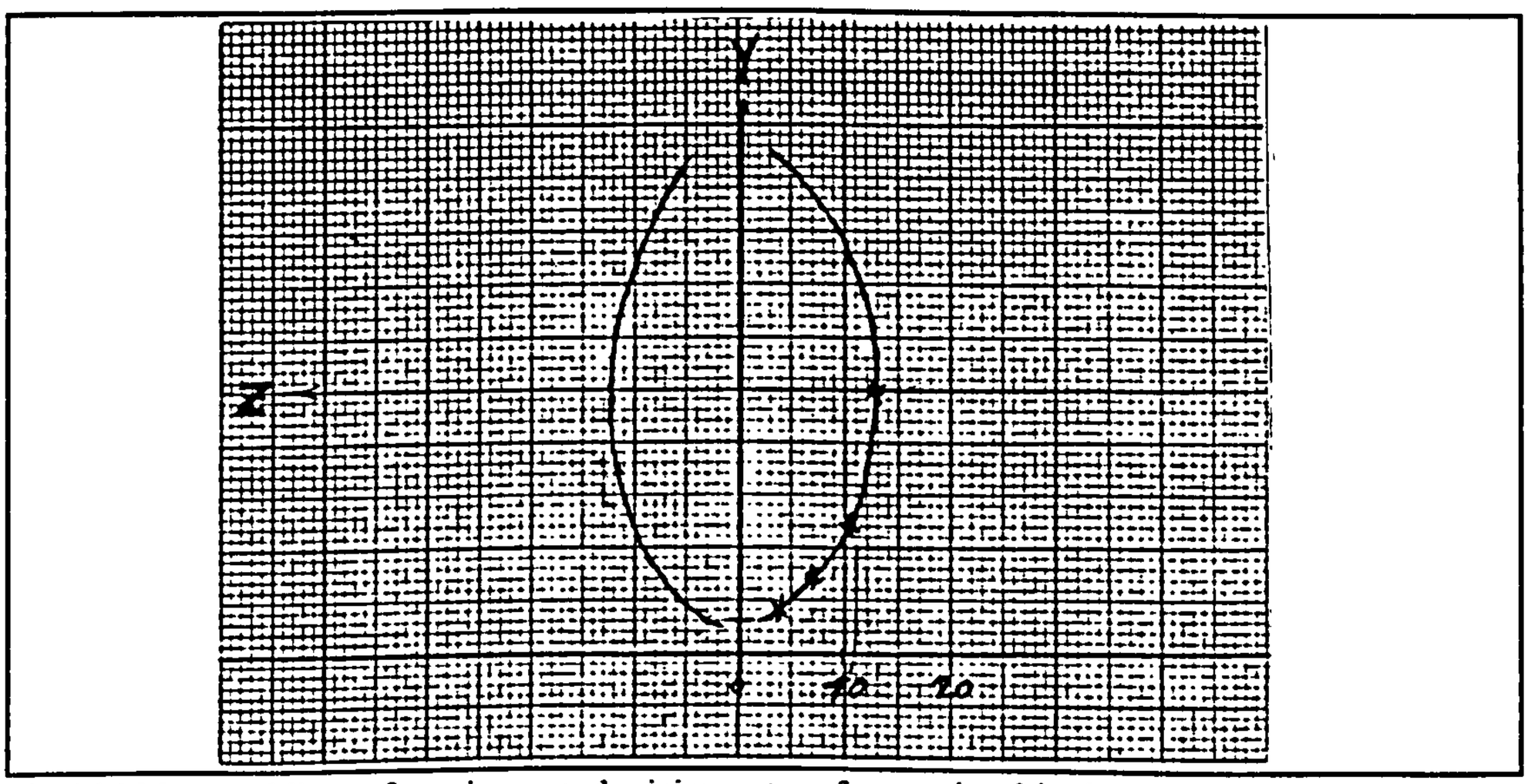

Fig.4.16 Measured lines of maximum and minimum transformer signal in the y-z-plane

4.3 Large electrodes

In addition to the point electrodes, larger electrodes are investigated. The two shapes considered are strip electrodes and area electrodes. Because both types of electrodes are meant to be noncontacting and only capacitively coupled to the fluid, they can be modelled as a number of independent point electrodes over which the total signal is averaged. This method has been described before in chapter3. In **Fig.4.17,** the transformer signal of a single ball is compared for all three types of electrodes.

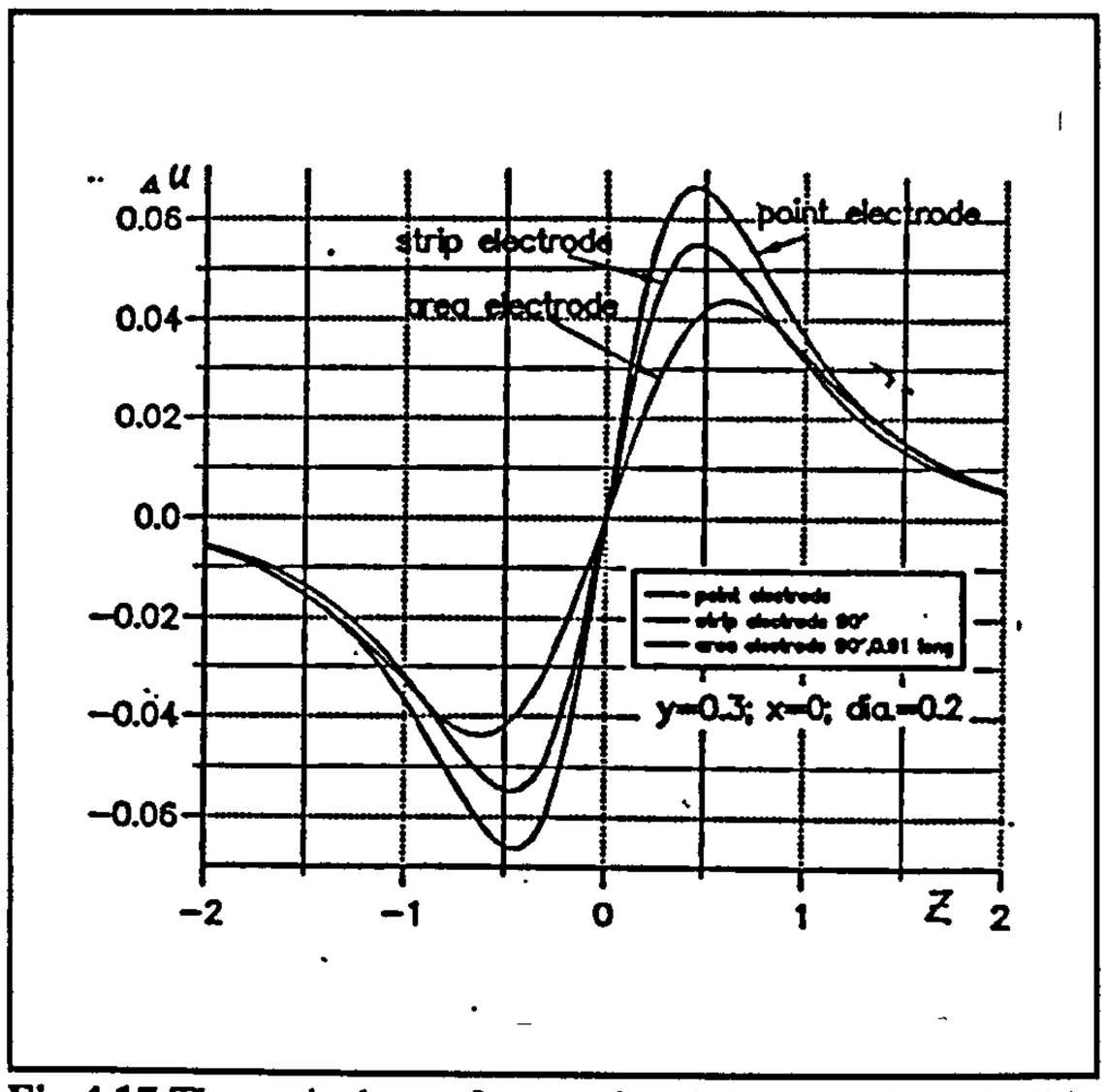

Fig.4.17 Theoretical transformer signal due to a single ball in E.M.flowmeter with area, strip and point electrodes

The variation in the transformer signal amplitude due to this ball is similar for point- and large electrodes. However, the distance between the maxima is larger for area electrodes than it is for point electrodes. All three signals decay equally fast but the absolute maximum of the transformer effect is highest for point electrodes and lowest for large area electrodes. A significant difference between the three electrode types becomes apparent in **Fig.4.18.** The magnitude of the transformer signal depends much less on the position of the ball.

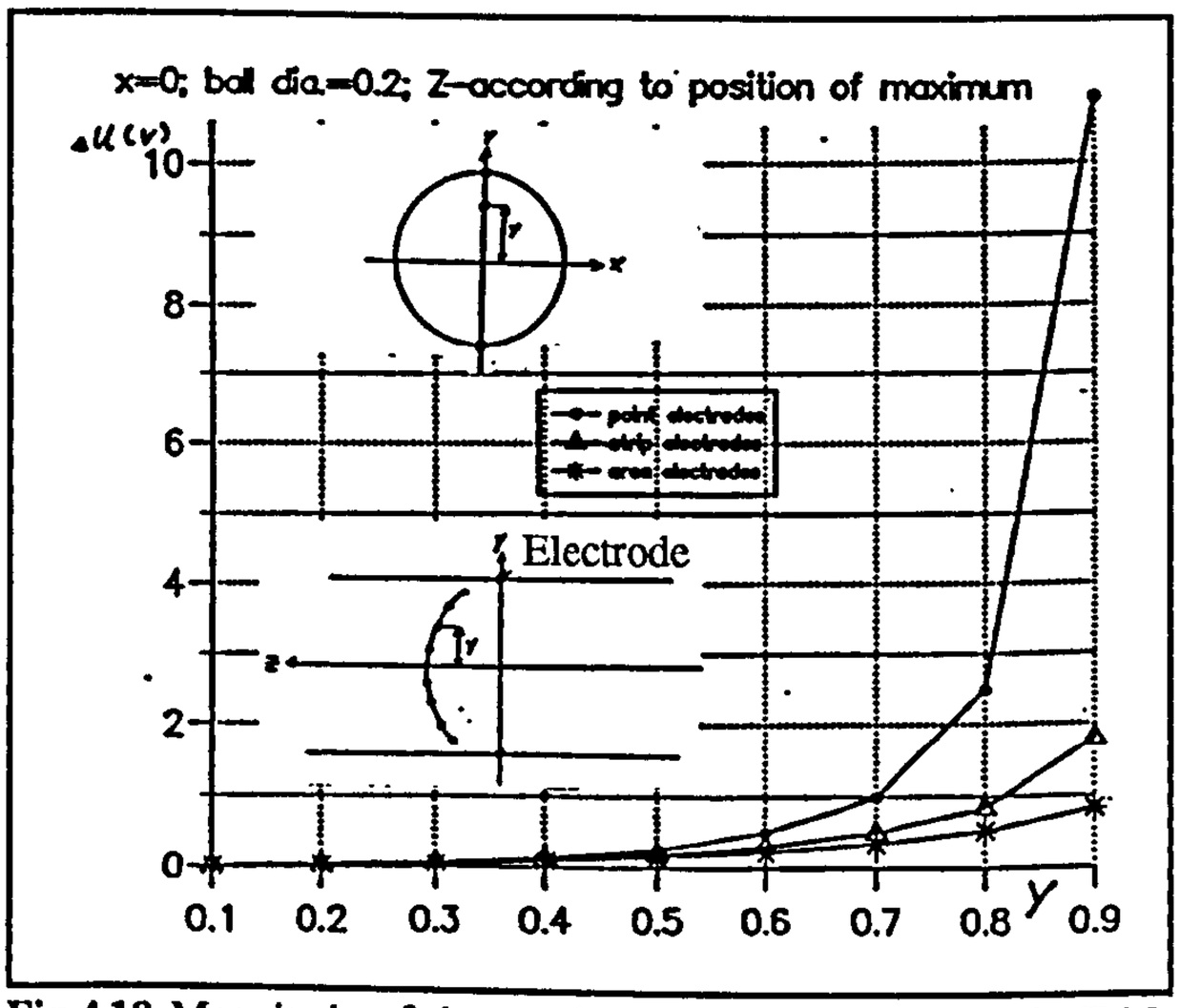

Fig.4.18 Magnitude of the maximum transformer signal in E.M-flowmeter with area, strip and point electrodes

For the computed examples, the magnitude of the signal with area electrodes is only about half of that with strip electrodes and much less than that with point electrodes. The position at which the maxima are reached are different for all three electrodes. The disadvantage of the lower signal with large area electrodes can be overcome by increasing the frequency at which the coils are operated because the strength of the eddy currents is directly proportional to the frequency.

The main advantage of large electrodes compared to point electrodes is, that the distance between the maxima is less sensitive to the position of the bubble in the pipe cross section. **Fig.4.19** and **eqn.4.20** show the lines of

maximum and minimum transformer signal for strip electrodes and area electrodes respectively. With strip electrodes, the lines are almost as curved as with point electrodes but they do not change much with the circumferential position of the bubble. Area electrodes show a low sensitivity of maximum and minimum to the position of the ball. The lines are less curved than with point- and strip electrodes and they are nearly the same for all angles. Apart from the lower sensitivity to bubble position, area electrodes have another small advantage: The average distance between the maxima is

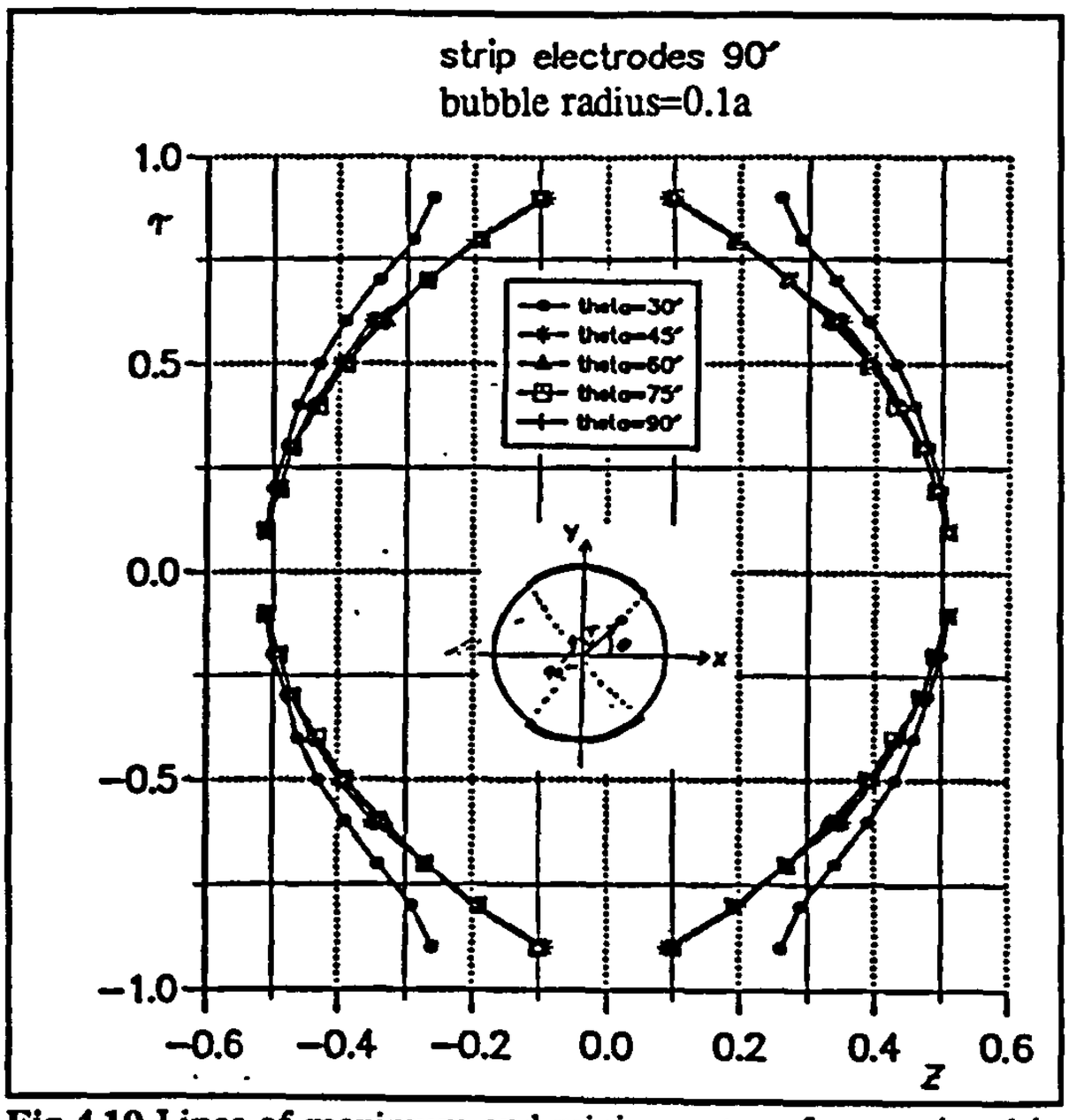

Fig.4.19 Lines of maximum and minimum transformer signal in E.M.-flowmeter with strip electrodes

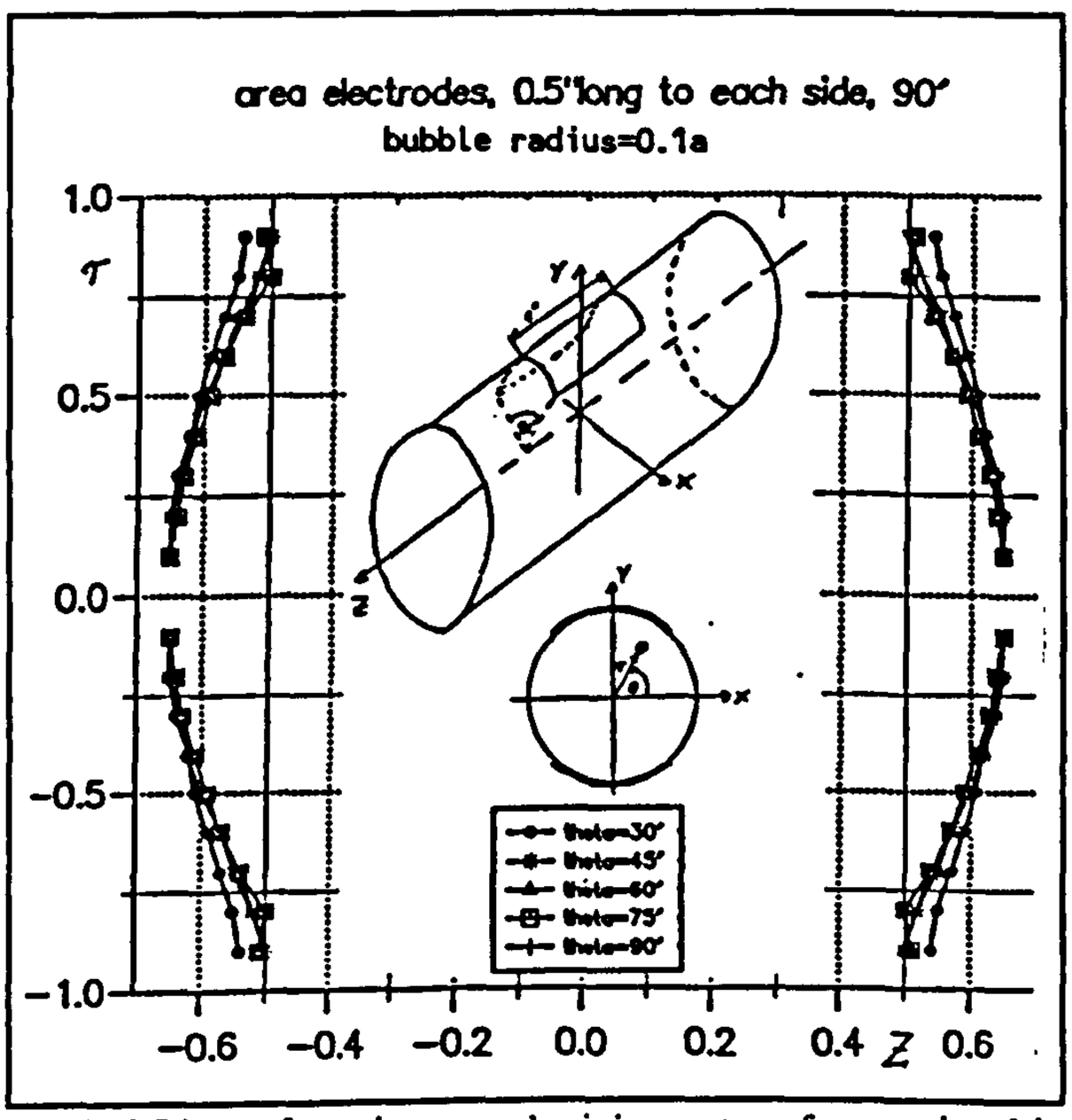

Fig.4.20 Lines of maximum and minimum transformer signal in E.M.-flowmeter with area electrodes of 1 pipe radius length

larger. This should help to overcome the aliasing effect because more samples can be taken during the pass of the bubble.

Fig.4.21 and **Fig.4.22** show the three dimensional shape of the surfaces of maximum transformer signal. For both types of electrodes the surfaces are roughly of spherical shape with different curvatures whereas point electrodes **(Fig.4.10)** give a strong saddle shape.

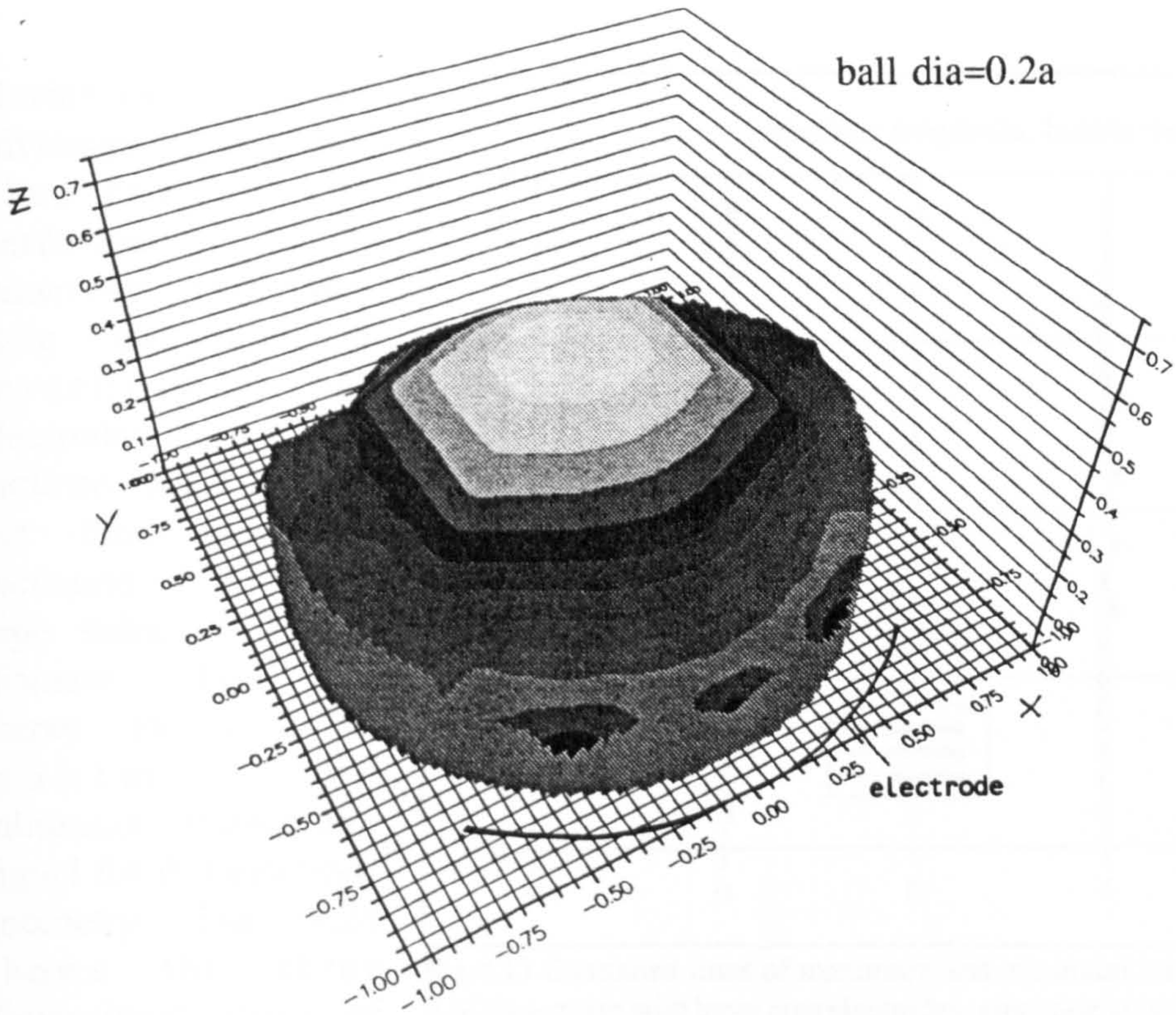

Fig.4.21 3-Dimensional path of maximum transformer signal in E.M.flowmeter with strip electrodes

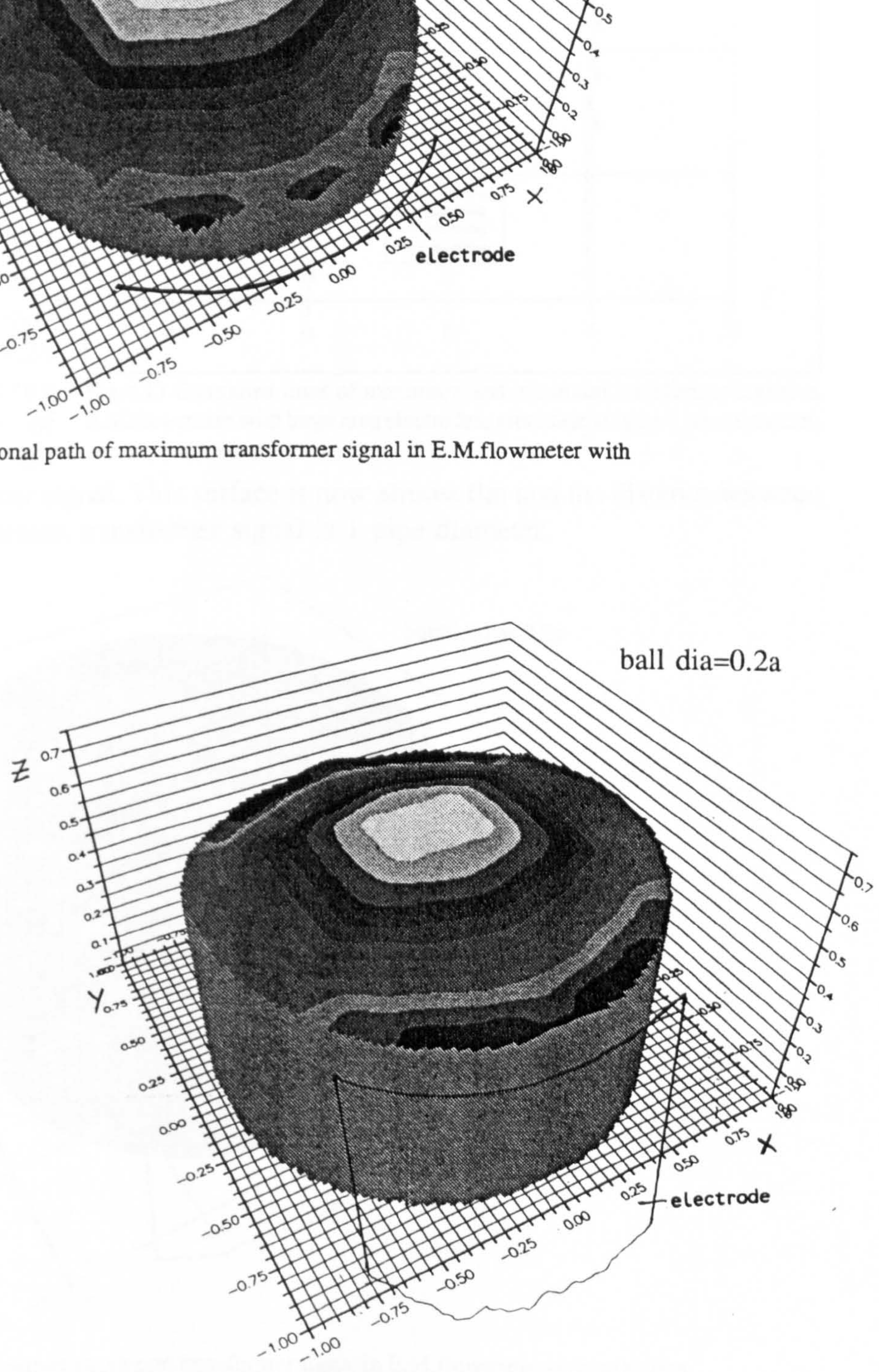

Fig.4.22 3-Dimensional path of maximum transformer signal in E.M-flowmeter with area electrodes; electrode length=1 pipe radius

Having established the advantages of large area electrodes, the performance of a flowmeter with very long electrodes is investigated. The electrodes have still an inclined angle of 90° but their length is increased from to 1 pipe radius to 1 pipe diameter. **Fig. 4.23** shows the lines of maximum and minimum transformer signal for this electrode geometry. Fig. 4.24 shows the three dimensional shape of the surface of maximum transformer signal. This surface is now almost flat and the distance between maximum and minimum transformer signal is 1 pipe diameter.

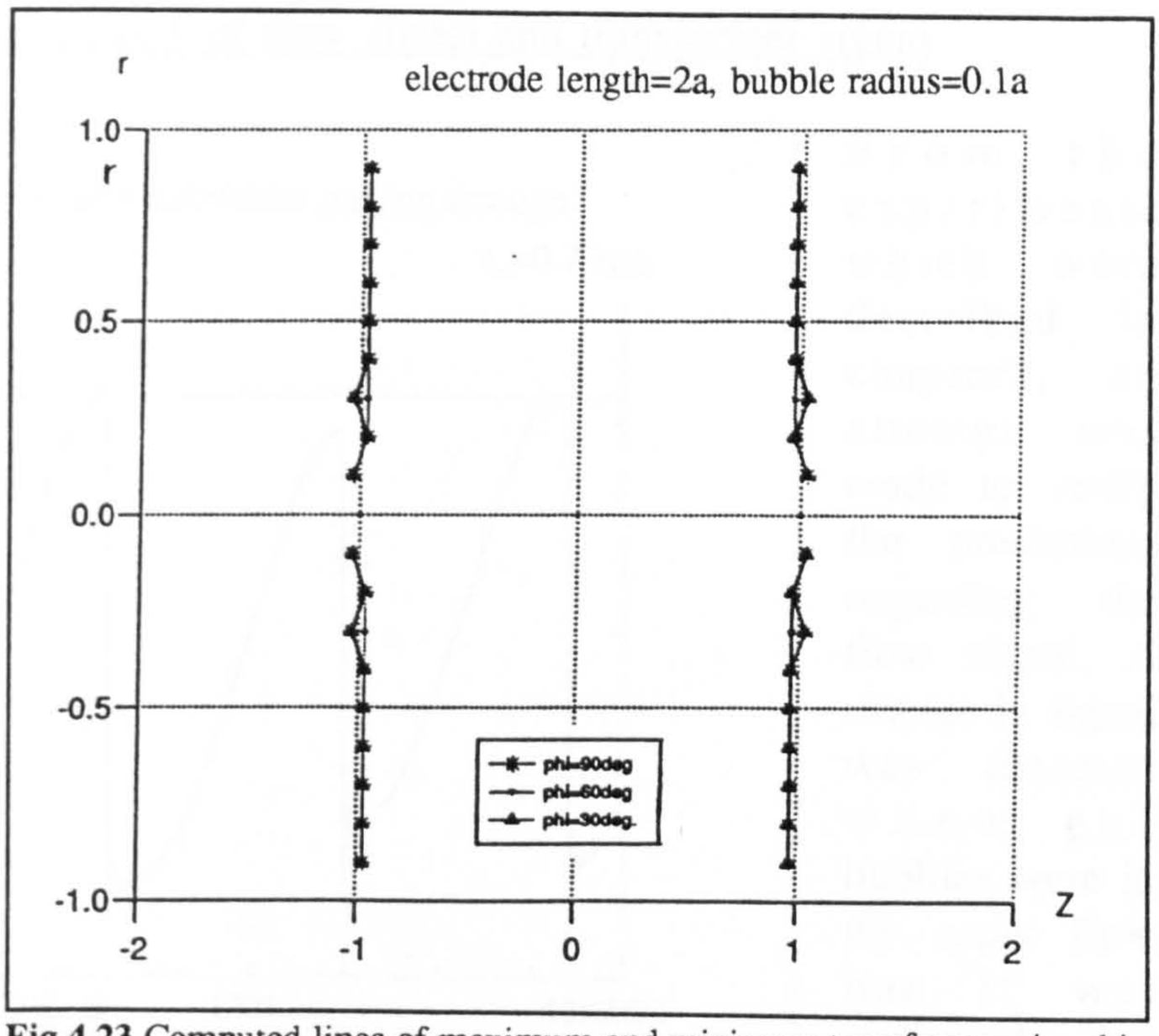

Fig.4.23 Computed lines of maximum and minimum transformer signal in E.M.flowmeter with large area electrodes; electrode length=1 pipe diameter.

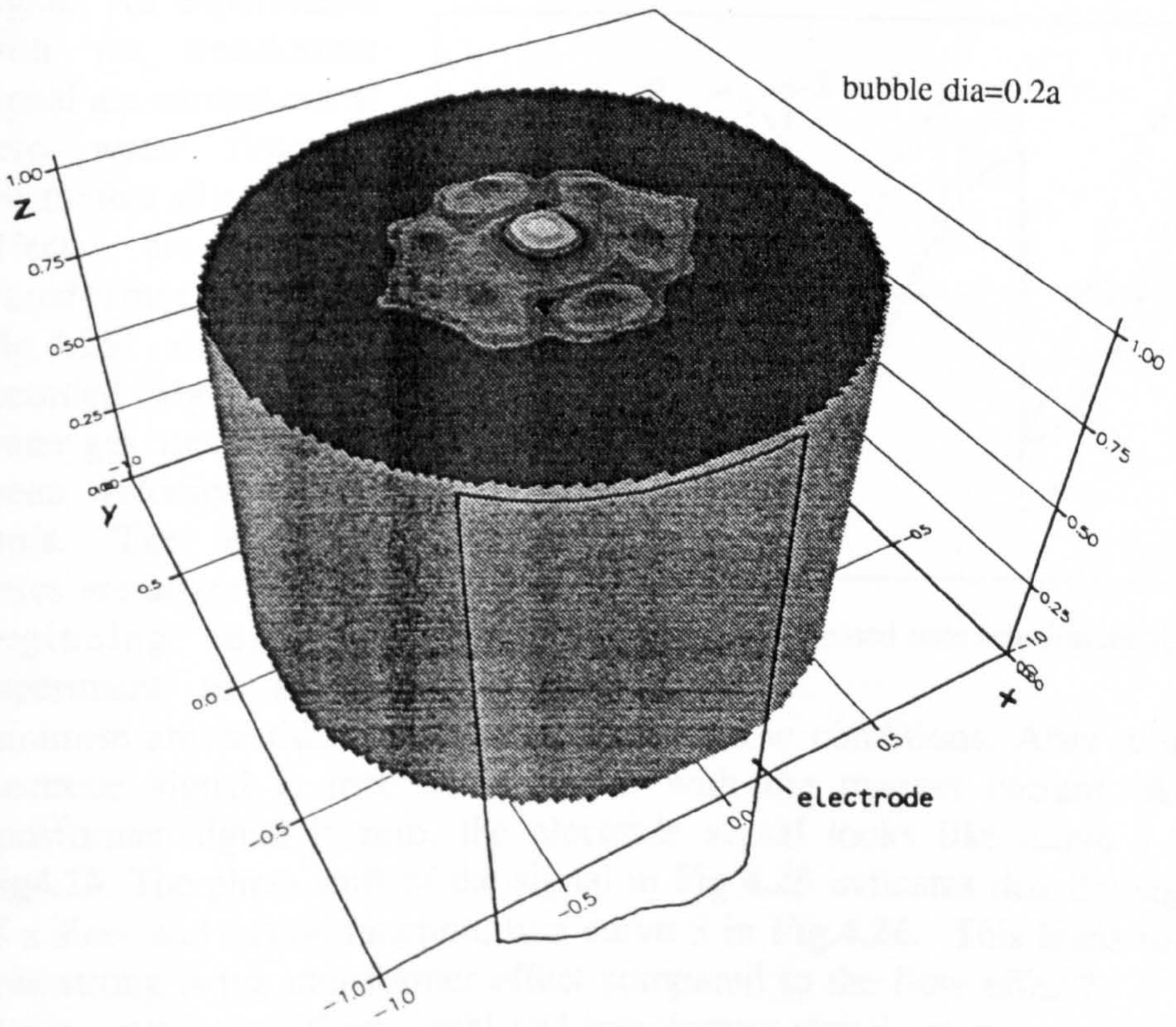

Fig.4.24 3-Dimensional path of maximum transformer signal in E.M.flowmeter with large area electrodes; electrode length=1 pipe diameter.

4.4 Comparison of the strength of flow signal and transformer signal

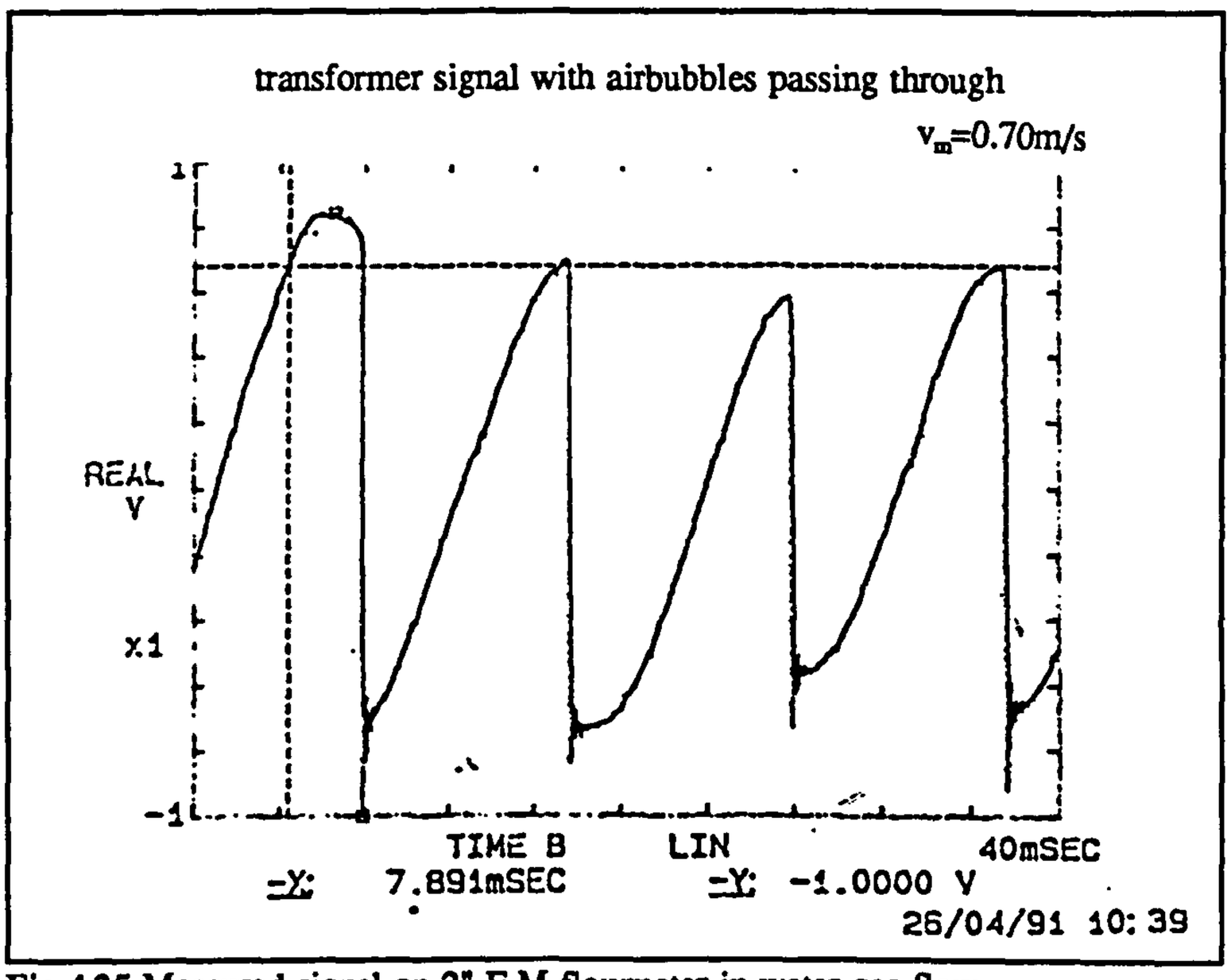

Fig.4.25 Measured signal on 2" E.M-flowmeter in water-gas flow

From the experiments which were described in chapter3, an attempt was made to verify the predictions regarding the flow signal. A change in signal was detected when gas bubbles were in the water flow but it was suspected that the measured effect was not entirely a change in the flow signal. All experiments with the transformer signal are carried out at zero water flow to ensure that all measured effects are entirely transformer effects. **Fig.4.25** shows the recorded signal of a water-gas mixture at a mean velocity of ca. 1m/s. The electrode wires are aligned at the beginning of the experiment so as to minimise any transformer signal under no-flow conditions. After amplification, the electrode signal is rectified in phase with the magnet current. As long as the transformer signal is zero, the electrode signal looks like curve 1 or curve 2 in **Fig4.26**. The phase shift of the signal in **Fig.4.25** indicates that the signal is the sum of a sine- and cosine function, like curve 3 in **Fig.4.26**. This leads to the question - how strong is the transformer effect compared to the flow effect?
The magnitudes of flow signal and transformer signal are now compared.

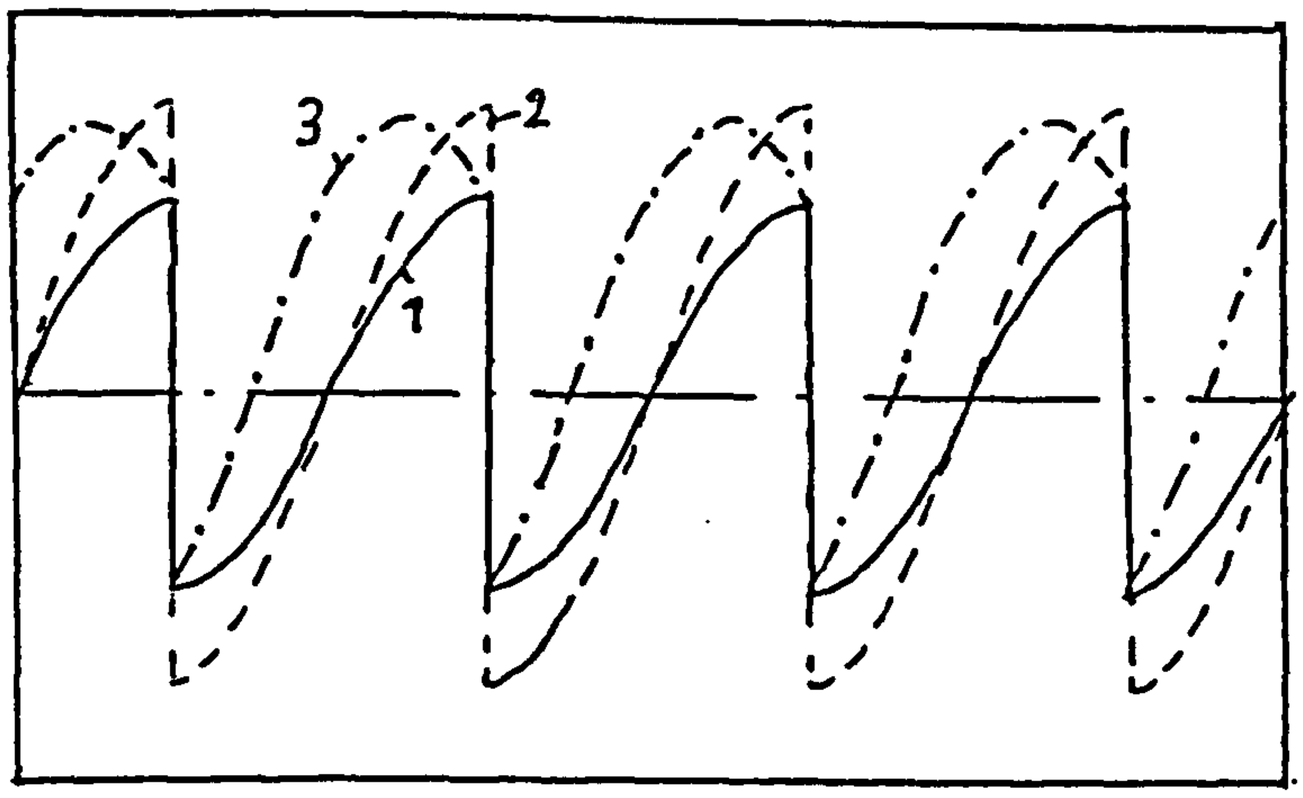

Fig.4.26 Flow signal superimposed onto transformer signal

In chapter 3 it was shown that the circulating current density for a parabolic flow profile is

$$\underline{j}=\frac{1}{2}\sigma B v_m\left[\left(\frac{r^2}{a^2}-1\right)\sin\theta\,\underline{a}_r+\left(3\frac{r^2}{a^2}-1\right)\cos\theta\,\underline{a}_\theta\right]$$

The magnitude of j, written in cartesian coordinates is

$$|\underline{j}|=\frac{1}{2}\sigma B v_m\sqrt{\left(-2\frac{xy}{a^2}\right)^2+\left[\frac{(3x^2+y^2)}{a^2}-1\right]^2}$$

The maximum magnitude of j is reached at x=a, y=0. Here,

$$|j_{max}|=\sigma\cdot B\cdot v_m \qquad (4.19)$$

From **eqn.4.1**, we see that for the eddy currents,

$$j=-\sigma i\omega By$$

For comparison of the strength of the currents, -i can be dropped because it only indicates the phase shift of the current to the magnetic field. Hence we obtain for the transformer effect the following maximum current j_{max} at y=a.

$$|j_{max}|=\sigma\omega Ba \qquad (4.20)$$

Comparing the current of **eqn.4.20** with **eqn.4.19** yields

$$\frac{|j_{max_{transf.}}|}{|j_{max_{flow}}|}=\frac{\omega a}{v_m} \qquad (4.21)$$

Taking some typical values, the ratio can be determined:

- pipe diameter = 2"
- mean flow velocity= 0.05 m/s (maximum possible velocity for laminar flow of water)
- frequency of coil = 50 Hz => $\omega=314$

$$\therefore \quad \frac{|j_{max_{transf.}}|}{|j_{max_{flow}}|}=\frac{314\cdot 0.0254}{0.05}=160$$

In this example, the transformer effect is therefore about two orders of magnitude larger than the flow induced effect, considering the current strength only. However, this calculation does not take into account that the maximum currents occur at different positions in the pipe. The maximum current due to the transformer effect occurs at the pipe wall near the electrodes; the flow induced current is a maximum at the pipe wall but in the x-z plane, at the largest possible distance from the electrodes. A dipoles' potential decays with the third power of the radius from its centre, it is therefore expected that the transformer effect is even stronger. Referring to equation **4.21**, one could suggest that the dominance of the transformer effect will be reduced with increasing velocity. Bearing in mind that **eqn.4.19** was derived for a parabolic flow profile, this is only true if the pipe diameter is reduced as well, in order to keep the Reynolds number low and the flow laminar. Otherwise, an increasing mean velocity will only flatten the velocity profile and reduce the flow induced currents even more.

Chapter 5

Theoretical power spectrum of transformer signal

In chapter 3.4, it was shown that the presence of a second, nonconducting phase in a continuous water flow changes the potential at the electrodes. The power spectrum of the signal alters its shape with varying flow velocity so that the peak of the spectrum moves almost linearly with the flowrate. In the last section of chapter 4 it was shown that this phenomenon is almost entirely caused by a transformer effect; the effect of the flow signal being 2 orders of magnitude lower. In this chapter, a theoretical model is build which is capable of predicting the power spectrum for randomly spaced balls at any transformer signal sampling rate. In a first stage however, the sampling rate is made infinitely fast.

5.1 Idealization of transformer signal for equally spaced balls

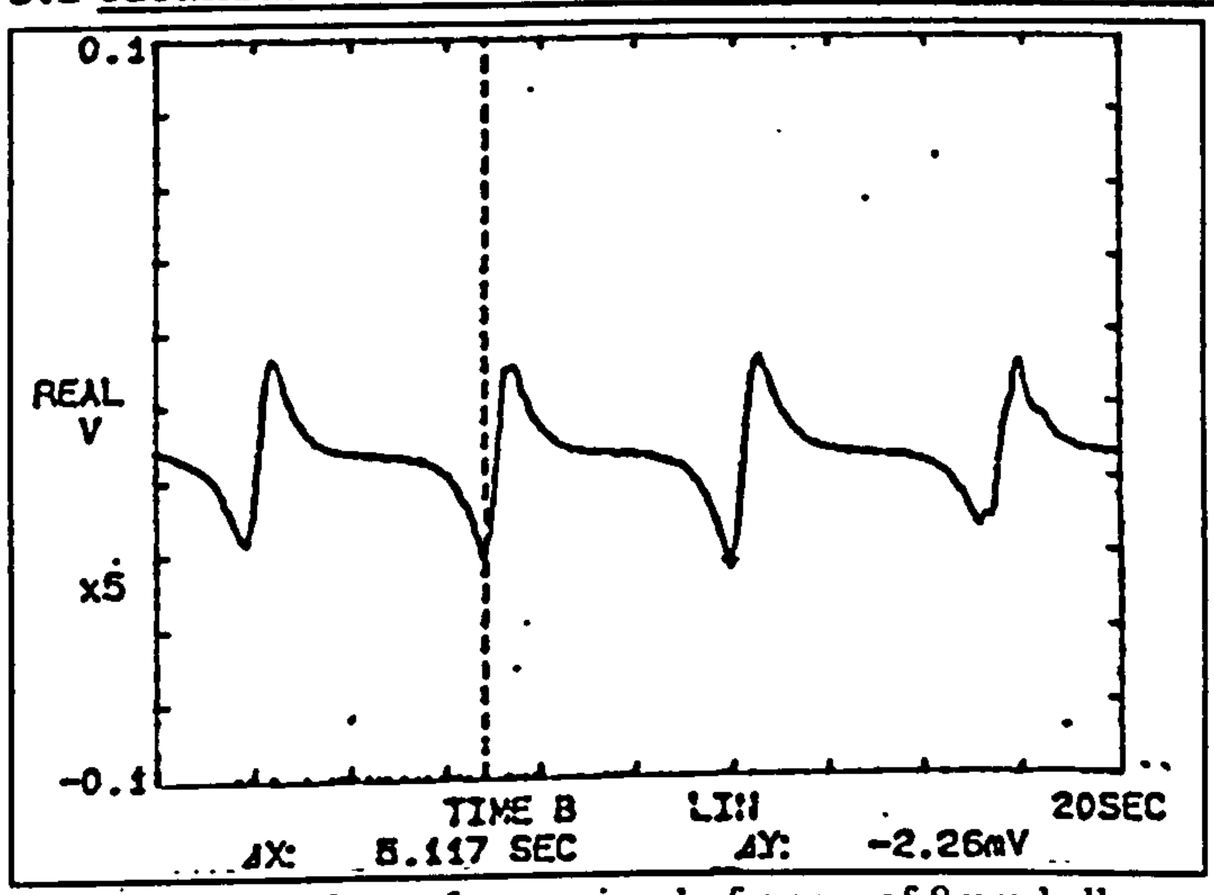

Fig.5.1 Measured transformer signal of a row of 8mm balls.

In order to compute the power spectrum of the transformer signal, it is necessary to describe the transformer signal as an infinitely long series. For simplicity, a row of equally spaced balls is considered first. A further limitation is that the balls are separated by a distance which is large enough to avoid interference. The transformer signal which then has to be modelled is shown in **Fig.5.1**.

The transformer signal of a single ball could be represented by a single high order polynomial function, a series of polynomials or as a combination of exponential- and trigonometric functions. For the ball along the centre of the pipe such a function is

$$f(x) = -e^{c_1 x} atan(-c_2 x); \quad x<0$$

$$f(x) = e^{-c_1 x} atan(c_2 x); \quad x \geq 0$$

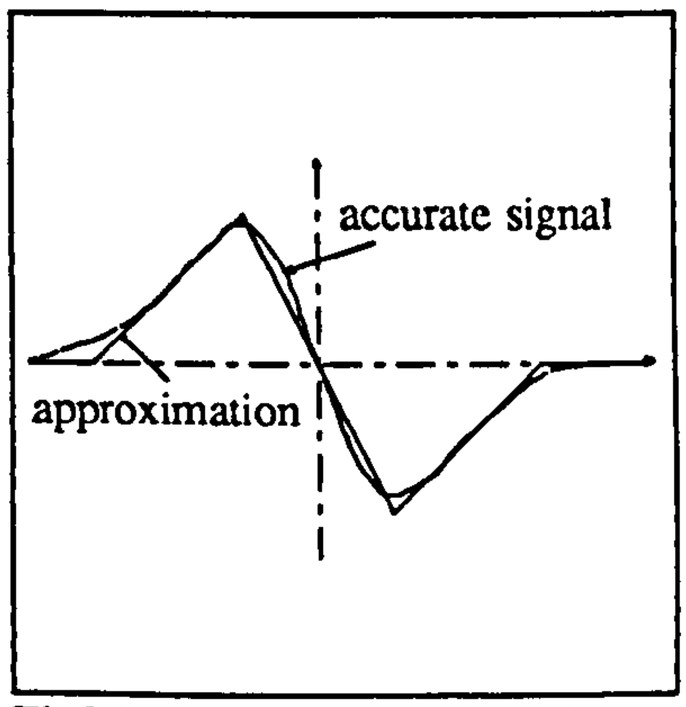

Fig5.2 Approximated transformer signal

where C_1 and C_2 are constants to match the shape of the transformer signal.
A series of these functions then has to be added in order to represent the repeated transformer signals of the balls. Because an infinite series of functions can conveniently be written in the form of a Fourier series, it was decided to approximate the function as a set of linear

functions as shown in **Fig.5.2.** Each single transformer signal is represented by a triangular wave. By altering the slopes of the linear functions, the idealized transformer signal can quickly be adjusted to the measured signals. Having expressed the string of transformer signals as a Fourier Series, the power spectrum can be computed. The method which is used to calculate the power spectrum is described in [3]: The function is shifted by the time delay τ and the autocorrelation function $R(\tau)$ is calculated using $R(\tau)=\frac{1}{T}\int f(t)f(t-\tau)\,dt$. **Fig.5.3** shows the autocorrelation function of a single triangular wave.

Performing a Fourier transformation of $R(\tau)$ yields the power spectrum G(f).

In the computation, only a limited number of cycles (i.e.number of balls) and a discrete Fourier Transform are used. Increasing the number of transformer signal cycles to more than 10 hardly alters the result, the spikes in the power spectra simply became narrower and higher. **Fig.5.4** and **Fig.5.5** show the computed power spectra for various speeds and spacings of the balls. The position of the maximum (ie of the highest peak) varies linearly with the speed of the balls. For higher velocities the height of the peaks decreases because the same amount of energy in the signal is spread over a wider frequency band. A variation of spacings between balls does not change the frequency of the maximum. However, a smaller spacing obviously allows more balls in the same time interval to pass through the meter and therefore increases the amount of energy and the magnitude of the spectrum.

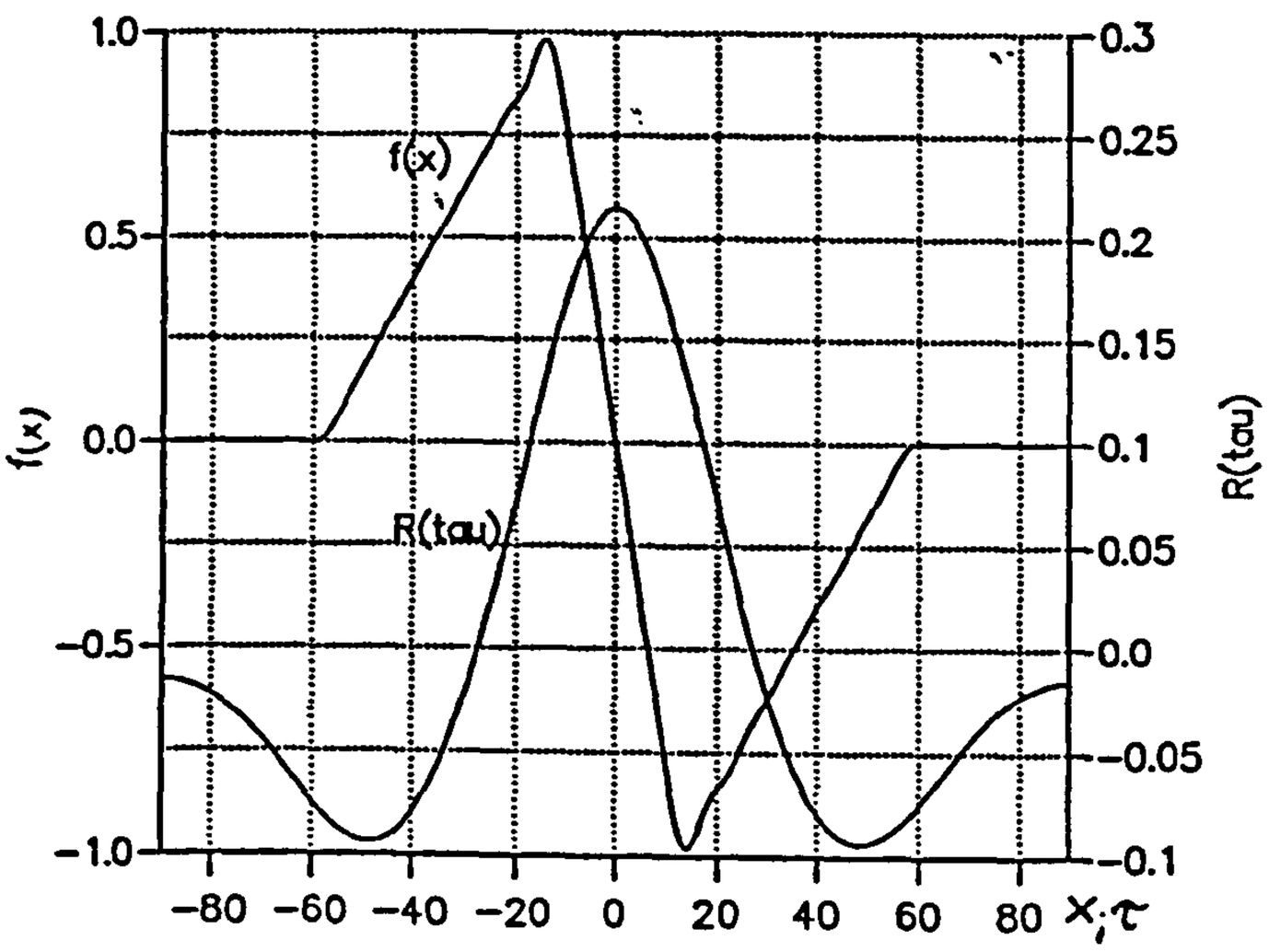

Fig.5.3 Autocorrelation function for a single idealized transformer signal.

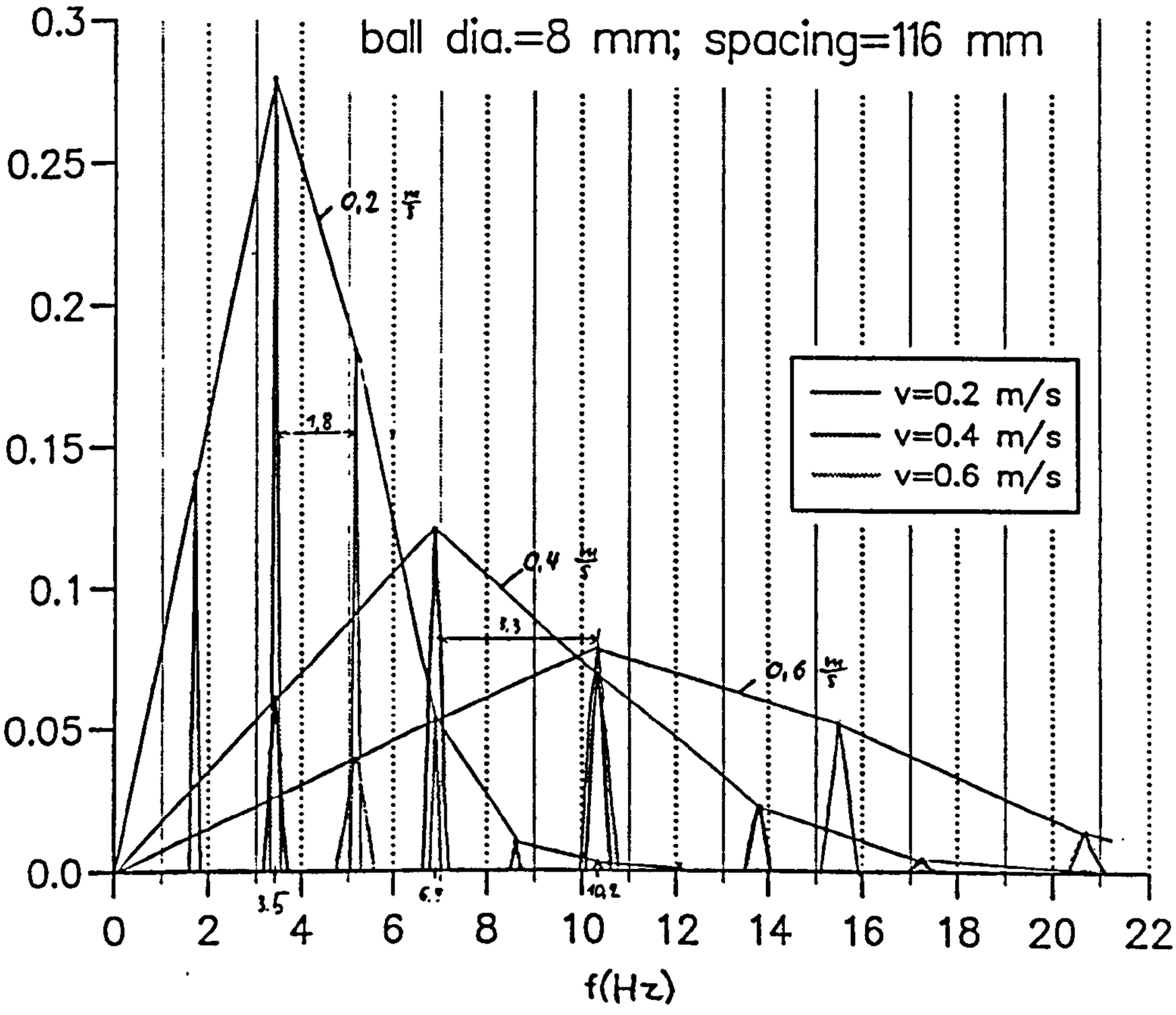

Fig.5.4 Computed power spectra of transformer signal for different ball speeds

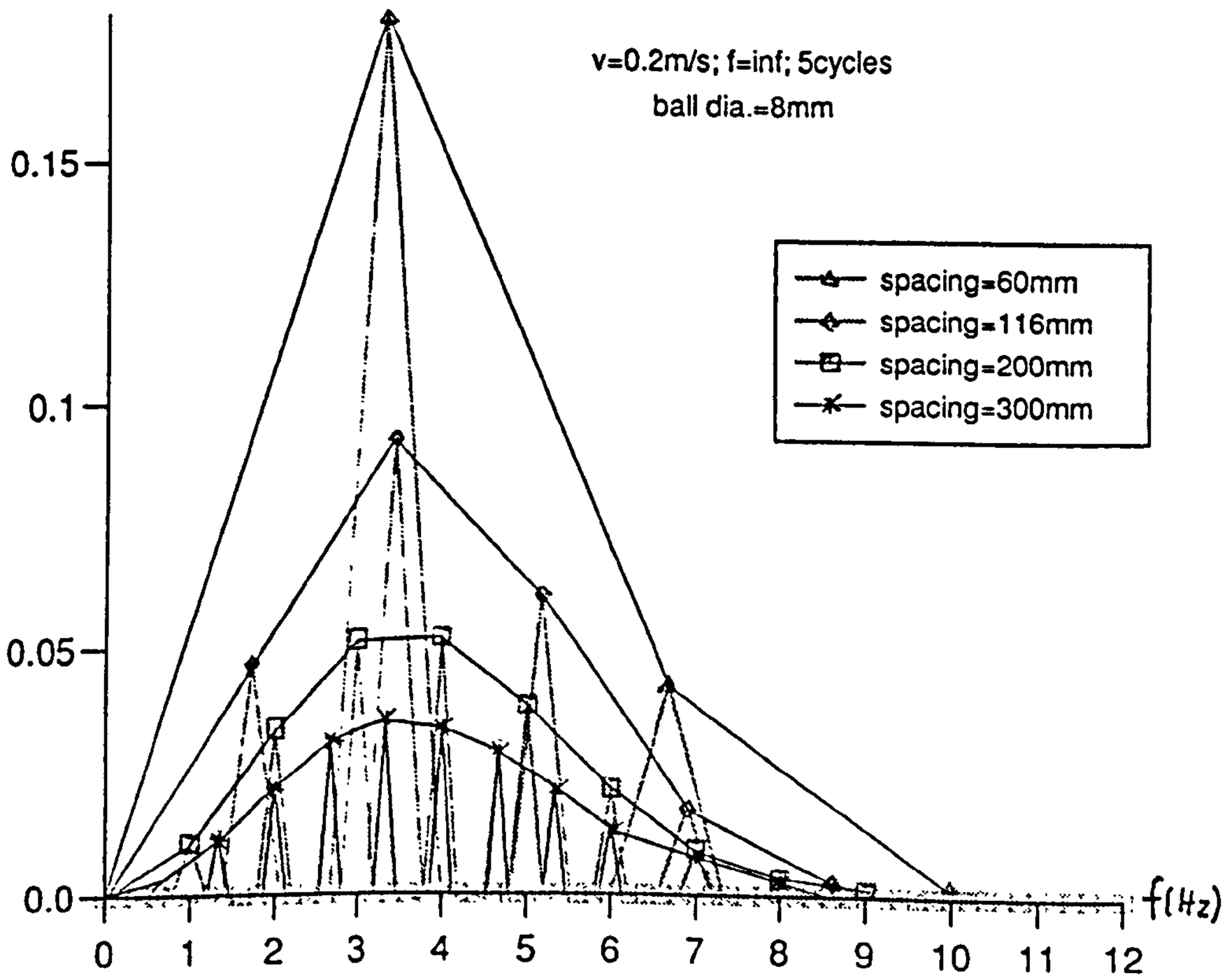

Fig.5.5 Computed power spectra of transformer signal for different ball spacings

5.2 Power spectrum for unevenly spaced balls

Having calculated the power spectrum for equally spaced balls the spacing is now allowed to vary, thus representing real bubble flow rather better. Now a series of transformer signals is combined to one signal (**Fig.5.6**). This is then written as a Fourier Series and processed as in 5.1. In principle it is possible to simulate a later experiment by combining into one signal as many transformer signals as there are balls are on a string . Practically, the large amount of computational time, needed to express the function as a Fourier series and integrate it, limits the possibilities to rows of about 10 signals with varying spaces between each.

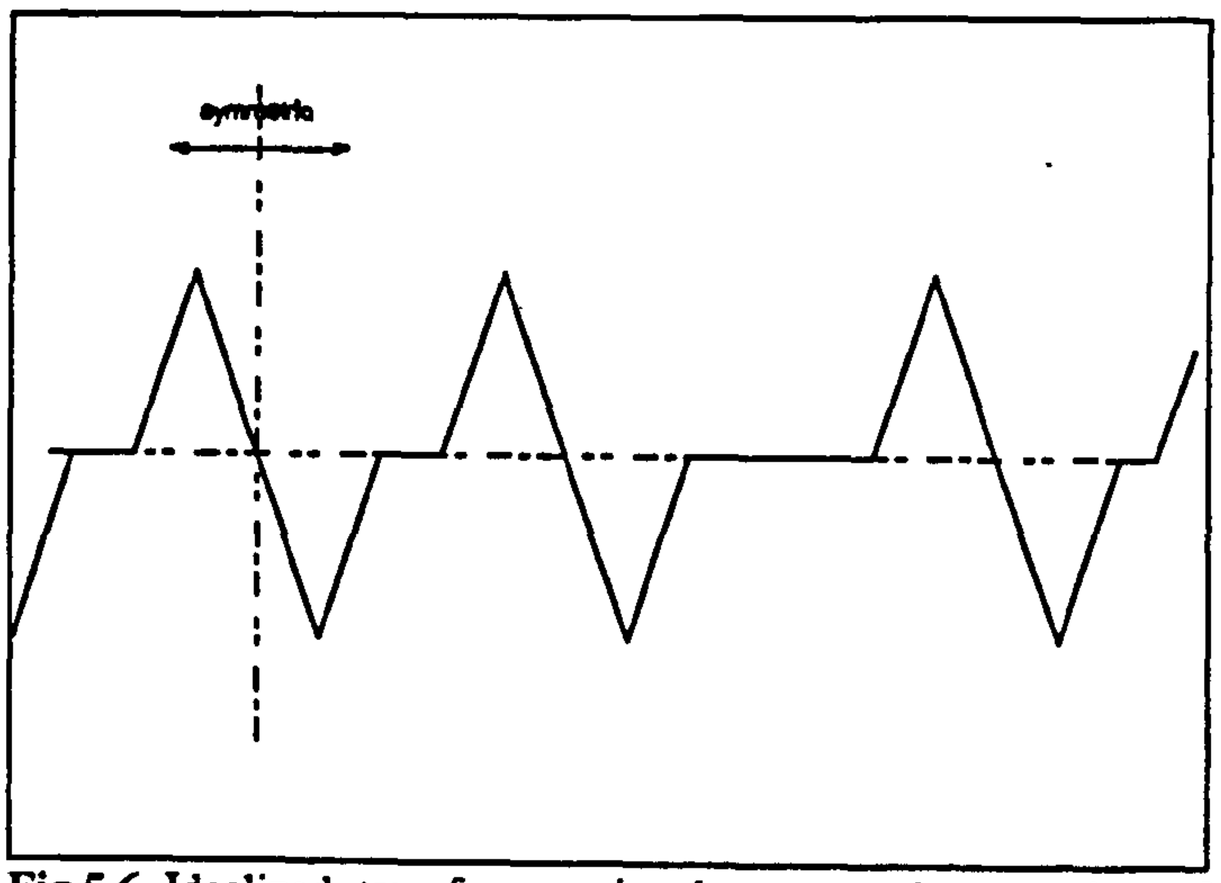

Fig.5.6 Idealized transformer signal, representing a string of randomly spaced balls

Fig.5.7 shows the computed power spectra for a string of balls moving at a velocity of 0.2m/s. The spacing varies between 65mm and 150mm and the signal repeats itself after 7 balls and 15 balls respectively. If one draws the envelope of the power spectra, the position of the maximum is again nearly at the same frequency as it was with the equally spaced balls in **Fig.5.5**.

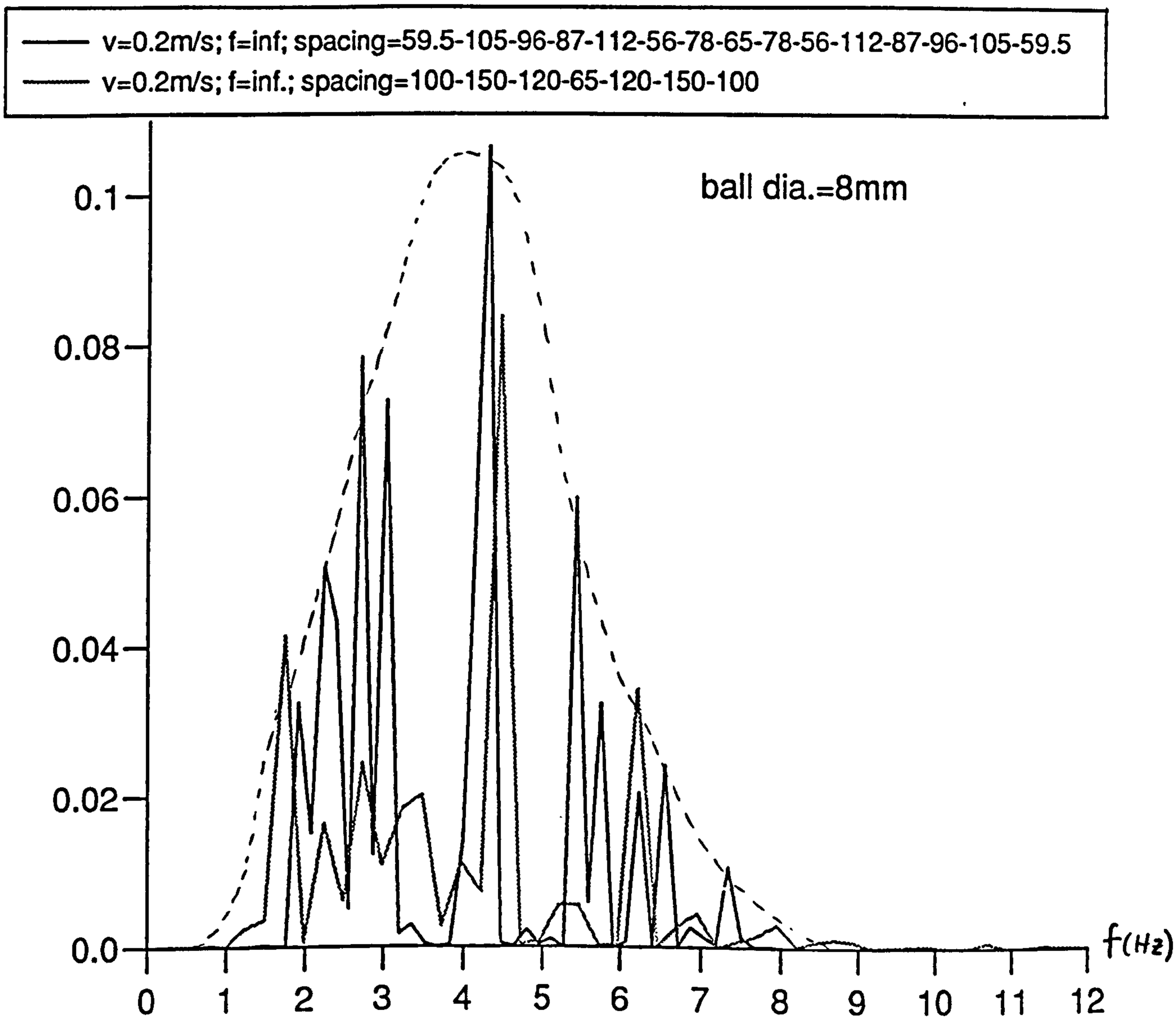

Fig.5.7 Computed power spectra for unevenly spaced balls

5.3 Power spectrum of equally spaced balls at low sampling rate

In the previous computations of the power spectrum, it is assumed that the transformer signal is always detected by the electrodes in its simplest form. This can only be the case if the rate of change of the magnetic field $\frac{\partial B}{\partial t}=const.$. In the commercial flowmeter used in the experiments however, the coils are mains driven and therefore $\frac{\partial B}{\partial t}=\omega B_0 \cos(\omega t)$,where B_0 is a constant. The eddy currents in the liquid vary sinusoidally. If the balls are moving fast enough through the flowmeter it is therefore possible that the eddy currents are very low at the moment one ball passes the electrodes. Consequently, only a small or zero transformer signal will be generated. An aliasing effect will occur and the signal will possibly be altered in a way that the information coming with it disappears. Such an altered signal may look like that shown in **Fig.5.8**. If the eddy currents which cause the transformer signal are constant, then the effect of a nonconducting sphere is given by the function $f_b(z)$ as seen in **Fig.4.5**. For a sphere at a velocity v the signal can be written as a function $f_b(t)$. Because the eddy currents are modulated by a function $f_e(t)=C\cos\omega t$, a superposition of $f_b(t)$ and $f_e(t)$ gives the final transformer signal for a single bubble. **Fig.5.9** to **Fig.5.11** show the idealized transformer signal multiplied by a rectified cosine function.

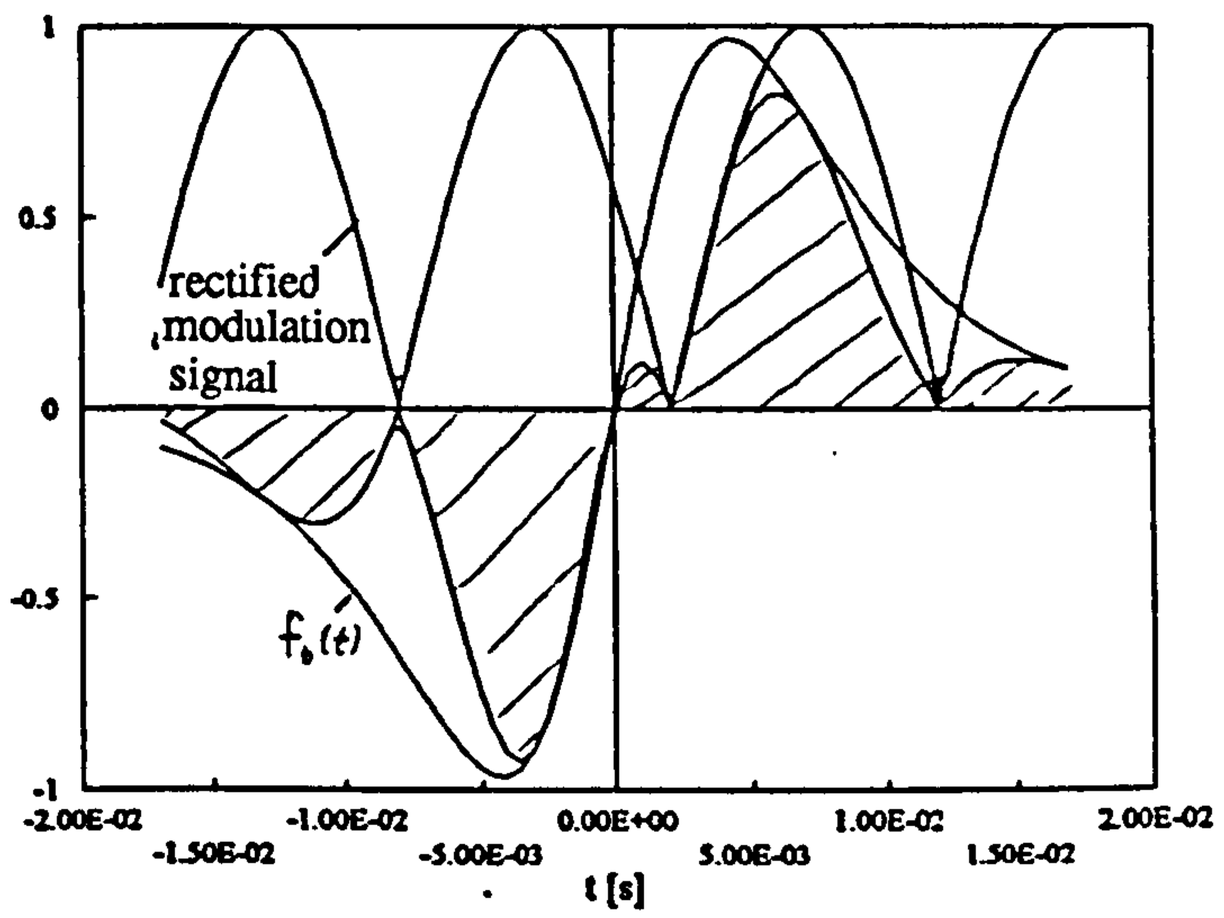

Fig.5.8 Modulated transformer signal

The larger the velocity of the balls or the lower the frequency of the B-field, the more distorted becomes the transformer signal. The effect of the non-constant eddy currents on the power spectrum is shown in **Fig.5.12**. In addition to the low frequency signal, the harmonics of the modulation signal are present at ±100Hz (for the 50Hz alternating magnetic field). However, although the basic transformer signal looks highly distorted at large velocities or low modulation frequencies, the power spectrum does not vary much. The reason is that an averaging takes place over a long time period. Even if the occasional transformer signal is completely skipped, the effect on the power spectrum is merely a decrease of its magnitude. In **Fig.5.13**, power spectra are compared with modulation frequencies of 10Hz to ∞. Apart from the extra harmonics, the main signal in unaltered in position and only varies in magnitude.

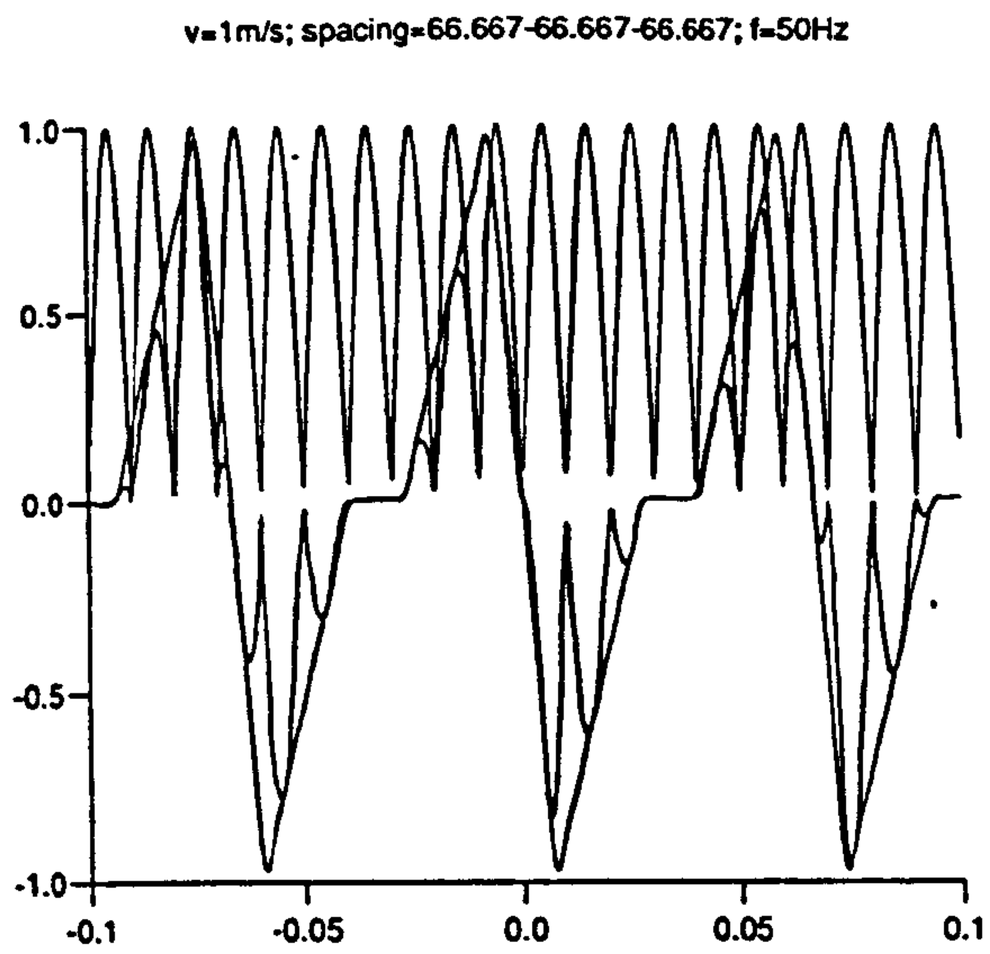

Fig. 5.9 modulated transformer signal

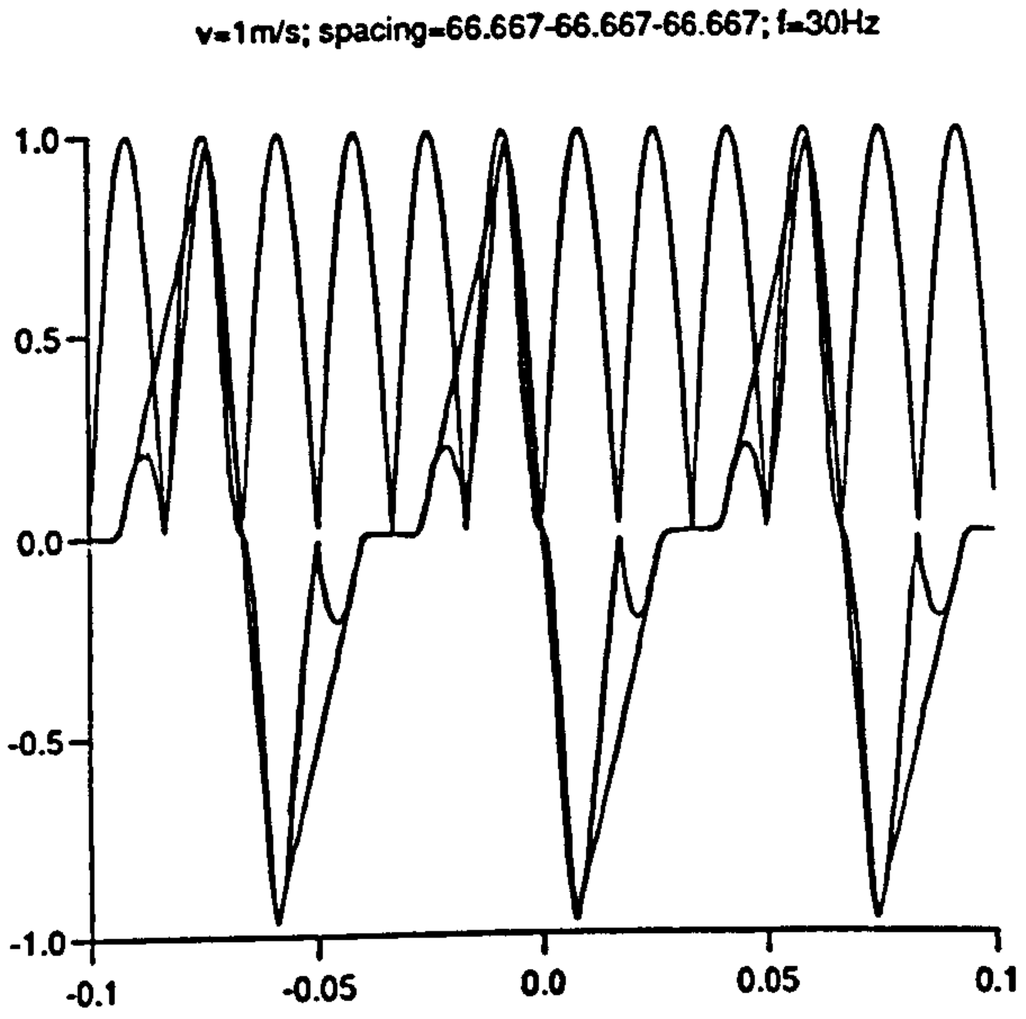

Fig. 5.10 modulated transformer signal

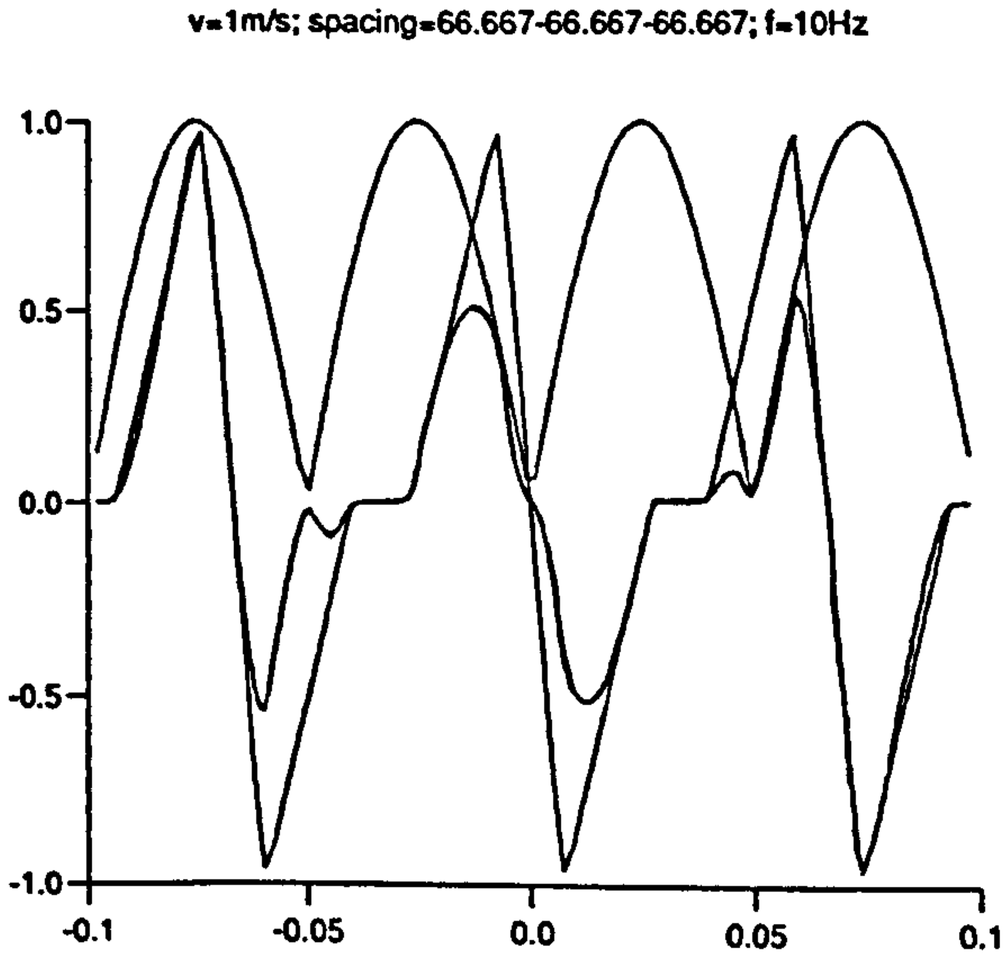

Fig. 5.11 modulated transformer signal

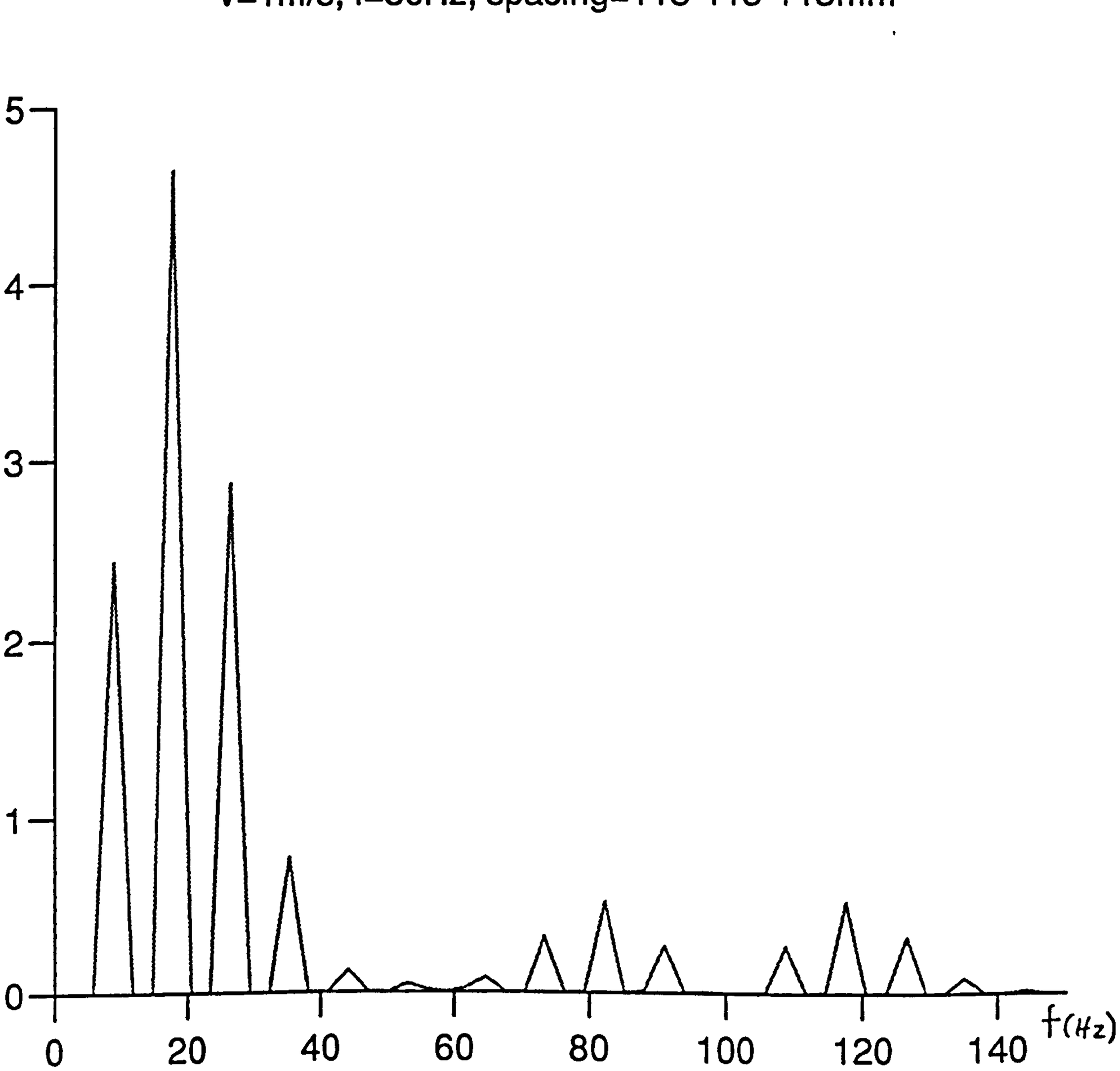

Fig.5.12 Computed power spectrum of 50Hz modulated transformer signal

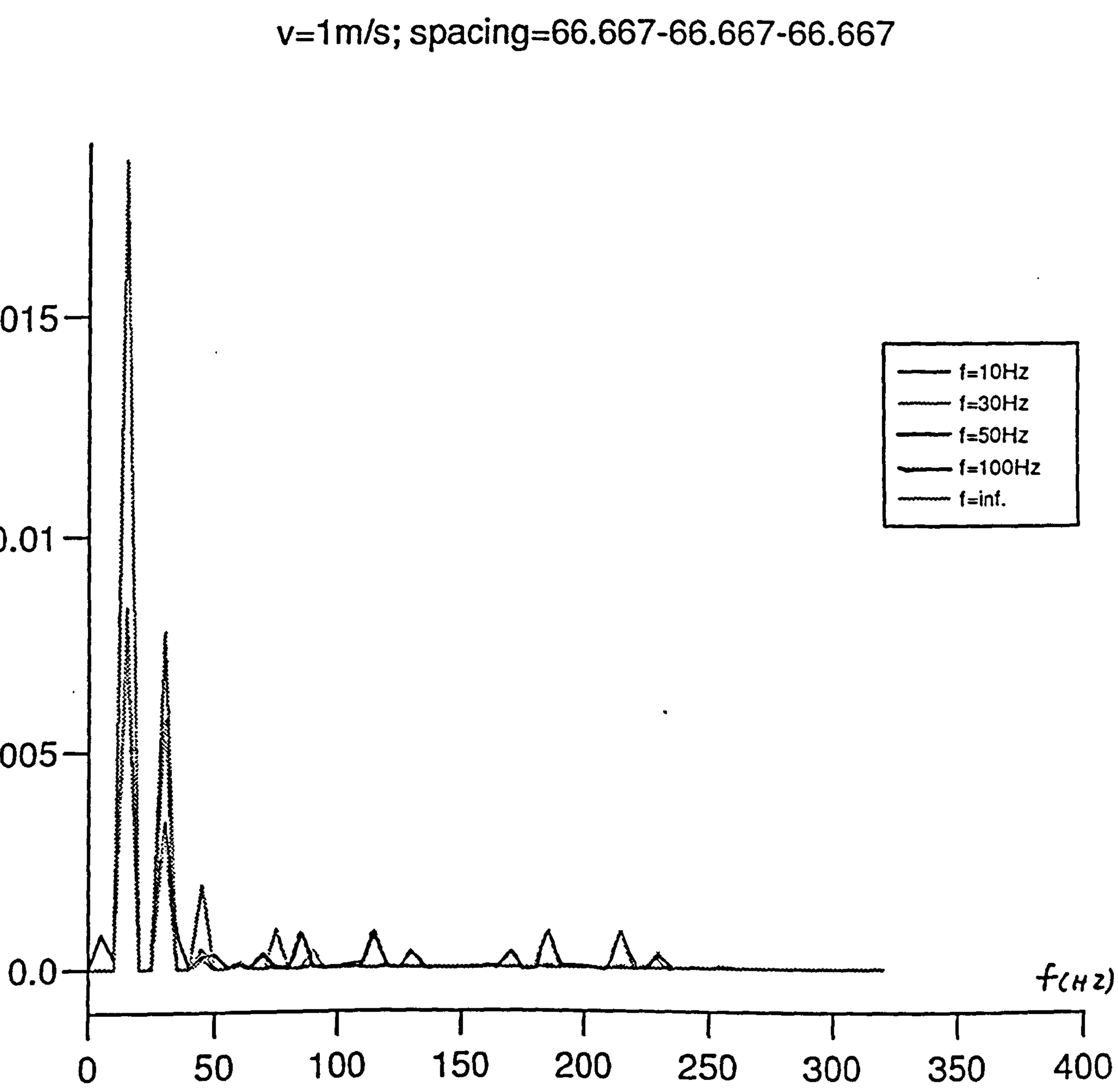

Fig.5.13 Power spectra for equally spaced balls and modulated transformer signal

5.4 Power spectrum of randomly spaced balls at low sampling rate

As in **5.2**, the power spectrum is here computed for randomly spaced balls with a modulated transformer signal as in **5.3**. **Fig.5.14** and **Fig.5.15** show the power spectra for two velocities. Despite the addition of some low level noise, the peaks of the power spectra are still at the same position as in the simpler models.

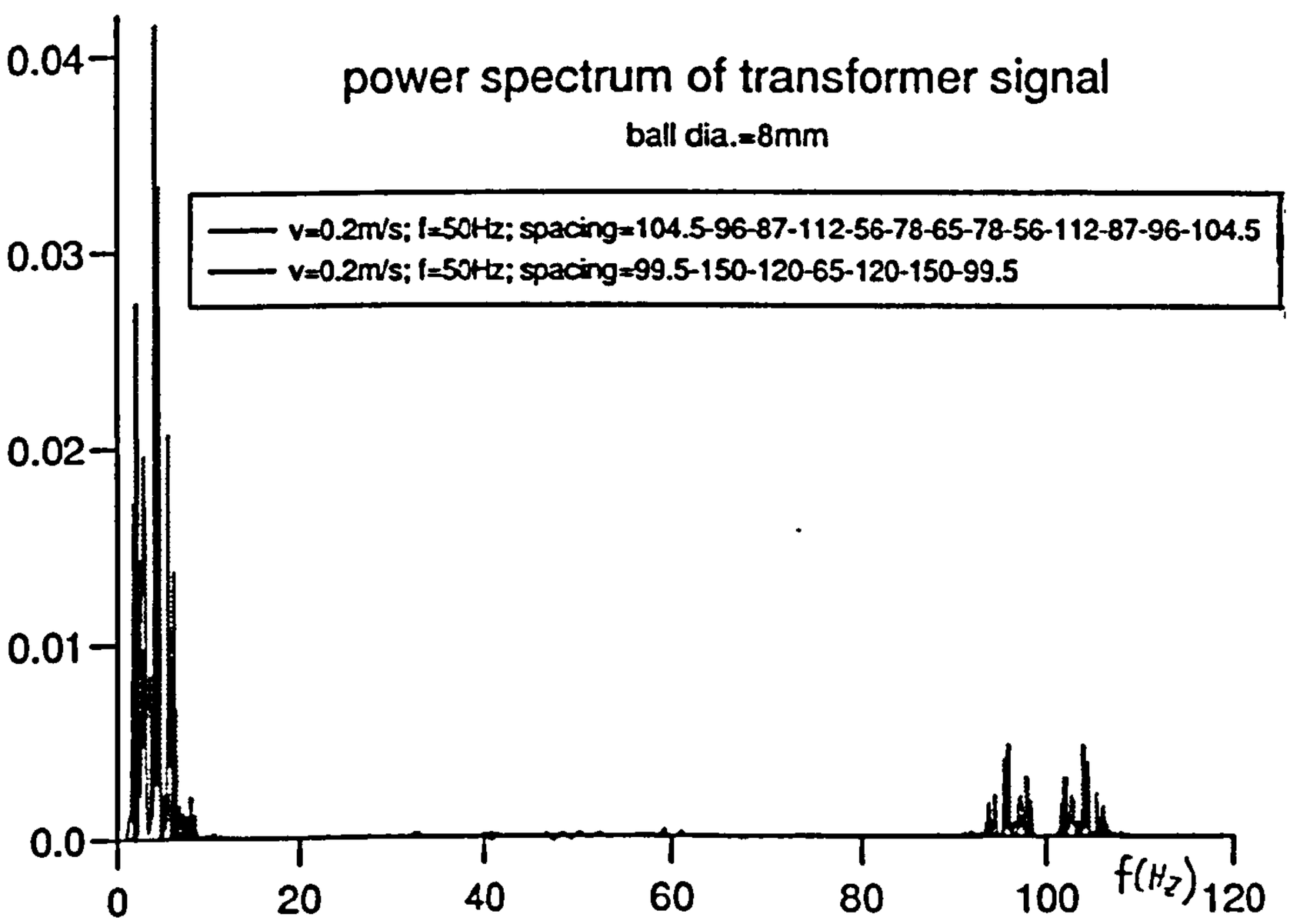

Fig.5.14

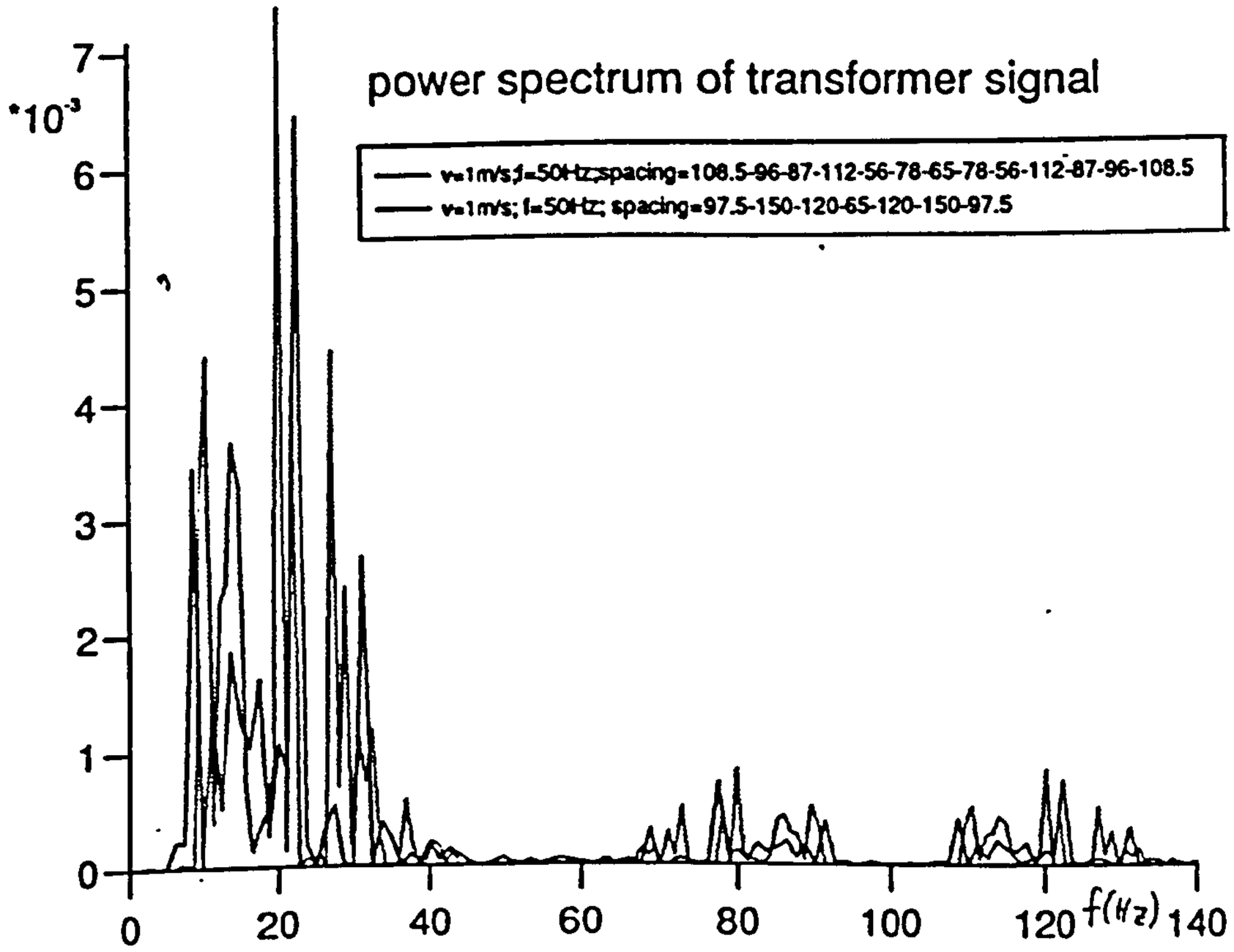

Fig.5.15

5.5 Leakage of transformer signal into the flow signal

The sinusoidal signal at the electrodes of a mains driven E.M-flowmeter alters its amplitude when the flowrate changes. When it is processed, it is rectified in phase with the magnetic field and averaged. In the case that a transformer signal is present due to the misalignment of the electrode wires or any other asymmetry, the transformer signal has no effect on the processed flow signal because it averages to zero. This however is only valid for a constant or slowly changing transformer signal. If the transformer signal changes fast enough compared to the chopping frequency, its average over each cycle will no longer be zero. **Fig.5.16** shows the transformer signal due to one passing bubble, rectified in phase with the magnetic field. The average

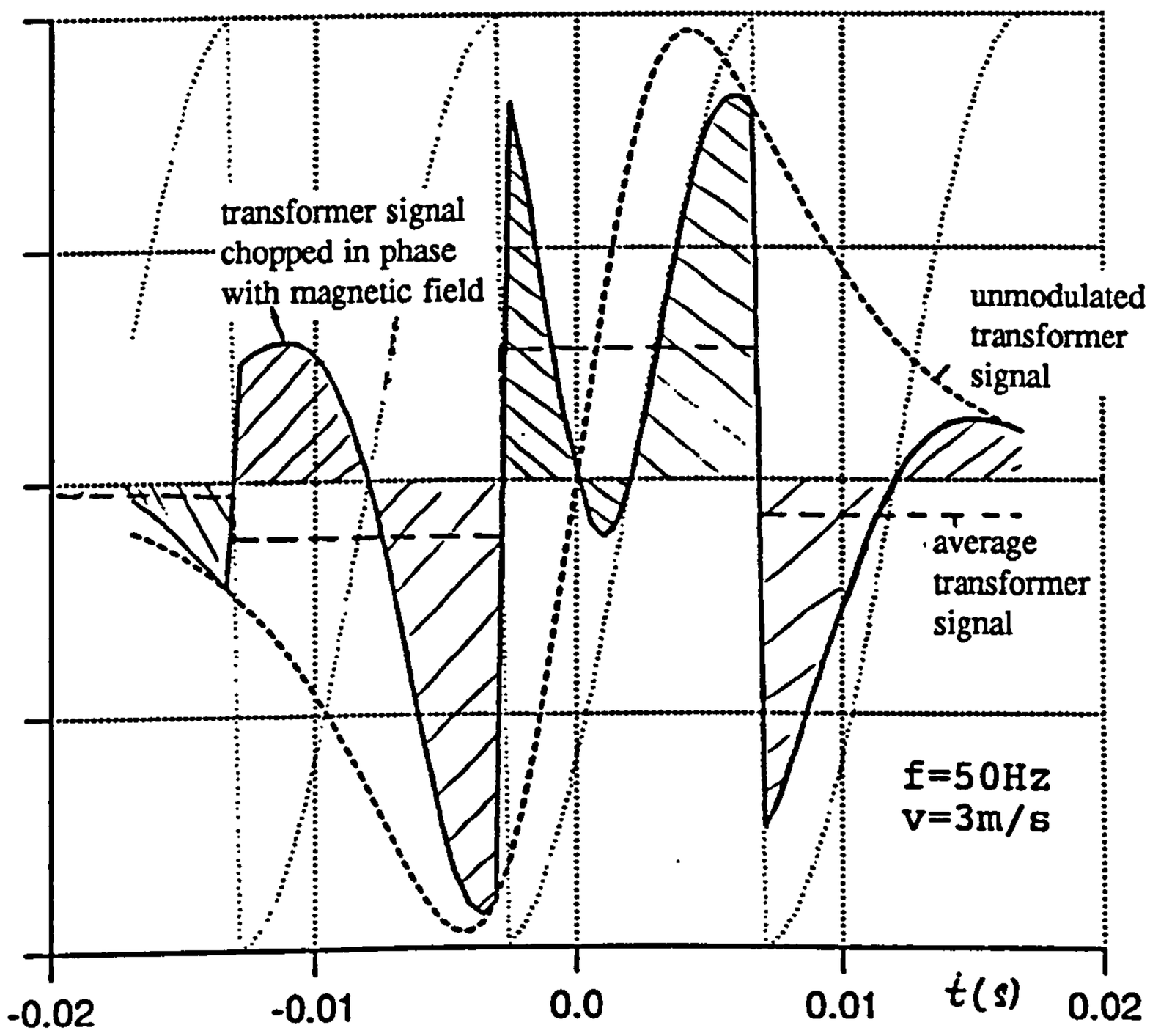

Fig.5.16 Leakage of transformer signal into the flow signal

over one cycle of the chopping frequency is clearly not zero. The amount by which the transformer signal leaks into the flow signal depends on the time over which the signal is averaged. As the modulation frequency increases, the transformer signal in the flow signal phase becomes more symmetric and its average approaches zero (**Fig.5.17** to **Fig.5.19**). In **Fig.5.20** power spectra for the modulated flow signal are shown. Without any transformer signal or with a constant transformer signal, the power spectrum only shows a DC value and spikes at 100Hz, 200Hz...etc. Because the transformer signal changes relatively quickly with regard to the modulation frequency, more noise appears around the harmonics of the fundamental frequency. These are in fact the same power spectra as those of the transformer signal but shifted by 100Hz and 200Hz respectively. The theoretical power spectrum of the transformer signal (**Fig.5.20**) which was rectified in phase with the 50Hz magnetic field compares very well with the measured power spectrum of the flow signal (**Fig.3.28**).

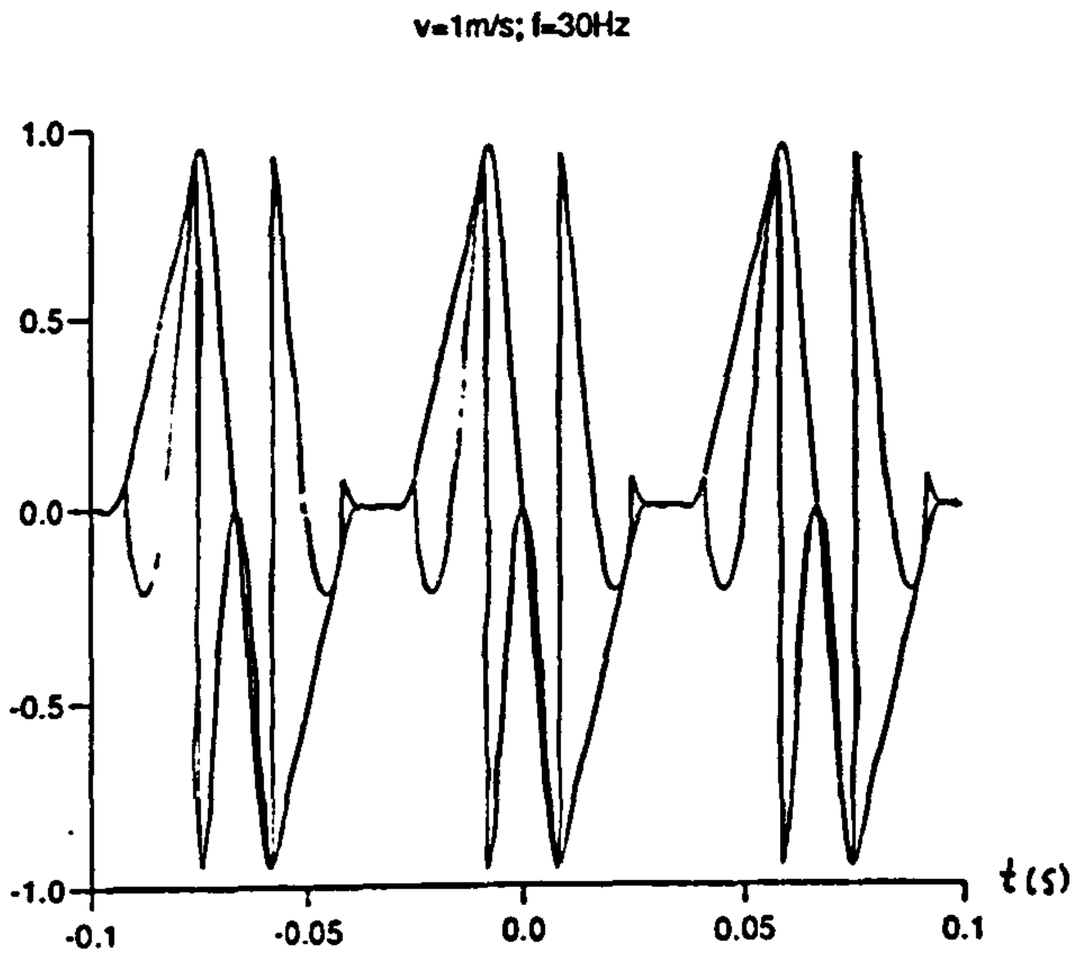

Fig.5.17 leakage of transformer signal into flow signal

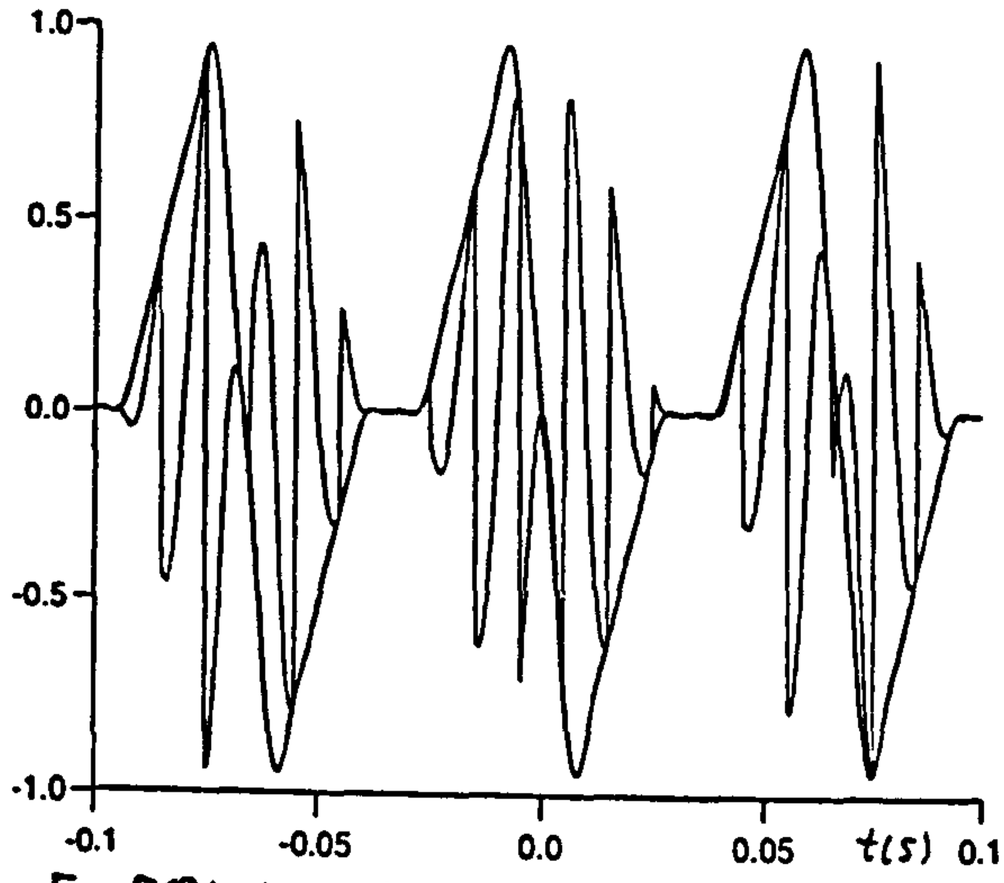

Fig.5.18 leakage of transformer signal into flow signal

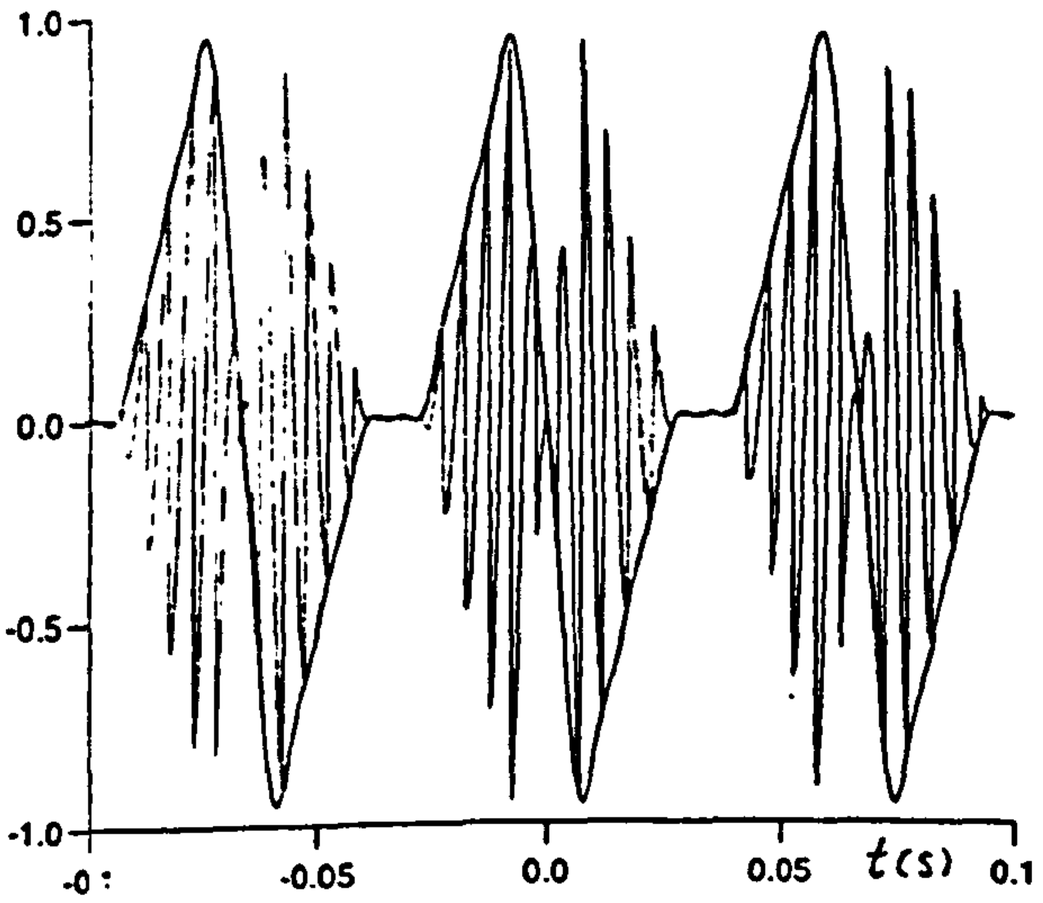

Fig. 5.19 transformer signal leaking into flow signal

This verifies that a nonconducting phase has almost no effect on the unprocessed flow signal and that the transformer effect is almost entirely responsible for the change in the processed signal from the electrodes.

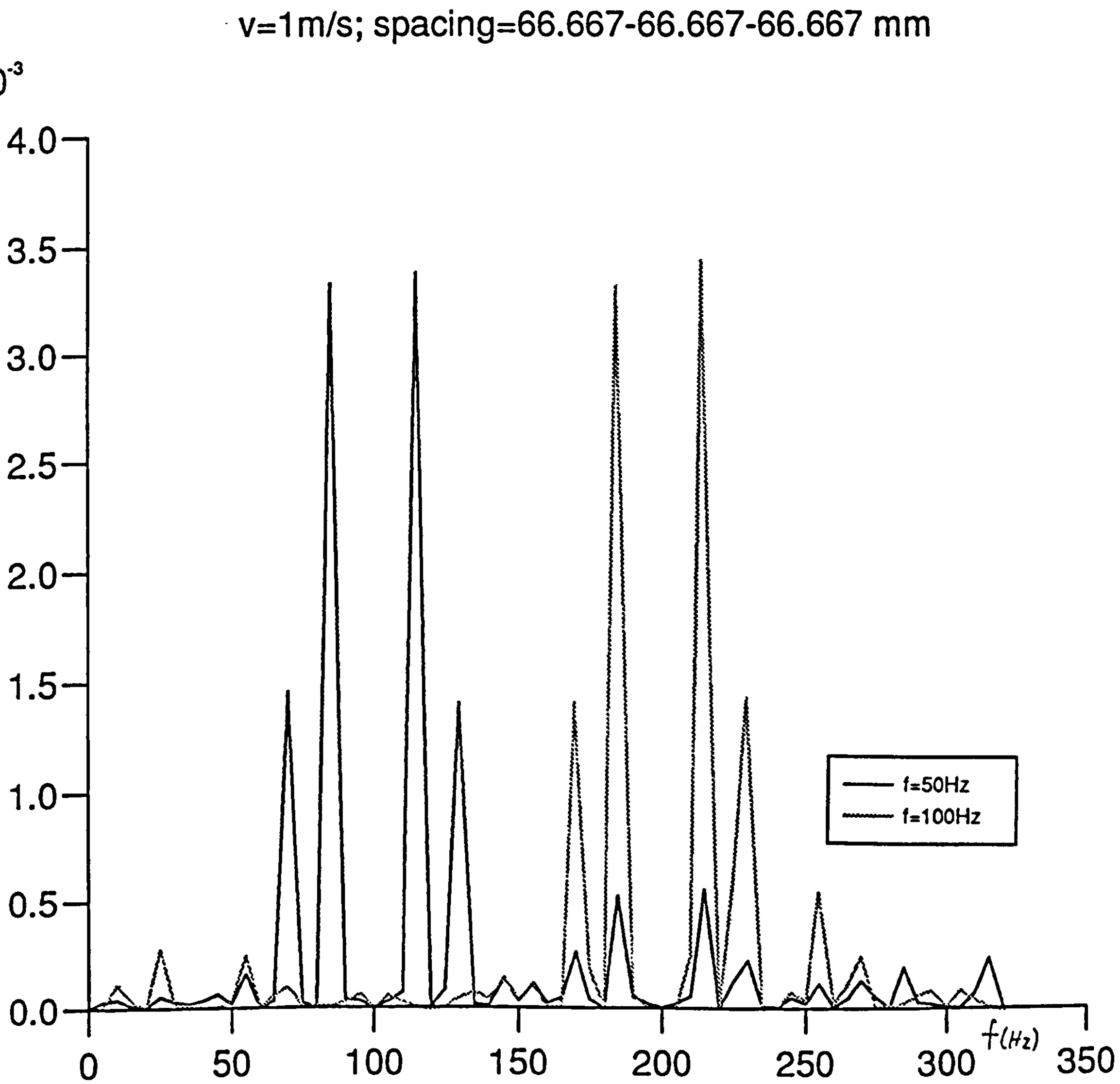

Fig.5.20 Power spectra of modulated flow signal for evenly spaced balls

Chapter 6

Measurement of the power spectrum of the transformer signal

6.1 Transformer signal without flow signal

Previous computations of the transformer signal have indicated that its power spectrum contains information which allows the determination of the velocity of the nonconducting phase. In order to verify that even the simplified model of the transformer signal as a triangular wave gives valid predictions, an experiment was set up as shown in **Fig.6.1.**

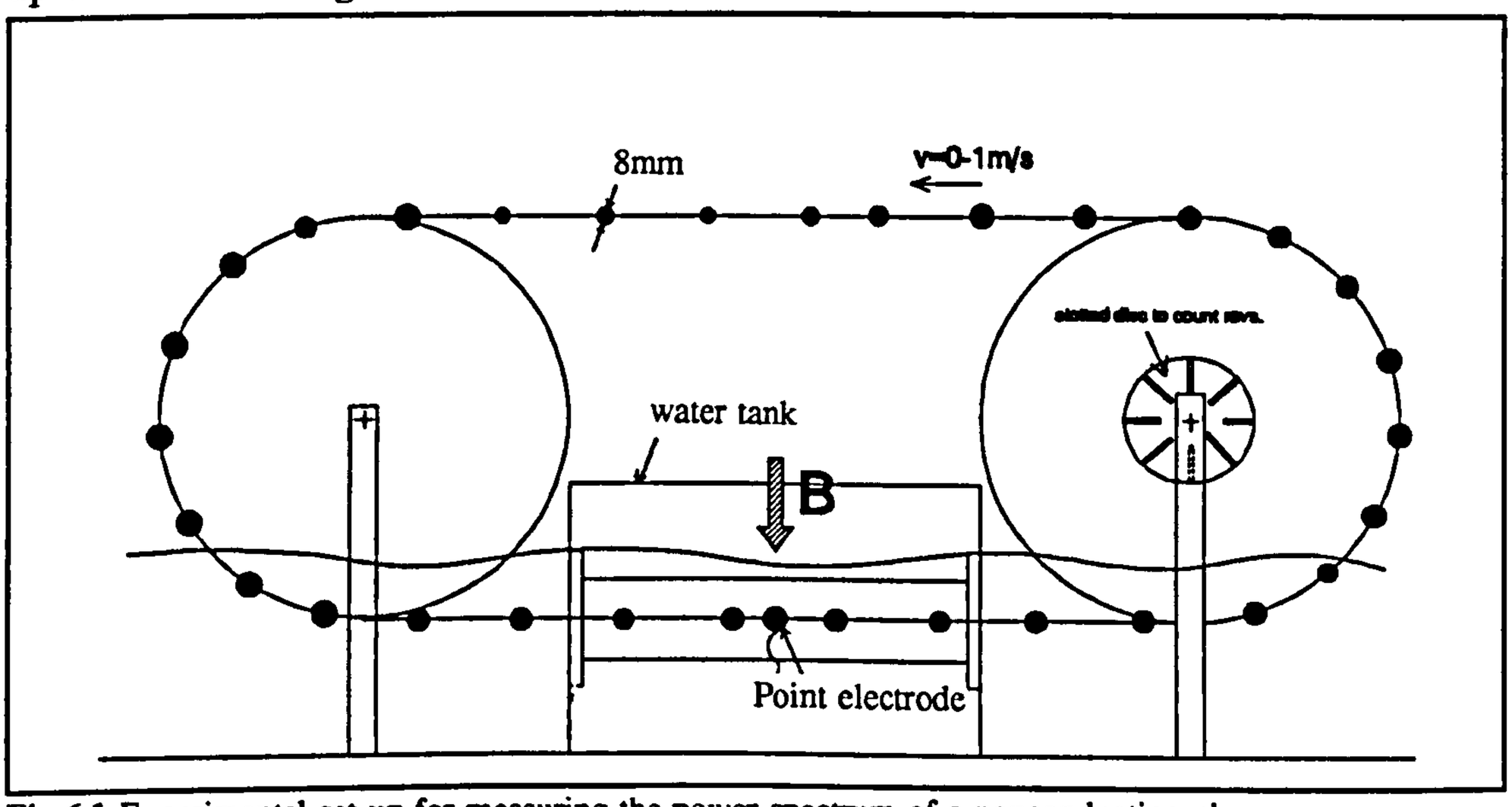

Fig.6.1 Experimental set up for measuring the power spectrum of a nonconducting phase.

The idea of the experiment is to generate a pure transformer signal by a nonconducting phase of known size and known velocity. The flow signal meanwhile shall be zero.
The bicycle rim is driven by a geared electro motor with a gear ratio of 8:1. Its rotational speed is measured using a slotted disk (with 8 slots), an opto switch and a frequency counter. The circumference of the driven wheel for a string with 8mm balls attached to it is 1860 mm. The velocity of the balls is therefore such that 1m/s ≡ 34.4 counts/s. Small errors occur due to the change in radius when either the line or a ball touches the wheel. These can be neglected when the experiment is run for a time long enough to average the effect out. The induced water velocity due to the balls motion is thought to be small as long as the ball size is small compared to the diameter of the pipe and the balls are moving slowly. In order to qualify this view, a short experiment is run in which the flow meter is used as a normal water flow meter: The device is run for 5 minutes and then stopped at a position where there are no balls closer than 100 mm to the electrodes. An immediate reading indicated an induced bulk water velocity equal to 16% of the ball velocity. In chapter 4 it was shown that the flow induced change in signal is two orders of magnitude lower than the transformer effect. Thus the flow induced signal will be negligible. With perfect chopping of the signal in phase with the rate of change of magnetic field, the flow signal would not matter as long as it changes slowly. However, because of slight distortions in the flow signal as well as not perfectly timed phase detection, small errors have to be accepted. The trend of the results however is still valid.
As indicated above, the speed of the balls has to be kept low for two reasons: Because the coils operate at 50Hz, the fully rectified transformer signal has a frequency of 100Hz. The maximum speed for a 10mm distance between the signal maxima is 1m/s. At a higher velocity, aliasing errors occur. Additionally, too high a velocity of the balls causes a larger flow signal, which, although small, can leak into the transformer signal in the same way as the transformer signal leaks into the flow signal.
The following experiments are therefore carried out at velocities between 0.02m/s and 0.4m/s. **Fig.6.2**, **Fig.6.3** and **Fig.6.4** show the power spectra measured for various speeds and spacings of the balls. For balls at the same speed, the envelope of the power spectrum has its maximum at the same frequency, independent of the distribution of the balls. The position of the maximum varies linearly with the speed of the nonconducting phase. Although the repeatability of each experiment is very good if done consecutively experiments, it is difficult to achieve the same result after the setup has been changed. This is mainly caused by the high sensitivity of the transformer signal to the distance between the balls and the electrodes. As shown before in section 4.16, the distance between the transformer maxima changes significantly when the balls come closer to the electrodes. In order to measure a high transformer effect, the experiment was set up with the balls very close to the electrodes. Small changes in this distance therefore cause a large variation in the measured power spectrum.
The best agreement between theory and experiment was obtained for evenly spaced balls. In **Fig.6.5** and **Fig.6.6**, the power spectra are compared for a ball speed of 0.2m/s and 0.4m/s respectively. The distance between the spikes is almost identical in experiment and computations. Also measured and computed result show the maximum at the same position.

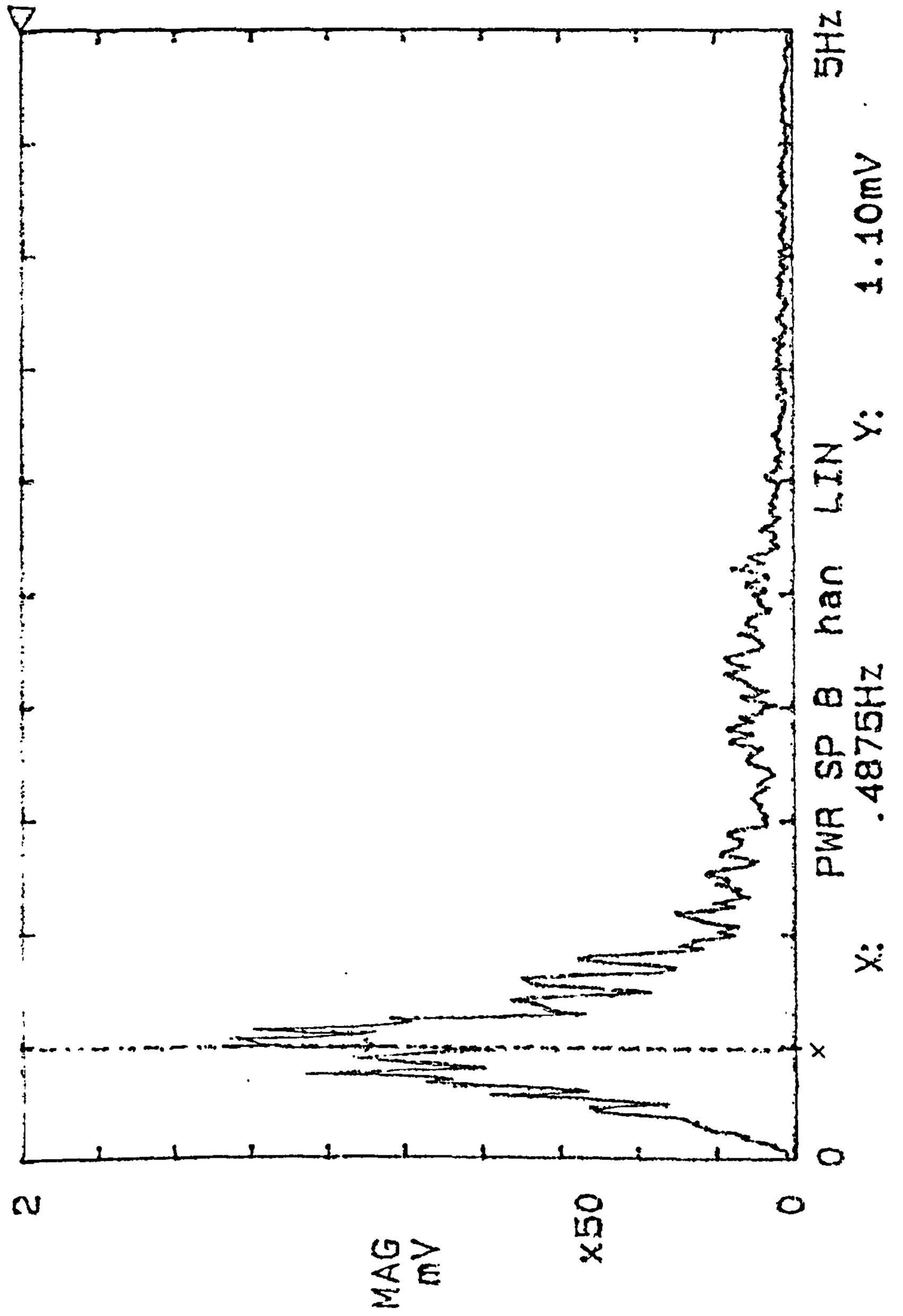

Fig.6.2 Measured power spectrum of transformer signal; ball speed=0.02m/s, balls randomly spaced

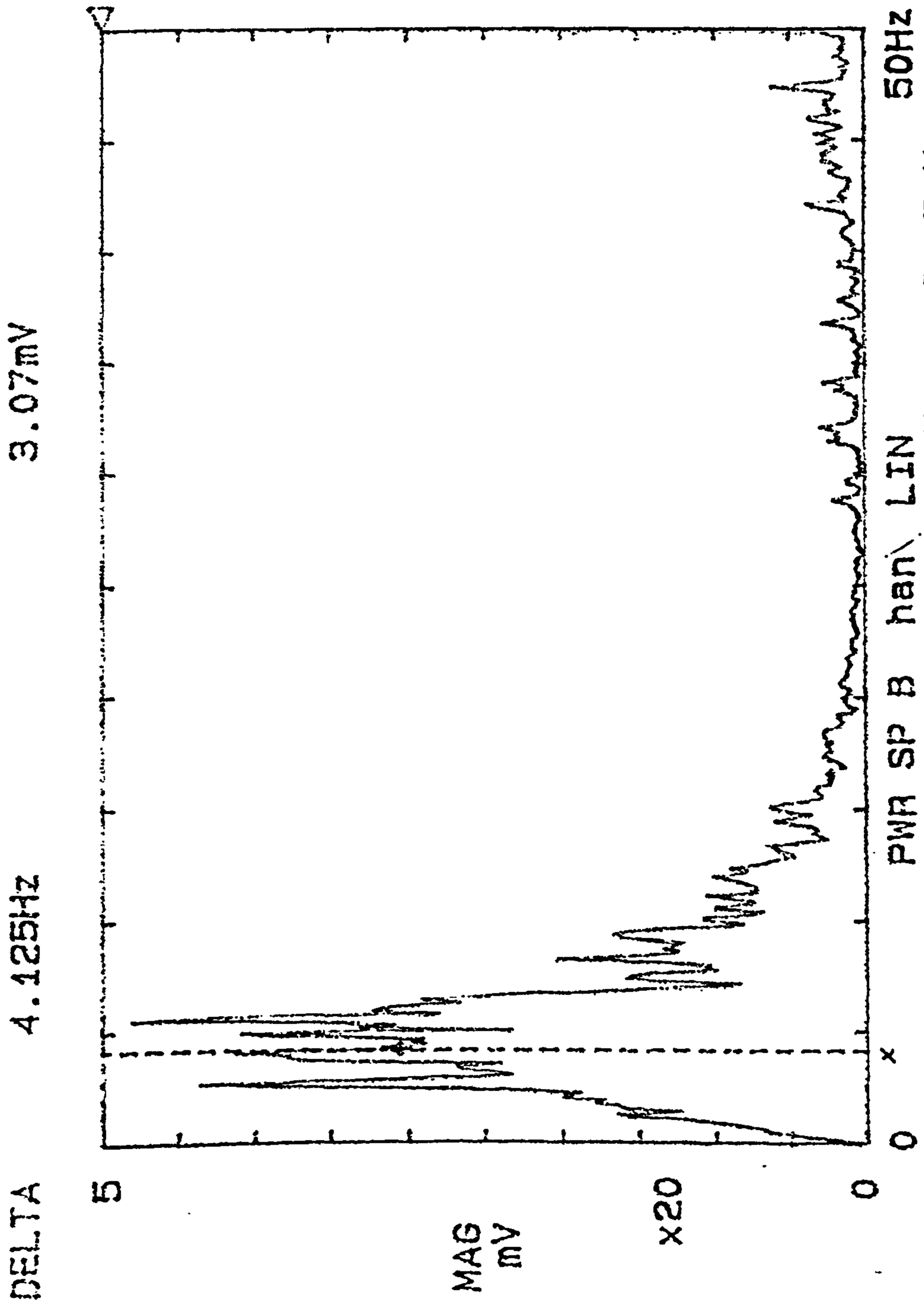

Fig.6.3 Measured power spectrum of transformer signal; ball speed=0.2m/s, balls randomly spaced

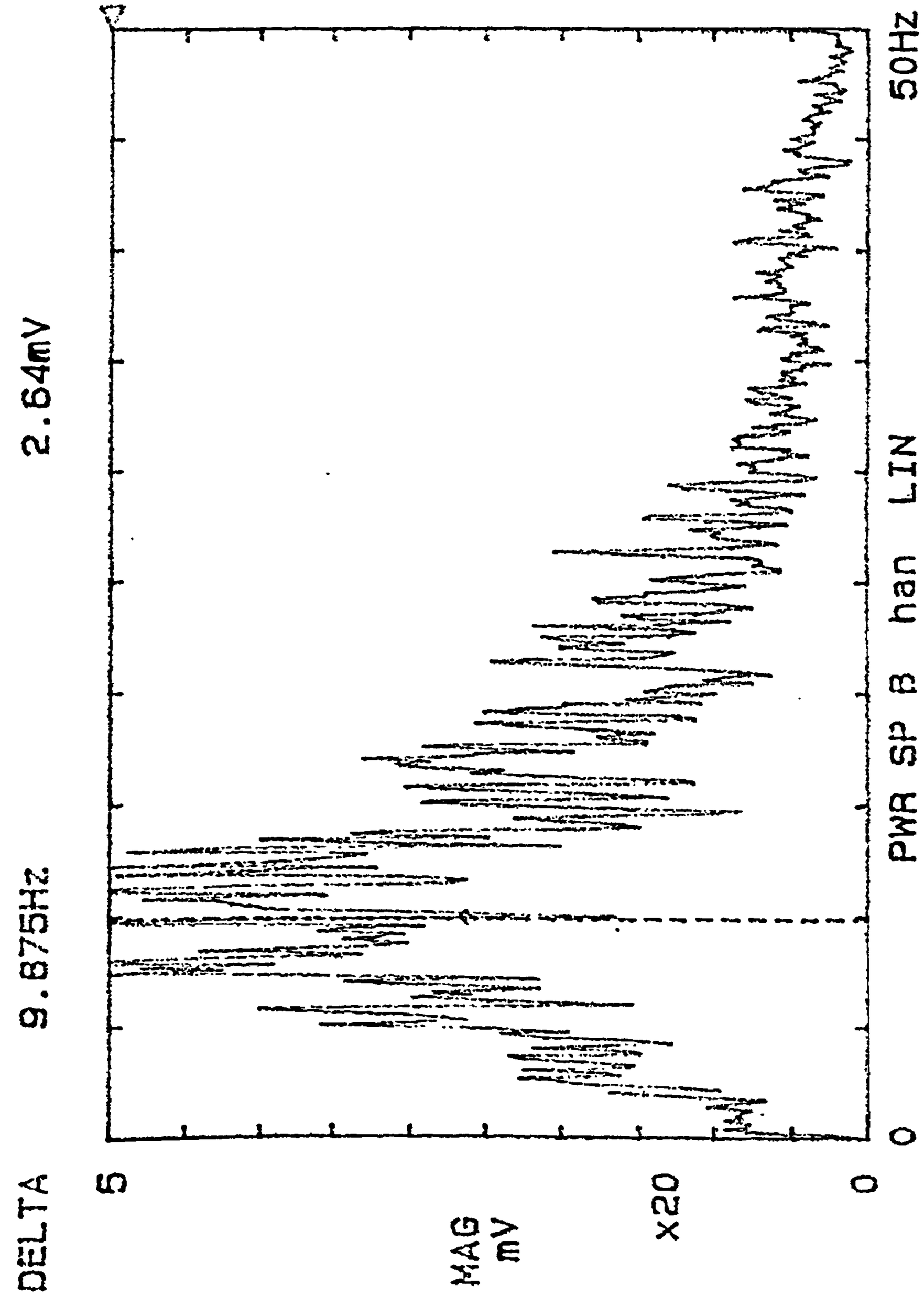

Fig.6.4 Measured power spectrum of transformer signal; ball speed=0.4m/s, balls randomly spaced

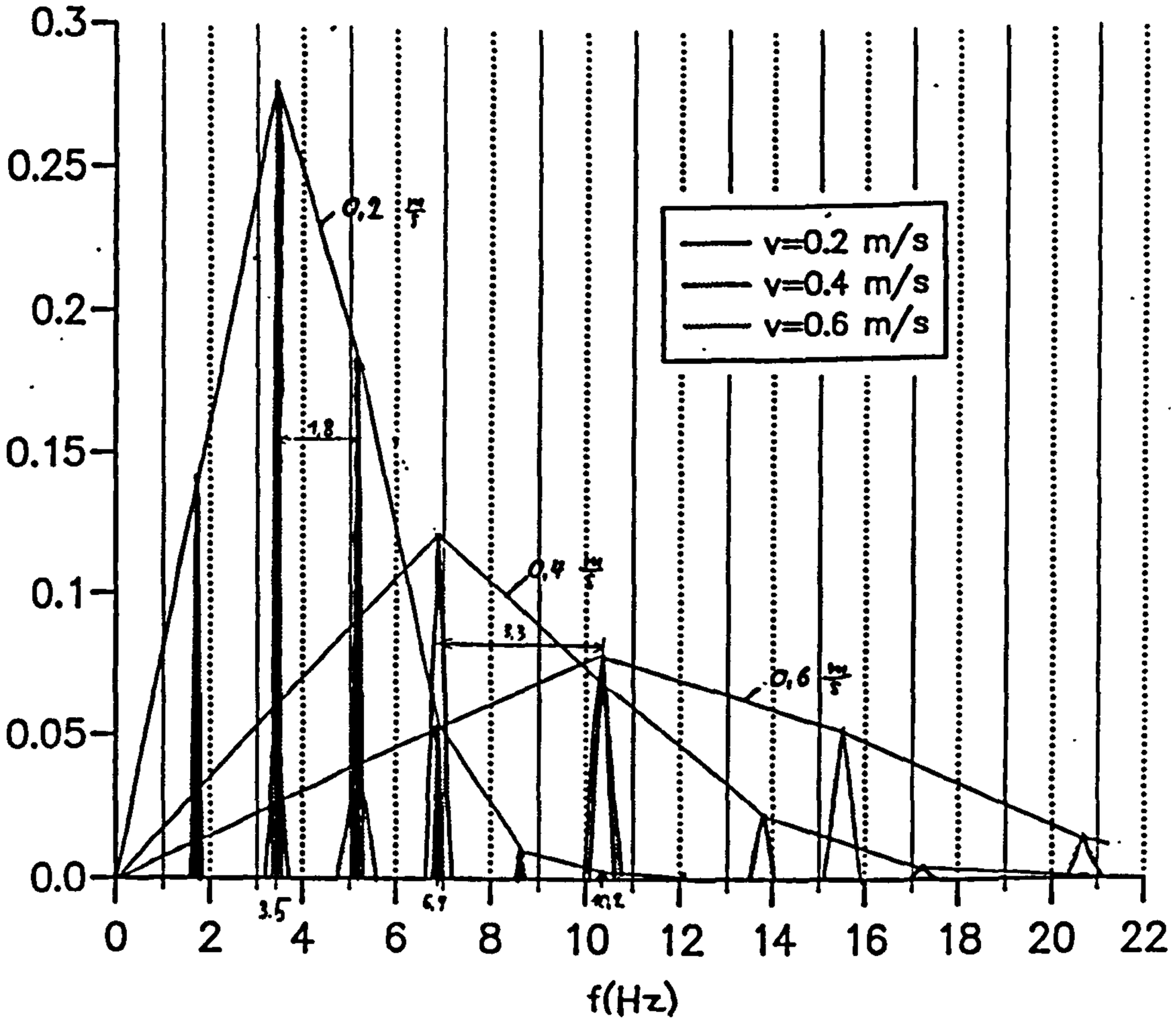

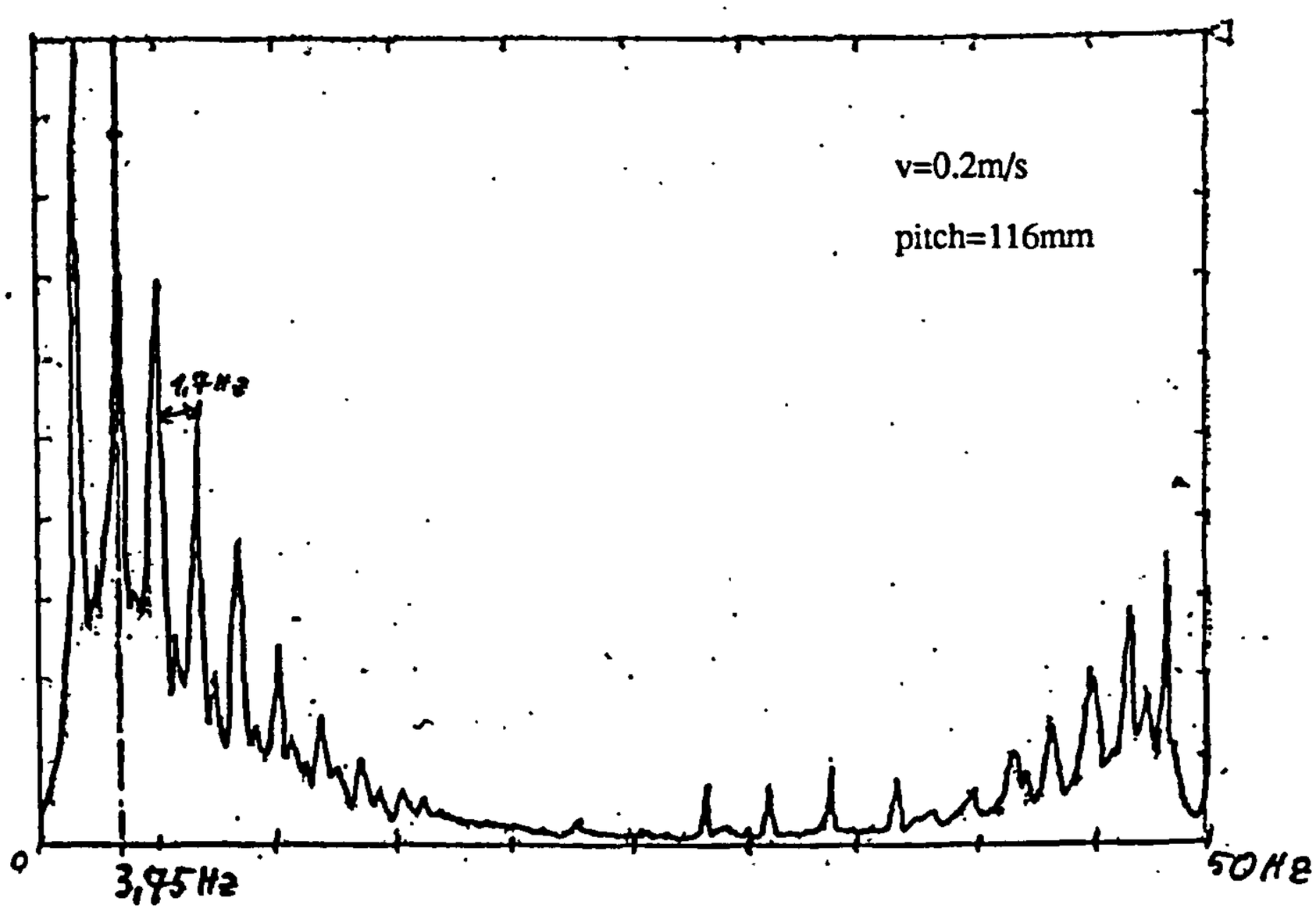

Fig.6.5 Comparison of measured and computed power spectrum

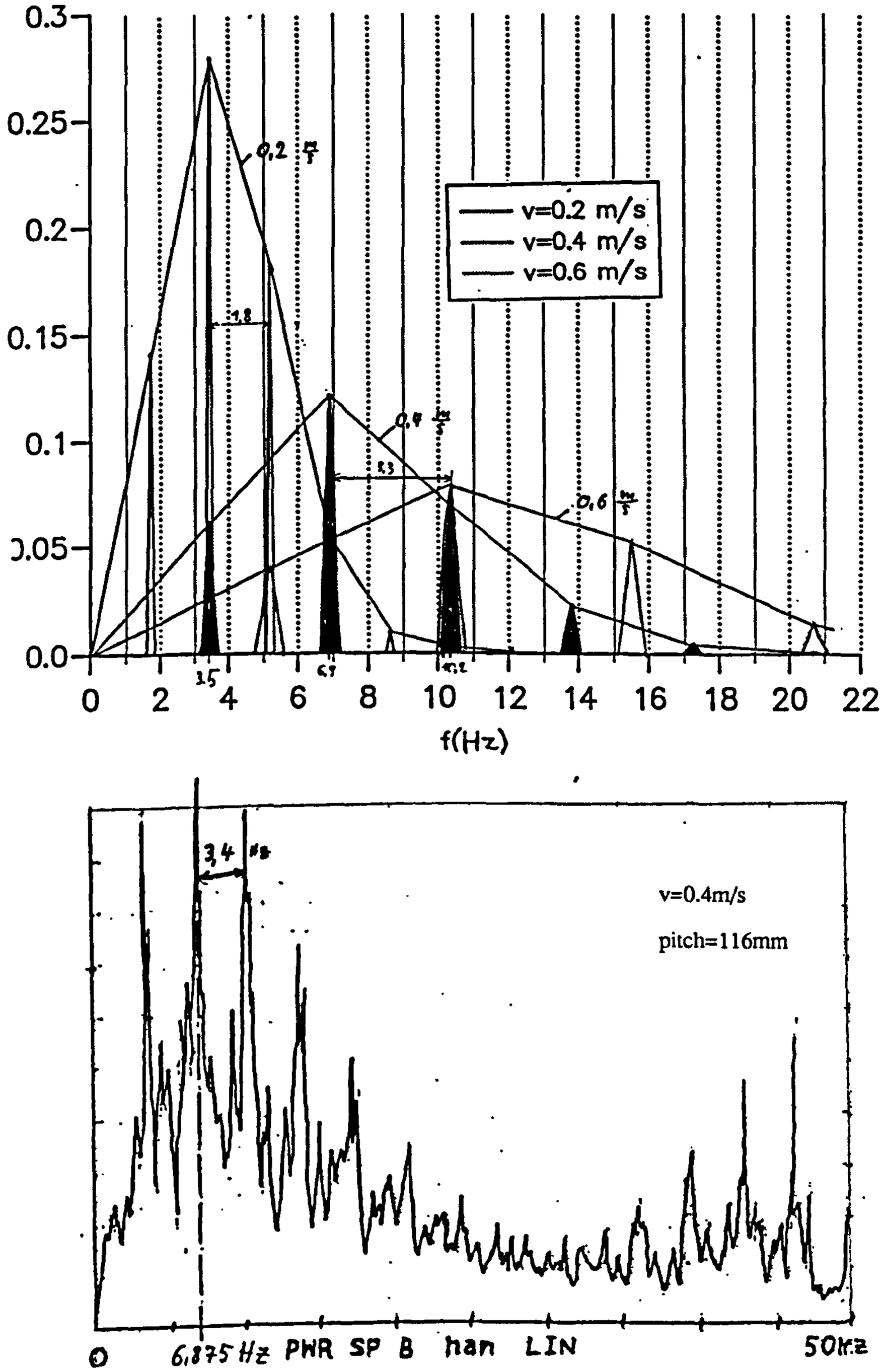

Fig.6.6 Comparison of measured and computed power spectrum

6.2 Transformer signal in the presence of a flow signal

Having demonstrated the existence of a transformer effect produced by a nonconducting second phase in the absence of a flow signal, the following experiments are now carried out under realistic flow conditions. In the first experiment, the device in chapter 3.4 is used again. Oil filled Plastic balls with a relative density close to 1 are injected into the pipe at rates between 1/2Hz and 2Hz. Because the rate at which the balls are injected is constant, the spacing between the balls is relatively constant as well. One would therefore expect a power spectrum similar to those found before for equally spaced balls. **Fig.6.7** and **Fig.6.8** show the measured power spectra for mean water velocities of 0.72m/s and 1.25m/s. At a mean velocity of 0.72m/s, the power spectrum has a maximum at 10Hz. As expected for these relatively high velocities, the spectra fall off with increasing frequency only slowly. The earlier mentioned signal at 50Hz adds additional noise. The high noise level towards the 100Hz is partly caused by the modulation of the transformer signal (as seen in **Fig.5.12**) and also, to a small degree by leakage of the flow signal into the transformer signal. With the increase of the mean flow velocity to 1m/s, the maximum of the power spectrum moves to the right. Balls injected at a rate of 1/2Hz generate obviously a lower level of transformer signal than balls which are injected at 2Hz. However, the maximum occurs at the same frequency. The good repeatability of the experiment can be seen in **Fig.6.7**. At a mean velocity of 1.25m/s, the power spectrum becomes considerably flatter than it was at v=0.72m/s. The maximum has still moved further to the right and is now at about 20Hz. This is slightly higher than expected. With a linear relation between the speed of the balls and the position of the peak in the power spectrum, one would have expected the maximum at about 17Hz. This assumes that the balls have the same speed as the water flow. The discrepancy is probably caused by the fact that the balls follow a slightly zig-zag path at lower speeds and they are therefore slower than the mean water velocity. With increasing flow rate the path of the balls becomes more straight.

Now the experiment is altered in that filled balls are used for the first reading and then empty balls are injected for the second part of the experiment. Due to the lower density, the empty balls rise faster than the filled ones (at the same water velocity). The flowrate is then adjusted until the velocity of the empty balls is equal to that of the filled balls in the previous reading. The power spectra are then compared. When comparing **Fig.6.9** with **Fig.6.10** and **Fig.6.11** with **Fig.6.12**, it is found that for those different flow rates at which the ball velocities are equal, the maximum of the power spectrum is at the same position. This demonstrates the dependence of the spectrum on the velocity of the nonconducting phase alone and its independence on the water flow rate.

After this series of experiments with single balls, a real 2 phase flow is used to measure the transformer effect. The flow is adjusted to a superficial water flow velocity of 0.7m/s. Then,keeping the water flow rate fixed, air is injected to create a bubbly flow regime and the power spectrum of the transformer signal is recorded. **Fig.6.13** and **Fig.6.14** show the averaged power spectra. The frequency of the maximum of the spectrum is each time at ca.12.5Hz. Comparing this result with the reading at v=0.72m/s and single balls injected, 12.5Hz seems to be too high.

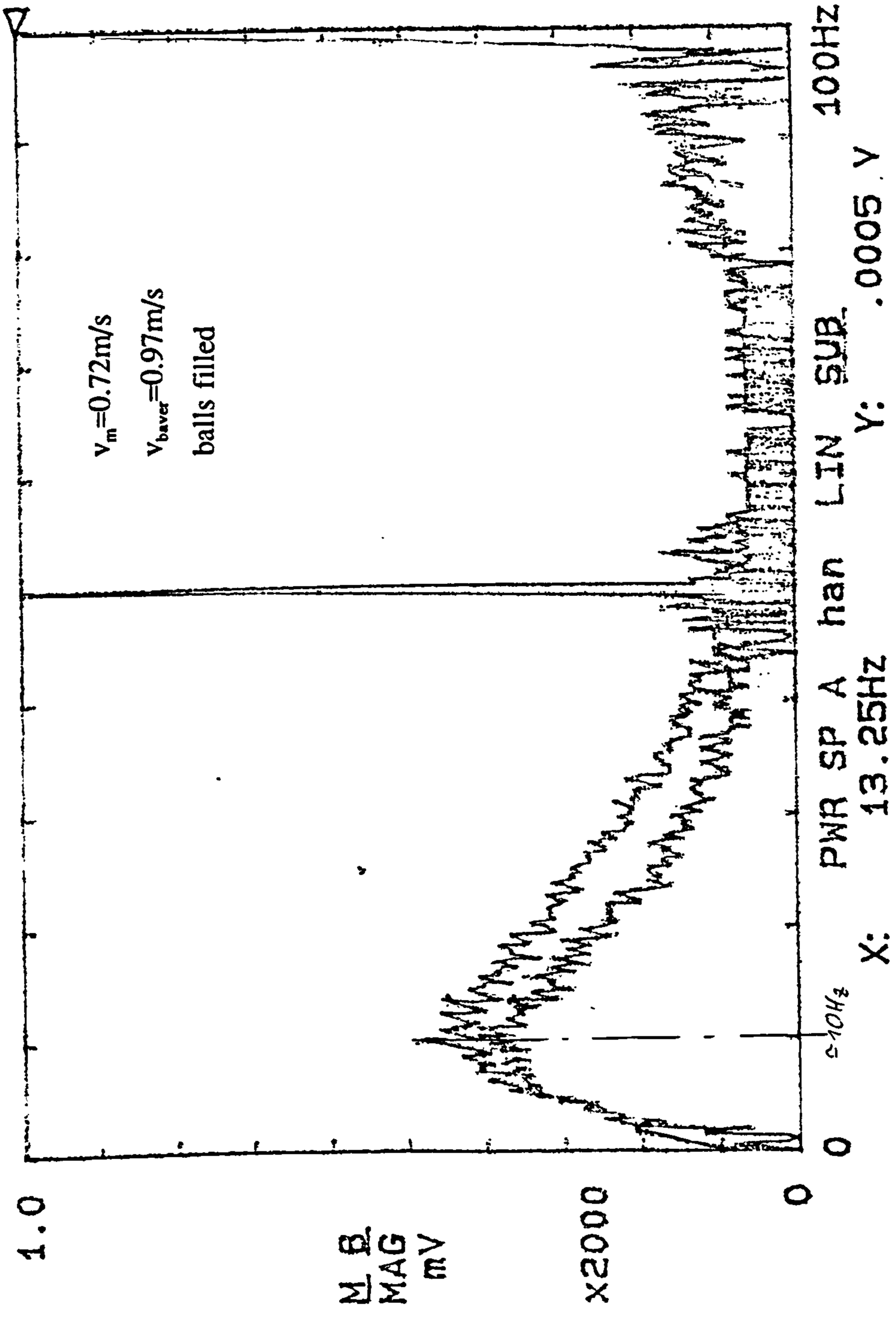

Fig.6.7 Measured power spectrum of transformer signal, oil filled balls injected

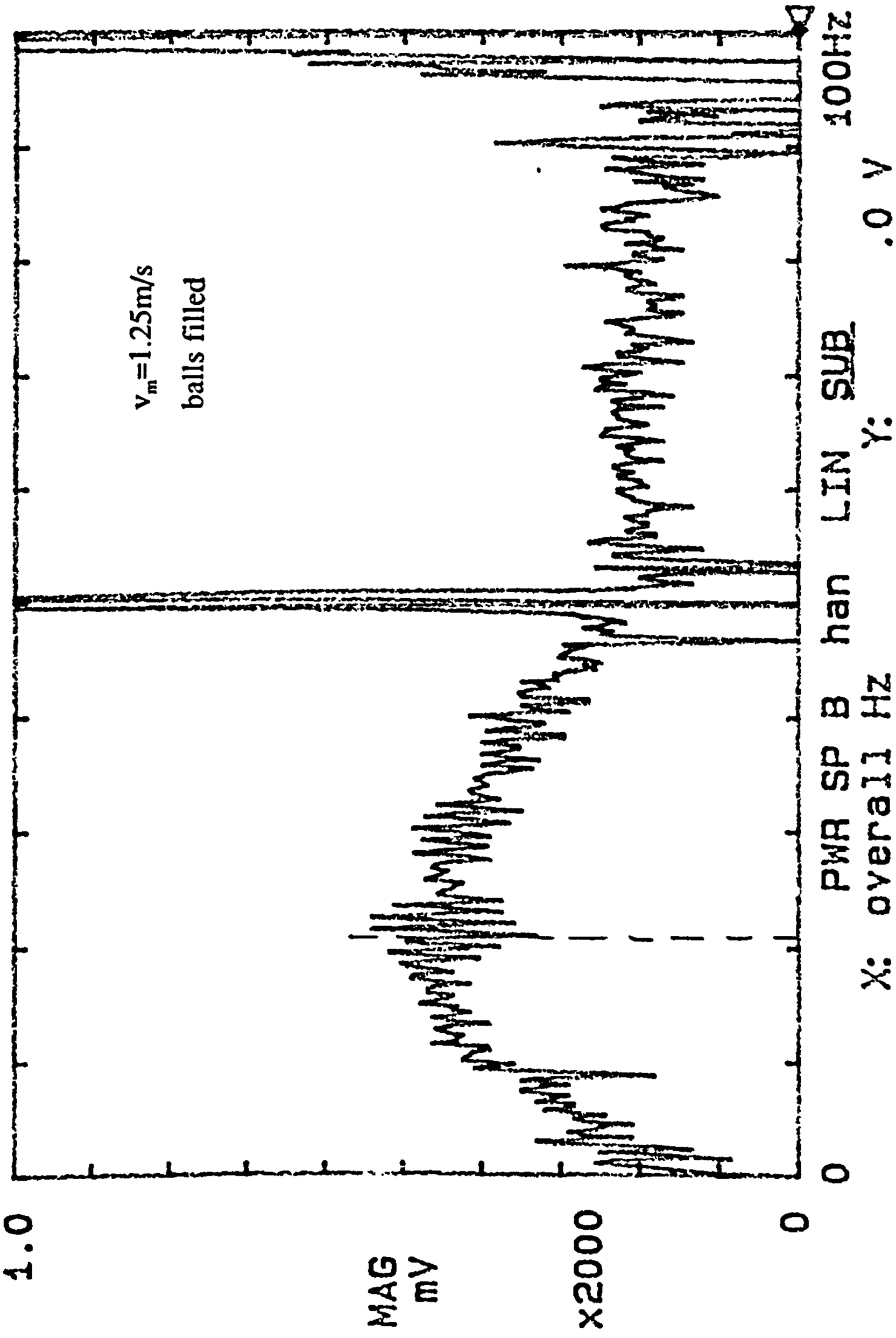

Fig.6.8 Measured power spectrum of transformer signal, oil filled balls injected

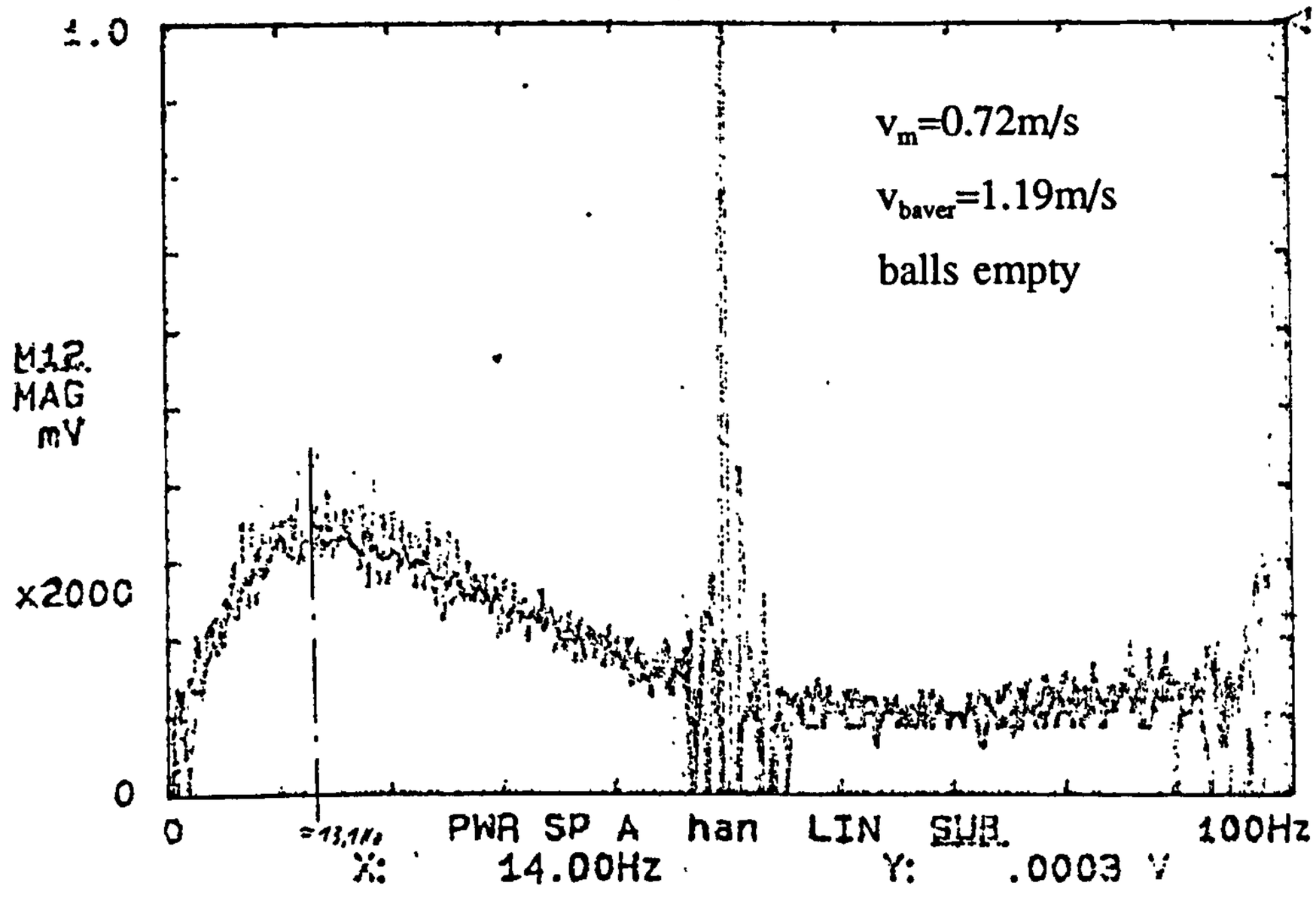

Fig.6.9 Measured power spectrum of transformer signal, empty balls injected

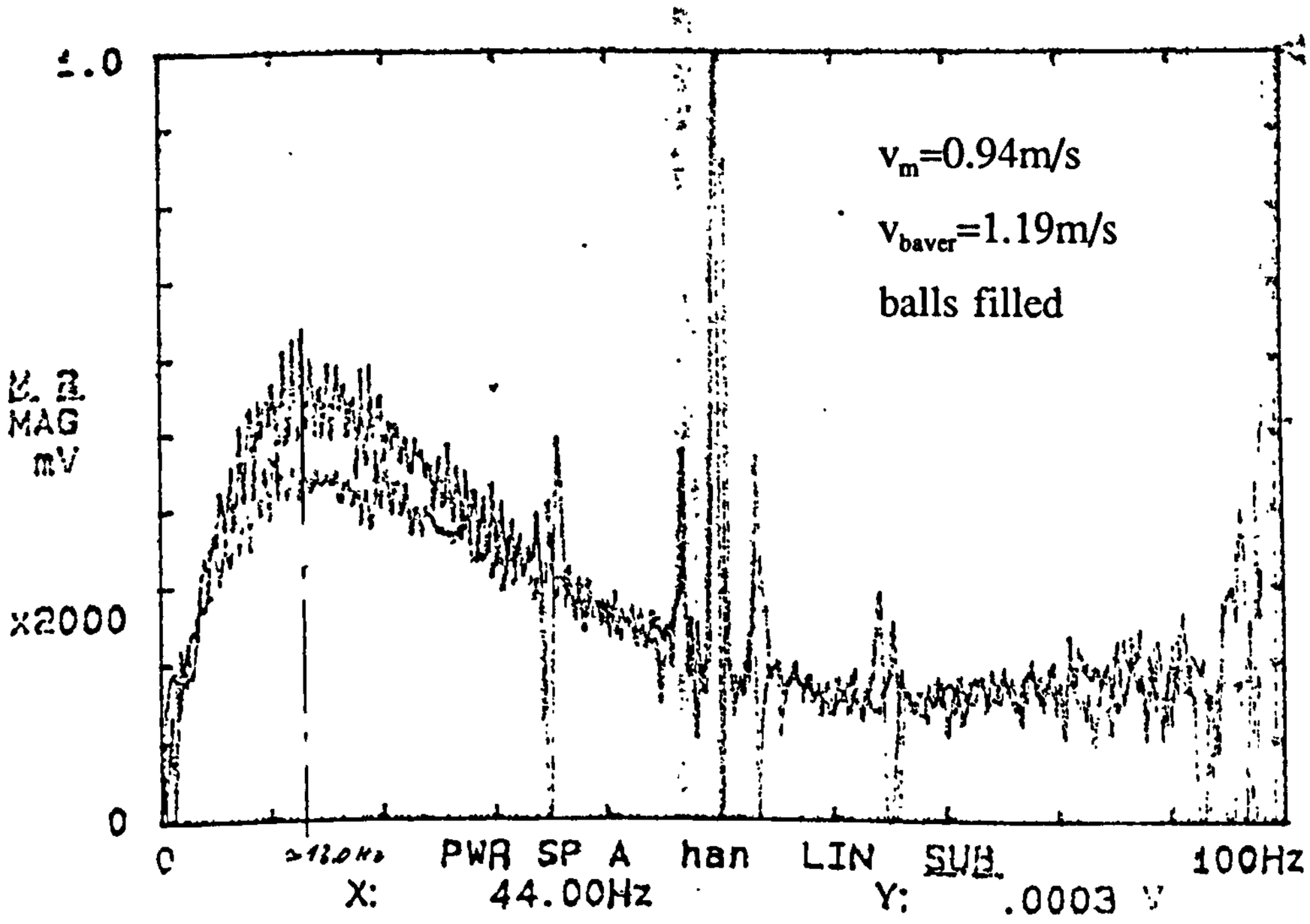

Fig.6.10 Measured power spectrum of transformer signal, oil filled balls injected

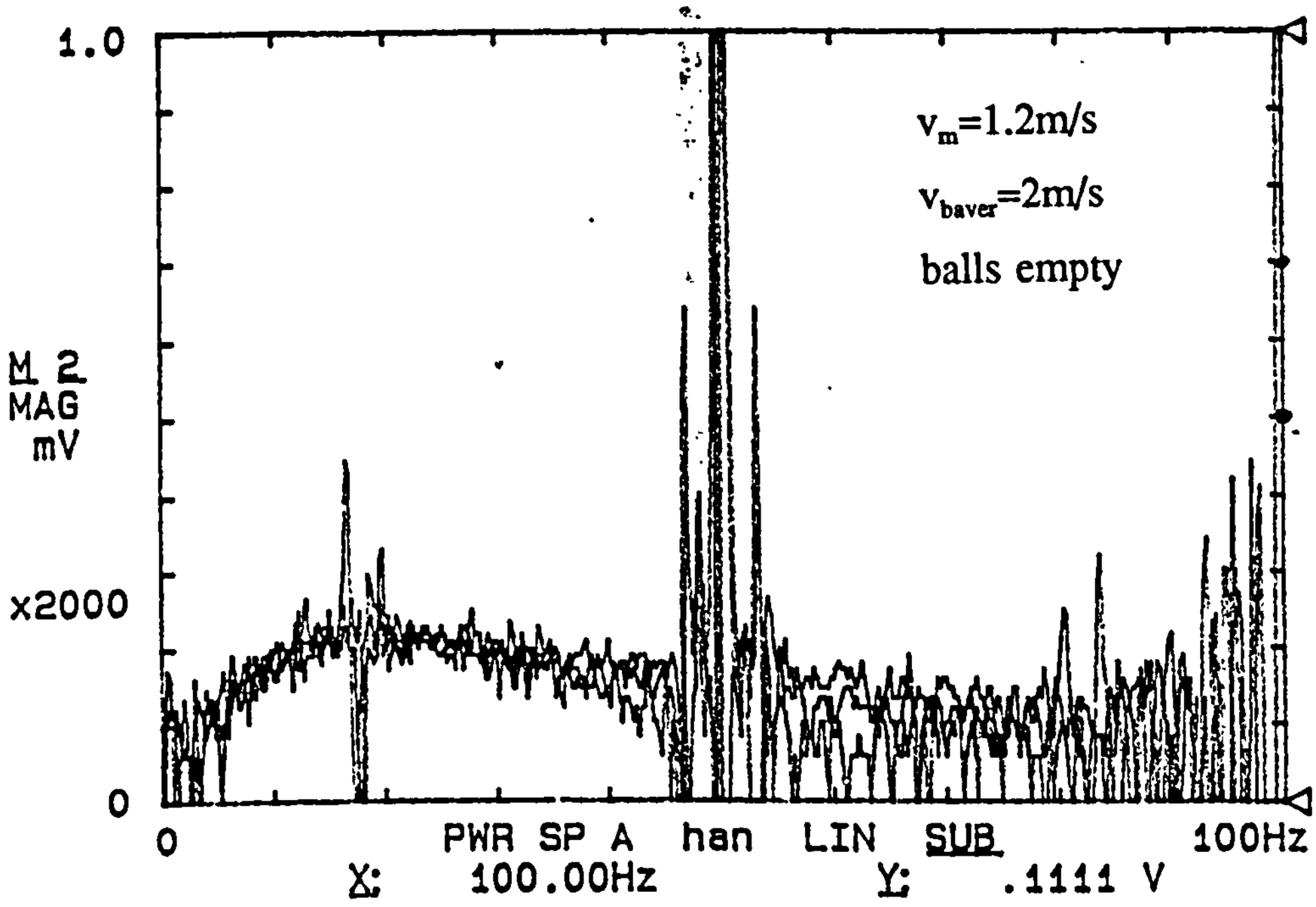

Fig.6.11 Measured power spectrum of transformer signal, empty balls injected

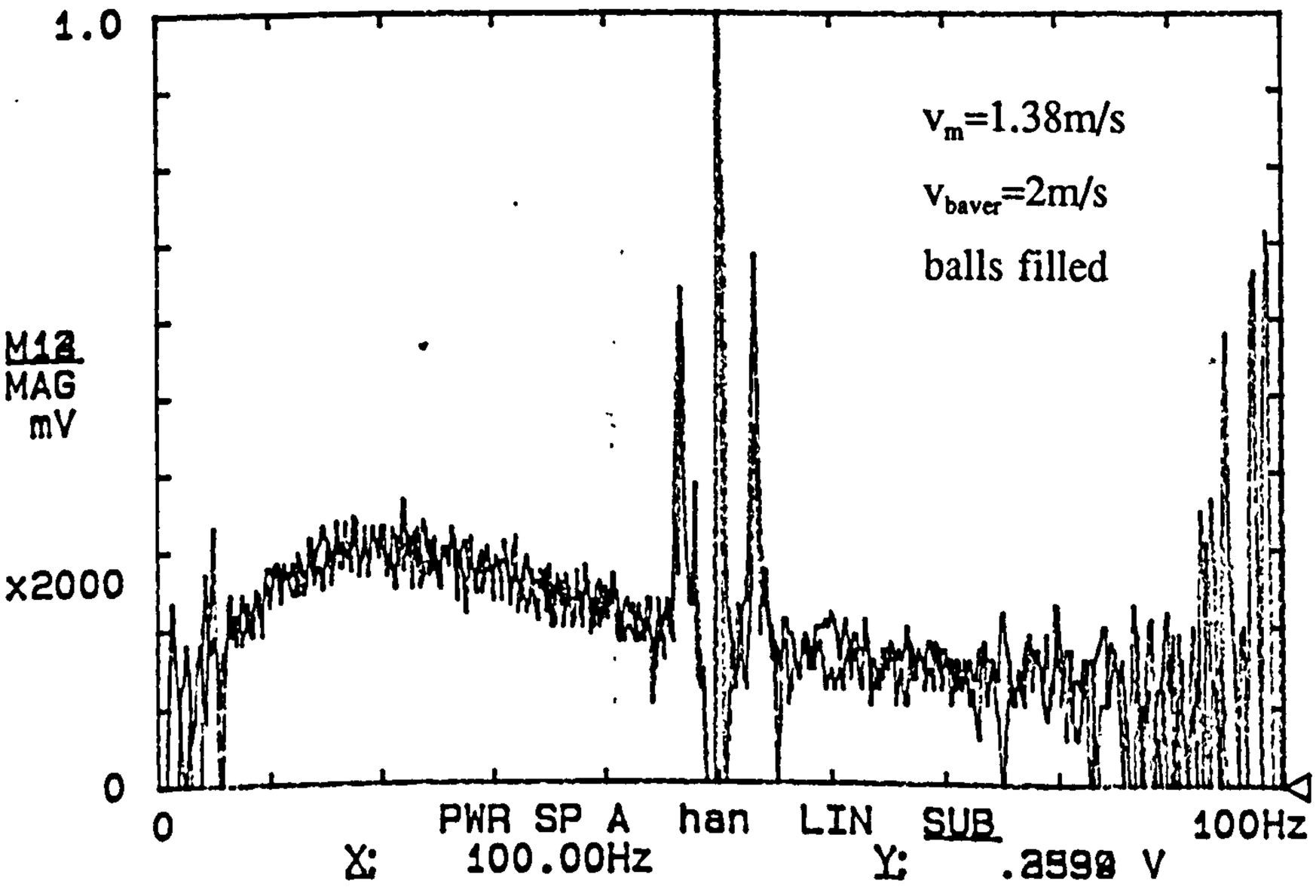

Fig.6.12 Measured power spectrum of transformer signal, oil filled balls injected

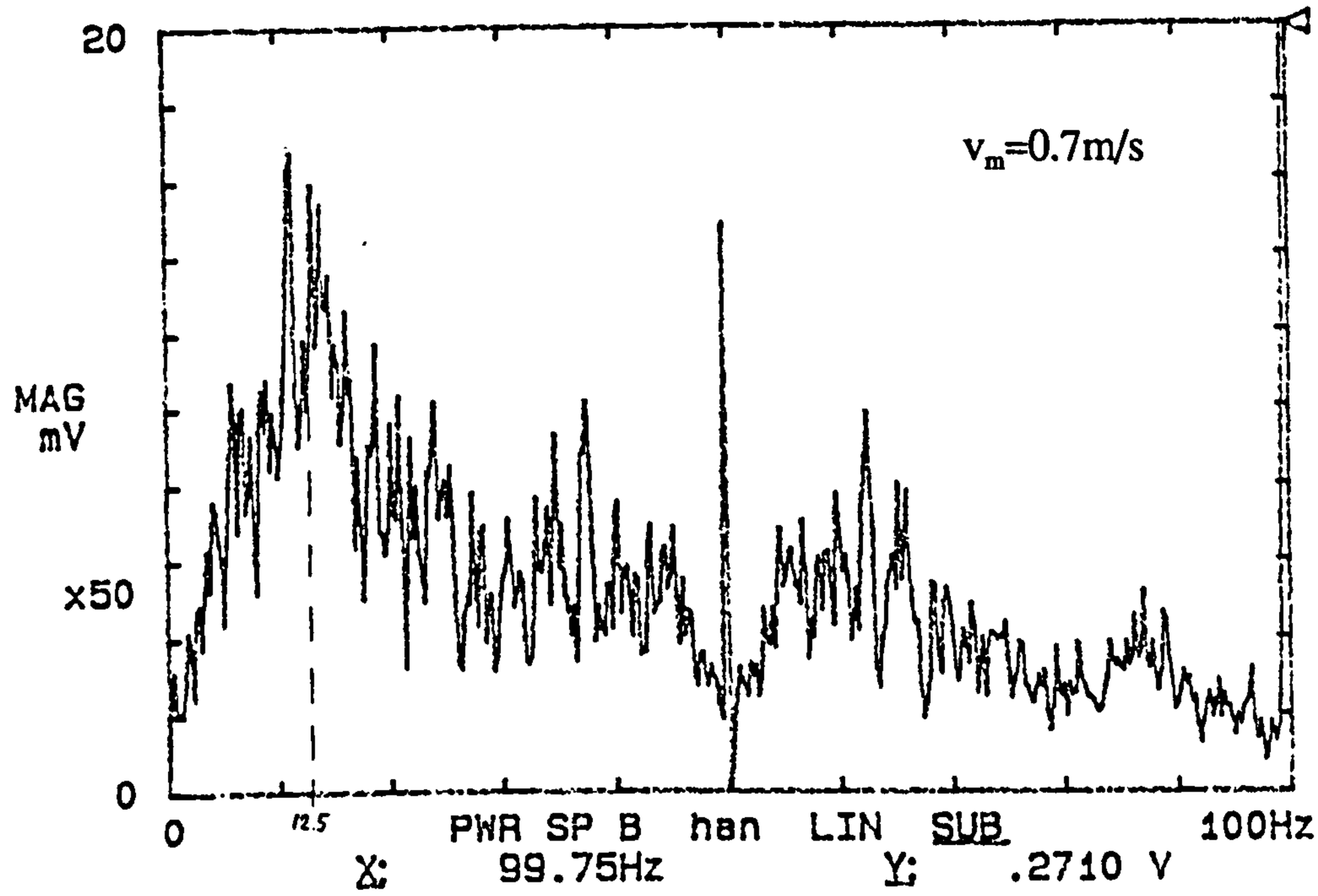

Fig.6.13 Measured power spectrum of transformer signal in air-water flow

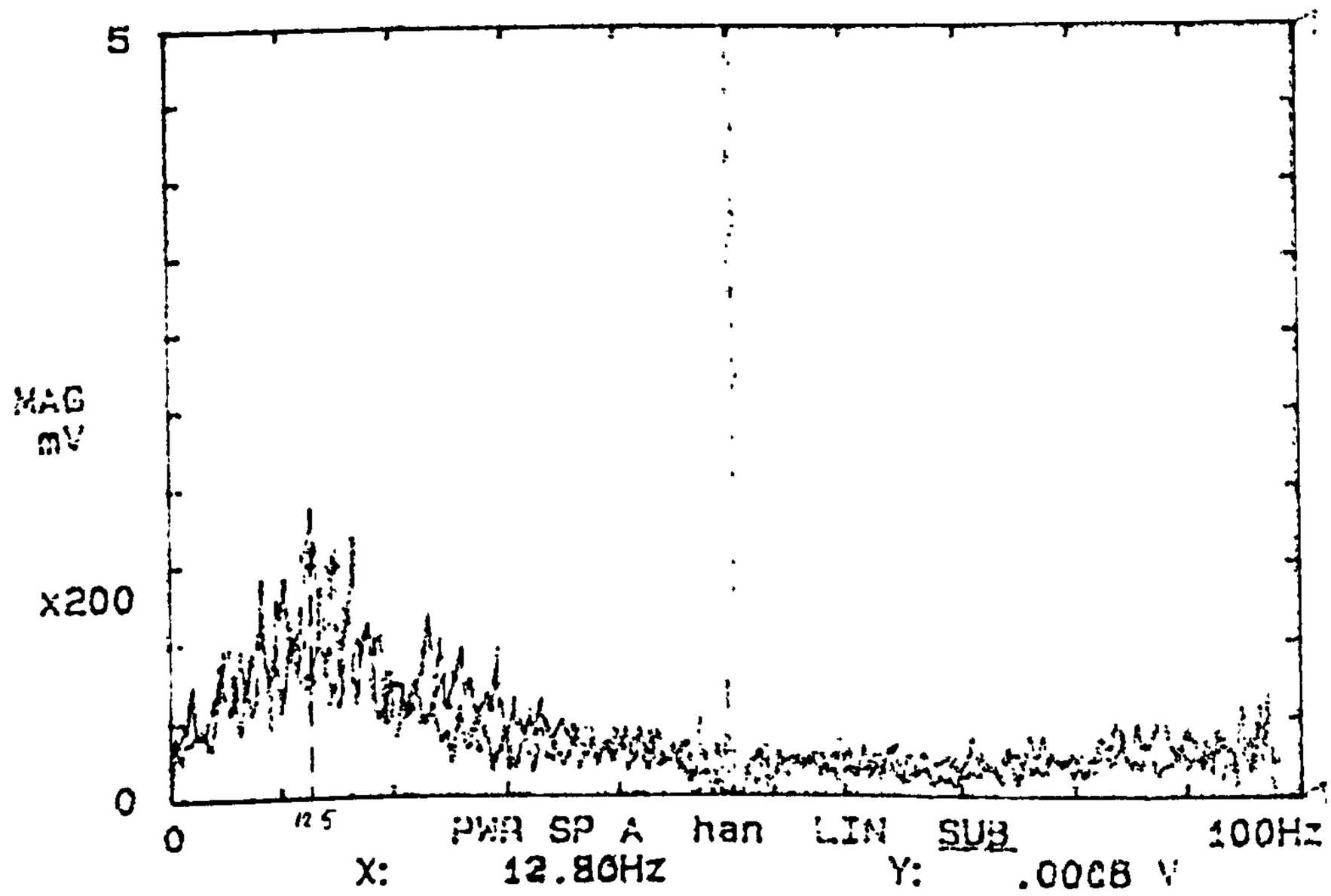

Fig.6.14 Measured power spectrum of transformer signal in air-water flow

This is not the case if one considers the fact that in the first experiment the superficial velocity is almost the same as the mean water velocity because the void fraction was negligible with only a single ball passing through every second. In the case of the air-water flow the void fraction is estimated to be at least 10%. Therefore, the mean water velocity is about 0.8m/s. In addition, the air bubbles are buoyant and they are therefore faster than the water flow. The third reason for the seemingly high reading is the fact that the balls are injected in the centre of the pipe. Even if they are not rising in a straight line, they rarely pass the electrodes closely. This means that there is a large distance between points of maximum absolute value of transformer signal. A large distance means a low frequency in the power spectrum. The airbubbles are distributed over the whole pipe cross section and therefore also close to the electrodes. Due to the weighting of the transformer signal with respect to the position of the 2nd phase in the pipe(**Fig.4.14**), bubbles near the electrodes generate a strong signal at a higher frequency. Those in the middle of the pipe generate a much weaker signal at a lower frequency.

The last experiment designed to show that it is possible to measure the velocity of the nonconducting phase with an E.M.flowmeter is again done with a 2 phase air water flow. The buoyancy of the gas phase is used to create a velocity difference of the nonconducting phase while the velocity of the water is kept constant. This is achieved by reversing the flow direction in the vertical section of the pipe. For a not too high flow rate we expect the velocity of the gas phase to be larger than the water velocity in the upward flow and lower on the downward flow. The difference reduces as the water velocity increases. The experiment is run at superficial water velocities from 0.4m/s to 2m/s. At each velocity the experiment is repeated 4 times and the result is averaged. Because of the earlier discussed aliasing effects at high velocities and the very flat power spectrum, the results at velocities above 1m/s were considered to be not accurate enough to measure a difference between the upward and downward flow. They are therefore not listed. **Fig.6.15** shows the measured results for superficial water velocities of 0.4m/s and 0.8m/s.

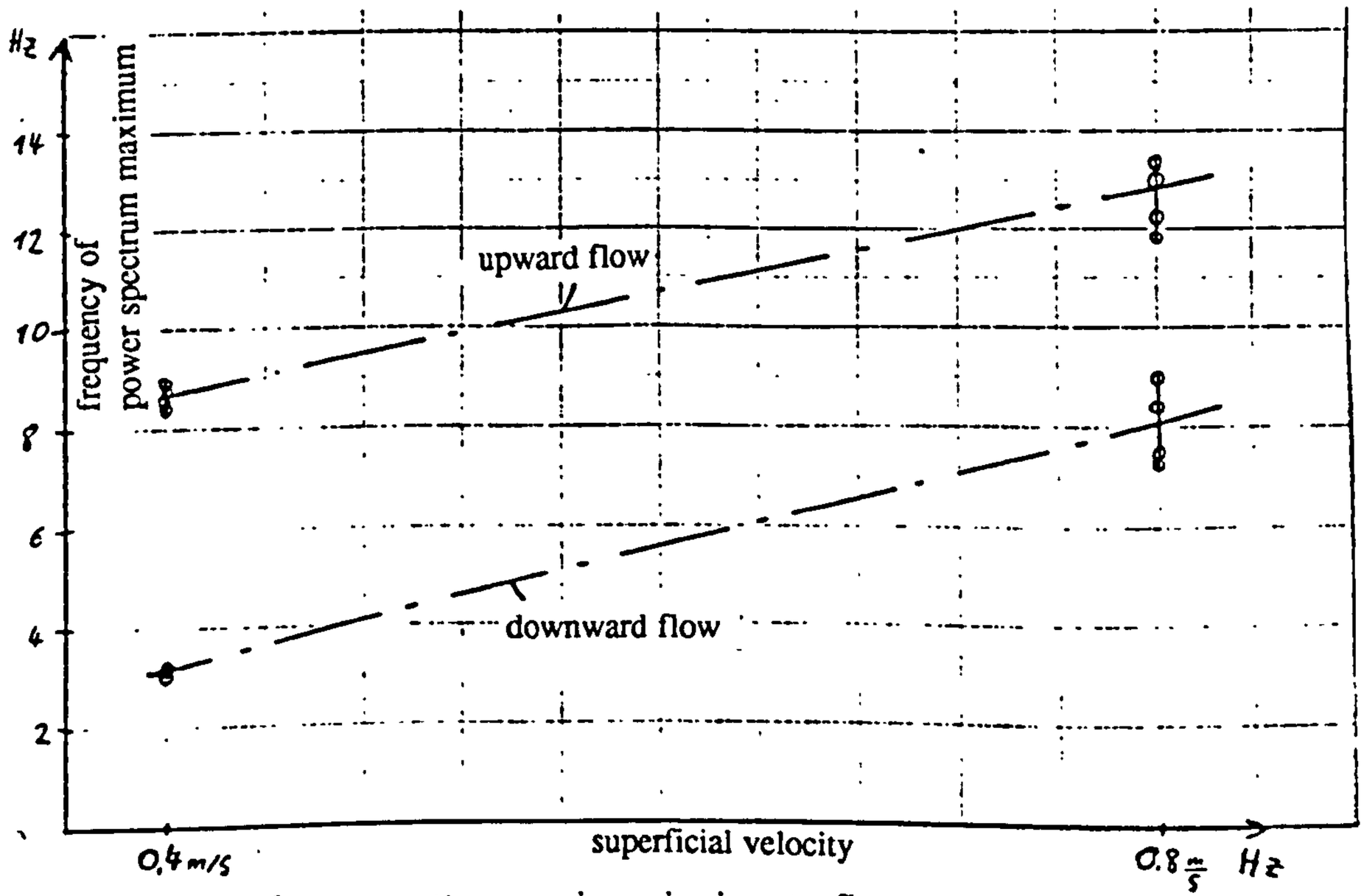

Fig.6.15 Frequency of power spectrum maximum in air-water flow

At the lower velocity, the readings are repeatable within 7%, at the higher velocity the results spread considerably more over a range of nearly 15%. At v=0.4m/s, the power spectrum has its maximum at 8.7Hz on the upward flow and at 3.1Hz on the downward flow. The difference is 5.6Hz, the average is 5.9Hz. A very rough comparison with **Fig.5.4** and **Fig.6.16** to **Fig.6.19** (Appendix B) shows the peak of the power spectrum at 6.9Hz for a ball velocity of 0.4m/s. The difficulty in comparing those two experiments is, that the ball were all passing the electrodes closely and hence generated a high frequency power spectrum whereas a large number of air bubbles move through the central part of the pipe and therefore they generate a lower frequency power spectrum. At the higher flow rate of 0.8m/s, the difference between the peak frequencies for upward and downward flow reduces from 5.6Hz to 4.5Hz. The average is at 10.3Hz. This can be roughly compared with **Fig.6.20,6.21** (Appendix C), where the neutral density balls were injected into a flow of v=0.75m/s and they generated a power spectrum with its maximum at 10Hz. Although the various experiments are sometimes difficult to compare with each other and with the theory, there is a consistency which leads to the conclusion that it is possible to determine the velocity of a nonconducting phase with an E.M.flowmeter. However, in order to obtain more accurate and repeatable readings, the mains driven flowmeter with point electrodes is not adequate. Therefore an improved meter is designed.

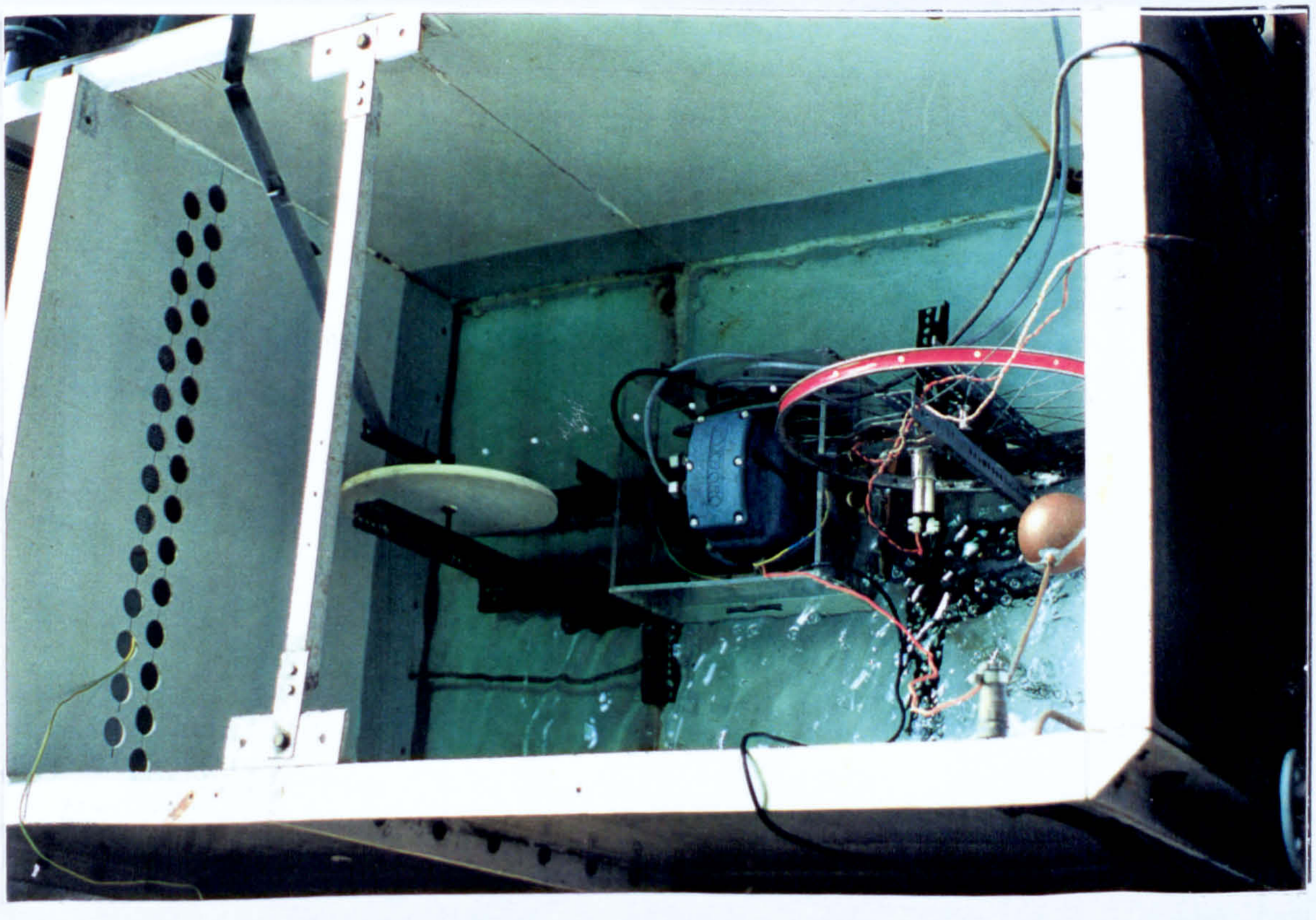

Chapter 7

7.1 Specifications for improved flow meter

Considering the results of both experiments and computational analysis, it is thought that an E.M.flowmeter can be developed which measures the velocity of the nonconducting phase as well as that of the continuous, conducting phase. The emphasis in the new design is on the transformer signal rather than on the flow signal. In order to measure the transformer signal more efficiently the following improvements are made:

- The magnetic field is operated at a higher frequency (300 Hz). This higher frequency will provide a stronger transformer signal which is not effected by aliasing problems up to a flow velocity of ca. 2m/s.
- The field is driven with a trapezoidal current wave form rather than with a sine wave. This will allow an easier separation of flow signal and transformer signal which are now separated in time rather than in phase (see illustration below).
- The electrodes are of a large, non-contacting type. The averaging effect of the large area electrodes providing a more uniform transformer signal over any cross section of the pipe and therefore a narrower frequency band in the power spectrum.

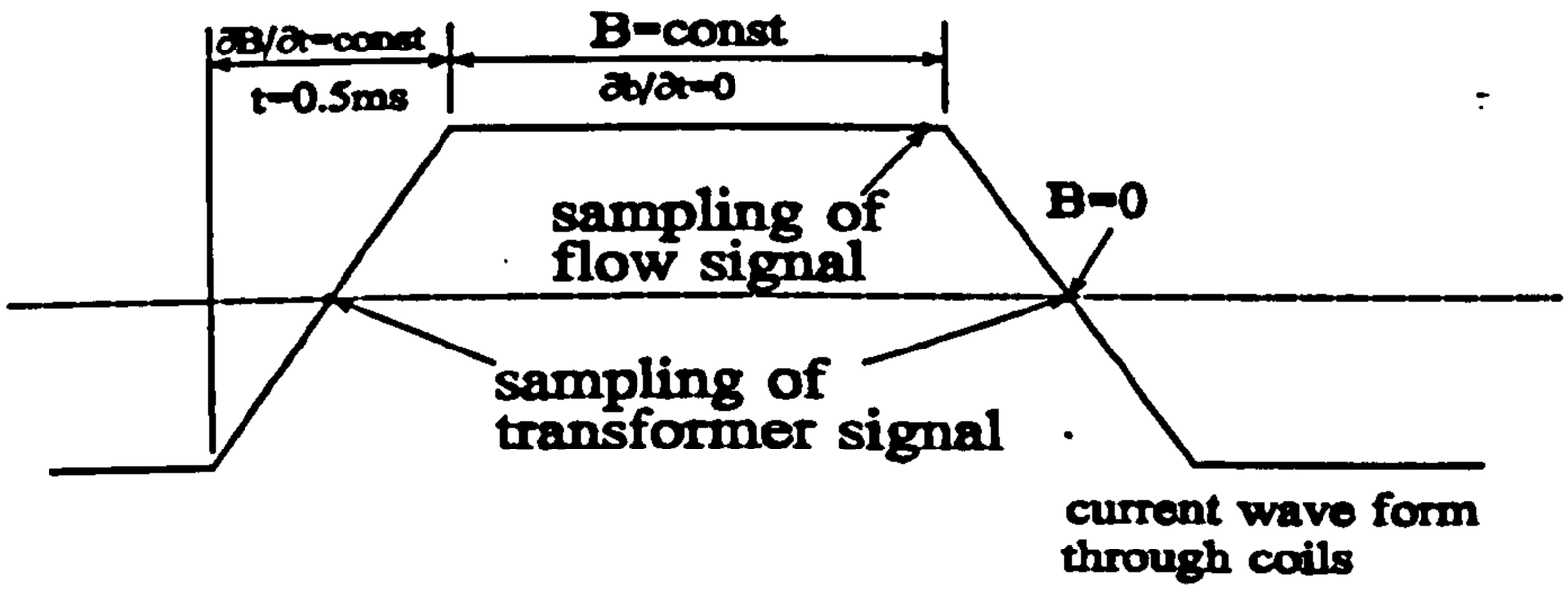

7.2 Estimation of Eddy Currents in large area electrodes

With large area electrodes in a quickly changing magnetic field, there is always the danger that eddy currents are generated, which themselves alter the magnetic field. A major factor is the thickness of the electrodes. In this design, they are assumed to be 0.1mm thick. For a 50mm diameter flowtube, the electrodes are approximated as shown in **Fig.7.1.**

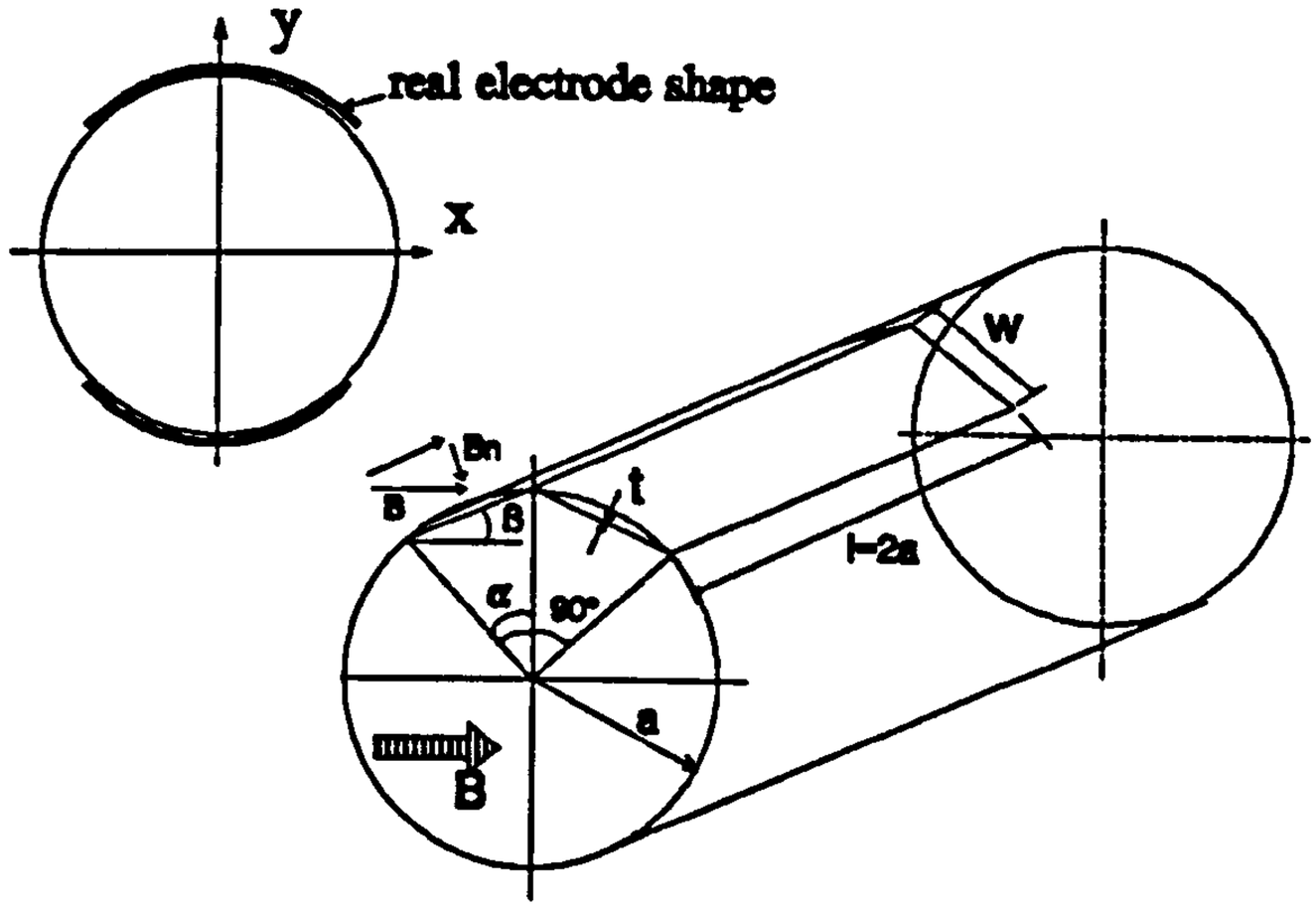

Fig.7.1 Approximate geometry of large area electrodes

The electrodes have an subtended angle of 90° at the tube axis and a length equal the diameter of the pipe.

Using Faraday's law, we choose a closed contour C around half of one electrode **(Fig.7.2):**

$$\oint_c E \cdot dl = -i\omega \int_s B \cdot dS$$

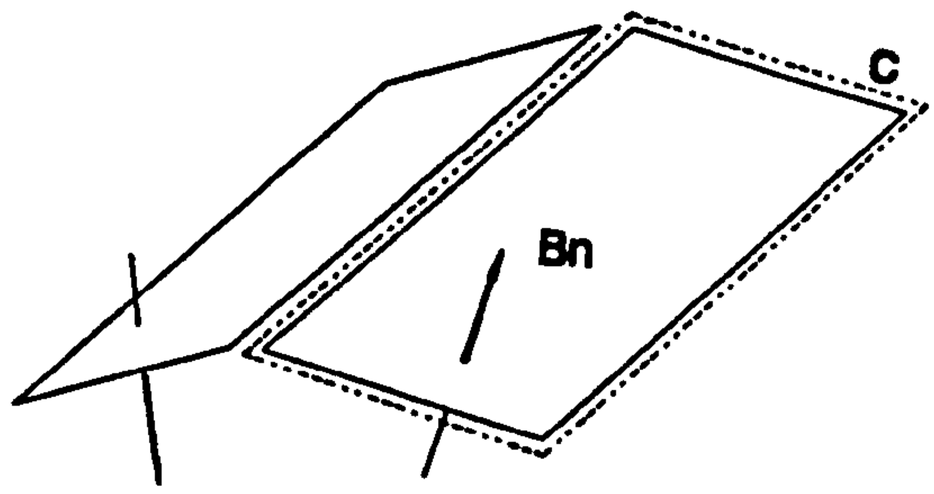

Fig.7.2a Integration boundary C of a half electrode

Now

$$\oint_c dl = 2(2a+w)$$
$$= 4a+2w$$

and

$$\int_s B \cdot dS = B_n w 2a$$
$$= B \sin\beta w 2a$$

$$\therefore \qquad E=-i\omega\frac{B\sin\beta w2a}{4a+2w}$$

from the proposed geometry, we have:

$$\beta=22.5°$$
$$\alpha=2\beta$$
$$a=25mm$$
$$w=2a\sin\frac{\alpha}{2}$$

$$\therefore \qquad E=-i\omega B\frac{4a^2(\sin22.5°)^2}{4a(1+\sin22.5°)}=-0.1059i\omega Ba$$

An eddy current I circulates in the electrode with $I=\sigma E\frac{w}{2}t$, where $\frac{w}{2}t$ =cross sectional area through which the current flows.
This eddy current I generates a secondary magnetic field B′. Let us consider the eddy currents to lie all at the top of the electrode, where the total current is 2I. Using Ampere's law:

$$\oint_{c'} B'\cdot dl=\mu_0 2I$$

Choosing a closed contour C′ of the dimension $w\times w$ **(Fig.7.2b)**, and assuming B′ is constant around it, we get

$$B'4w=\mu_0 2\sigma E\frac{w}{2}t$$

$$\therefore \qquad B'=\frac{0.1059}{4}\mu_0\sigma\omega Bat$$

The ratio of B′/B is then

$$\frac{B'}{B}=\frac{0.1059}{4}\mu_0\sigma\omega at$$

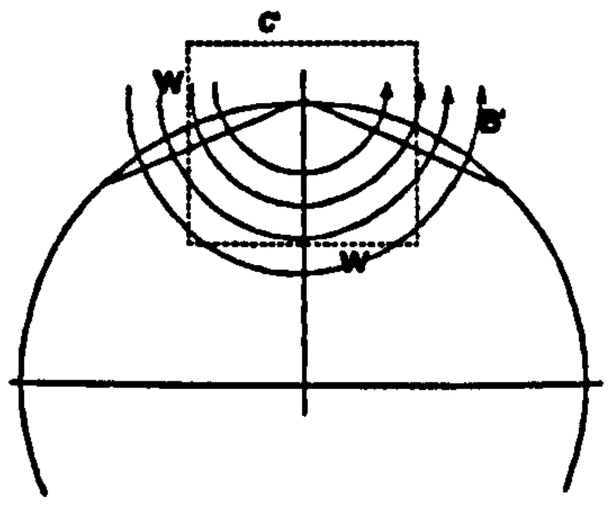

Fig.7.2b Integration boundary C′

Substituting some typical values into the equation above, we get:

$$\mu_0 = 4\pi E{-}7$$
$$\sigma = \frac{1}{1.6E{-}8} \quad (copper)$$
$$\omega = 300\,2\pi$$
$$t = 0.1E{-}3m$$
$$a = 0.025m$$

$$\therefore \qquad \frac{B'}{B} = 0.98\%$$

In the worst case therefore the eddy currents generate a secondary field of about 1% of the strength of the main field. This value can be tolerated, particularly as the undisturbed field cannot be predicted to more than a few percent accuracy anyway.

In the above estimation a sinusoidal magnetic field was used with $\dot{B} = -i\omega B$ whereas in the actual design a trapezoidal current wave form is used where $\dot{B} = const$. However as long as the maximum $\dot{B}$ is the same in both cases the approximation is still valid.

7.3 Current distribution for uniform magnetic field

In the computations of the transformer signal, a uniform magnetic field is assumed inside the flowtube. With the new flowmeter an attempt is therefore made to design the coils in such a way that a magnetic field as uniform as possible can be achieved with reasonable effort.
Firstly, the current distribution needed to produce a uniform field is calculated. After calculating the inductance of the coils, the boundary conditions are applied to give the final design.

Consider a tube of radius b and a z-directed current density $j(\theta)$ on its surface over a thickness t. The magnetic flux **B** has a potential F_i on the inside of the tube and F_o on its outside (**Fig.7.3**).

The equations governing this magnetic field are:

$$\underline{B}=\nabla F$$

$$\nabla^2 F=0$$

$$B_r\Big|_{r=b-}=B_r\Big|_{r=b+}$$

$$\left(H_\theta\Big|_{r=b+}-H_\theta\Big|_{r=b-}\right)b\,d\theta=j(\theta)\;t\;b\,d\theta$$

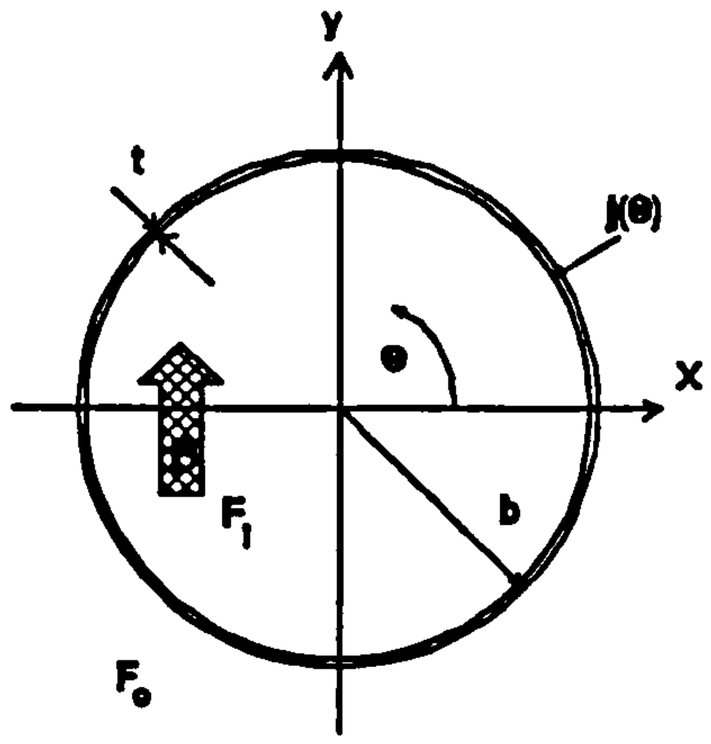

Fig.7.3 Current density distribution around pipe wall

therefore we have

$$\left.\begin{aligned}&\frac{\partial F_i}{\partial r}\Big|_{r=b-}=\frac{\partial F_0}{\partial r}\Big|_{r=b+}\\ &\textit{and}\\ &\frac{I}{\mu_0}\left(\frac{\partial F_0}{b\,\partial\theta}\Big|_{r=b+}-\frac{\partial F_i}{b\,\partial\theta}\Big|_{r=b-}\right)b\,d\theta=j(\theta)\;t\;b\,d\theta\end{aligned}\right\}\quad(7.1)$$

A solution for $\nabla^2 F=0$ is:

$$\left.\begin{aligned}F_0&=A\,\frac{1}{r}\sin\theta\\ F_i&=B\,r\sin\theta\\ j&=C\cos\theta\end{aligned}\right\}\quad(7.2)$$

From **eqn.7.1** and **eqn.7.2**, we get

$$B=-\frac{A}{b^2}$$

and

$$\frac{A}{b}-B\,b=\mu_0\,b\,t\,C$$

$$\therefore \qquad \frac{A}{b}+\frac{A}{b^2}\,b=\mu_0\,b\,t\,C$$

$$2A=\mu_0\,t\,b^2\,C$$

Because $B=B_y$ inside the tube,

$$\frac{\partial F_i}{\partial y}=B_y=B=-\frac{A}{b^2} \qquad (7.3)$$

$$\therefore \qquad B=-\frac{1}{2}\,\mu_0\,t\,C\ .$$

The total current on the surface of the tube in the region from $0 \leq \theta \leq \pi/2$ is

$$\int_0^{\frac{\pi}{2}} j(\theta)\,t\,b\,d\theta\ .$$

Substituting $j=C\cos\theta$ into the equation above yields.

$$C\,tb\int_0^{\frac{\pi}{2}}\cos\theta\,d\theta=C\,t\,b\,\sin\theta\Big|_0^{\frac{\pi}{2}}=C\,t\,b$$

Practically, this total current flows as the current I through N turns of wire. Instead of spreading the wires across the whole surface, they are bundled as coils. Again, for practicality, three coils are chosen, evenly distributed over the circumference (**Fig.7.4**). From **eqn.7.2**, we can determine the required ratio of numbers of turns of each coil. Through each coil with N_i turns flows the same current I, therefore

$$N_1:N_2:N_3=\int_{60^\circ}^{90^\circ}\cos\theta\,d\theta\ :\int_{30^\circ}^{60^\circ}\cos\theta\,d\theta\ :\int_{0^\circ}^{30^\circ}\cos\theta\,d\theta$$

$$=\sin\theta\Big|_{60^\circ}^{90^\circ}\ :\ \sin\theta\Big|_{30^\circ}^{60^\circ}\ :\ \sin\theta\Big|_{0^\circ}^{30^\circ} \qquad (7.4)$$

$$=0.134\ :\ 0.366\ :\ 0.5$$

$$=0.268\ :\ 0.732\ :\ 1$$

With two sets of coils opposite to each other, the total magnetic flux Φ is

$$\Phi=2(\Phi_1+\Phi_2+\Phi_3)$$

$$=2\sum B_i\,N_i\,2x_i\,l_i$$

But $\Phi=IL$ and B is constant inside the flowmeter, therefore we find for the total inductance L:

$$L=4\frac{B}{I}(N_1x_1l_1+N_2x_2l_2+N_3x_3l_3) \qquad (7.5)$$

The total current in one quadrant is given by

$$C\,t\,b=(N_1+N_2+N_3)\,I$$

Also, from **eqn.7.3**, we obtain

$$Ctb=2B\frac{b}{\mu_0}$$

$$\therefore \qquad \frac{B}{I}=\frac{\mu_0}{2b}(N_1+N_2+N_3) \qquad (7.6)$$

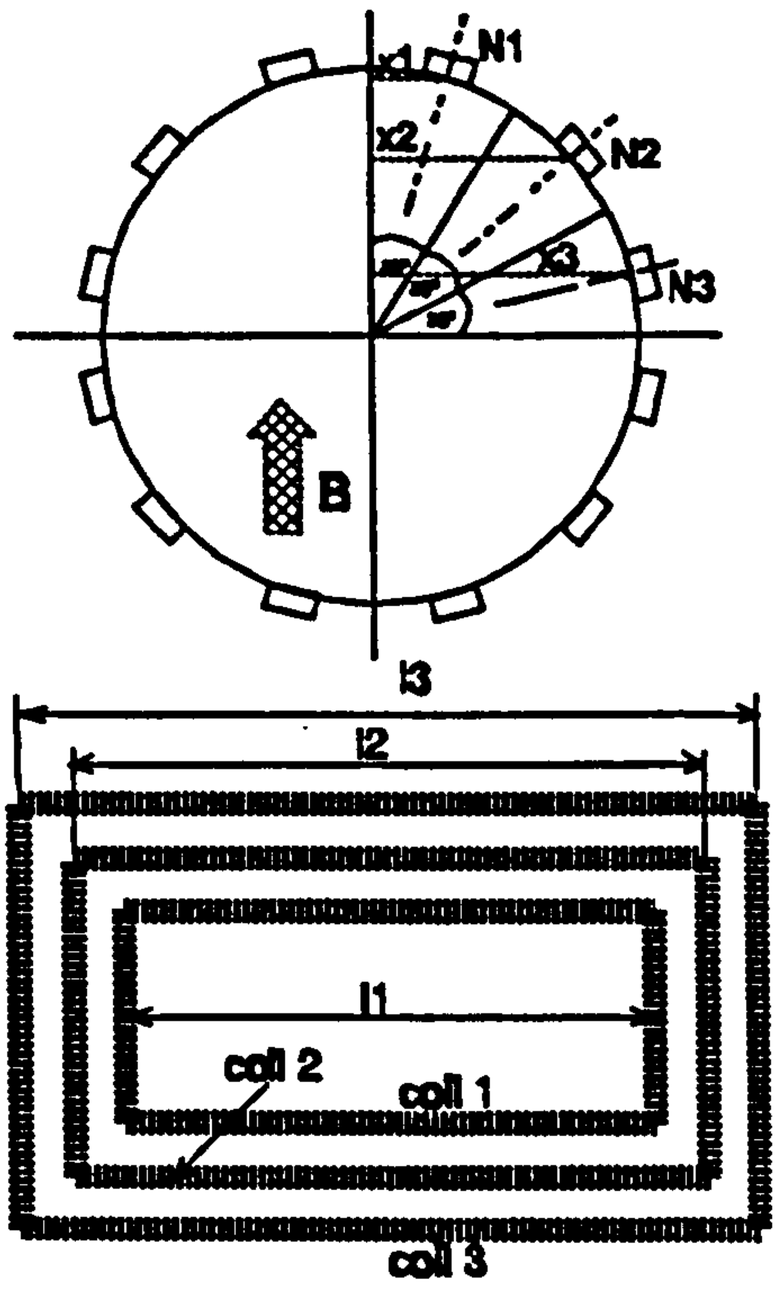

Fig.7.4 Distribution of coils on meter body

The expression above is then substituted into **eqn.7.5** to obtain the final expression for the inductance:

$$L=2\frac{\mu_0}{b}(N_1+N_2+N_3)(N_1x_1l_1+N_2x_2l_2+N_3x_3l_3) \qquad (7.7)$$

Having obtained an expression for the inductance of the set of coils, their physical dimensions can be determined. Hereby, the following constraints are considered:

- the coils are driven by a trapezoidal voltage containing Fourier components up to 300Hz frequency. The ramp up and -down time is 0.5ms.
  The previously tested flowmeter with point electrodes was sufficiently sensitive to the change in transformer signal. It is therefore reasonable to assume that the new flowmeter can be operated with a similar rate of $\frac{\partial B}{\partial t}$. The magnetic field strength perpendicular to the electrodes is measured with a search coil with N=100 turns and a diameter d=25mm. With that coil, a peak value of 0.5V is measured in the centre of the pipe.

  With $V=N\frac{\partial \Phi}{\partial t}=N\frac{\partial B}{\partial t}\pi\frac{d^2}{4}=N\pi\frac{d^2}{4}B_{max}\omega\cos(\omega t)$, we can determine B_{max} and $\frac{\partial B}{\partial t}$. Thus Bmax=324Gauss and $\left(\frac{\partial B}{\partial t}\right)_{max}=10.2\frac{V}{m^2}$.

  For a rise time of 0.5ms we therefore need a maximum field strength $B=10.2*0.25*10^{-3}=25.5$ Gauss. The design requires a magnetic shielding which itself increases the field strength in the pipe. Therefore the coils are designed to generate a field of 20 Gauss.
- due to the short rise and fall time of the B-field, the time constant of the coils has to be no more than τ=0.1ms.
- the maximum current to drive the coils is limited to I=2A because of equipment available.
- in order to avoid overheating of the coils, the current is also limited to $I/(\pi\frac{d^2}{4})=6A/mm^2$. At this value, the coils reach a steady state temperature of ca 30°C.
- the coils have to be long enough to provide a uniform field over the length of the electrodes. They also have to be as short as possible in order to minimise the inductance and therefore their time constant.
  The computations have shown that an electrode length of 1 pipe diameter gives an almost flat plane in which the transformer signal becomes a maximum. Although the signal strength decreases slightly with increasing electrode length, a signal of the order of 1mV is considered to be large enough. Therefore the electrodes are chosen to be 50mm long. For a relatively uniform magnetic field in the area of the electrodes, the coils are chosen to be 2 diameters long.

The half widths of the coils are according to **Fig.7.4**

$x_1=\cos 75° \; b$
$x_2=\cos 45° \; b$
$x_3=\cos 15° \; b$

The lengths of the coils are chosen as

$l_1=90mm$
$l_2=95mm$
$l_3=100mm$

Substituting the geometric values above into **eqn.7.7** gives

$$L=2\frac{\mu_0}{b}(0.2679N_3+0.73205N_3+N_3)(0.2679N_3\cos 75° \; b0.090 + 0.73205N_3\cos 45° \; b0.095+N_3\cos 15° \; b0.100)$$

$$\therefore \quad L=4\,\mu_0 N_3^2 0.152009 \quad ; \; \mu_0=4\pi 10^{-7} \tag{7.8}$$

also from **eqn.7.5** we have

$$L=4\frac{B}{I}(0.2679N_3\cos 75° b0.09+0.73205\cos 45° \; b0.095+N_3\cos 15° \; b0.100)$$

$$\therefore \quad L=4\frac{B}{I}N_3 \; b0.152009 \tag{7.9}$$

The resistance R_c of all six coils in series can be calculated as

$$\left.\begin{aligned} R_c&=2(R_1 N_1+R_2 N_2+R_3 N_3) \\ &\textit{with} \\ R_1&=2(l_1+\tfrac{\pi b\, 30°}{180})\tfrac{\rho}{\pi\frac{d^2}{4}} \\ R_2&=2(l_2+\tfrac{\pi b\, 90°}{180})\tfrac{\rho}{\pi\frac{d^2}{4}} \\ R_3&=2(l_3+\tfrac{\pi b\, 150°}{180})\tfrac{\rho}{\pi\frac{d^2}{4}} \end{aligned}\right\} \tag{7.10}$$

Here, d is the wire diameter and ρ is the resistivity of copper; ρ=1.6E-8Ωm. The radius b to the coils is chosen to be 35mm. This allows for a sufficient wall thickness of 10mm to cater for all structural problems.

$$R_c=\frac{16\rho}{\pi d^2}N_3 \cdot 0.33044161$$

$$\therefore \quad R_c = 2.693E{-}8 \; \frac{N_3}{d^2} \tag{7.11}$$

The time constant τ of the coils is $\tau=L/R_c$. Therefore, for any configuration of the coils, τ can be expressed as

$$\tau=\frac{4b\cdot 0.152009\ \frac{B}{I}N_3}{2.693E-8\ \frac{N_3}{d^2}}$$

$$\therefore \qquad \tau=790244\ \frac{Bd^2}{I}$$

The current limit for a given wire diameter is $6A/mm^2$ and the required strength is B=20E-4T.

$$\therefore \qquad \frac{I}{d^2}=6\frac{\pi}{4}\ A/mm^2=4.712\ A/mm^2$$

$$\therefore \qquad \tau=\frac{790244}{4.712E6}\ 20E-4=0.335\ ms$$

The time constant is therefore longer than the required 0.1 ms. One way to overcome this problem is, to add a ballast resistor in series with the coils. Even though this is not efficient, it is acceptable for an experimental flow meter.
In order to determine the value of this resistor, it is necessary to introduce another constraint. With regard to the available power supply, the maximum voltage drop across the coil and resistor is chosen to be $V_{max}=25V$.
The total resistance is now the resistance of the coils R_c plus the ballast resistance R_b.
In a new approach, the number of turns N_3 are calculated, which are necessary for a field strength of 20 Gauss. From **eqn.7.4** and **eqn.7.6** we have

$$B=\frac{\mu_0}{2b}2\ N_3\ I$$

$$\therefore \qquad N_3=\frac{bB}{\mu_0 I}$$

After substituting the limits for B and I into the equation above, we obtain

$$N_3=\frac{0.035\cdot 20E-4}{4\pi E-7\cdot 2}=27.9\sim 28$$

Using **eqn.7.9**, the inductance of the coils is then

$$L=4\cdot 4\pi E-7\cdot 28^2\cdot 0.152009=0.599\ mH$$

From the maximum current of 6A/mm², the minimum wire diameter d can be calculated. It is:

$$\frac{I}{\pi\frac{d^2}{4}}=6$$

$$\therefore \qquad d=\sqrt{\frac{4\cdot 2}{\pi\cdot 6}} = 0.651\ mm$$

A copper wire of 0.65mm is not available, so the next larger size is chosen with d=0.71mm. The resistance of the coils then can be calculated according to **eqn.7.11:**

$$R_c = 2.693E{-}8\ \frac{28}{(0.71E{-}3)^2}=1.50\ \Omega \qquad \textbf{(7.12)}$$

The value for the ballast resistor R_b is obtained from

$$\tau=\frac{L}{R_c+R_b}$$

$$\therefore \qquad R_b=\frac{L}{\tau}-R_c$$

$$R_b=\frac{0.599E{-}3}{0.1E{-}3}-1.5 = 4.50\Omega$$

Now the voltage can be checked, which has to be applied to the system of coils and resistor:

$$V=(R_c+R_b)I=(1.5+4.5)2=12V$$

A voltage of 12V at 2A current is well within the limits. If a shorter time constant becomes necessary at a later stage, then there is still some margin left. **Fig.7.5** to **Fig.7.8** show graphs which can be used to select another combination of ballast resistor, maximum current and maximum voltage.

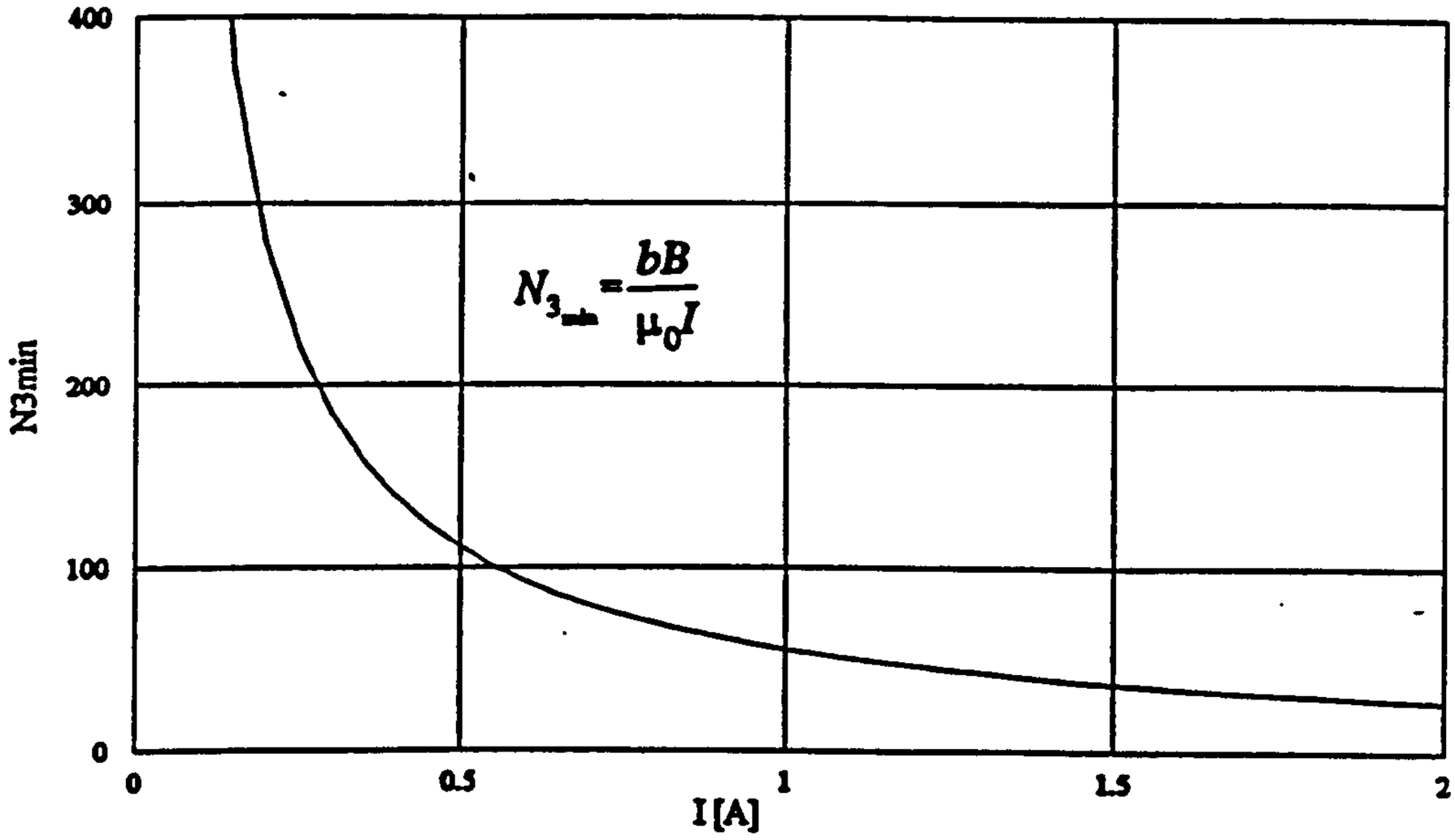

Fig.7.5 Minimum number of turns for B=20 Gauss

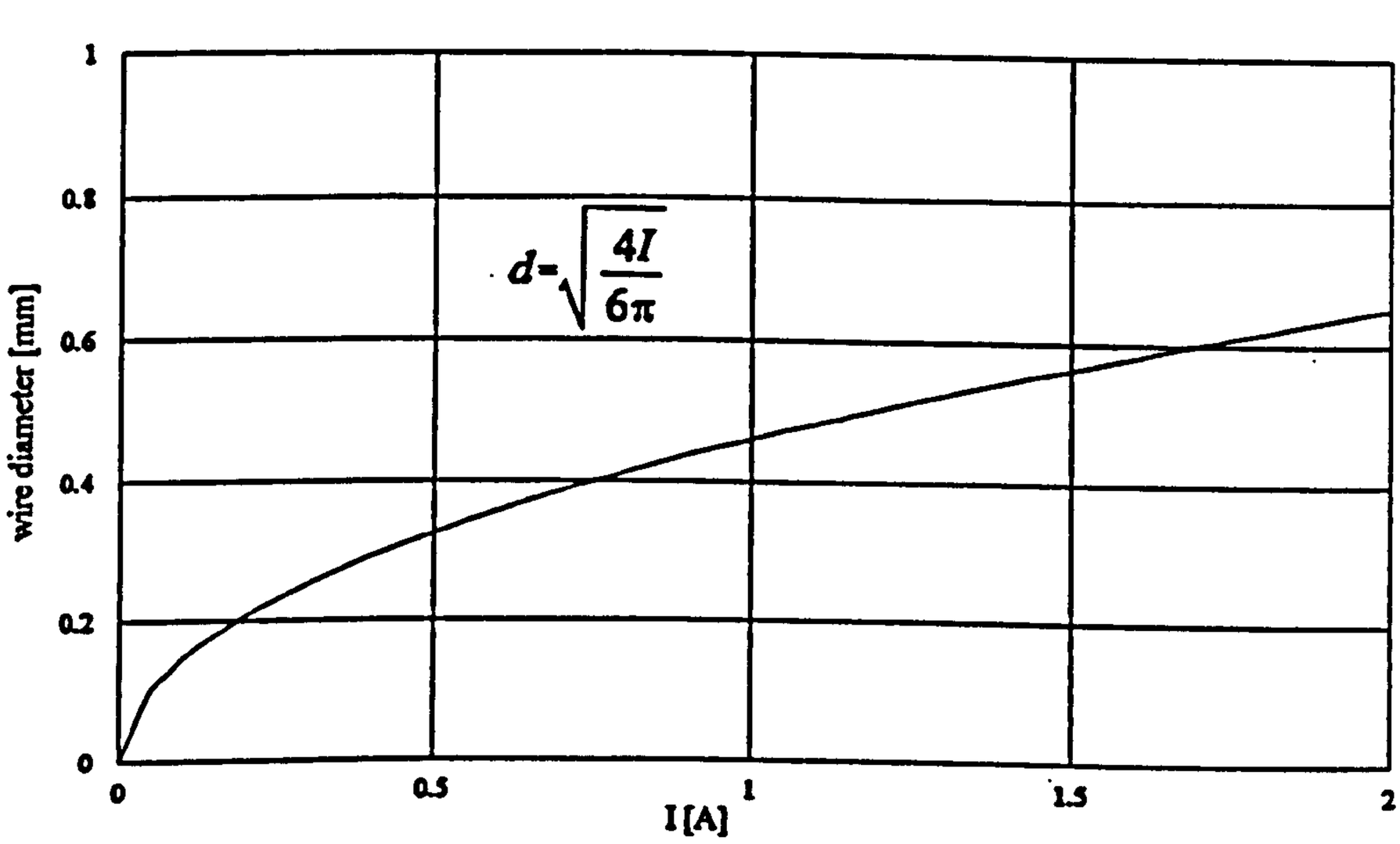

Fig.7.6 Minimum wire diameter at I/a=6A/mm²

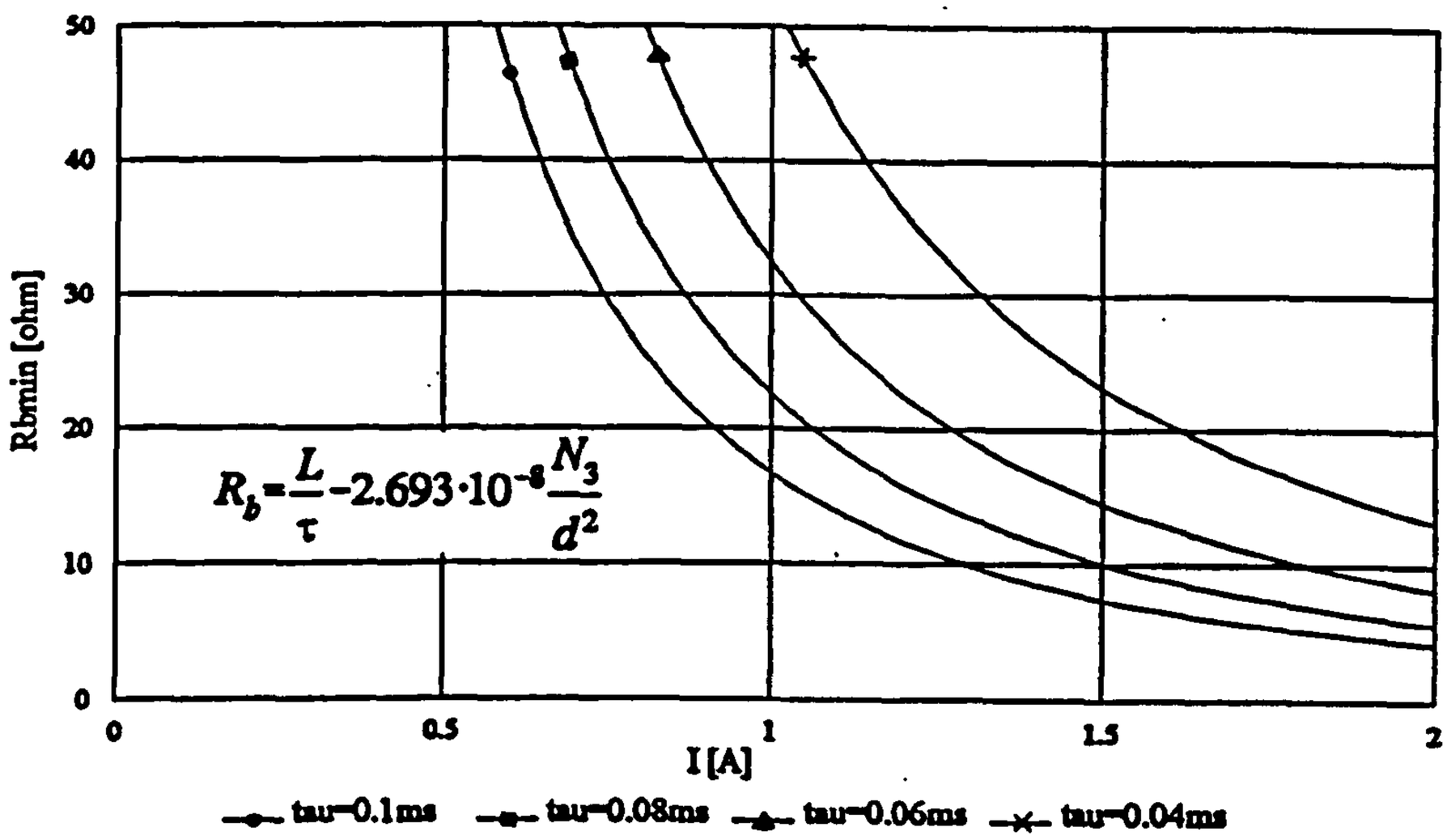

Fig.7.7 Minimum ballast resistor required for various time constants

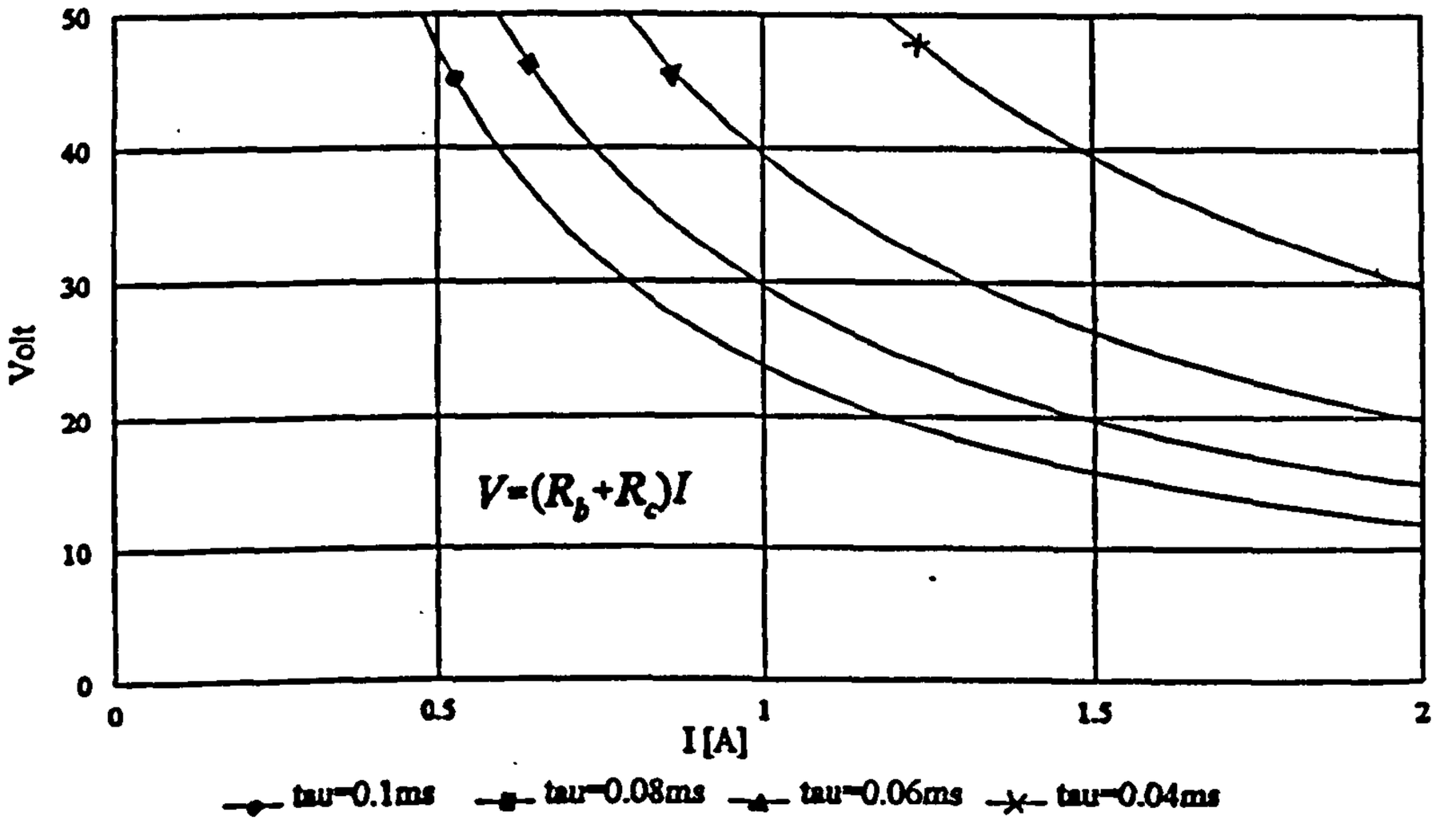

Fig.7.8 Required voltage to drive coils in steady state for various time constants

7.4 Measurement of the magnetic field

Having determined the design parameters of the coils, they are now built. The coils are wound on plywood formers. The number of turns is rounded up, so that

N_3=28
N_2=21
N_1=8

The wire diameter d is 0.71mm.

After winding the coils, they are shaped and attached to a thin walled plastic tube (see picture below). The assembly is then wrapped in one layer of 0.1mm Permalloy. The tube itself is mounted on a graduated brass traverse. A Hall probe is mounted on a vertical brass rack which can be traversed via a pinion . The coils are then powered with a stabilized power supply at a current of just over 2A. After 20 min warming up, the temperature of the coils is stabilized and the current is held constant at 2045mA. The magnetic field is then mapped in 5 horizontal planes at z= -2"; -1.2"; -0.4"; 0" and 0.4".

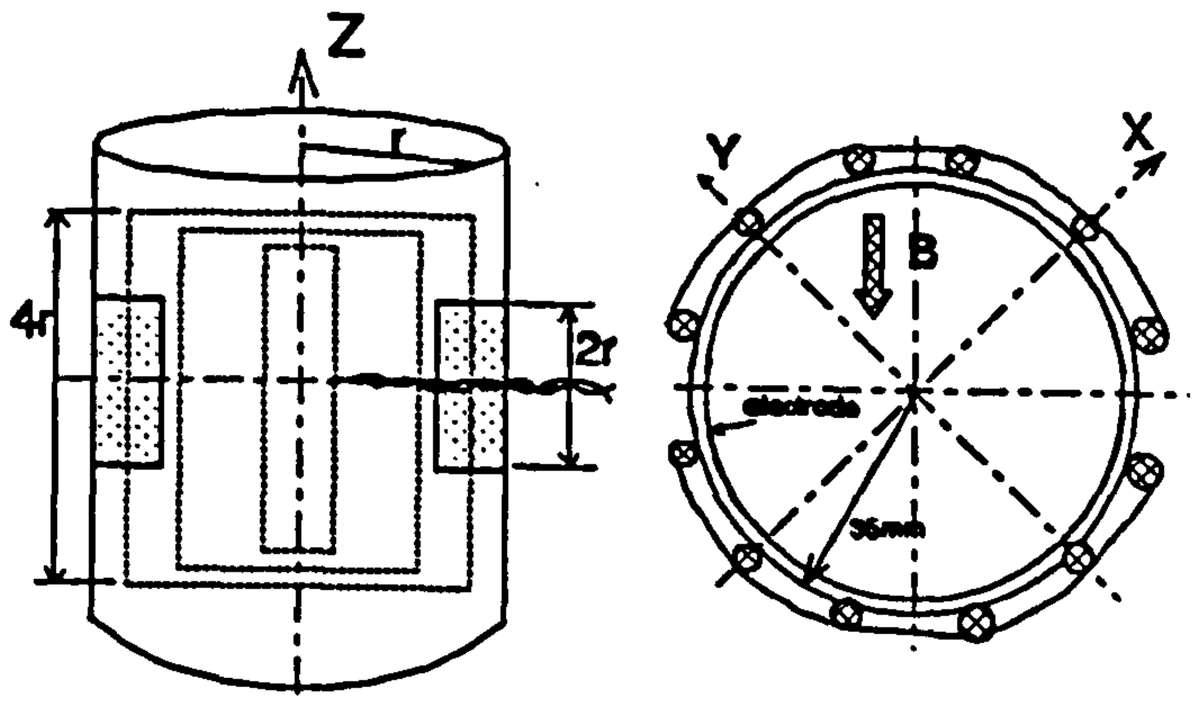

In **Fig.7.9** to **Fig.7.13**, the strength of B-field in the shielded tube is plotted for each plane. At the end of the coils, the field is less than 50% of its maximum value but is still quite uniform with a variation of only 10%.
At z =-1.2", the field has already increased to 94% of the maximum and it varies 18% across the plane. At z=-0.4" the field has reached its full strength of ca.31 Gauss. The variation of the field is only 11%. Towards the middle of the coils the field retains its strength and uniformity. The maximum field strength is 31.5 Gauss. In any plane, the maximum strength is near the smallest coils.
After the mapping of the 5 planes, the field strength is measured perpendicular to the coils. Ideally, this field component is zero. However, a small component of B is measured in that direction. In the centre of the pipe it is a fraction of a Gauss, towards the end of the coils and along the sides of the largest coils it reaches about 2 Gauss. This had to be expected because the three coils per side only approximate a uniform field.
With an average error of about 10%, the field is considered to be uniform enough for the following experiments. A more uniform field could have been achieved but it would have been much more time consuming. For completeness, two more parameters of the coils are measured, its resistance and inductance. The measured values are:

R_c=1.7Ω
L=1.27mH

The inductance here is twice as high as the calculated value. This is mainly due to the iron shield.
In addition to the measurements above, the magnetic field is checked at a few points without a shield. Here, as predicted, the maximum field strength is 20 Gauss. The percentage error is again about 10%. The inductance is 0.83mH±10%. One reason for this error is that the coils come out slightly larger than the calculated sizes. The outermost turns of the larger coils for example span an area which is 15% larger than assumed than that calculated. Also, the number of turns was rounded up.
As a result of this higher inductance, the required voltage rises. But even an increase by a factor of 2, as measured with the shielded pipe, is no problem for the power supply.
A measurement of the magnetic field after the tube has been shielded with a second layer of Permalloy shows only a further increase of 4.5% compared with the single layer field strength.
The required drive voltage for different inductances and a time constant of 0.1ms is shown in **Fig.7.14** .

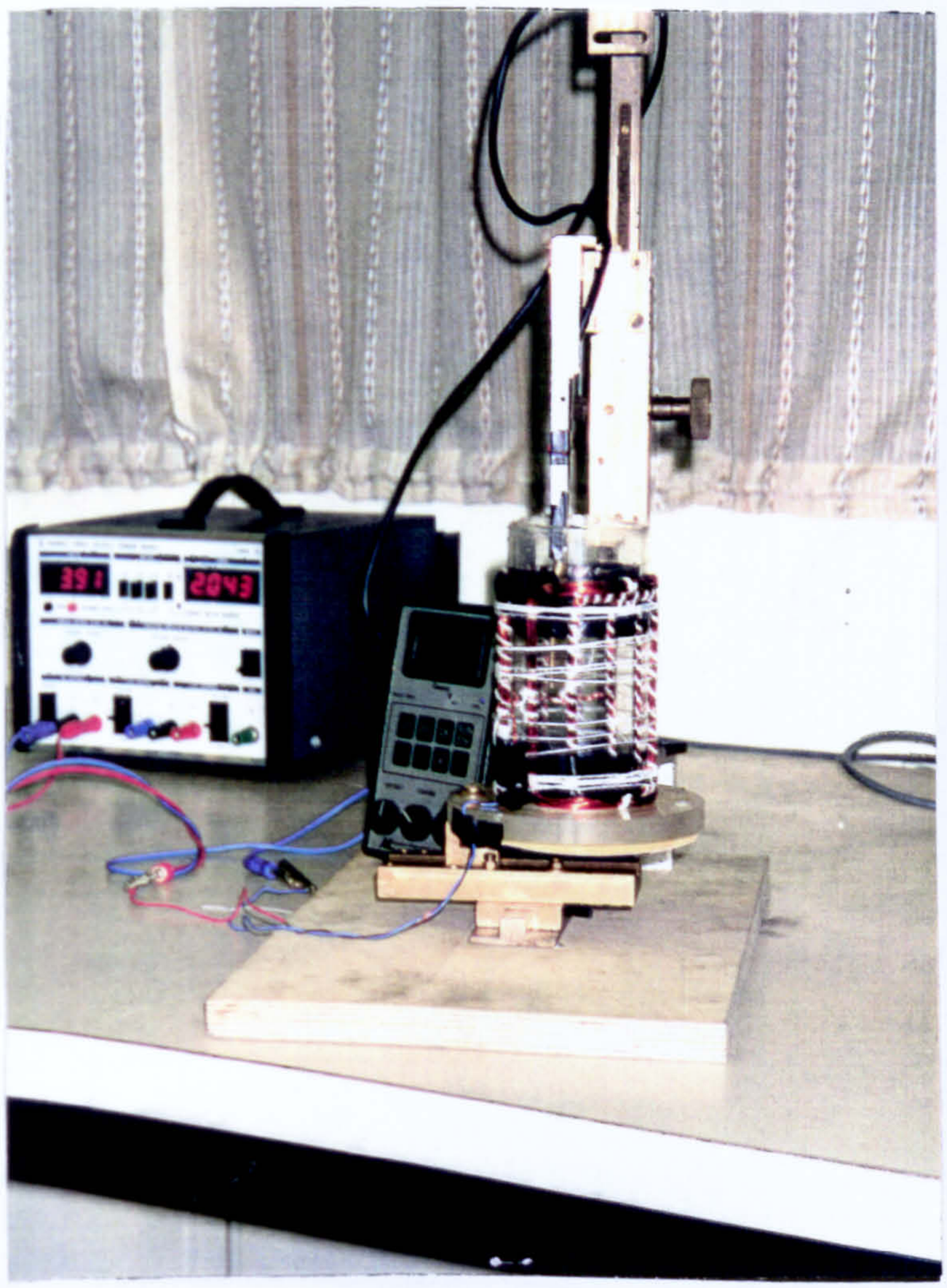

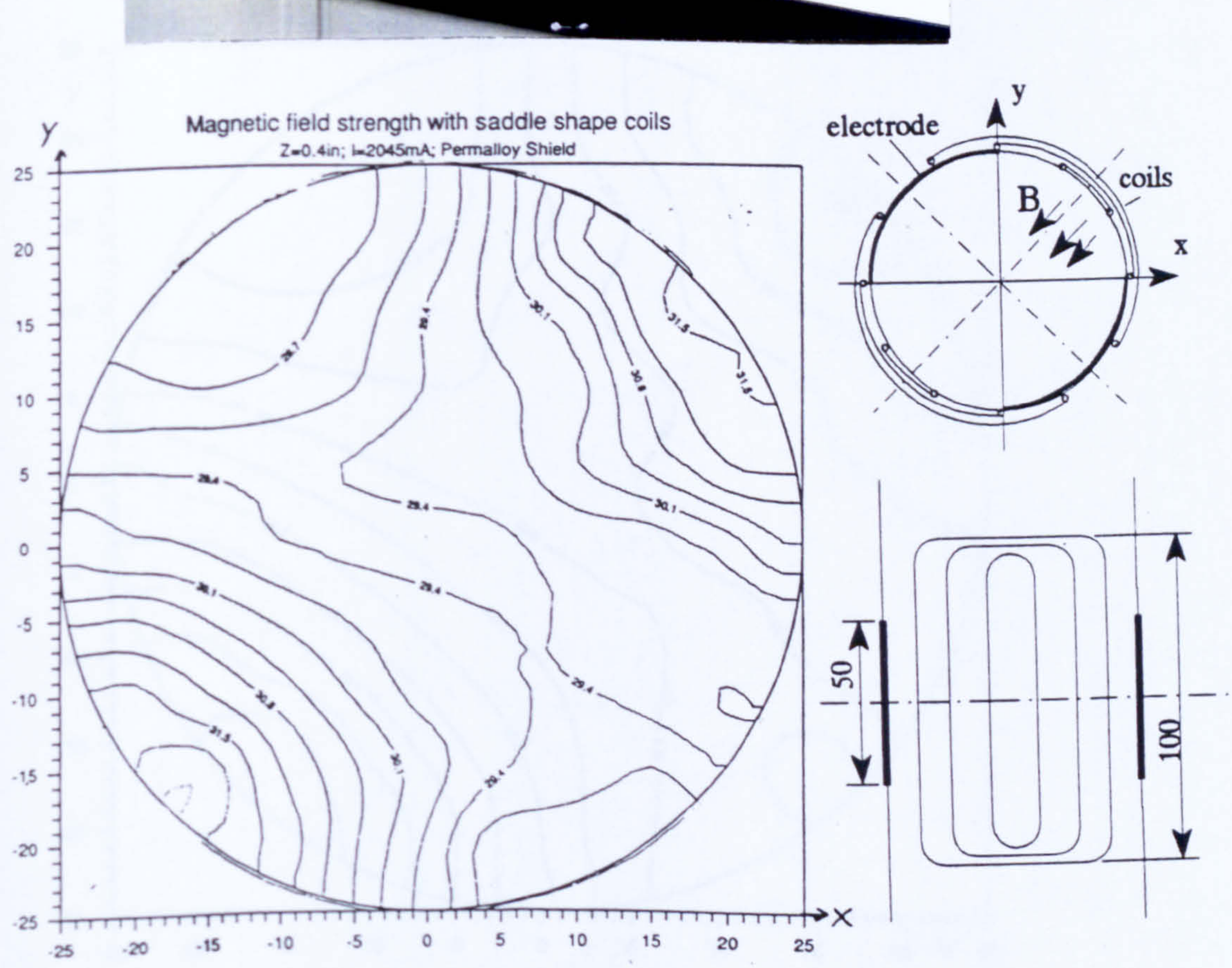

Fig.7.9 Measured magnetic field strength with 3 pairs of nested coils, z=0.4"

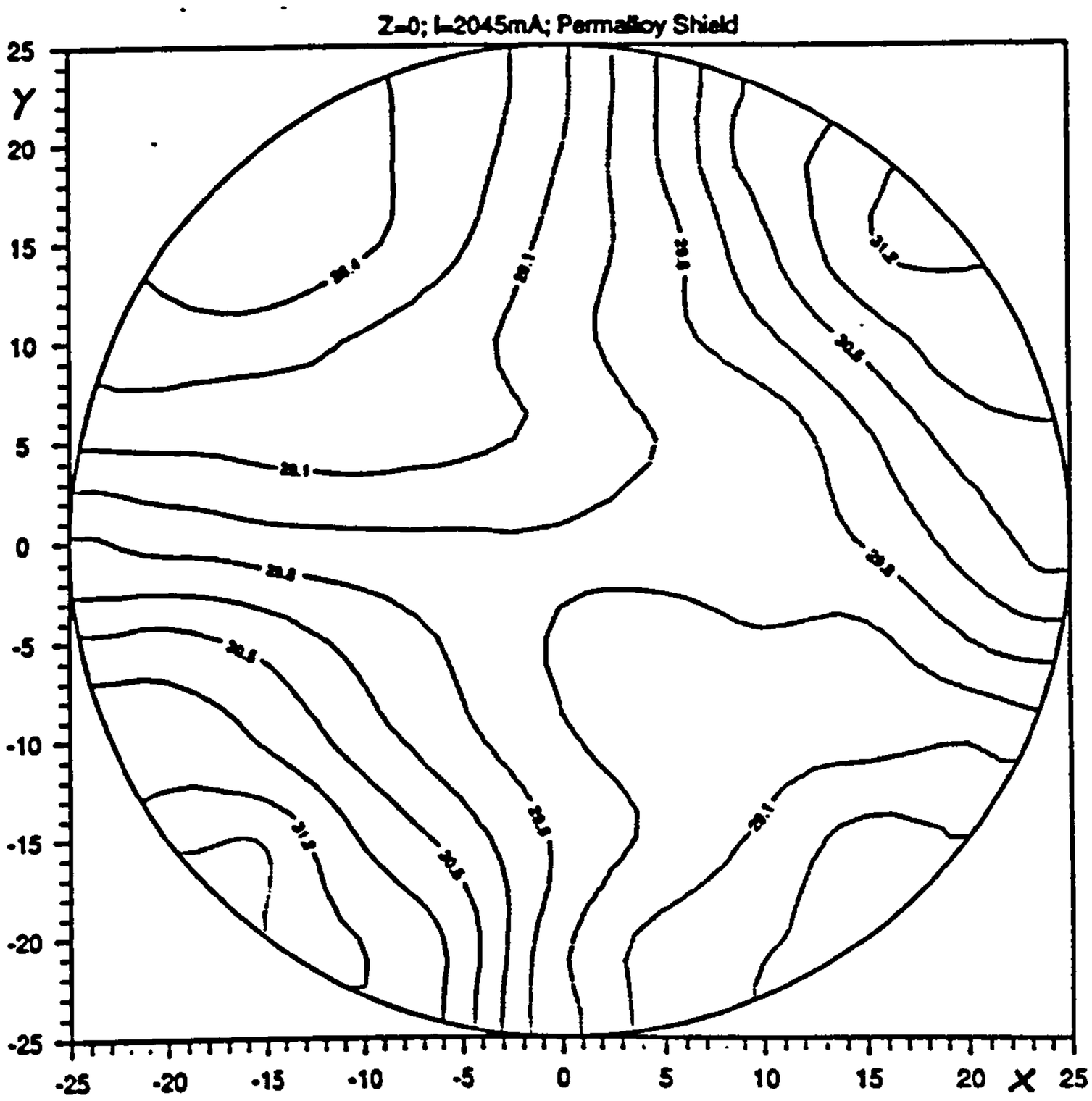

Fig.7.10 Measured magnetic field strength with 3 pairs of nested coils, z=0

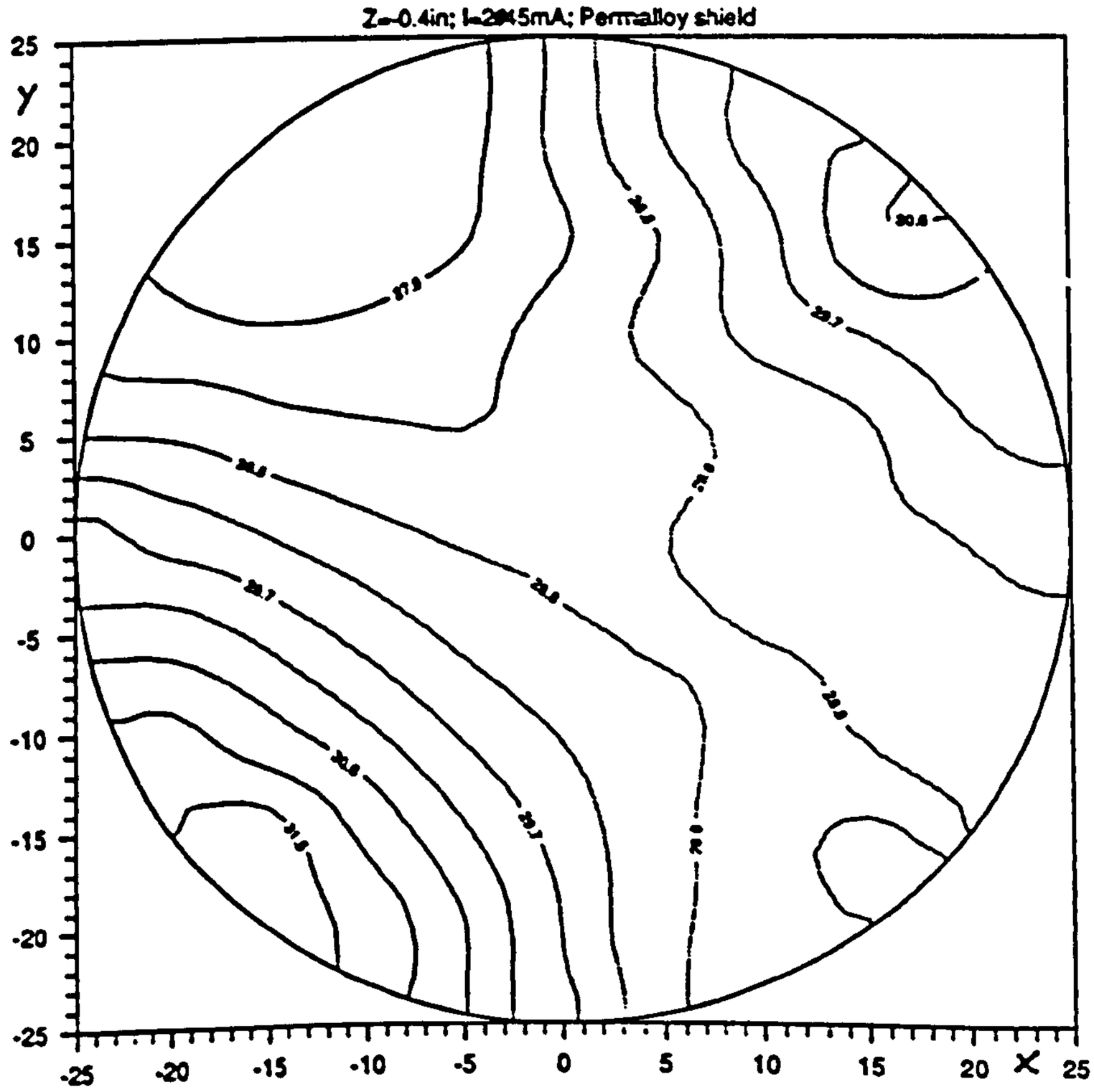

Fig.7.11 Measured magnetic field strength with 3 pairs of nested coils, z=-0.4"

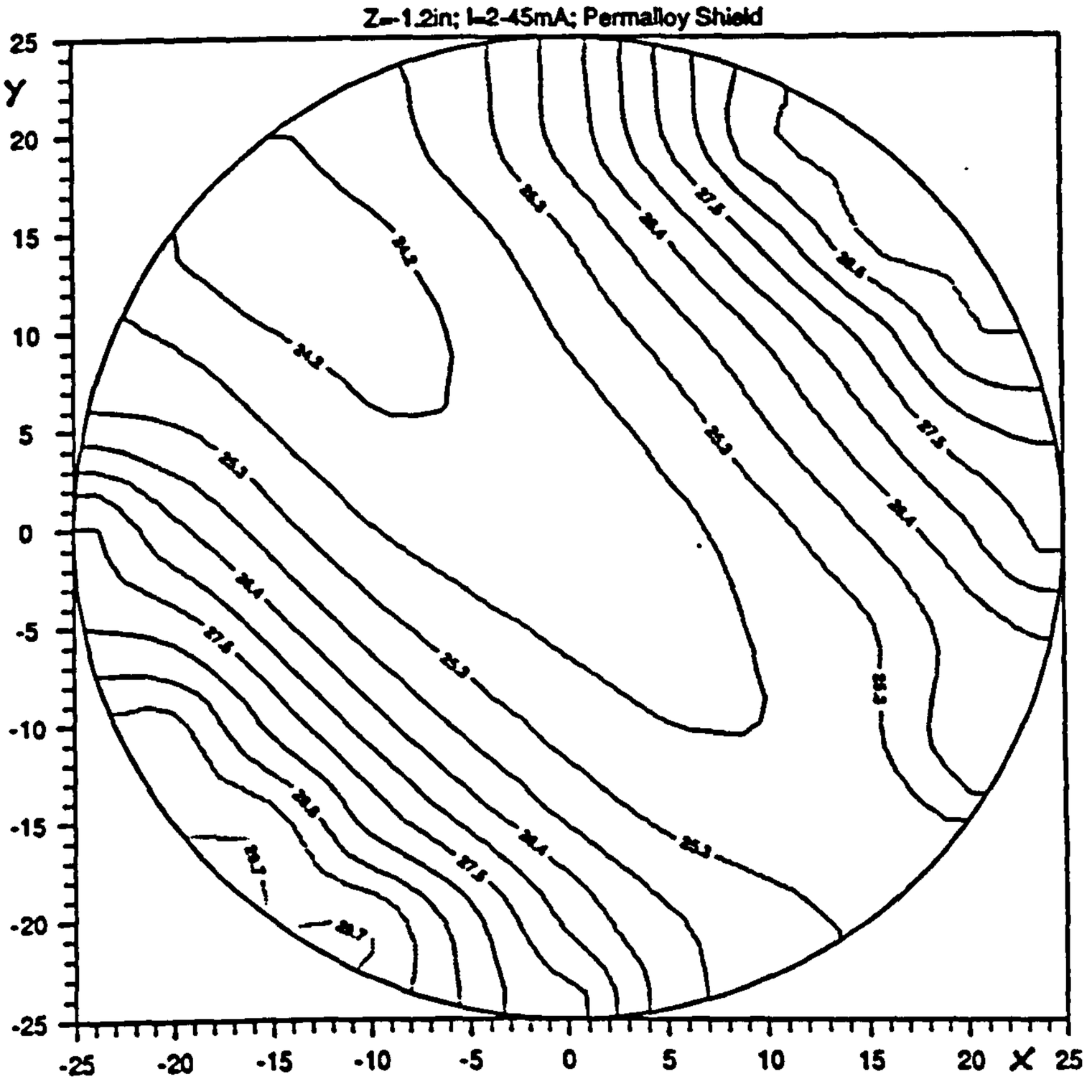

Fig.7.12 Measured magnetic field strength with 3 pairs of nested coils, z=-1.2"

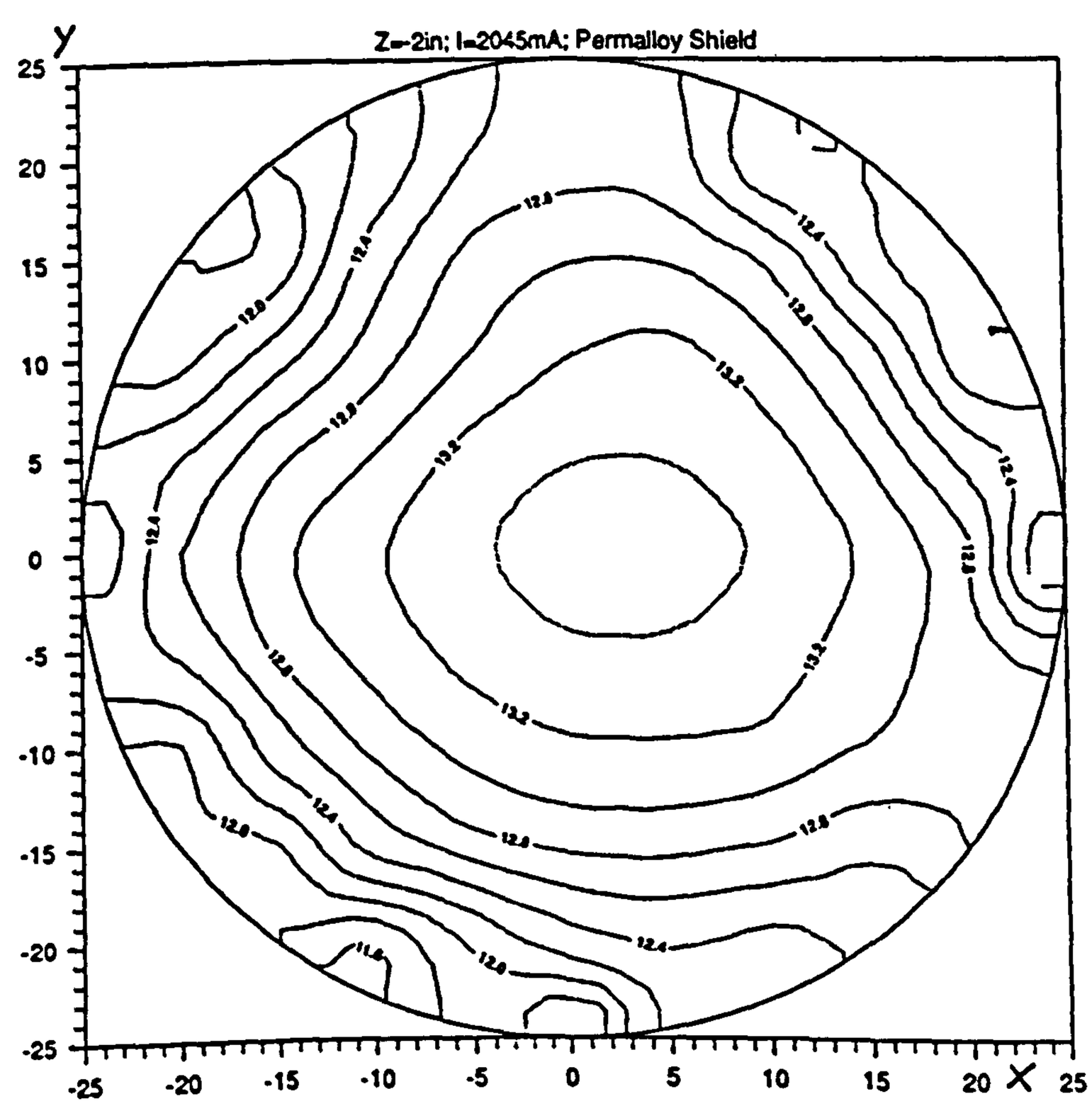

Fig.7.13 Measured magnetic field strength with 3 pairs of nested coils, z=-2"

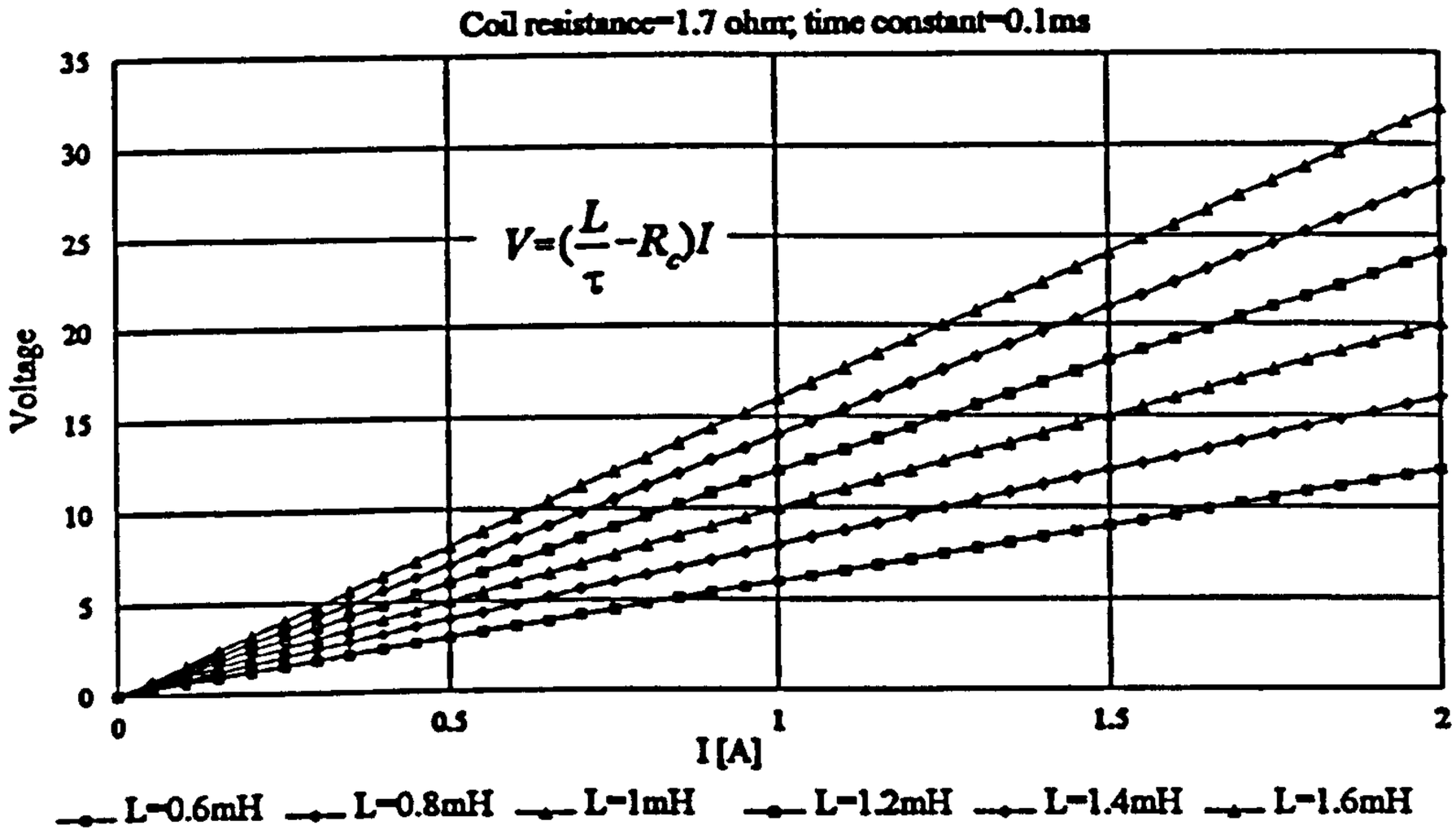

Fig.7.14 Required voltage to drive coils in steady state (τ=0.1ms)

Chapter 8

Experiments with improved flowmeter

8.1 Amplitude of transformer signal for a single sphere in a flowmeter with large area electrodes

In chapter **4.2.3**, the transformer signal is computed for a single insulating sphere in a flowmeter with large area electrodes. The prediction is that in a flowtube of 50mm diameter and area electrodes of 50mm length the distance between the maximum and the minimum transformer signal is almost constant throughout the pipe cross section (**Fig.4.23, 4.24**). In order to verify the results, an experiment is set up

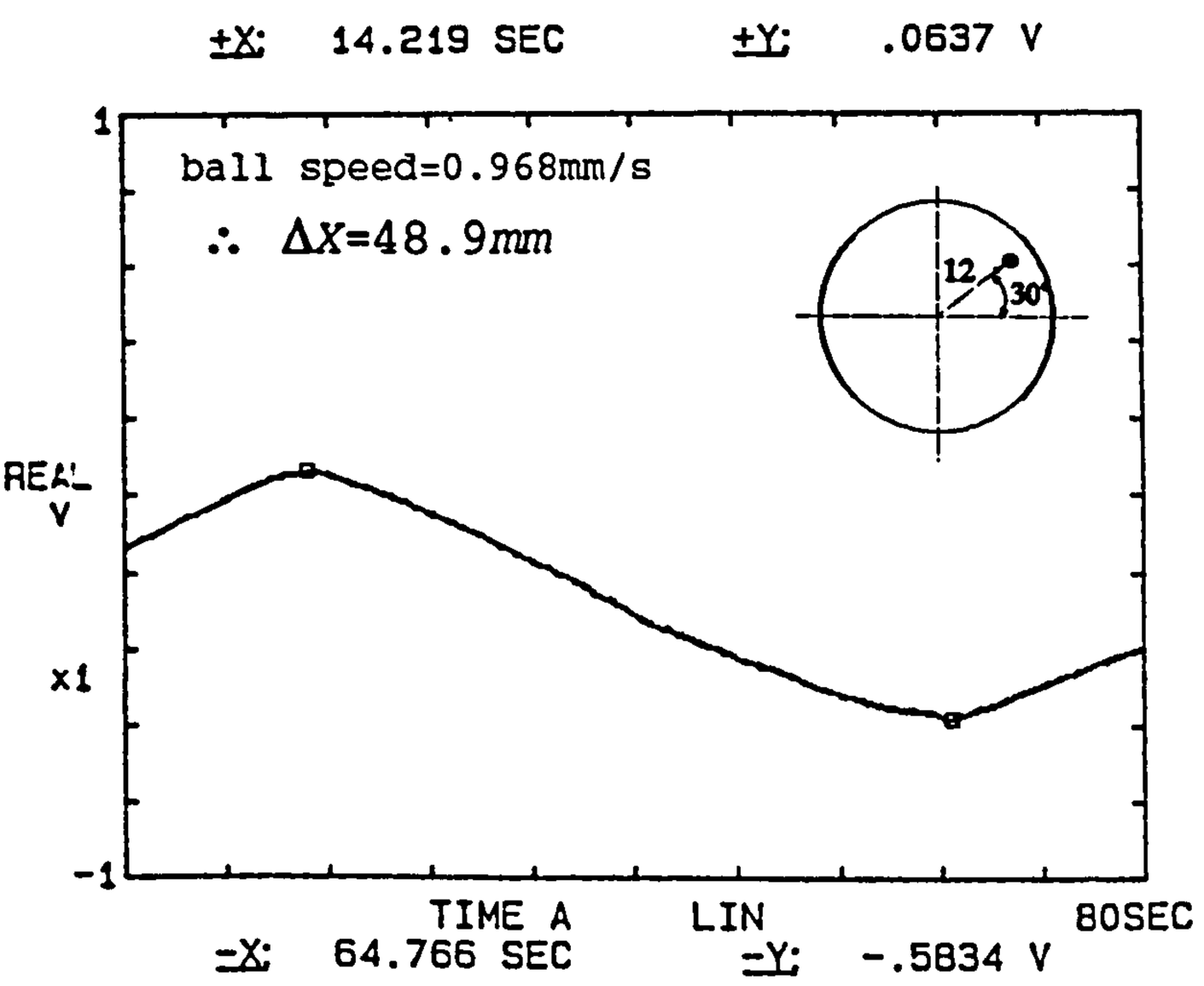

Fig 8.1 Amplitude of transformer signal due to a single plastic ball

which is similar to those shown in **Fig.4.11** and **Fig.4.13**.

A plastic ball is moved at a constant very slow speed on a path parallel to the pipe axis and the transformer signal is recorded. **Fig.8.1** and **Fig.8.2** show the amplitude of the transformer signal as a function of z. The speed of the ball is only about 1mm/s and the motion can therefore be regarded as quasi static. The distance between the peaks of the transformer signal is

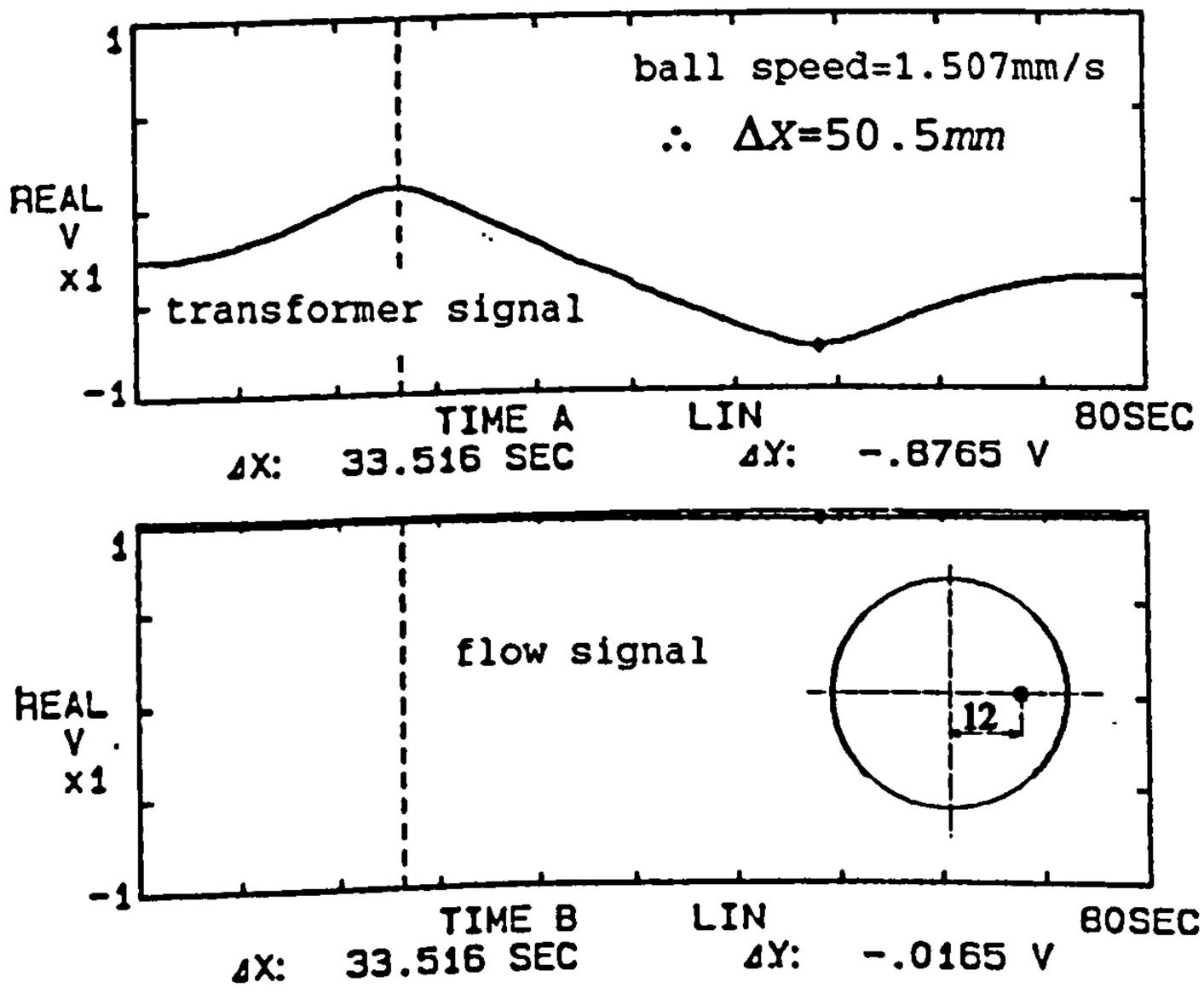

Fig.8.2 Transformer signal due to a single plastic ball as a function of z

49mm and 50.5 mm respectively. This matches the predicted 50mm very closely. In **Fig.8.2** the flowsignal is recorded simultaneously with the transformer signal. Because the water flow is zero, the flowsignal is expected to be zero or at least constant. It can be clearly seen that while the transformer signal varies by 0.88V, the flow signal is constant. The DC offset of the flow signal can be ignored, at a later stage the signal processing may be refined and the offset removed. An experiment with a flowmeter having sinusoidally driven coils and the usual chopping circuit as described in section 5.5 produces the same result. However, the real time signal picked up on such meter is not zero. The amplitude of the signal changes as the ball passes the electrodes. Only when the signal changes slowly and it is rectified exactly in phase with the magnetic field then its average is zero. With the coils driven by a trapezoidal current waveform also the real time flow signal is zero. This is because the flow signal is sampled when the magnetic field is constant and no eddy currents exist which can cause a transformer signal. Therefore the flow signal cannot be effected by any nonconducting phase regardless of the effects on the transformer signal.

8.2 Surfaces of maximum and minimum transformer signal

Experiments on the 2" flowmeter with point electrodes as well as computations for the point electrode flowmeter showed a large dependence of the distance between the maximum and the minimum of the transformer signal on the position of the ball in the pipe cross section (**Fig.4.10, Fig.4.16**). The measured distances in the new flowmeter with large electrodes are shown in **Fig.8.3**. The plastic balls used have a diameter of 15mm and 25mm. Such large balls are used in order to obtain a clear signal. Independently of the position of the path along which the ball moves parallel to the pipe axis, the maximum and minimum of the transformer signal is approximately 25mm to either side of the electrodes centre line. **Fig.8.4** shows the almost flat plane at which the transformer signal is a maximum. It agrees well with the predictions seen in **Fig.4.24** in shape and in position. Consequently, a flow with bubbles all with the same velocity is expected to generate a sharper power spectrum of the transformer signal than it does with point electrodes.

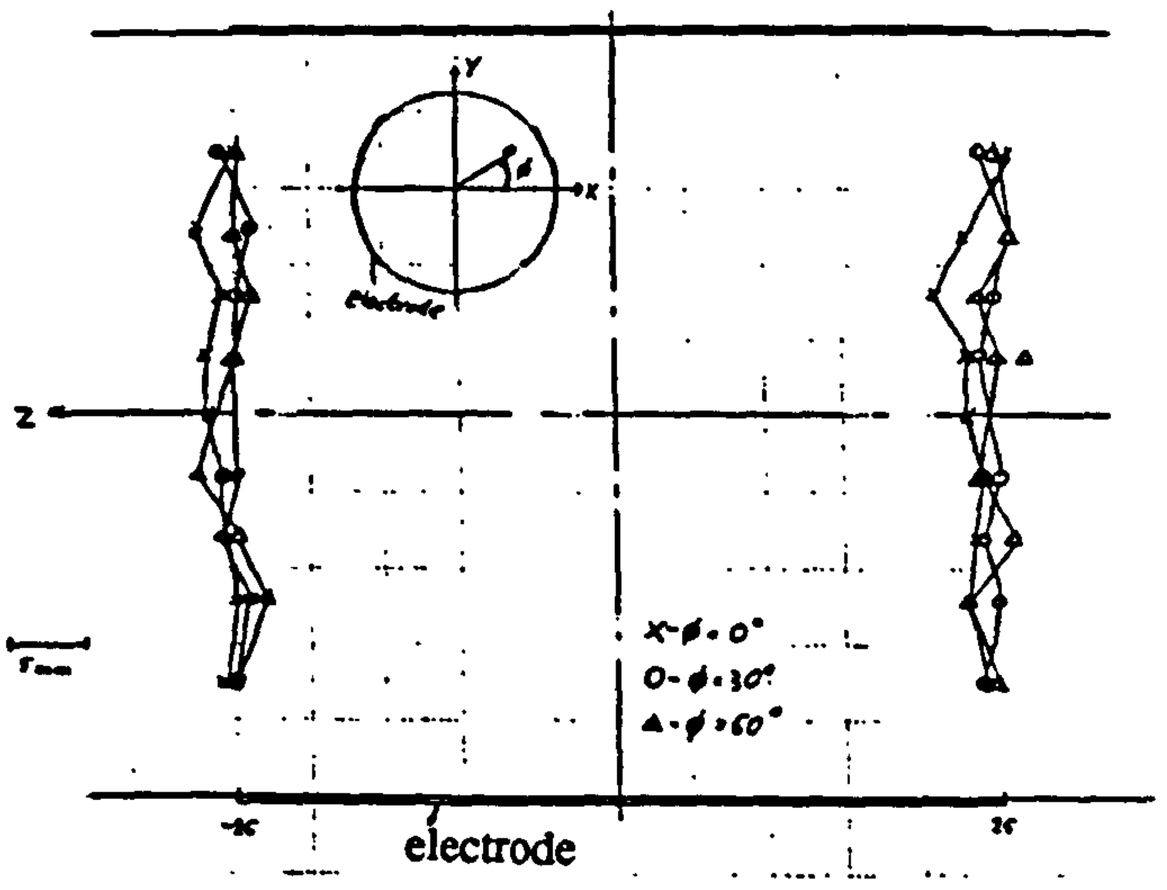

Fig.8.3 Lines of minimum and maximum transformer signal in an E.M.flowmeter with large area electrodes and uniform magnetic field

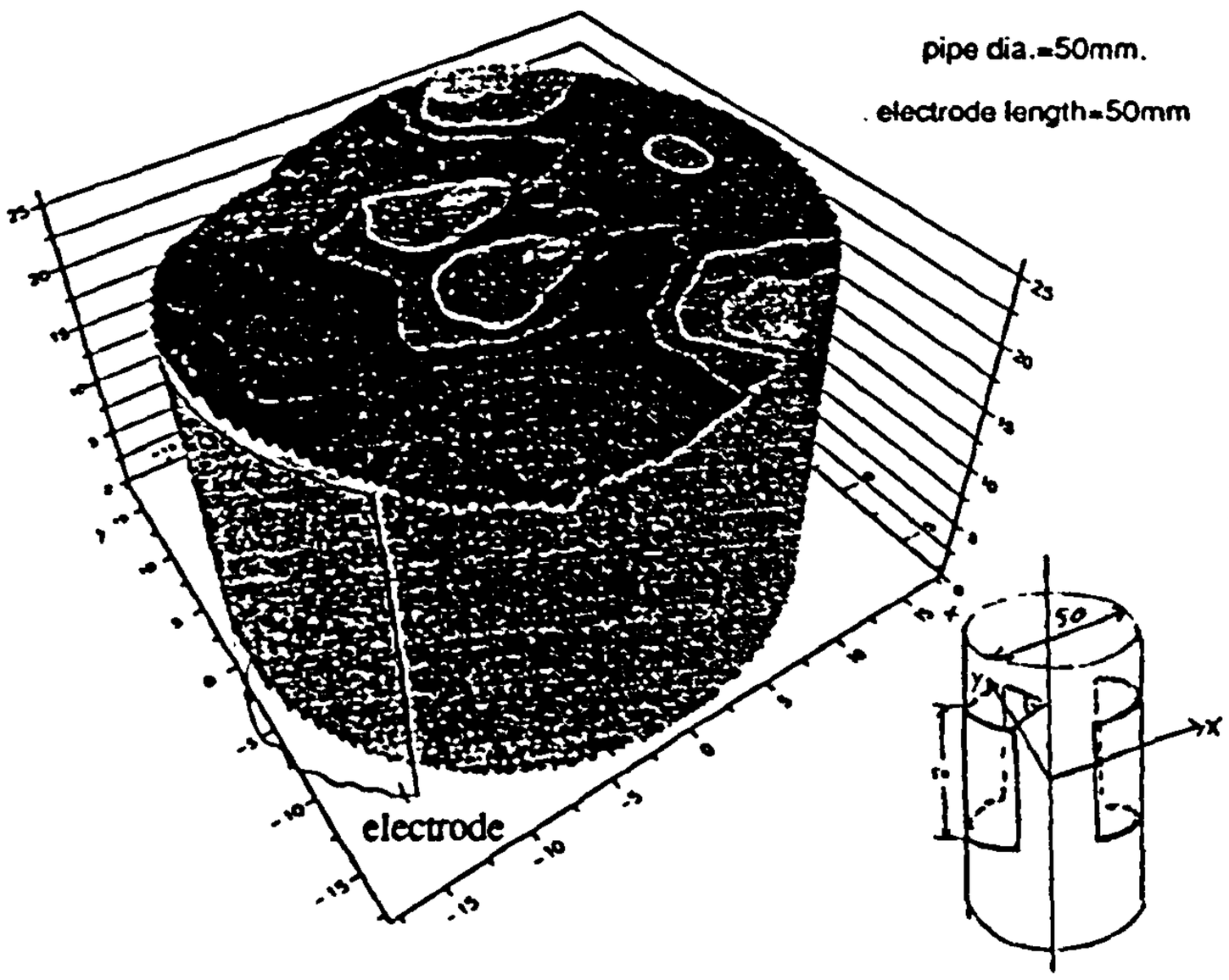

Fig.8.4 Plane of maximum transformer signal in E.M.flowmeter with large area electrodes

8.3 Calibration of new flowmeter in single phase water flow

Although the new flowmeter was mainly built to investigate its performance in a two phase flow, it obviously has to work as well as a flowmeter in a single phase flow. **Fig.8.5** shows the calibration curves of the flowmeter.

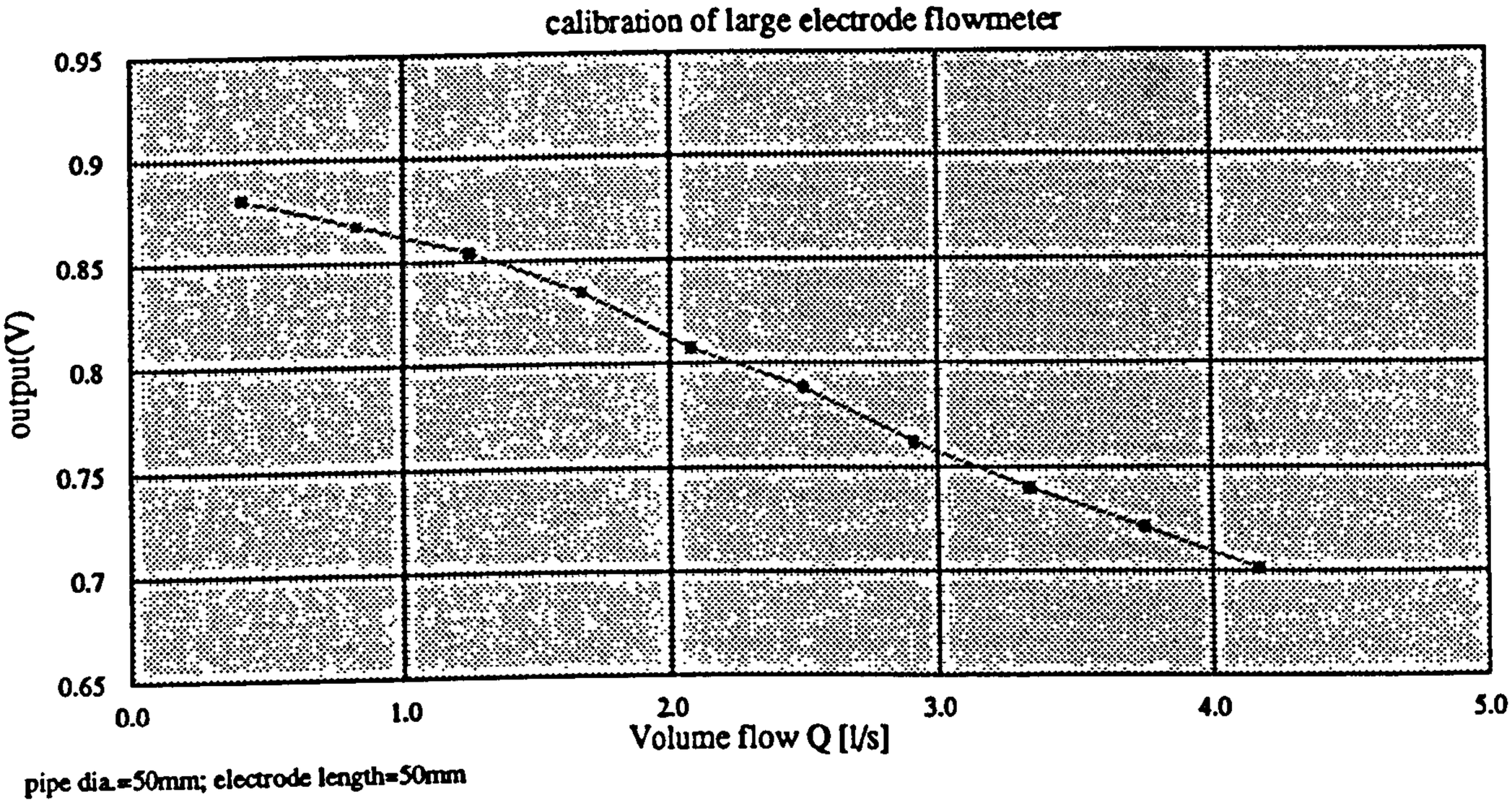

Fig.8.5 Calibration curves of E.M.flowmeter with large electrodes for water

It was mentioned earlier that the circuitry for processing the flowsignal produces a Dc-offset, therefore the zero flow output is not 0V. With the flow direction reversed, the calibration curve has a positive slope. Despite the fact that the signal processing needs refinement, the calibration curve is an almost straight line which proves again that the meter is usable in its present condition.

8.4 Reference measurement of the velocity of airbubbles

In **Fig.8.4** it was shown that the distance between the maximum and minimum of the transformer signal for a single ball is constant throughout the pipe cross section. This removes one uncertainty in the measurement of the velocity of the nonconducting phase. In order to calibrate the flowmeter with respect to the velocity of the nonconducting phase a reference measurement is needed. It is known that ultrasonic flowmeters which work on the principle of the Doppler shift, can measure the velocity of solid particles or air bubbles in a continuous water flow. However, this method works only for a secondary phase with particle sizes small compared to the ultrasonic beam. In an experiment it is verified that no reasonably accurate results can be obtained with such a meter when the bubble sizes are up to 4 times as big in diameter as the transducer itself. Because no other conventional flowmeter could be found which measures the velocity of the gas phase, a photographic method is attempted. The two phase flow in the perspex pipe is recorded with a video camera and then played back frame by frame. With a rate of 50 frames/s, the bubble speed can be determined by measuring the distance it moves in a given number of frames. An improved version of this method is to lighten the flow with a flashlamp at a multiple rate of the frame rate. At a flash rate of 200Hz 4 shots of a bubble are seen on one frame. Ideally, the lamp has to be synchronized with the shutter of the video camera. The method works reasonably well at low flow rates with bubble velocities well below 1m/s. At larger velocities bubbles move (between frames) out of the sharply focussed region of the camera view. When the bubble

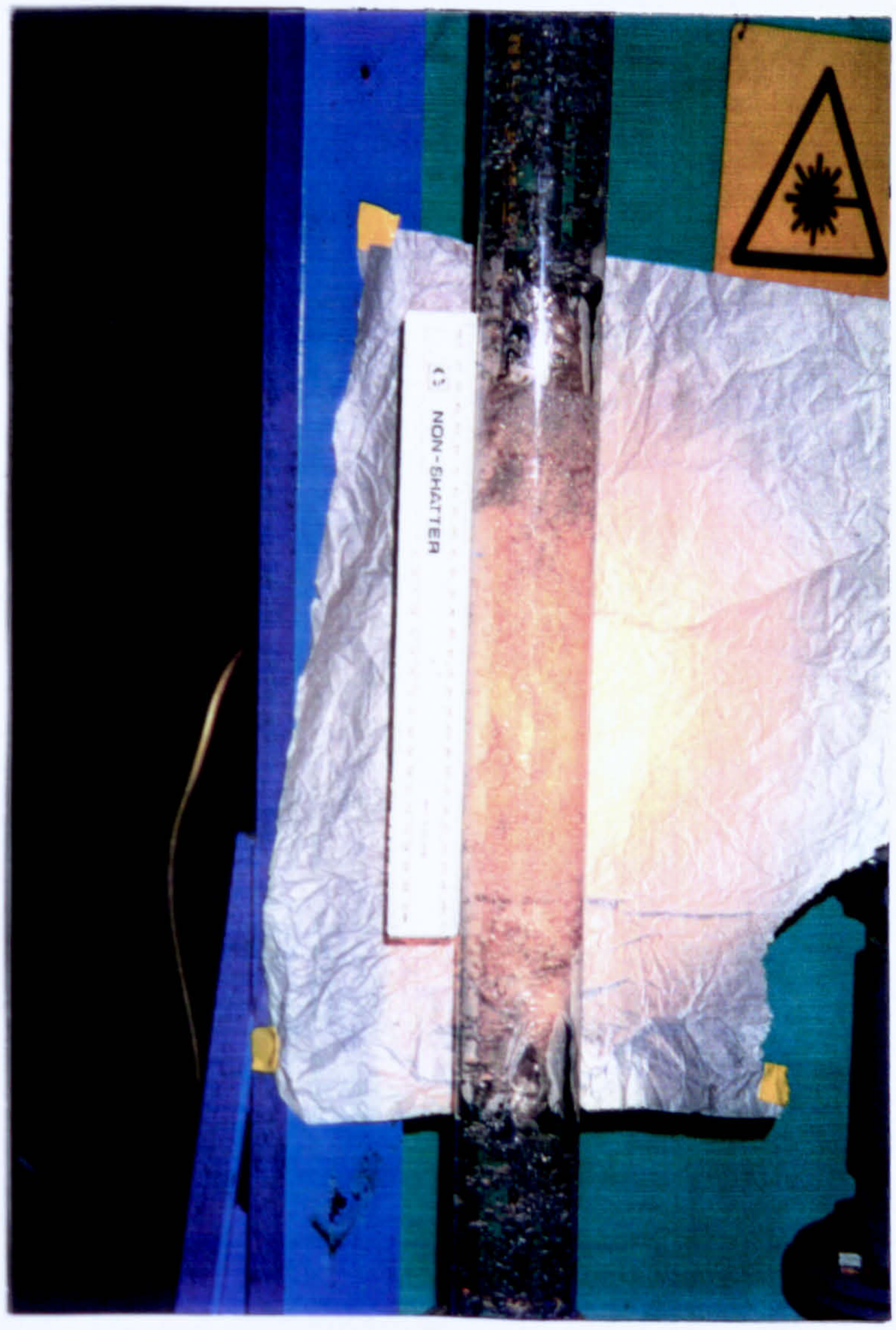

moves between two frames more than 3 or 4 cm, the trace of the bubble is also easily lost. The flow regime therefore must allow the identification of single bubbles. A void fraction of about 5% combined with the low flow velocity of 0.5m/s is just acceptable. In a bubbly flow regime like that shown on the photograph above this identification is certainly not possible any longer. A major improvement of this measuring technique could be achieved using a high speed camera with a frame rate of several hundred frames/s. However, one problem would still remain:
The bubbles in the pipe cross section don't move all at the same speed. Dependent on the their size and on the position in the pipe cross section, their speed can vary by at least 50%. It therefore is necessary to measure the speed of a large number of bubbles and then take the average. Considering the limitation of this photographic method and the fact that no other reference meter is available, the results of the following experiments with the 50mm large electrode flowmeter will only be qualitative, no accurate calibration can be obtained.

8.5 Power spectrum of transformer signal in a two-phase flow

In section 8.1 and 8.2 the transformer signal was investigated for a single nonconducting sphere. It was concluded that the power spectrum of the transformer signal in a two phase flow has to be narrower than the spectrum measured with the point electrode flowmeter. Because the distance between maximum and minimum transformer signal is 50mm compared to 25mm or less in the point electrode meter, one expects the frequencies in the power spectrum to be lower, ideally by a factor of 2. A series of systematic experiments are carried out. The flowmeter is installed in the vertical pipe section with 1m straight pipe upstream and downstream. A perforated plate with holes of ca.5mm diameter is mounted 1m upstream of the flowmeter. A 2" turbine meter is used as reference meter for the water flow and a pelton wheel meter measures the amount of air injected at constant pressure. A pressure gauge at the entry to the E.M.flowmeter allows one to compensate for the gas expansion between air inlet and flowmeter. The experiment covers water-flowrates from 0.5l/s to 2l/s and ratios of gas to gas-water mixture between 10% and 50%. This ratio is calculated from the water and gas flow rates at the position of the E.M meter. It is only equal to the void fraction for a gas phase having no slip velocity with respect to the continuous water phase. In the experiments some slip velocity is undoubtedly present (though unknown) but the term 'void fraction' used below is calculated from the flow rate ratios as already described.
In order to verify that the principle of driving the coils with a trapezoidal current wave

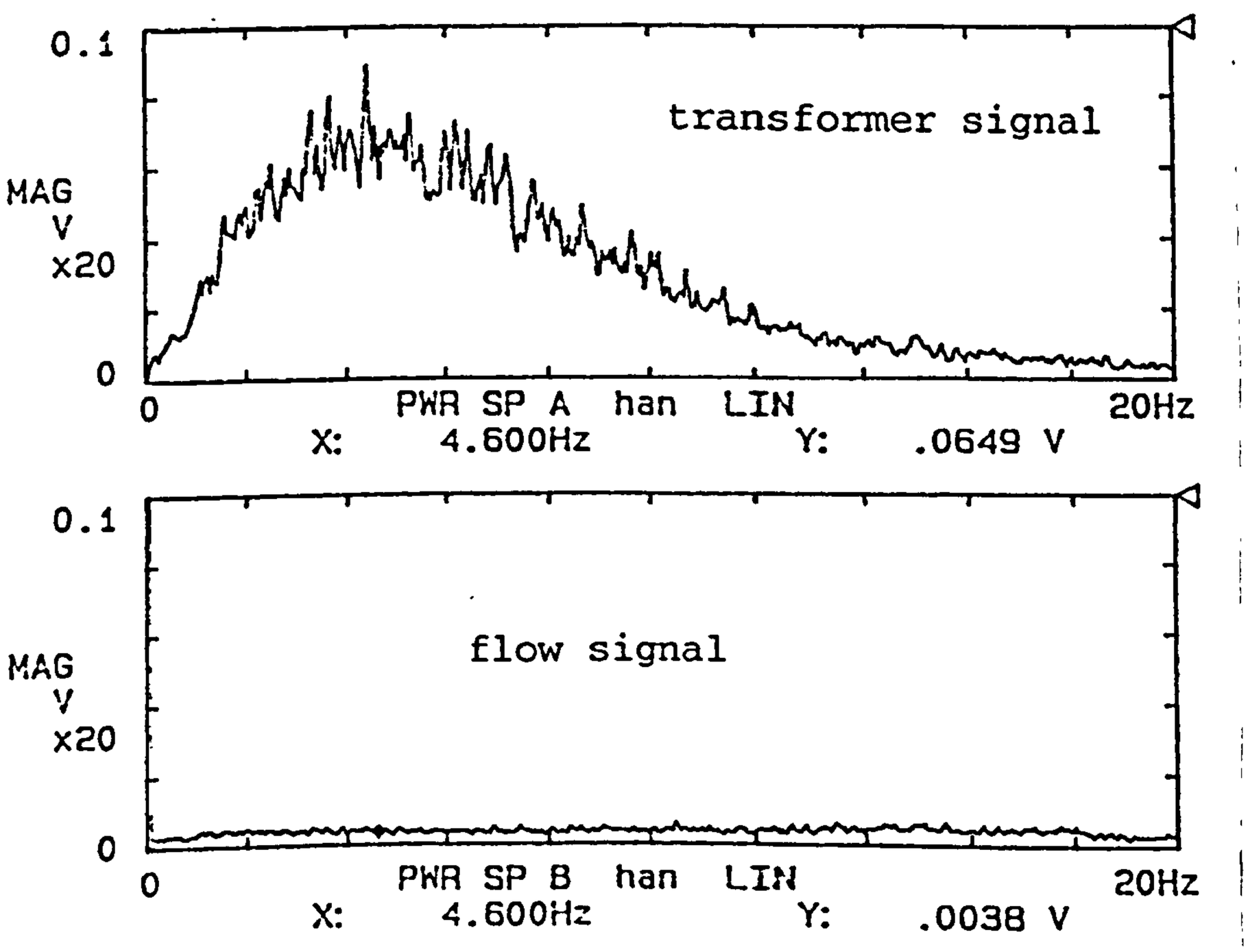

Fig.8.6 Comparison of power spectra of transformer signal and flow signal in an E.M.flowmeter with large electrodes and trapezoidal current drive.
Water flow=0.75l/s, α=50%

form allows a clean separation of transformer signal and flow signal, the power spectrum of both signals is recorded simultaneously. A large void fraction of 50% is chosen, the mean velocity of the mixture without slip being 0.79m/s. **Fig.8.6** shows the recorded power spectra. While the transformer signal has a definite peak, the flow signal shows only a constant very low noise level.
Having recorded the power spectra for all flow rates and void fractions, the frequency at which the envelope of the power spectrum is a maximum is plotted against the mean velocity of the water-air mixture. This mean velocity is not equal to the bubble velocity because there can be a considerable amount of slip between both of the phases. The magnitude of the slip velocity depends mainly on the bubble size and therefore on the flowrate as well as on the void fraction. Maximum slip occurs at high void fractions combined with low water velocities, minimum slip is found at high water velocities together with small void fractions. However, as long as no other method is found to measure the speed of the gas phase, the use of this mean velocity will suffice. **Fig.8.7** shows the peak frequencies for all measured void fractions.

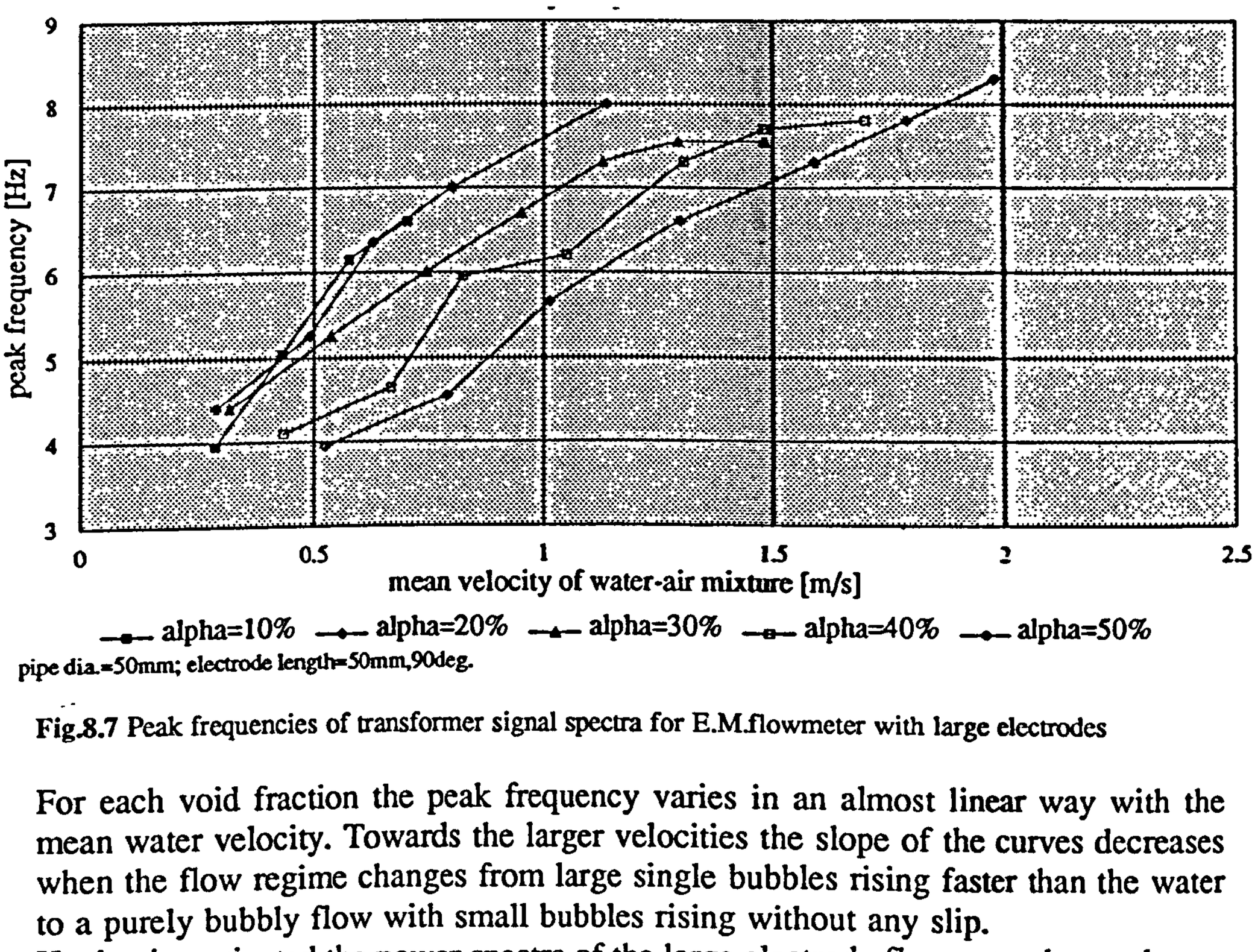

Fig.8.7 Peak frequencies of transformer signal spectra for E.M.flowmeter with large electrodes

For each void fraction the peak frequency varies in an almost linear way with the mean water velocity. Towards the larger velocities the slope of the curves decreases when the flow regime changes from large single bubbles rising faster than the water to a purely bubbly flow with small bubbles rising without any slip.
Having investigated the power spectra of the large electrode flowmeter the results are now compared with the power spectra obtained with the point electrode flowmeter. In **Fig.8.8** the peak frequencies are compared for two void fractions. The peak frequency from the flowmeter with point electrodes is higher than that from the meter with large electrodes. At the lower void fraction the difference between the two meters is more significant than it is with the higher void fraction. The expected factor of 2 however is never reached. One reason for this discrepancy is that at greater void fractions the bubbles become very large. Very large cap bubbles and plugs which occupied the whole pipe cross section were seen. A short experiment with a plastic plug of 45mm

dia. and 40mm length revealed that the distance between the maximum and minimum transformer signal in the flowmeter with point electrodes increased to 33mm. At the meter with large electrodes a distance of 47mm is measured. This reduces the ratio of the expected peak frequencies between large electrode- and point electrode flowmeter from 2 to 1.4. One also has to consider the fact that large bubbles contribute more to the power spectrum than small ones.

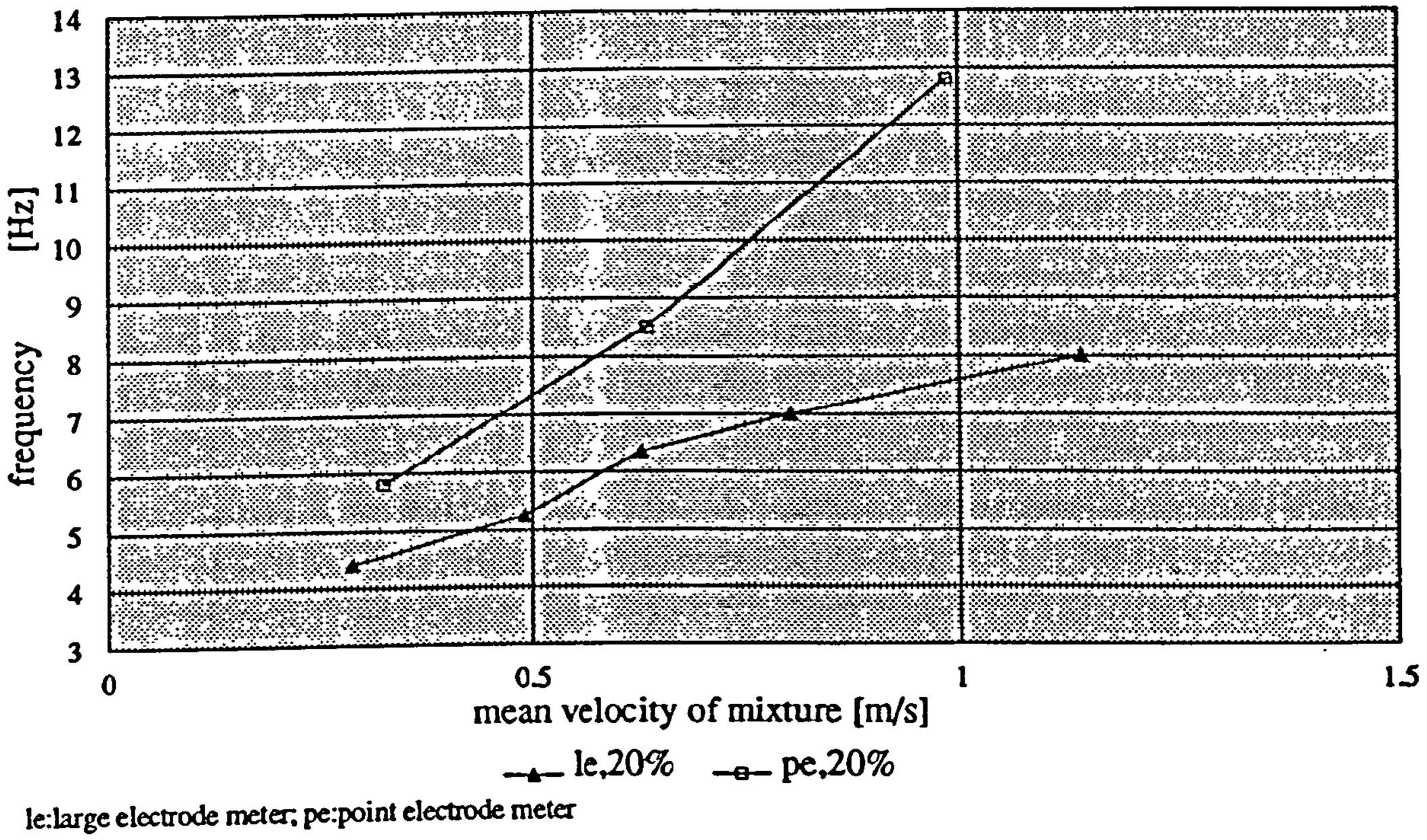

le:large electrode meter; pe:point electrode meter

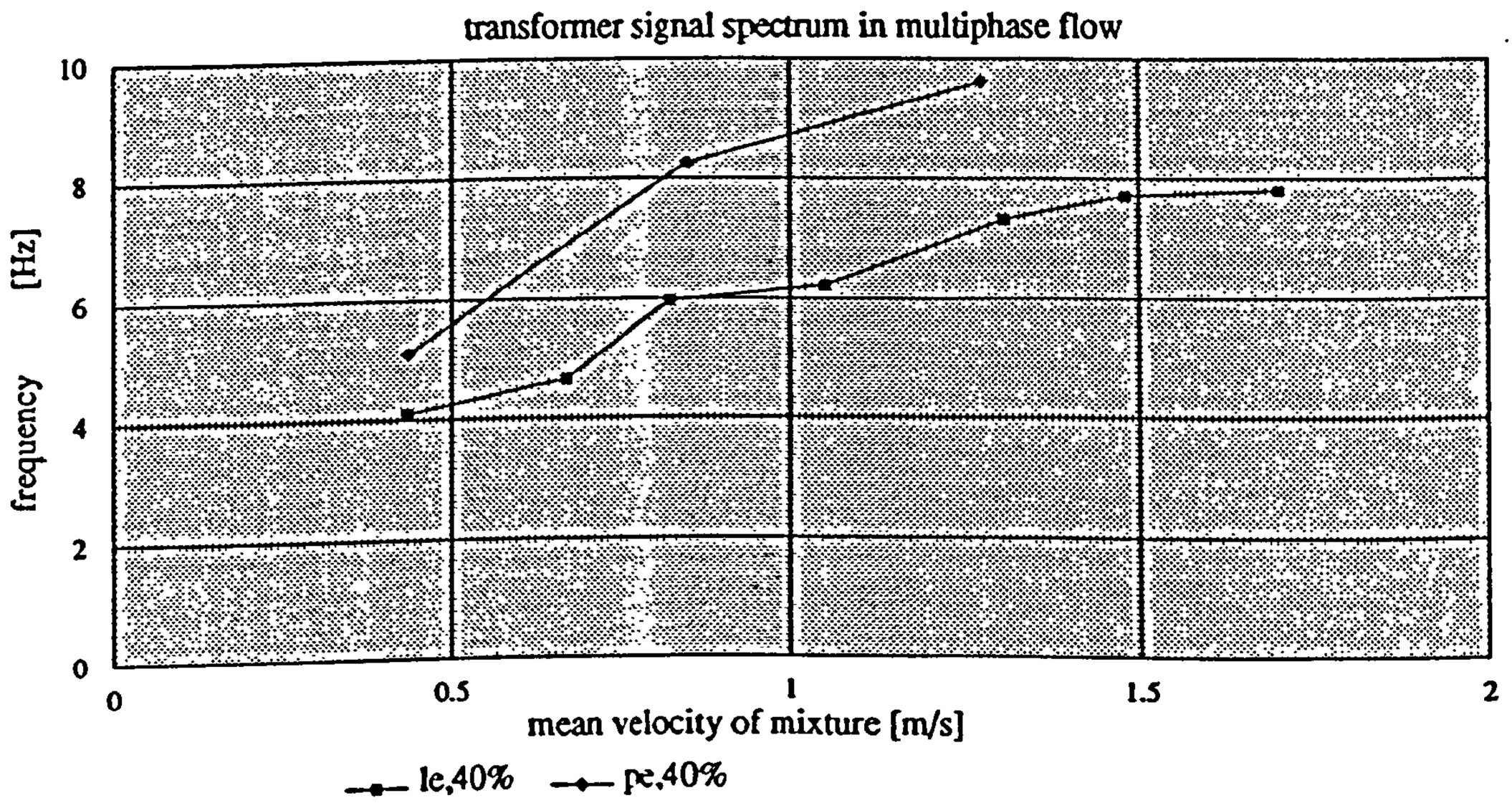

le:large electrode meter; pe:point electrode meter

Fig.8.8 Comparison of the peak frequencies of transformer signal power spectra for large electrode- and point electrode flowmeter

Apart from the lower peak frequency it is predicted that the power spectrum of the flowmeter with area electrodes is narrower than that of the point electrode flowmeter. **Fig.8.9** shows an example which verifies the prediction. As a guide, frequencies are compared at which the envelopes of the power spectra have either levelled off or decreased to 25% of their maximum. In the case of the two power spectra shown the spectrum of the large electrode meter has decreased to 1/4 of its maximum value at 16.5 Hz whereas the spectrum of the point electrode meter has decreased to 25% at 32Hz.

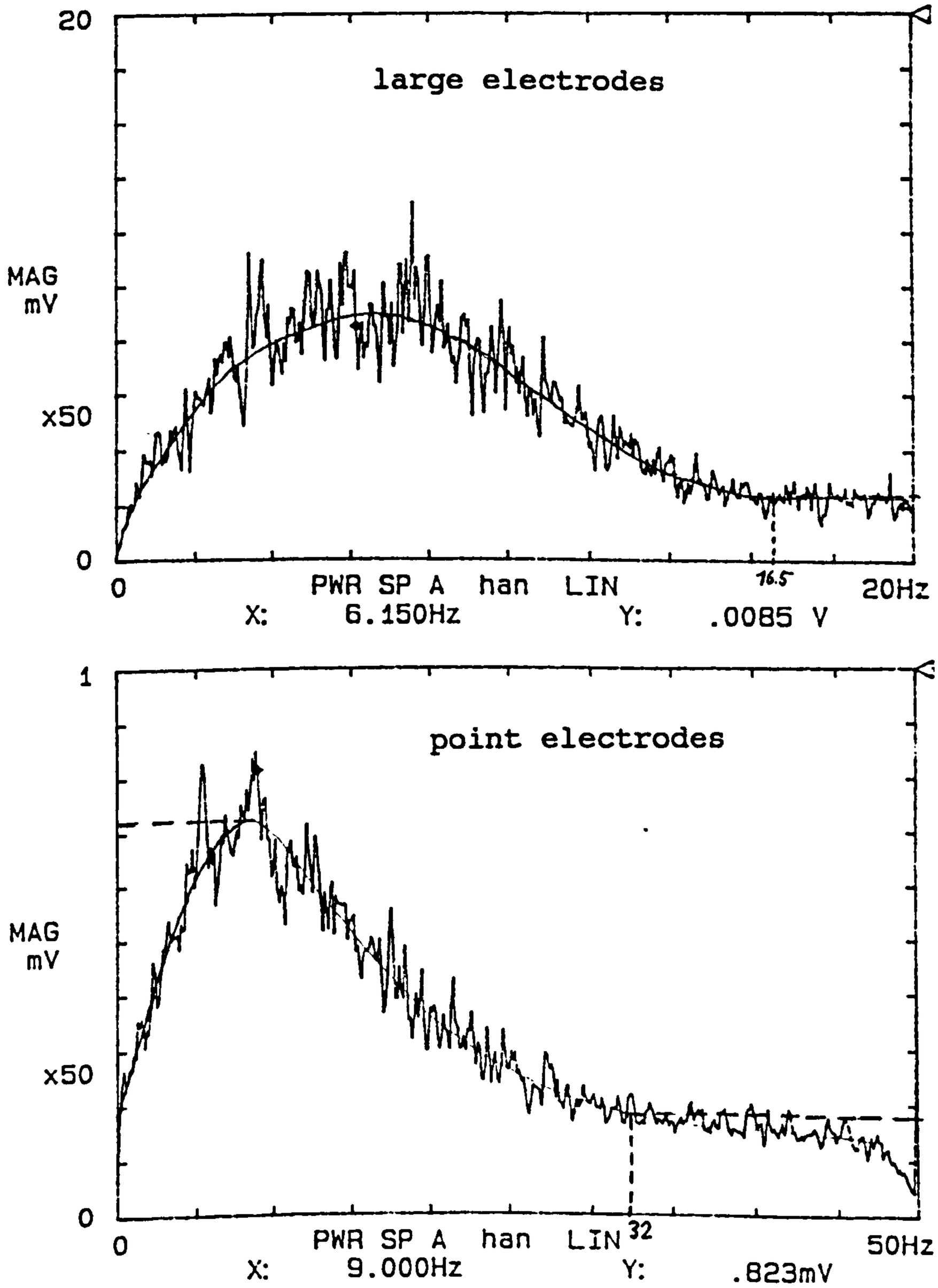

Fig.8.9 Decay of power spectra on flowmeters with large electrodes and point electrodes. mean flow velocity=0.28m/s, α=10%

Although the difference is not always so distinctive, the power spectra of the new flowmeter with large electrodes are in all experiments narrower than those with the point electrode meter.
Bernier and Brennen showed (in 1983) in theory and experiment that, within certain limits, an electromagnetic flowmeter can measure the average liquid velocity in a two phase flow. They carried out an experiment with two E.M.flowmeters in line. Between the meters air was injected so that one meter was measuring a single phase water flow and the other a two phase flow. Applying the relation that the potential difference on the electrodes is $\Delta\Phi=\frac{2B\ Q_l}{\pi b\ (1-\alpha)}$, where Q_l is the liquid flow rate, b the pipe radius B the magnetic field strength and α the void fraction and dividing the output from the meter monitoring the single phase by (1-α)output from two-phase monitoring meter, the result should be unity. In their experiment they achieved this result within a band of 2% for void fraction up to 20%. In a similar experiment with the new flowmeter and void fractions up to 50% I could not achieve this result. With increasing void fraction the ratio of the outputs from single phase and two phase flow increased (**Fig.8.10**). One explanation may be that the condition of a well dispersed flow with no slip between both phases does not hold in my experiments. The same experiment repeated with the 2" point electrode flowmeter shows an increase in the signal ratio as well.

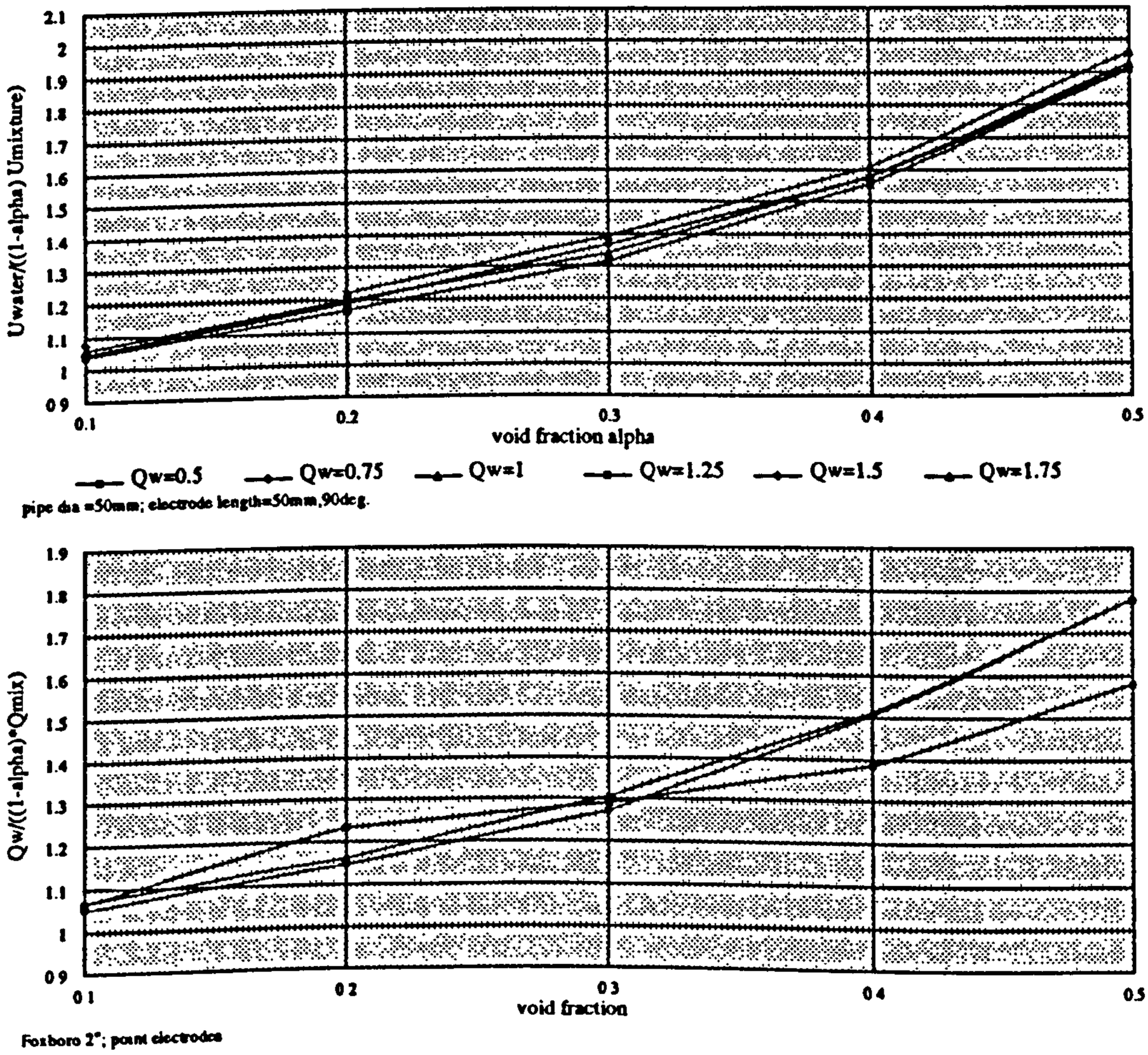

Fig.8.10 Flow signal response to two phase flow

Chapter 9

Conclusions and suggestions for future work

The work in this thesis has been concerned with general information which can be extracted from an electromagnetic flowmeter in a multiphase flow consisting of a continuous conducting phase and any secondary nonconducting phase. The two main areas dealt with are the flow signal and the transformer signal. In addition, the noise signal in the absence of a magnetic field has been investigated. For the flow signal it is shown that a nonconducting phase has only a small effect on it. The theoretical analysis is based on modelling a dipole's potential distribution which counteracts the flow induced currents circulating in the pipe cross section. At small Reynolds numbers when the velocity profile is almost parabolic, a small single nonconducting sphere alters the flow signal only by a factor of 1E-3. At higher Reynolds numbers this effect becomes even less and for a flat velocity profile in a uniform magnetic field it is zero. An attempt was made to measure the flow signal effect in experiments, however the effect was too small to be made visible. Another problem was that the flow signal could not be separated well enough from the transformer signal. These experiments lead to the investigation of the transformer signal in more detail. The basic theoretical model is similar to that used for the flow signal. A dipole's potential is superimposed onto eddy currents in the fluid and the resulting potential difference at the electrodes is computed. It is found that a single nonconducting small sphere generates a transformer signal that has a minimum and maximum to either side of the electrodes and decreases to zero further away from the electrodes. The distance between the minimum and maximum transformer signal depends on the position of the sphere in the pipe cross section and very much on the electrode shape. With point electrodes the distance varies by a factor of 5 dependent on the position of the ball in the pipe cross section. Large electrodes average the transformer effect and can render the distance almost constant throughout the cross section. Because the eddy currents are independent of the liquid flow, the information in the transformer signal can be used to determine the velocity of the nonconducting phase. The power spectrum of the transformer signal shows a characteristic frequency which relates to the velocity of the secondary phase and the distance between the peaks of the transformer signal. Because this distance is not constant in a flowmeter with point electrodes, the frequency spectrum is very wide even if the spheres all have the same speed. A flowmeter with large electrodes has, on account of the constant distance between the transformer signal peaks, a narrower frequency spectrum. In the

theoretical study of the transformer signal and its power spectrum only the simplest case of a row of spheres which don't interfere with each other was analyzed. Although the predictions of this model bare some relation to the experimental measurements in a real 2-phase flow, it becomes apparent that much more work is needed to fully simulate the effect of real 2-phase flows. A major result was obtained regarding the coil drive method. Instead of using a sinusoidal current the coils were driven with a trapezoidal current wave form. It was shown that with a sinusoidal current the quickly changing transformer signal leaks into the flow signal and generates noise. In the newly build flowmeter with large area electrodes and trapezoidal coil drive the flow signal and the transformer signal are truly separated. The power spectrum of the flow signal shows no additional noise due to the secondary phase.

Having demonstrated the principles of generation of a flow related signal and a transformer signal, there is much scope for refinement. Many idealisations have been made and although the theoretical results have been validated by numerous experiments it would be useful to know the limits of the theory. The flow induced signal as well as the transformer signal were derived for an infinitely small sphere only. This allowed the idealisation that the circulating currents as well as the eddy currents are uniform at the position of the sphere. A single current dipole was sufficient to model the flow of the current over the surface of the bubble. With increasing size of the insulating particle it is necessary to take into account that the currents are not uniform any longer and it may be necessary to use multiple current dipoles to model the current around the particle which does not necessarily have to be spherical. The investigation of the effects on flowmeters with point electrodes always assumed that the electrodes were significantly smaller than the pipe diameter, ideally the size of a point. The tested commercial meter however has 10mm diameter electrodes with only 50mm tube diameter. This will change the boundary conditions on the pipe wall such that the normal component of the currents is not zero over 13% of the pipe wall. Throughout the analysis the effect of a single bubble has been considered. If two small bubbles are very close to each other or even touch then their effect is similar to that of a single larger bubble. If they are more than a few pipe diameters apart then they don't interfere. At a distance between those extremes they will interfere with each other. The potential of two more current dipoles then has to be superimposed to find the resultant effect. The bubbles can of course be of different size. For the computation of the power spectrum the signal of a single sphere was idealised as a series of linear functions. This can be improved by using a computed or measured signal with the shape of a function like $f(x)=e^{-c_1|x|}atan(c_2x)$. Again more than one function can be superimposed to model the effect of several bubbles at different positions in the pipe cross section and along the pipe axis. In addition to the theoretical refinements there is also scope for some more experimental work. With the theory being extended to multiple bubbles a

means of verifying the predictions has to be found. Like the experiment where a single string of beads was moved through the flowtube a similar device with more than one string could be used. As an alternative an open ended vertical pipe could be used into which a number of heavy balls are released. The velocity of those ball could be measured photographically as attempted in a previous experiment. However, a more sophisticated faster camera would have to be used.

The newly built flowmeter with large area electrodes and a magnetic field driven with a trapezoidal wave form proved to be better suited for use of the transformer effect and also suppresses it when measuring the flow signal. The electronics however could do with some refinements such as removing the offset in the front end amplifier stage and speeding up the ramp up/down time of the current to increase the transformer signal. As far as the coils are concerned, an even more uniform magnetic field could be obtained by using more than three coils each side and it may be possible to shorten the coils without reducing the transformer effect too much. This would also lead to a further theoretical investigation of end shorting effects of the eddy currents.

Appendix A

Derivation of coefficients f_{nm} in Bessel Fourier series

Any function $f(r)$; $0 \le r \le a$ *for which* $\frac{\partial f}{\partial r}=0$ *at* $r=a$ *can be written as*

$$f(r)=\sum_{n=1}^{\infty} f_n \cdot J_m(j'_{m,n}\frac{r}{a}) \qquad (1)$$

Here, $J_m(z)$ is the Bessel function of order m(=0,1,2...) and $j'_{m,n}$ are the n_{th} zeros of the derivative of the Bessel function $J'_m(z)$,i.e where $\left[\frac{\partial}{\partial z}J_m(z)\right]_{z=j'_{m,n}=0}$ $n=1,2,3...$.

If we write $J_m(z)=w$, following condition is satisfied:

$$z^2\frac{d^2w}{dz^2}+z\frac{dw}{dz}+(z^2-m^2)=0$$

Formula for the coefficients f_n in terms of f(r) can be found by inverting **eqn.1**:

$$\int_0^1 t J_m(j'_{m,n})\cdot J_m(j'_{m,p})\,dt=\begin{cases}0 & n\neq p\\ \frac{1}{2j'^2_{m,p}}[j'^2_{m,p}-m^2][J_m(j'_{m,p})]^2 & n=p\end{cases}$$

Multiplying both sides of(1) by $rJ_m(j'_{m,p}\frac{r}{a})$ and integrate, gives:

$$\int_0^a f(r)J_m(j'_{m,p}\frac{r}{a})r\,dr=\sum_{n=1}^{\infty} f_n\int_0^a J_m(j'_{m,n}\frac{r}{a})J_m(j'_{m,p}\frac{r}{a})r\,dr$$

$$=\sum_{n=1}^{\infty} f_n\int_0^1 J_m(j'_{m,n}t)J_m(j'_{m,p}t)t\,dt\,a^2$$

$$=f_p\frac{1}{2j'^2_{m,p}}[j'^2_{m,p}-m^2][J_m(j'_{m,p})]^2a^2$$

$$\therefore \qquad f_p = \frac{\int_0^1 f(r) J_m(j'_{m,p}\frac{r}{a}) r\,dr}{\frac{a^2}{2j'^2_{m,p}}[j'^2_{m,p} - m^2][J_m(j'_{m,p})]^2}$$

Similarly to the Bessel series above, the coefficients f_{nm} in terms of $f(r,\theta)$ for the Fourier Bessel series are determined.

From **eqn.3.6**, $f(r,\theta) = \sum_{m=-\infty}^{\infty} \sum_{n=1}^{\infty} f_{n,m} e^{im\theta} J_{|m|}(j'_{|m|n}\frac{r}{a})$, we find for q=-2,-1,0,1,2...

$$\int_{-\pi}^{\pi}\int_0^a f(r,\theta)\, e^{-iq\theta} J_{|q|}(j'_{|q|p}\frac{r}{a}) r\,dr\,d\theta = \sum_{m=-\infty}^{\infty} \sum_{n=1}^{\infty} f_{nm} \int_{-\pi}^{\pi} e^{i(m-q)\theta} d\theta \int_0^a J_{|m|}(j'_{|m|,n}\frac{r}{a}) J_{|q|}(j'_{|q|,p}\frac{r}{a}) r\,dr$$

$$= f_{p,q} \cdot 2\pi \cdot \frac{a^2}{2j'^2_{|q|,p}}[j'^2_{|q|,p} - q^2][J_{|q|}(j'_{|q|,p})]^2$$

$$\therefore \qquad f_{pq} = \frac{\int_{-\pi}^{\pi}\int_0^a f(r,\theta)\, e^{-iq\theta} J_{|q|}(j'_{|q|p}\frac{r}{a}) r\,dr\,d\theta}{\frac{\pi a^2}{j'^2_{|q|p}}[j'^2_{|q|p} - q^2][J_{|q|}(j'_{|q|p})]^2}$$

Appendix B

Measured power spectra of transformer signal at zero flow velocity

Fig.6.16 to Fig.6.19

Foxboro E.M.flowmeter

2" diameter

Point electrodes

Mains driven coils

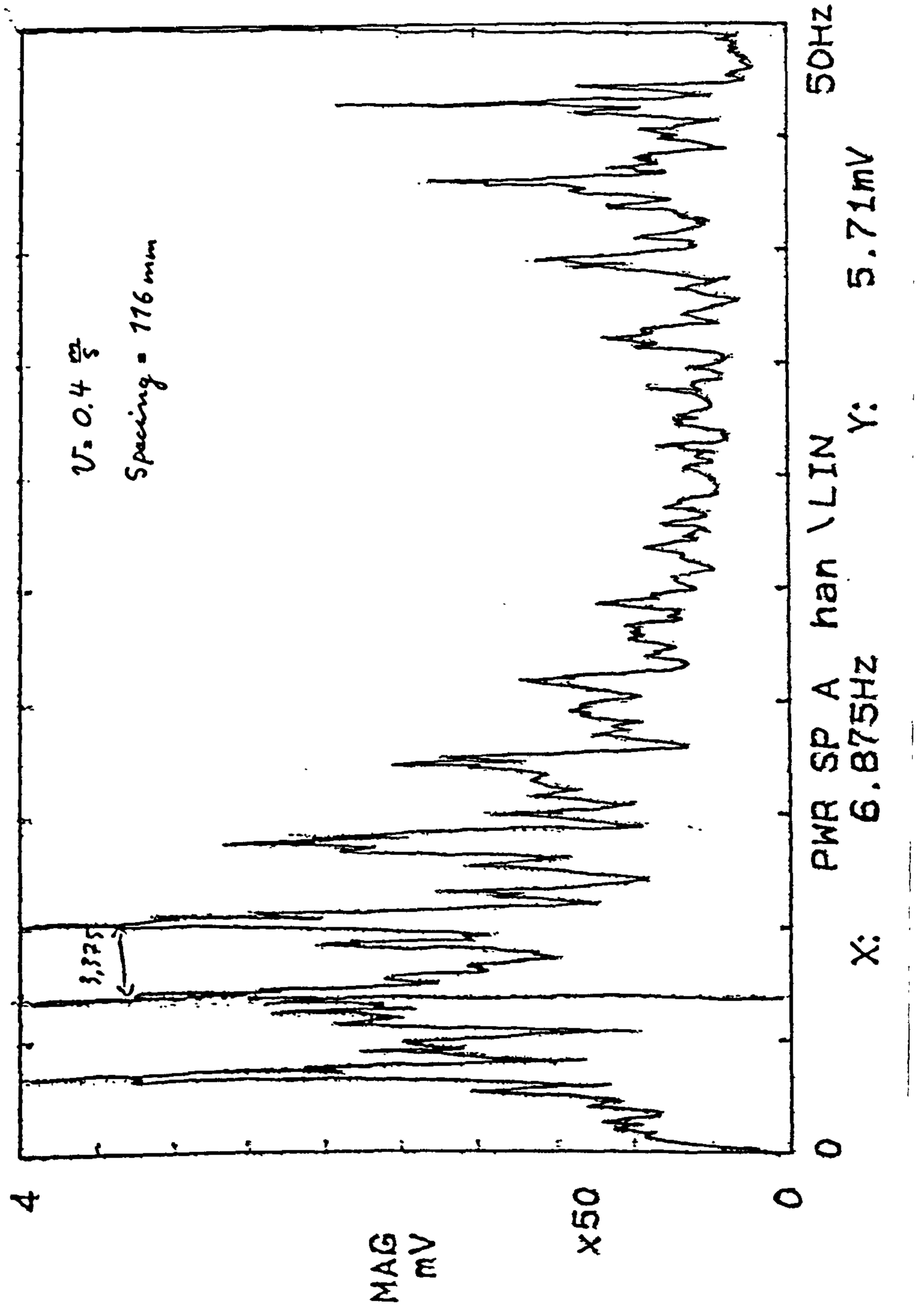

Fig.6.16 Measured power spectrum of transformer signal due to string of equally spaced balls

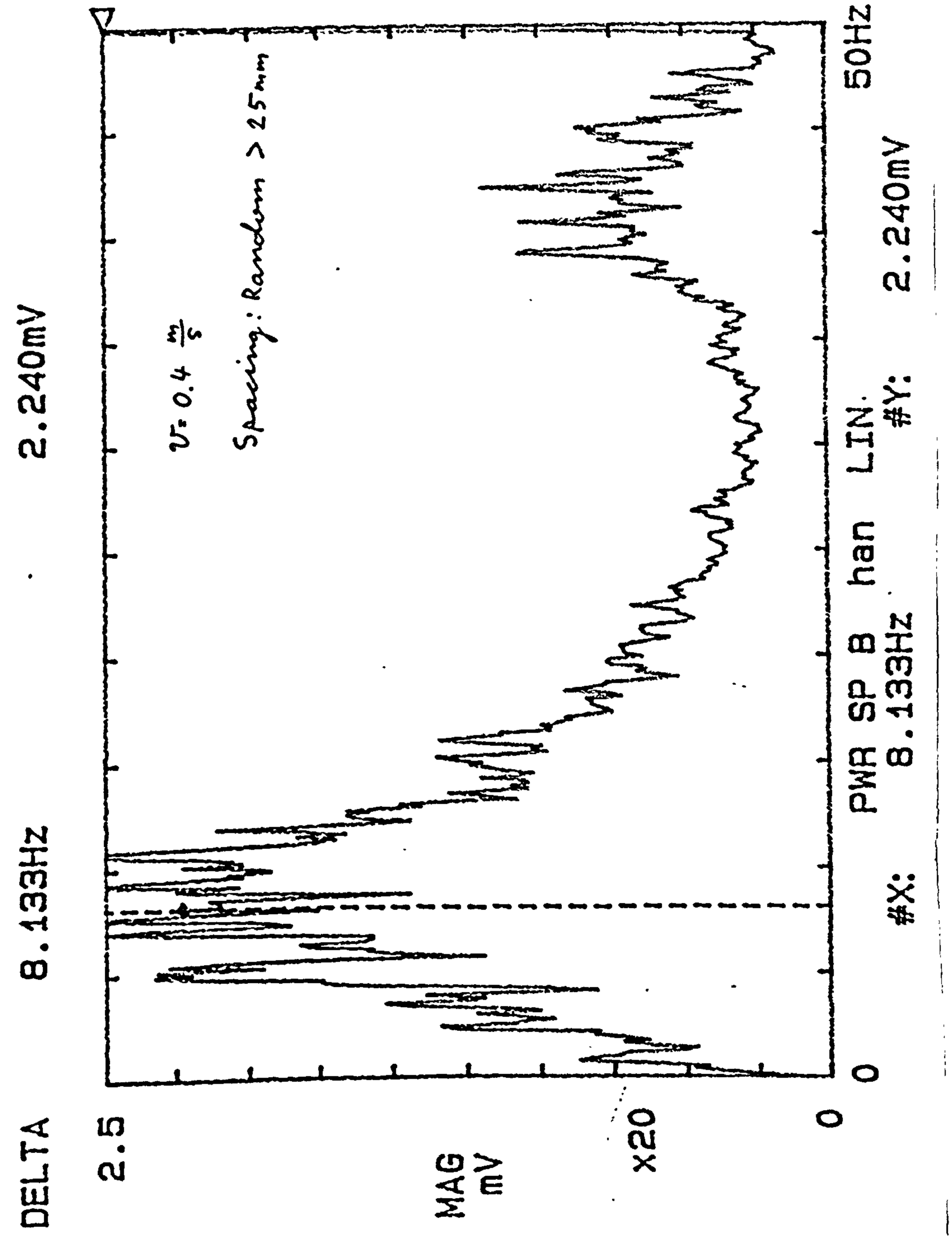

Fig.6.17 Measured power spectrum of transformer signal due to string of randomly spaced balls

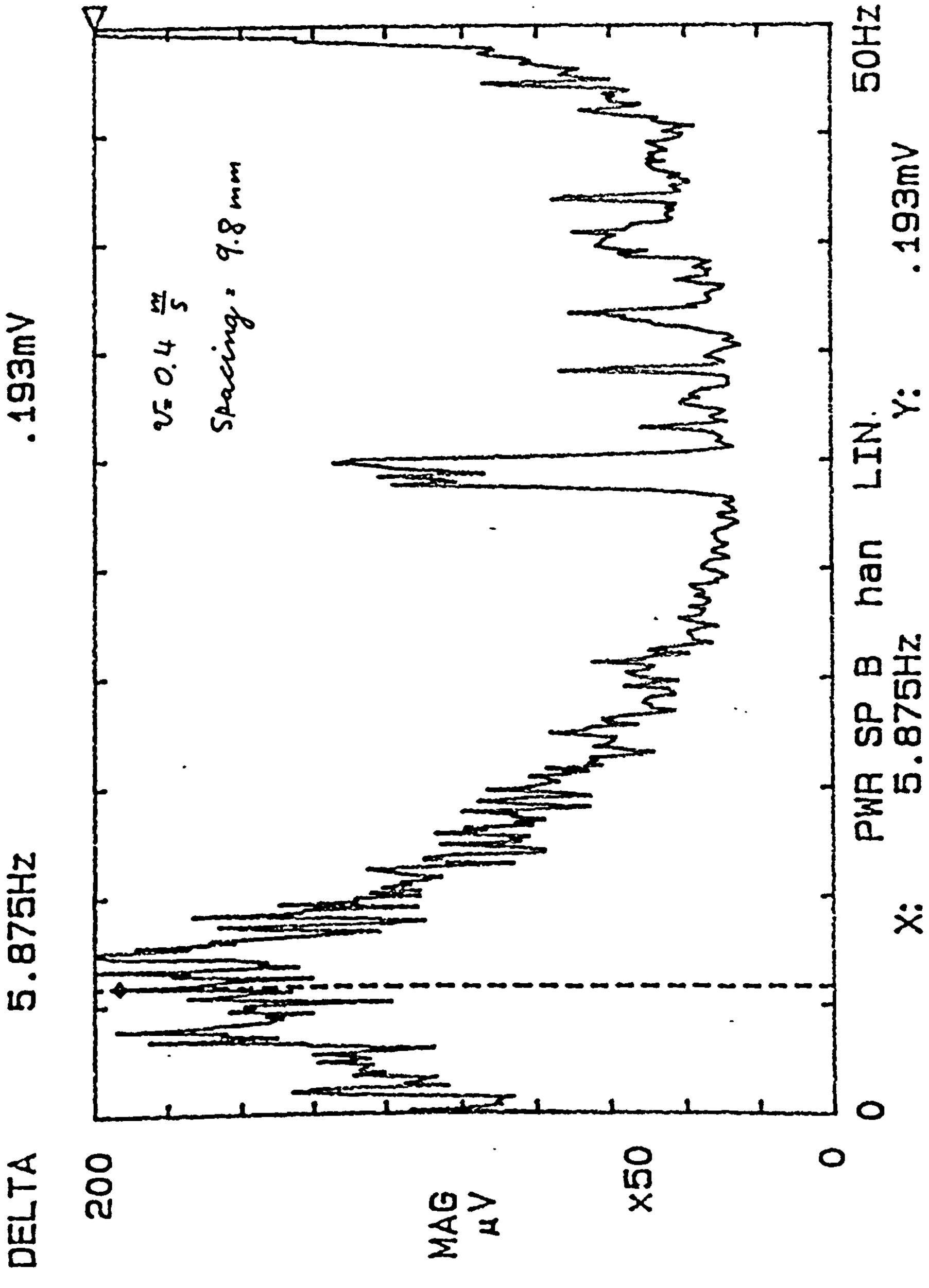

Fig.6.18 Measured power spectrum of transformer signal due to string of equally spaced balls

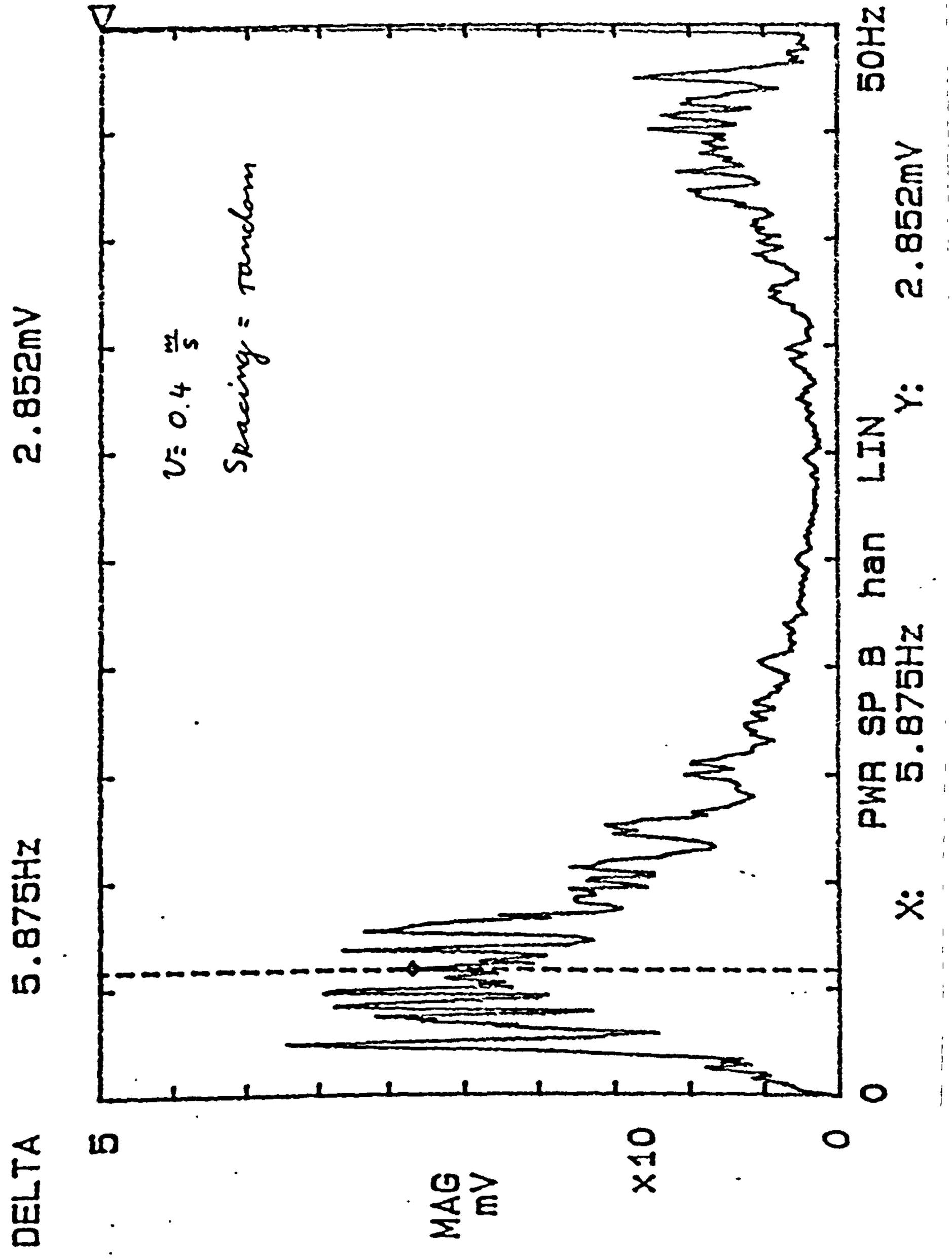

Fig.6.19 Measured power spectrum of transformer signal due to string of randomly spaced balls

Appendix C

Measured power spectra of transformer signal with water flow

Fig.6.20 , Fig.6.21

Foxboro E.M.flowmeter

2" diameter

Point electrodes

Mains driven coils

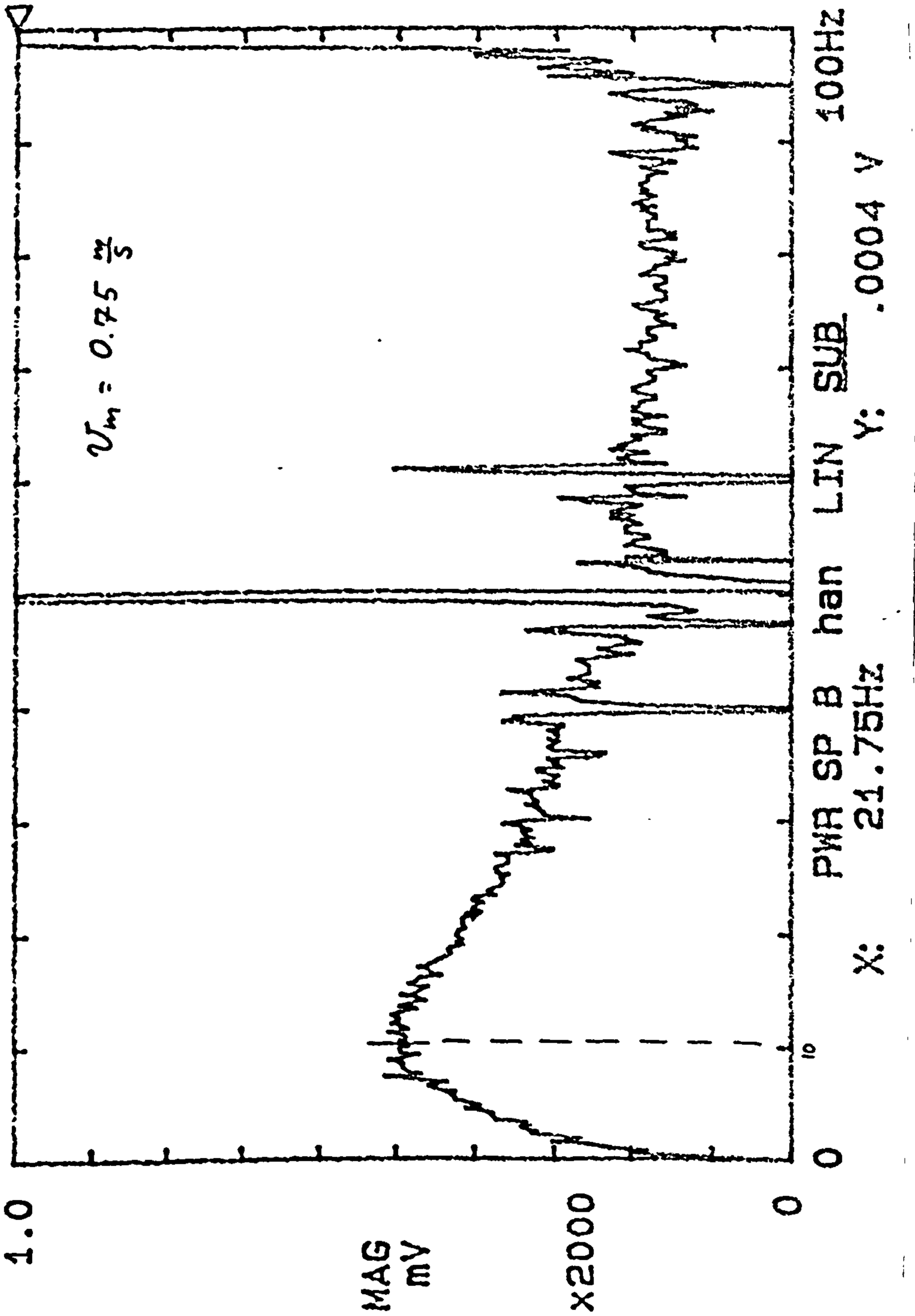

Fig.6.20 Measured power spectrum of transformer signal due to balls injected into water flow

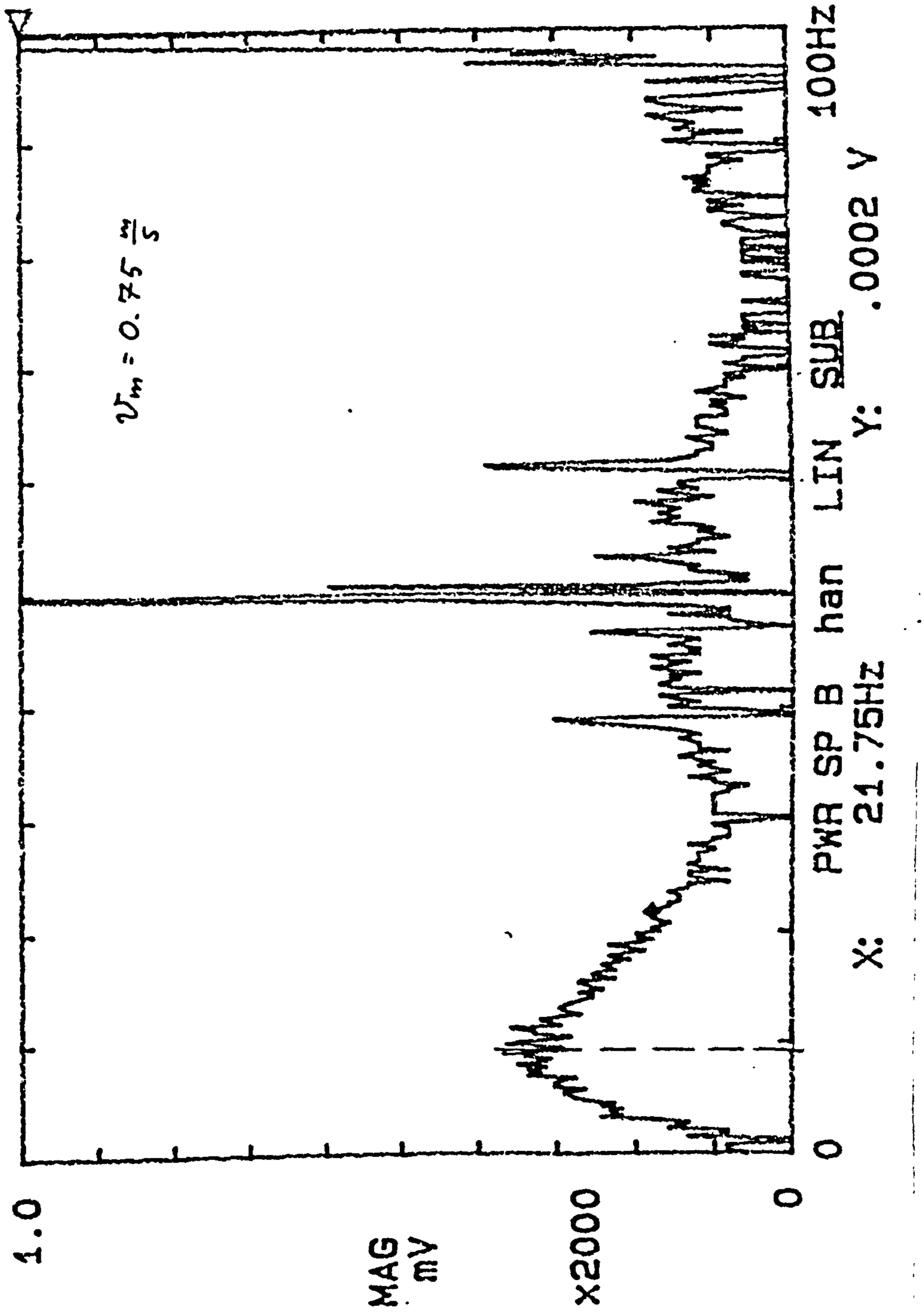

Fig.6.21 Measured power spectrum of transformer signal due to balls injected into water flow

Appendix D

Calibration curves of reference flow meters

2" turbine water flowmeter

Quadrina pelton wheel gas flowmeter

QUADRINA PWG7

SER. NO. 7543

QUADRINA CAL. APRIL 1986

$Q = 2.92398 \cdot f - 46$

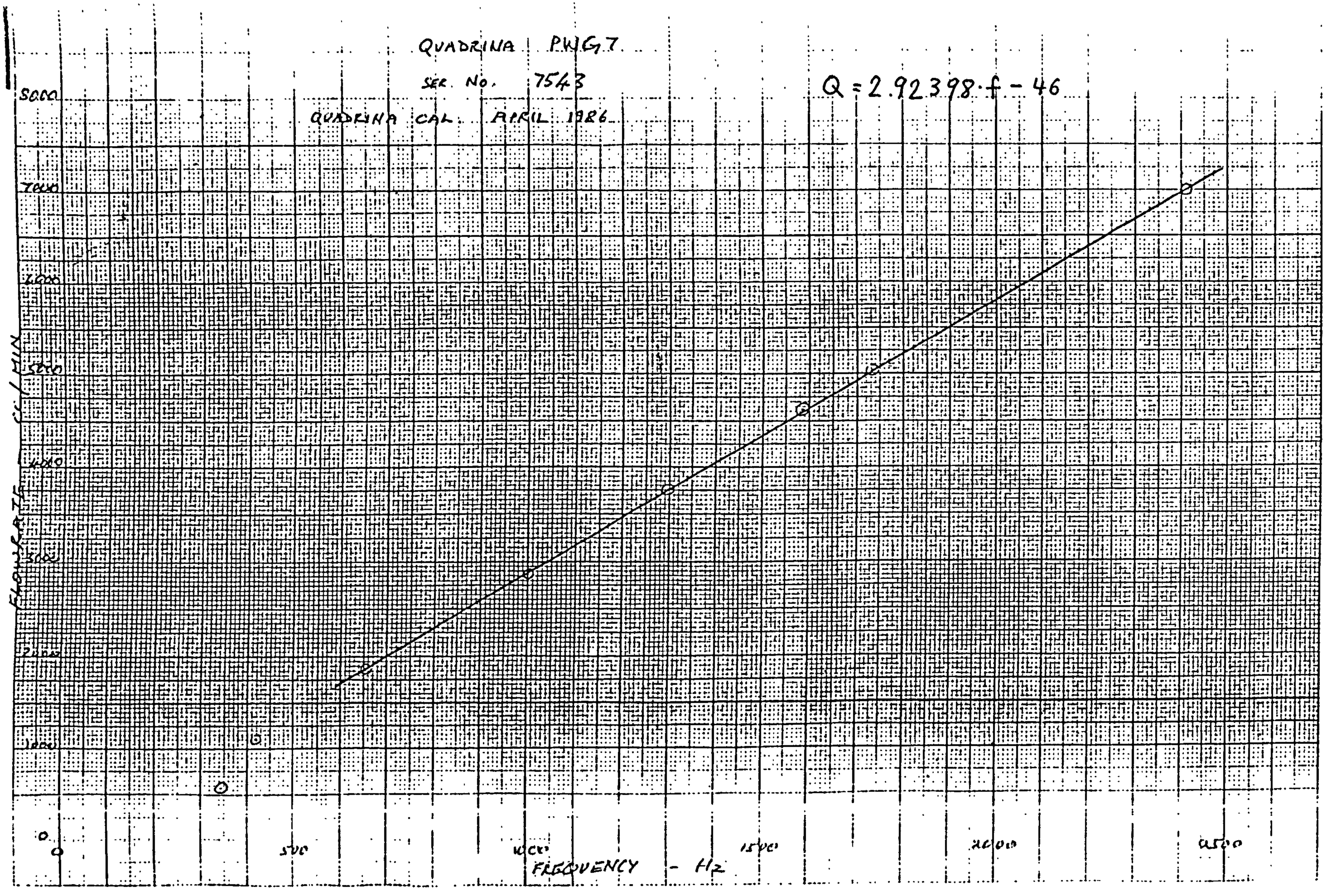

2ª Turbina

Serial Nr. 7102/14199/84
cal. from: 2.4.87

$Q = 0.016682 \cdot f - 0.0056$

$v = 0.008166293 \cdot f - 0.0002777727$

v_m (m/s)

Q [l/s]

f (Hz)

Appendix E

Circuit diagrams and layouts

Coil drive

and

signal processing unit

Coil drive

The task of the coil driver circuit is to power the coils on the flowmeter with a current having a trapezoidal wave form. Here IC4046 generates a TTl signal of the required frequency. in this circuit the frequency is set to 400Hz initially. The following comparator LM311 (IC7) switches the square wave between the positive and negative supply voltage. Two complementary transistors (2 and 4) are driven by the output of IC7. They in turn drive another pair of complementary transistors which charge and discharge the capacitor C with constant current, thus providing a ramped input to IC5. The Op-Amp IC5 controls a transistor which itself drives a pair of MOS FET transistors. For the current sensing a high power low value resistor is used. The feedback path of the current sensing is connected to IC5.
The main difficulties in the coil driving circuit are oscillations while the current is ramped up or down. With careful tuning most of these oscillations are now suppressed.

Signal processing

The signal processing circuit separates flow signal and transformer signal and processes each signal separately. The Op-Amps IC1 and IC2 work as a window detector, sensing when the current through the sensing resistor R crosses at point 1 and 2. The pulse from the window detector triggers the sample and hold device IC6. Its output is the processed transformer signal. The pulse from the window detector also triggers the timer IC3. It sends a delay pulse to timer IC4 which then triggers at point 3 and 4. The output from IC4 activates the sample and hold device IC7. The output of IC7 is the processed flow signal.

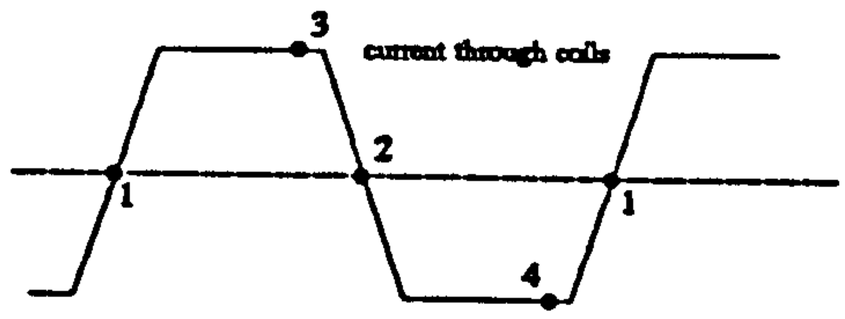

The signal picked up by the electrodes is amplified in the differential amplifier based on IC11 and a following amplifier IC10. At the output of the amplifier the transformer signal is alternating in sign because $\frac{\partial B}{\partial t}$ changes sign. The phase sensitive detector based on IC5 switches the signal to its correct sign. The signal is then fed into IC6. The flow signal is rectified with the precision rectifier IC8 before it is input to IC7. The following diagrams illustrate the processing of the signals.

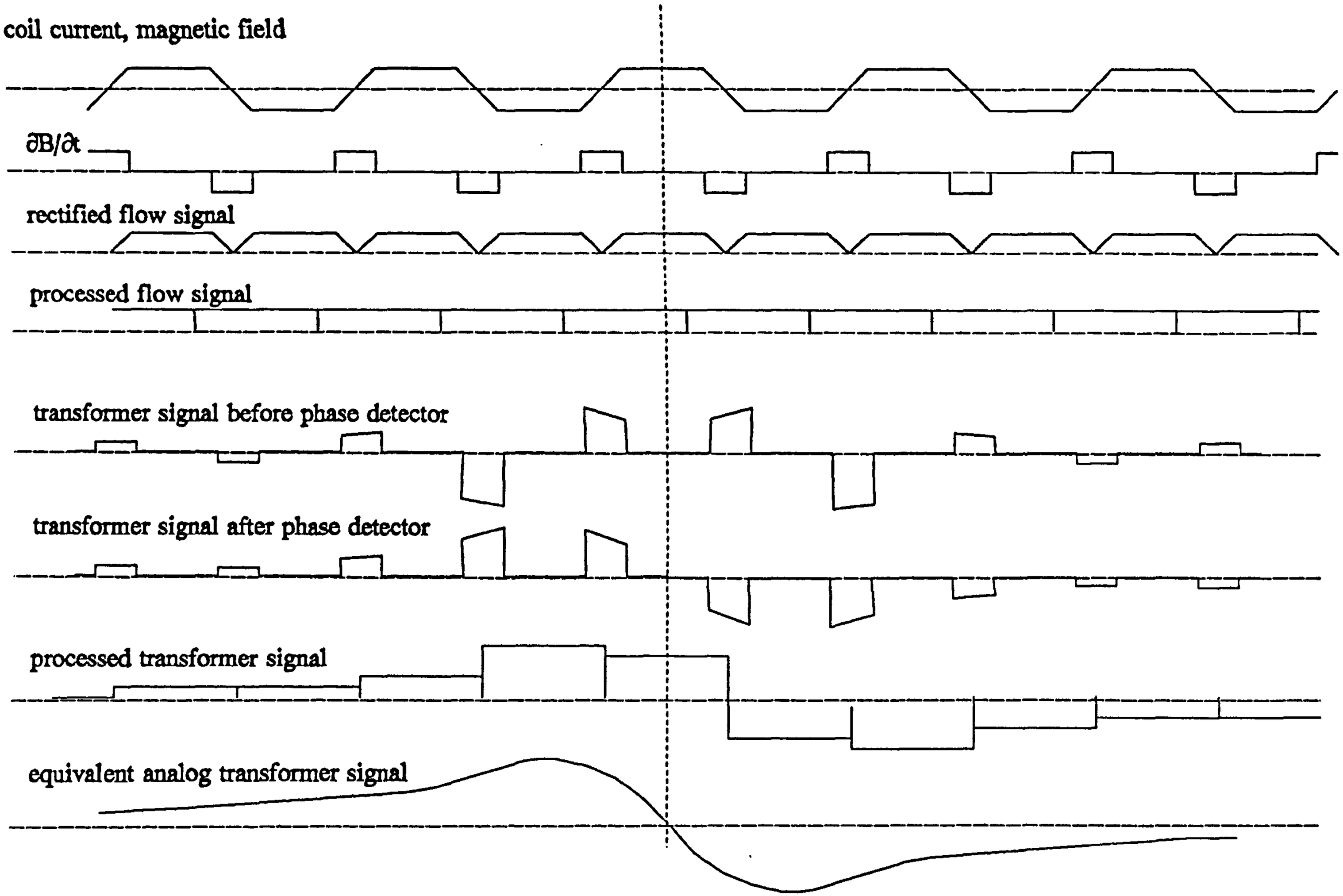
coil current, magnetic field
∂B/∂t
rectified flow signal
processed flow signal
transformer signal before phase detector
transformer signal after phase detector
processed transformer signal
equivalent analog transformer signal

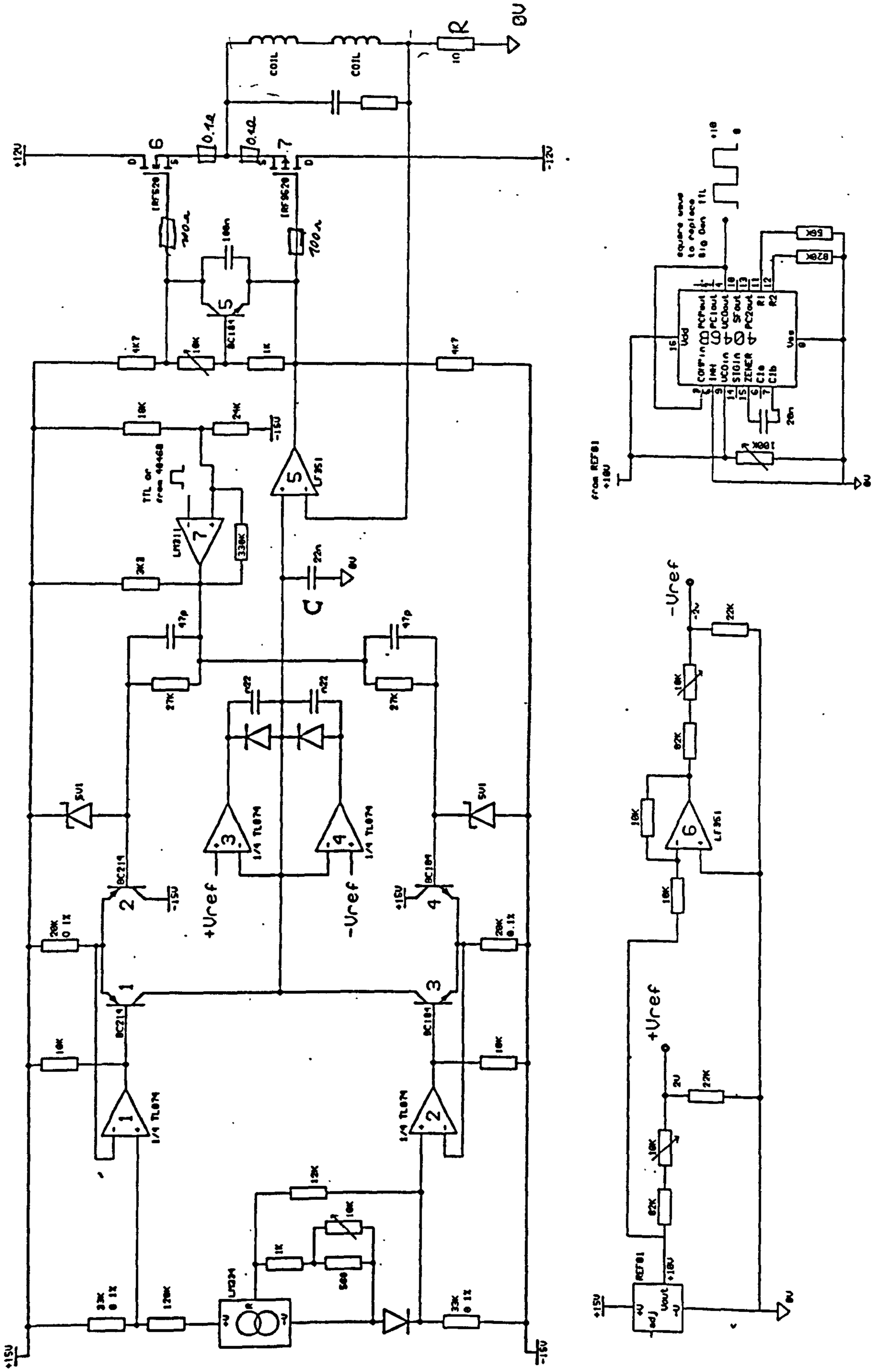

Schematic of coil drive circuit

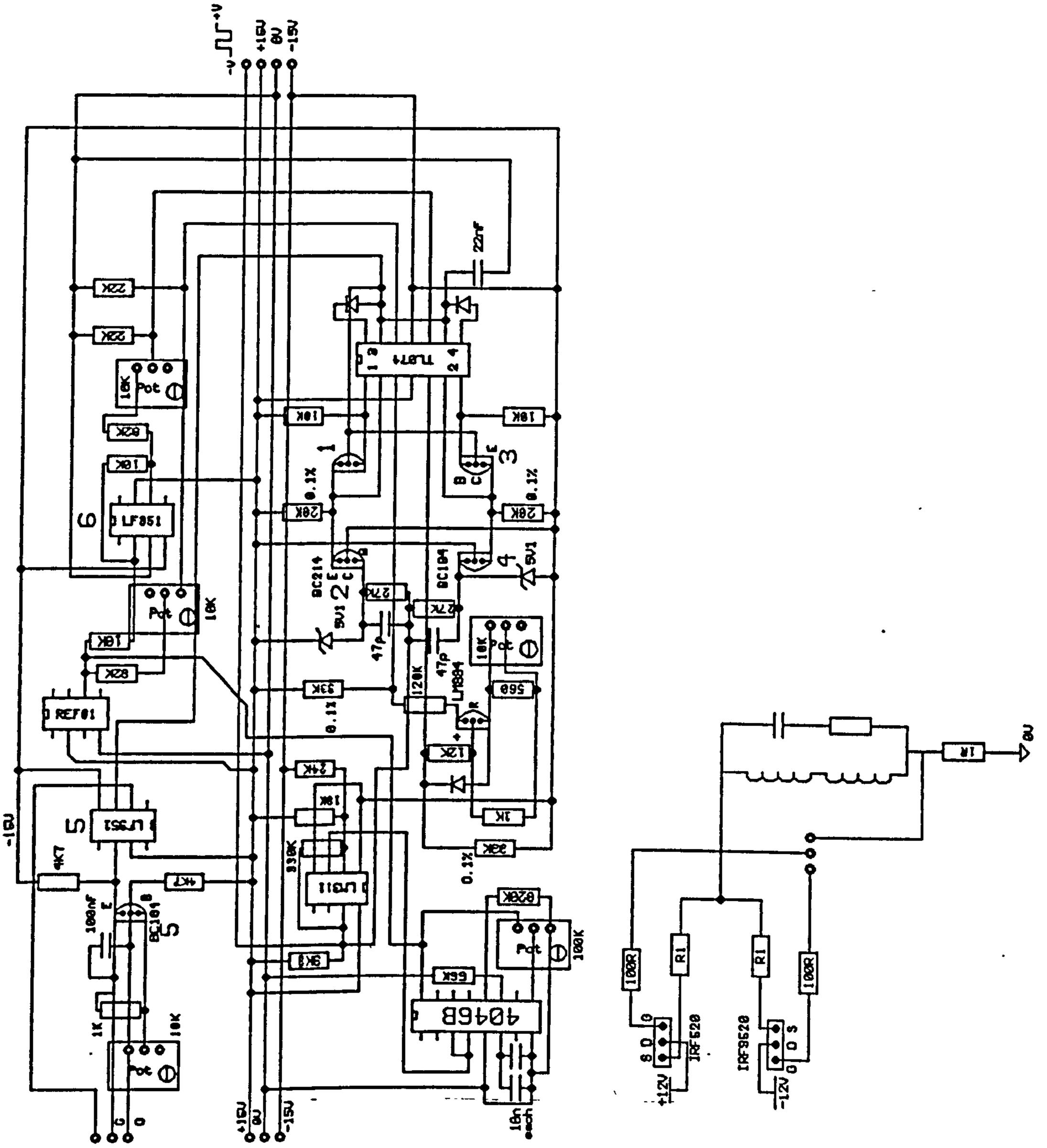

Layout of coil drive circuit

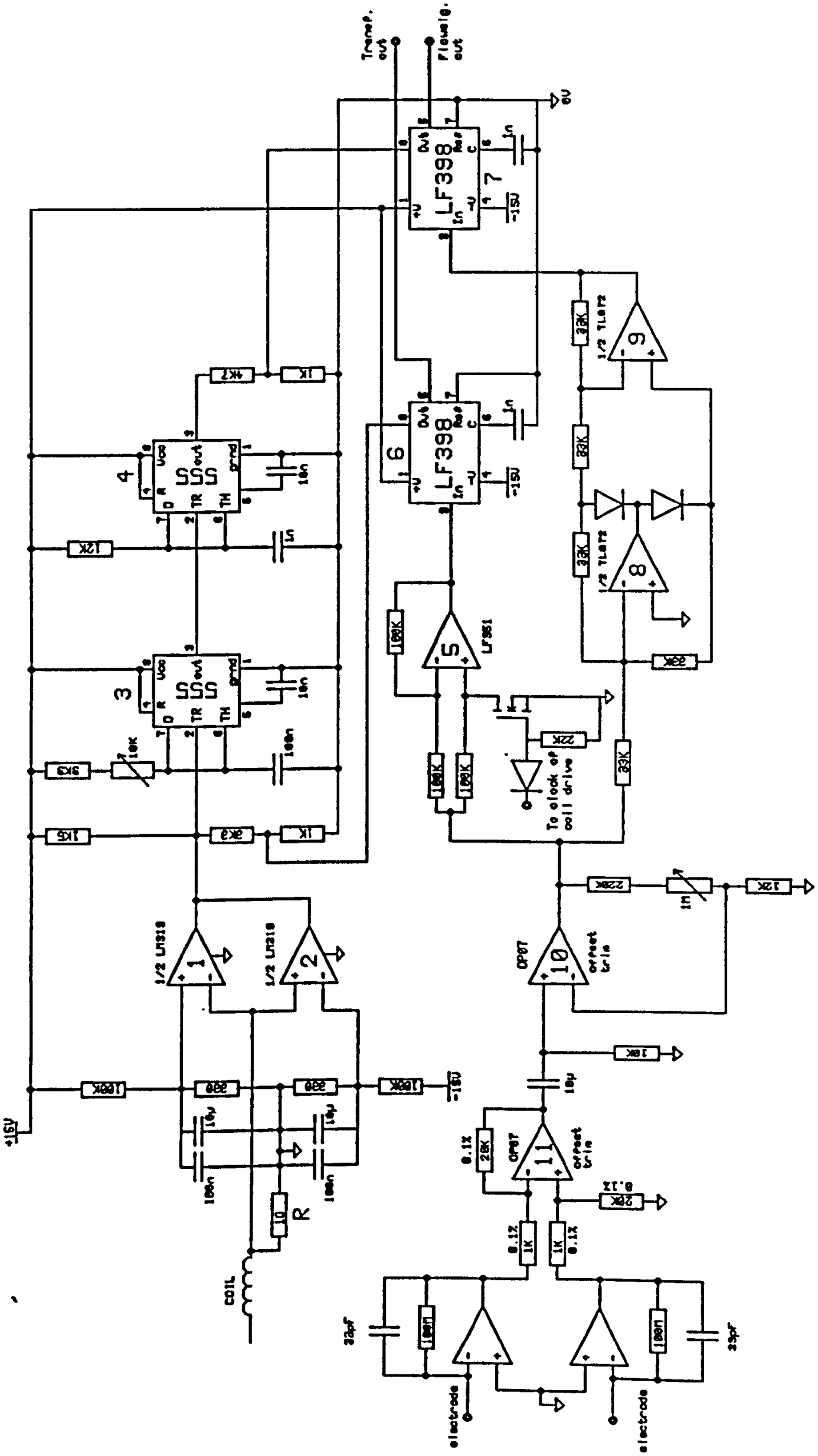

Schematic of signal processing circuit

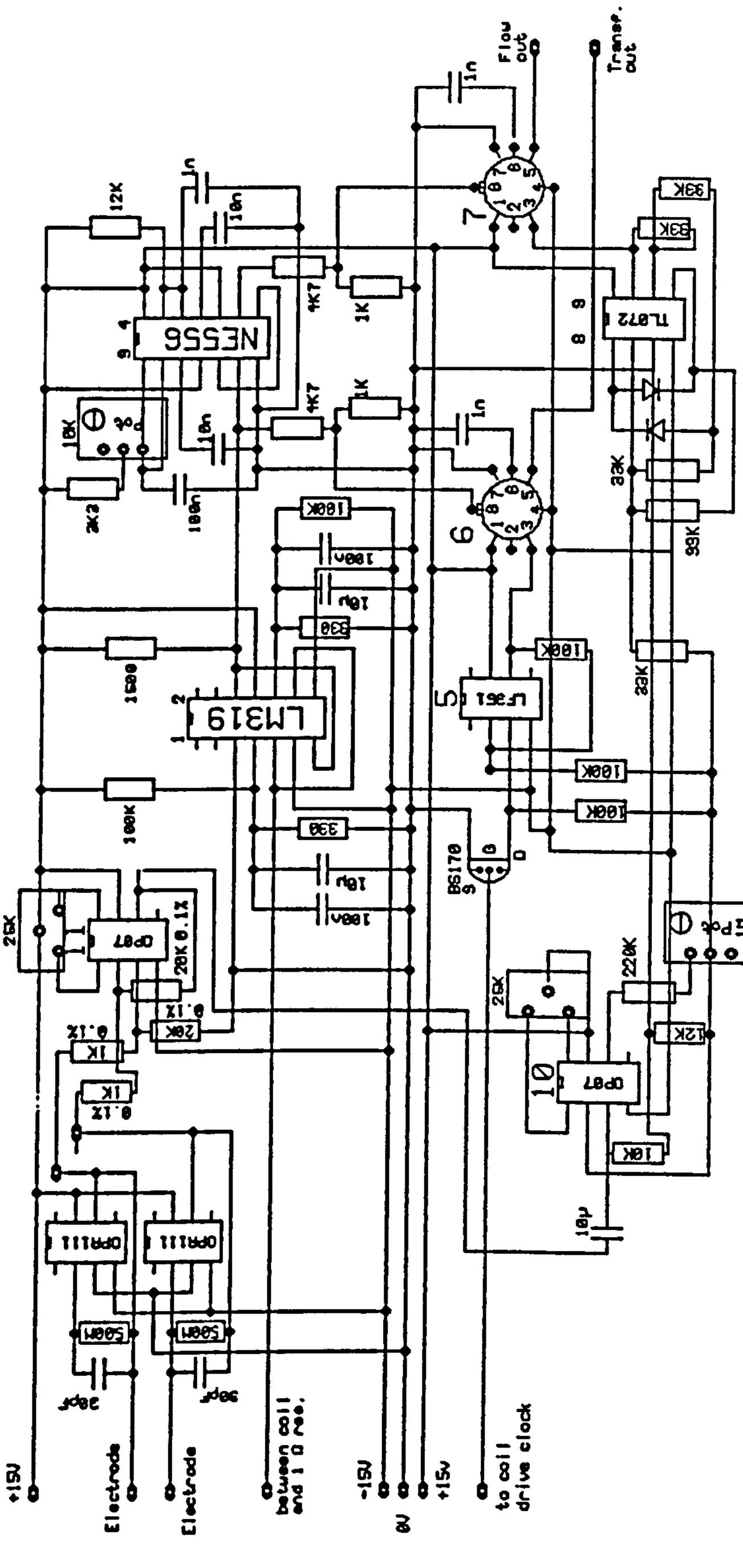

Layout of signal processing circuit

List of programs

BESSEL:	Calculates the value of any Bessel function at X
BESSEL-DER ZERO:	Calculates the zeros of the derivative of a Bessel function
DIPH:	Computes potential of a radially directed dipole in a pipe with point electrodes in a X-Y plane
DIPHL:	Computes the potential of a radially directed dipole in a pipe with point electrodes in a Y-Z plane
DIPV:	Computes the potential of a circumferentially directed dipole in a pipe with point electrodes in a X-Y plane
DIPVL:	Computes the potential of a circumferentially directed dipole in a pipe with point electrodes in a Y-Z plane
DIPZX-Y:	Computes the potential of a dipole in Z-direction in a X-Y plane
DIPZY-Z:	Computes the potential of a dipole in Z-direction in a Y-Z plane
DIPZLIMY-Z:	Computes the potential of a dipole in Z-direction in a Y-Z plane, now using the limit $l \rightarrow 0$ instead of a finite distance between sink and source
FOURIER8IRREG:	Computes the power spectrum of the transformer signal for irregular spaced 8mm dia balls
FOURIERINPUT:	Generates input file for FOURIER8IRREG
POTBATCH:	Calculates the potential difference of a dipole in X-Y plane in a pipe with point electrodes. Electrode type can be point-, strip- or large area electrode. The dipole can move in Z-direction, radially or circumferentially.
POTIN:	Generates input file for POTBATCH
POWSPECMODULA:	Computes the power spectrum of a modulated transformer signal for irregular spaced balls of 8mm dia. The modulation frequency is variable.

POWERSPECIN:	Generates input file for POWSPECMODULA
TRANSLEAK:	Computes the power spectrum of the transformer signal, modulated by a rectified sine wave in phase with the flow signal.

All programs above are written in Fortran77 and they are executable on the VAX or on DEC-stations.

POWSPECMODULA

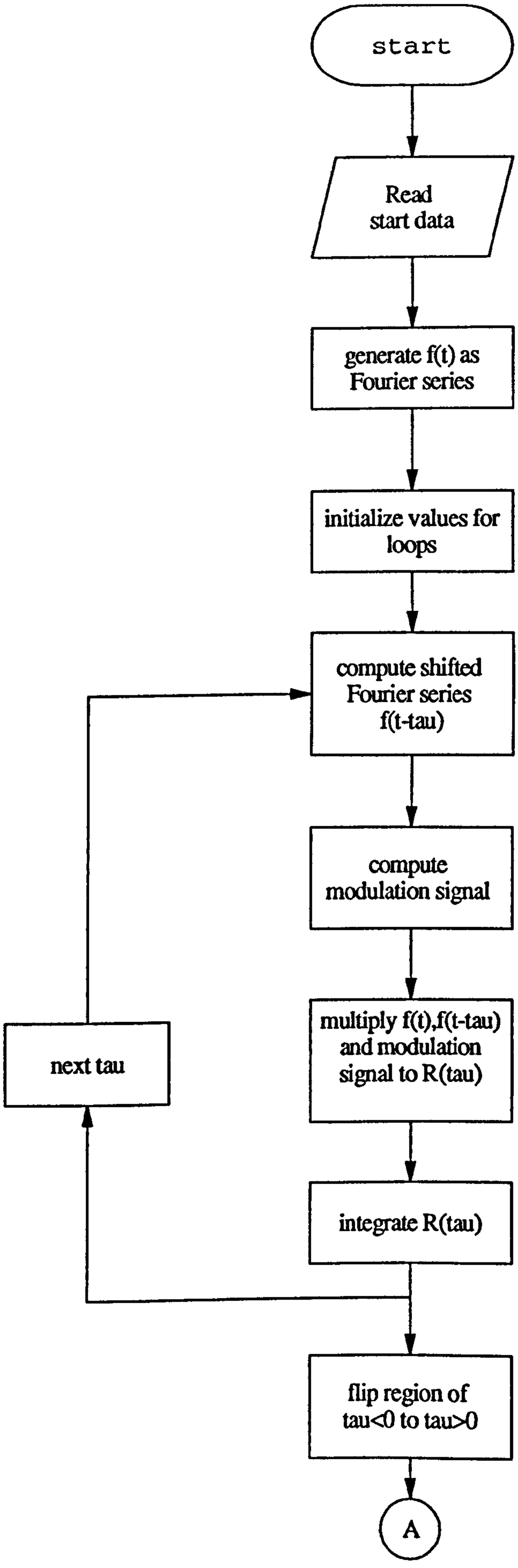

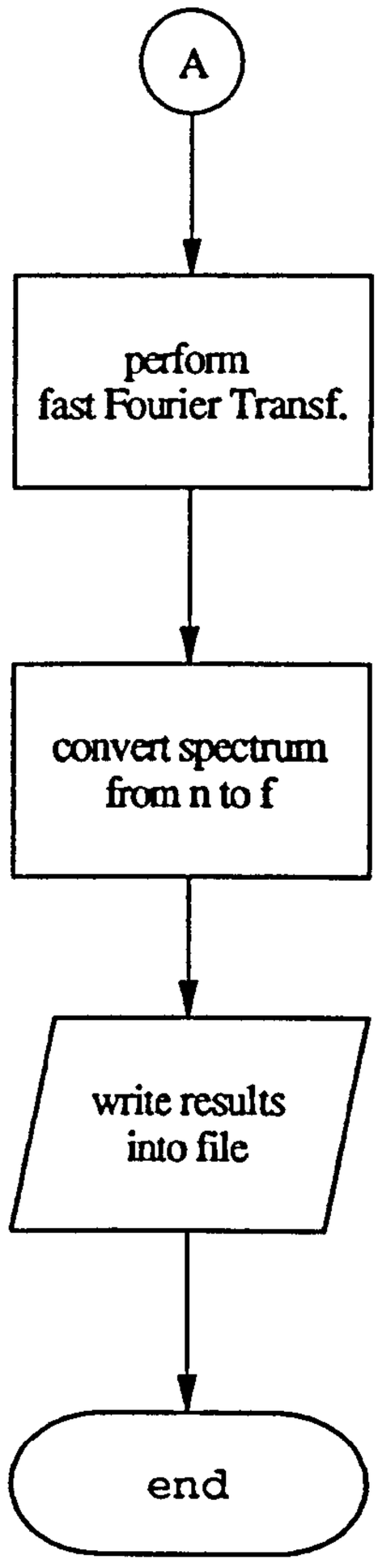
A
perform
fast Fourier Transf.
convert spectrum
from n to f
write results
into file
end

POTBATCH

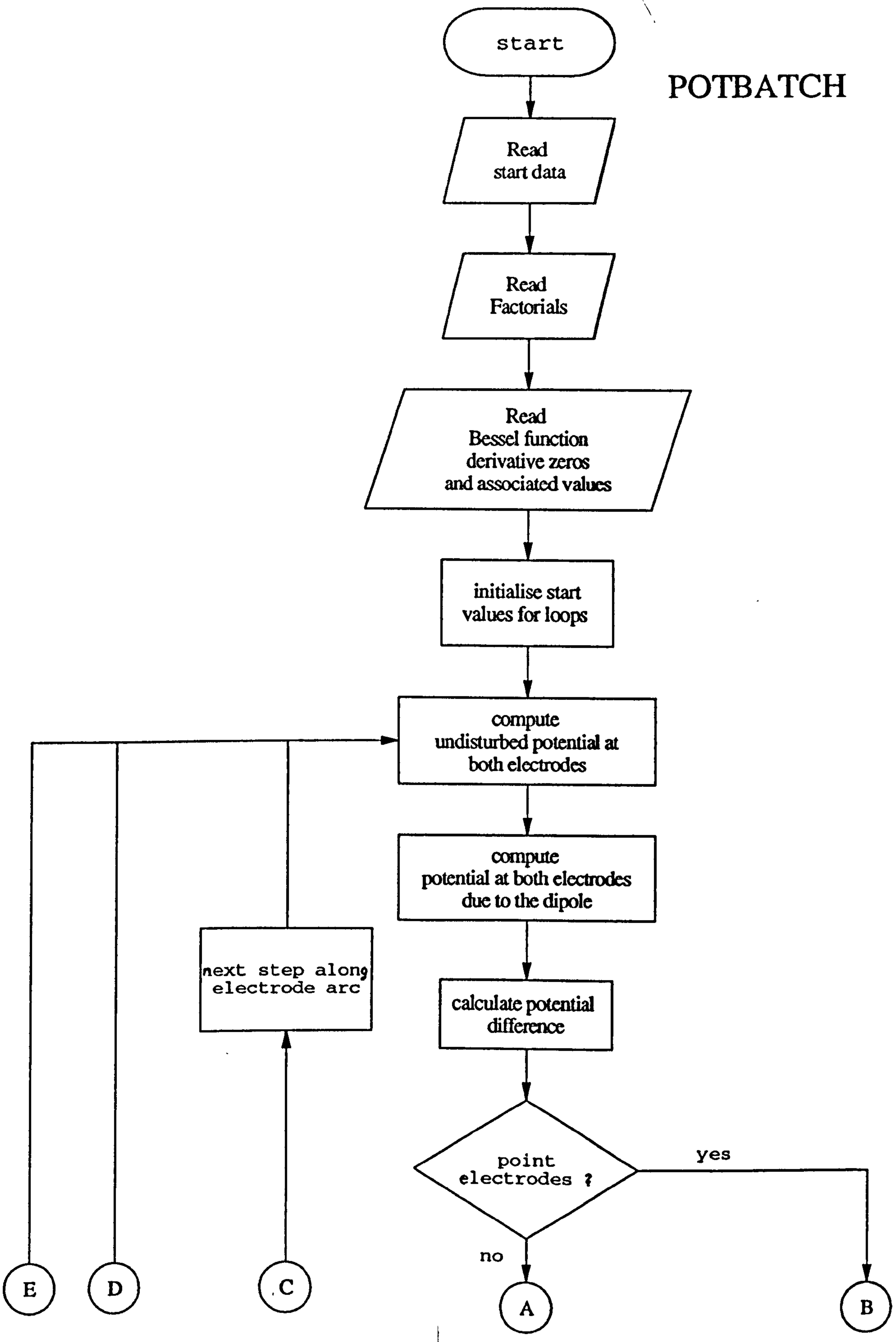
start
Read
start data
Read
Factorials
Read
Bessel function
derivative zeros
and associated values
initialise start
values for loops
compute
undisturbed potential at
both electrodes
compute
potential at both electrodes
due to the dipole
calculate potential
difference
point
electrodes ?
yes
no
next step along
electrode arc
A
B
C
D
E

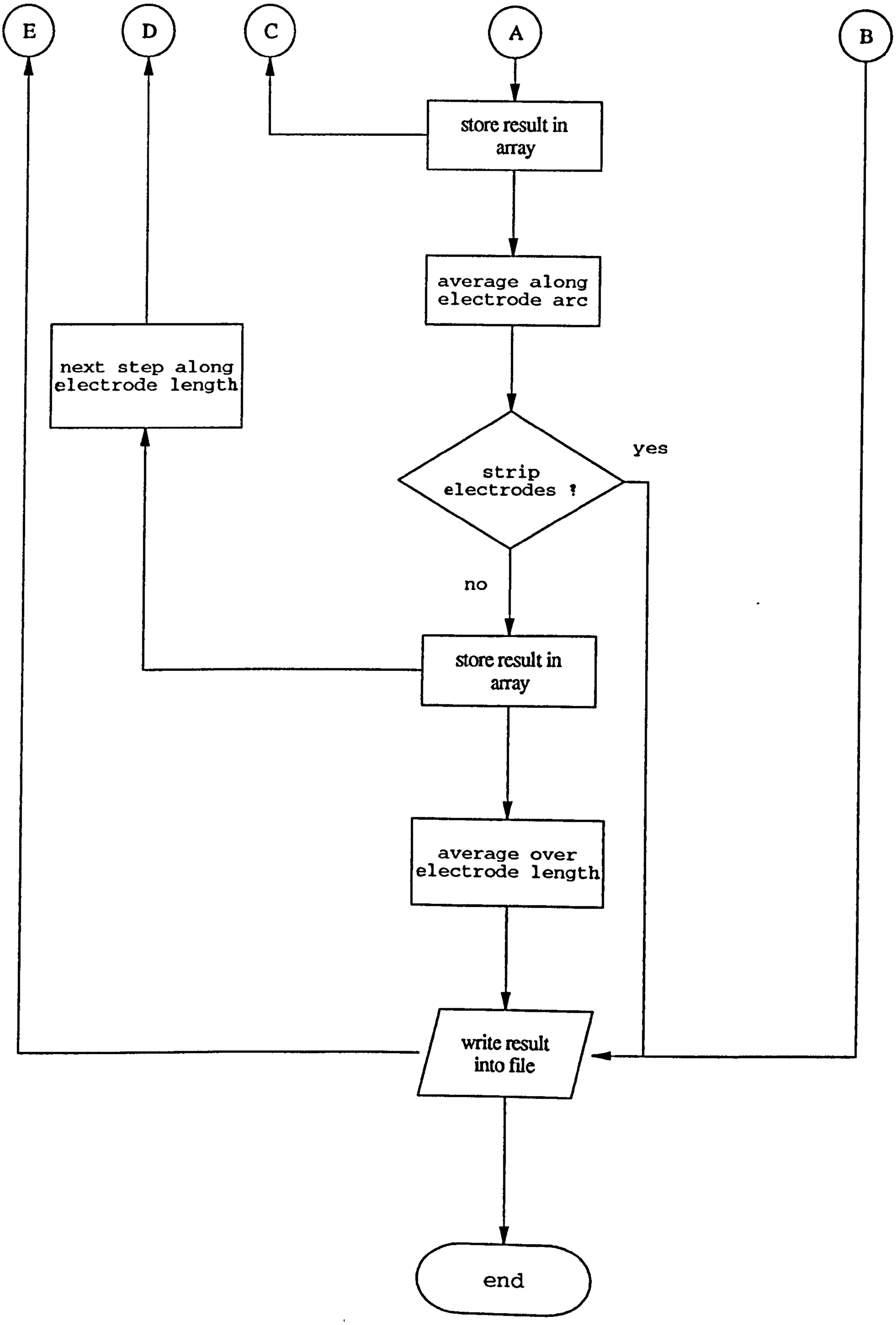
E
D
C
A
B
store result in array
average along electrode arc
next step along electrode length
strip electrodes ?
yes
no
store result in array
average over electrode length
write result into file
end

References

1) Perry Moon & Domina Eberle Spencer
Field Theory for Engineers

2) Abramowitz & Stegun(1965)
Handbook of Mathematical Functions

3) John Hemp (31.08.90)
Theory of eddy currents in electromagnetic flowmeters

4) J.A. Shercliff (1962)
The theory of Electromagnetic Flow-Measurement

5) M.K.Bevir
The theory of induced electromagnetic flowmeters.
J. Fluid Mech 43 (1970)

6) R.N. Bernier; C.E. Brennen
Use of the Electromagnetic Flowmeter in a Two-Phase flow
Int. J. Multiphase Flow Vol.9, No.3 1983

7) D.G. Wyatt
Electromagnetic Flowmeter Sensitivity with Two-Phase flow
Int. J. Multiphase Flow Vol.12, No.6 Nov-Dec 1986

8) I.D. Velt; V.I. Petrushaitis; B.S. Sprjgin; I.V. Krasilnikov; Yu.V. Mikhailov; V.R. Tuleninov
Correlation Technique for Flow Rate Measurement of Electroconductive Fluids and Two-Phase Media and device for its Implementation
(Patent No. 30.01.82)

9) M.Hori, T.Kobori, V.Ouchi
Method for measuring void fraction by electromagnetic flowmeters.
JAERI-1111, (1966)

10) R.C.Baker
Theory and practical applications of Electromagnetic Flowmeters.
Tech. Mess. TM v.52 1.Jan.85

11) J.M Delhaye
Two phase flow measurements
Bull. Inf. Sci.&Tech. no.197, Nov.74. CEN, Grenoble, France

12) R.C.Baker, J.E.Deacon
Tests on Turbine, vortex and electromagnetic flowmeters in 2-phase air water upward flow
Fluid Eng. Unit, Cranf. Inst. of Techn. Paper of international conference on the physical modelling of multiphase flow, Coventry, England 19-21.04.83

13) R.W.W. Scott
A practical assessment of the performance of electromagnetic flowmeters.
Conference on Fluid Flow Measurements. Nel,Scottland (1975), paper E1

14) M.K.Bevir, V.T.O'Sullivan, D.G.Wyatt
Computation of electromagnetic flowmeter characteristics from magnetic field data.
J.Phys. D 14 (1972)

15) J.T Cox, D.G.Wyatt
An electromagnetic flowmeter with insulated electrodes of large surface area.
J.Phys.E Sci.Instrum. 17 (1981)

16) R.C.Baker, Y.A.Al-Khazraji
Analysis of the performance of three large electrode electromagnetic flowmeters
J.Phys.D 12(1979)

17) R.H.Al-Rabeh, R.C.Baker
Optimasiation of conventional electromagnetic flowmeters.
NEL Fluid Mech. Silver Jubilee Conf., Paper 6.1

18) T.J.Cox
D Phil Thesis, University of Oxford, 1979

19) D.G.Wyatt
Computation of electromagnetic Flowmeter characteristics from magnetic field data II, errors
J.Phys. D 6 (1983)

20) V.T.O'Sullivan, D.G.Wyatt
Computation of electromagnetic Flowmeter characteristics from magnetic field data III, Rectilinear Weight function
J.Phys. D, 16 (1983)

21) V.T.O'Sullivan
Performance of an Electromagnetic Flowmeter with six point electrodes
J.Phys. E, 16 (1983)

22) J.Hemp
Improved magnetic field for an electromagnetic flowmeter with point electrodes
J.Phys. D, 8 (1975)

23) M.Tarabad, R.C.Baker
Computation of pulsed field Electromagnetic Flowmeter response to profile change
J. Phys. D, 16 (1983)

24) Y.A.Hussain, R.C.Baker
Optimised noncontact Electromagnetic Flowmeter
J. Phys. E 18 (1985)

25) J.Hemp, M.L.Sanderson
Electromagnetic Flowmeters, a state of the art review
Int. Conf. on Advances in Flow Measurement Techniques
Warwick, 1981

26) Al-Khazraji, J.Hemp
Electromagnetic flowmeters and Methods of measuring flow
Patent Appl. No 8011624, 1980

27) M.Tarabad, R.C.Baker
The performance of Electromagnetic Flowmeters in magnetic slurries
J.Phys. D, 11 (1978)

28) M.K.Bevir
The predicted effect of red blood cells on electromagnetic flowmeter sensitivity
J.Phys. D, 4 (1971)

29) D.G.Wyatt
theory, design and use of Electromagnetic Flowmeters
chapter 2 from: Cardivascular flow dynamics and measurements (1977),
N H C Hwang, N A Normann

DRAWING No. PB25875

ISSUE	MODIFICATION
A	———

ALL DIMENSIONS IN MILLIMETRES UNLESS OTHERWISE STATED.

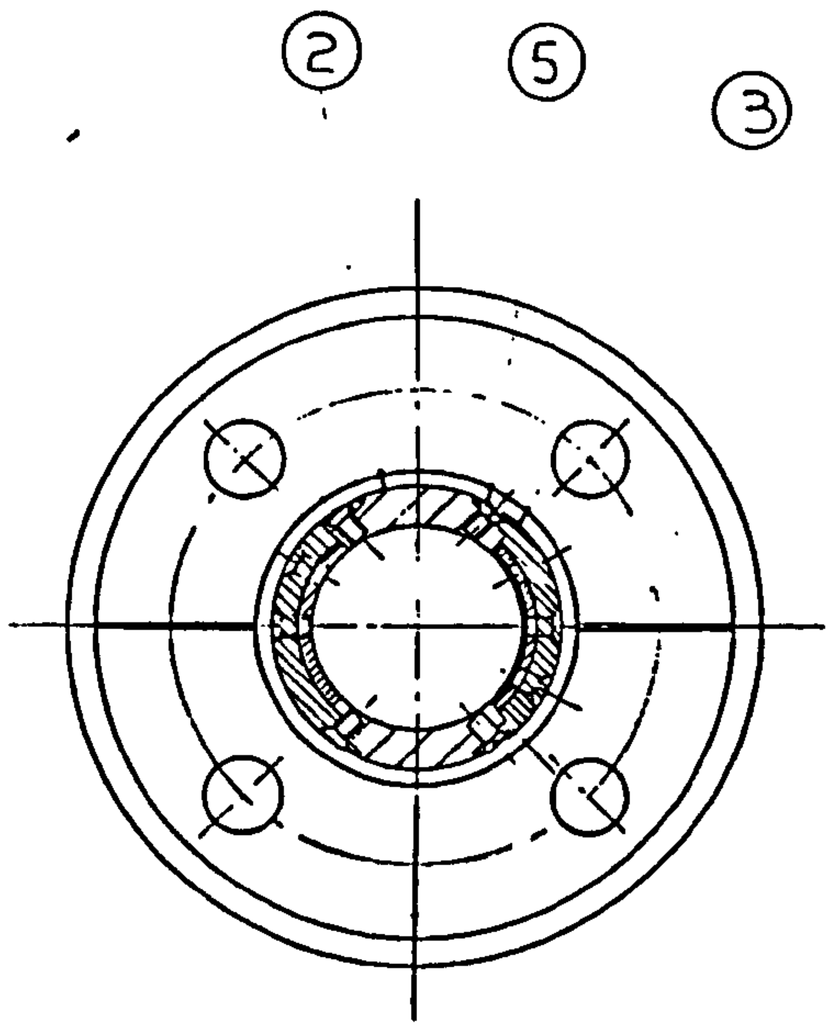

SECTION AA

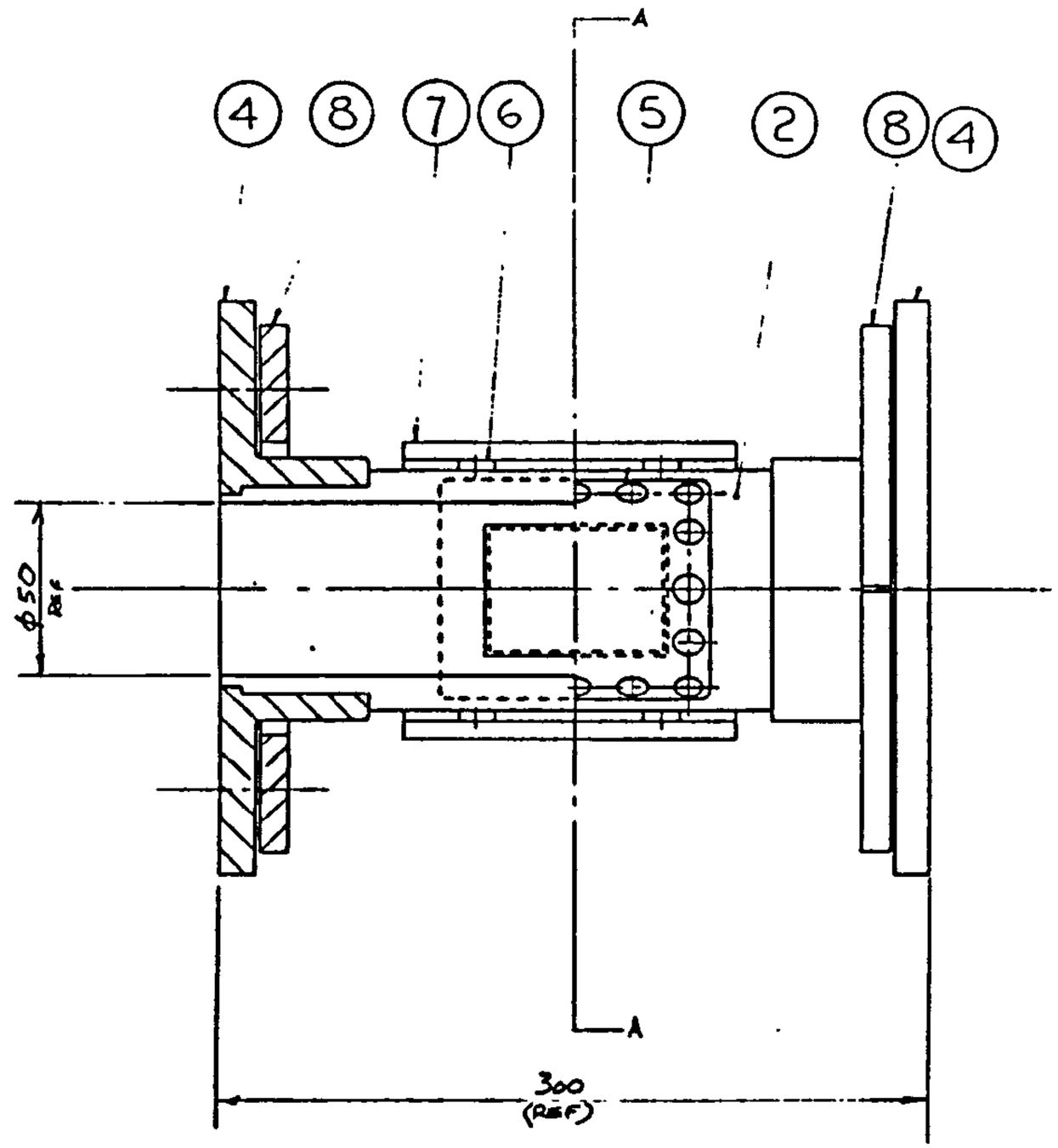

NOTES

1. MACHINE BORE WITH INSERTS SEALED IN SITU TO ϕ50, OR USE 0·5 TK PVC SHEET WITH NO MACHINING
2. FIX FLANGES TO CENTRE BODY USING PVC CEMENT. (FLANGE HOLES TO ALIGN WITH EACH OTHER).
3. BACKING RINGS ITEM 8 TO BE SPLIT ON HORIZONTAL CENTRE LINE

ITEM	PART No.	DESCRIPTION	No. OFF	MATL	SPEC.	REMARKS
8	———	BACKING RING	2			OR Alt. MAT (1" BSP S/N)
7	———	ELECTRICAL STEEL SHIELD	1			
6	———	COIL	2			
5	———	C'SUNK SCREW	32	NYLON		M5 (CUT TO LENGTH)
4	———	FLANGE	2	PVC		(TYPE OF BSP S/N)
3	PB25877	INSERT ASSY	2			
2	PB25876	CENTRE BODY	1			
1	PB25875	FLOWMETER ASSY	1			

THIRD ANGLE PROJECTION

GENERAL TOLERANCE ON DIMENSIONS
MACHINED —
UNMACHINED – ·
OTHER DIMENSIONS AS STATED

WELD WHERE SHOWN THUS ⌒

MACHINE WHERE SHOWN THUS ✓

JOB No. 89005

No. OF SETS REQ. 1

USED ON DRG. ———

SHEET SIZE A1

SCALE 1/1

FINISH SELF

	DRAWN	CHKD	APPVD	OTHER APPR.
	E.CLARK	RHD		
	15-1-93	22-1-93		

TITLE: GENERAL ASSEMBLY OF FOIL FLOWMETER

SCHOOL OF MECHANICAL ENGINEERING
CRANFIELD INSTITUTE OF TECHNOLOGY

DRAWING No. PB 25875

SHT. 1 OF 1 SHEETS

DRAWING No. PB 25876

ISSUE	MODIFICATION
A	—

ALL DIMENSIONS IN MILLIMETRES UNLESS OTHERWISE STATED.

ENLARGEMENT SHOWING SEALING LAND GEOMETRY
SCALE 2/1

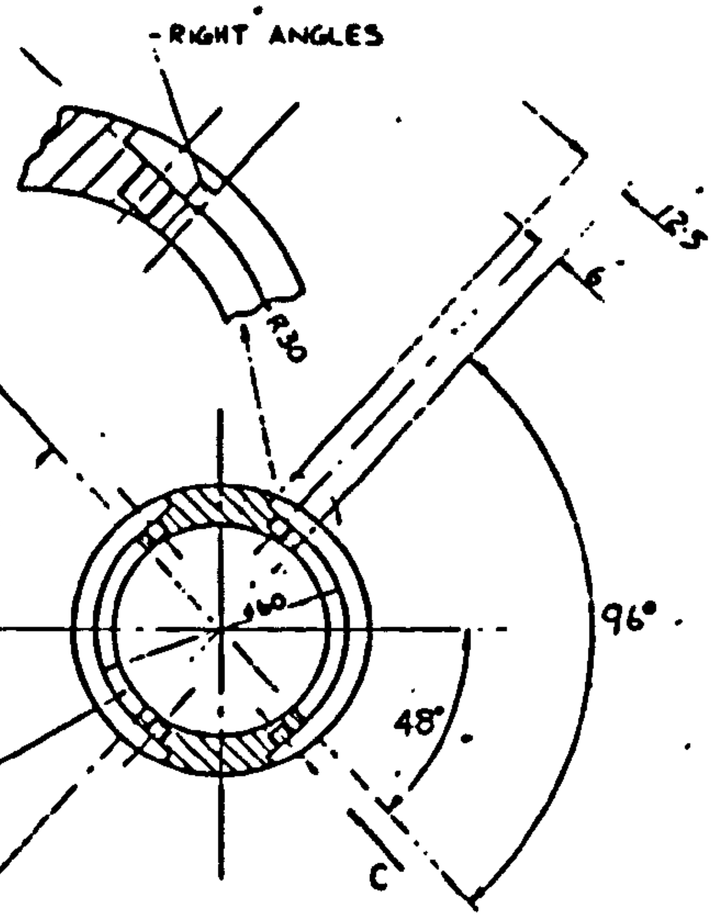

TO CUT OUTS POSITION DIAMETRICALLY OPPOSITE

SECTION AA

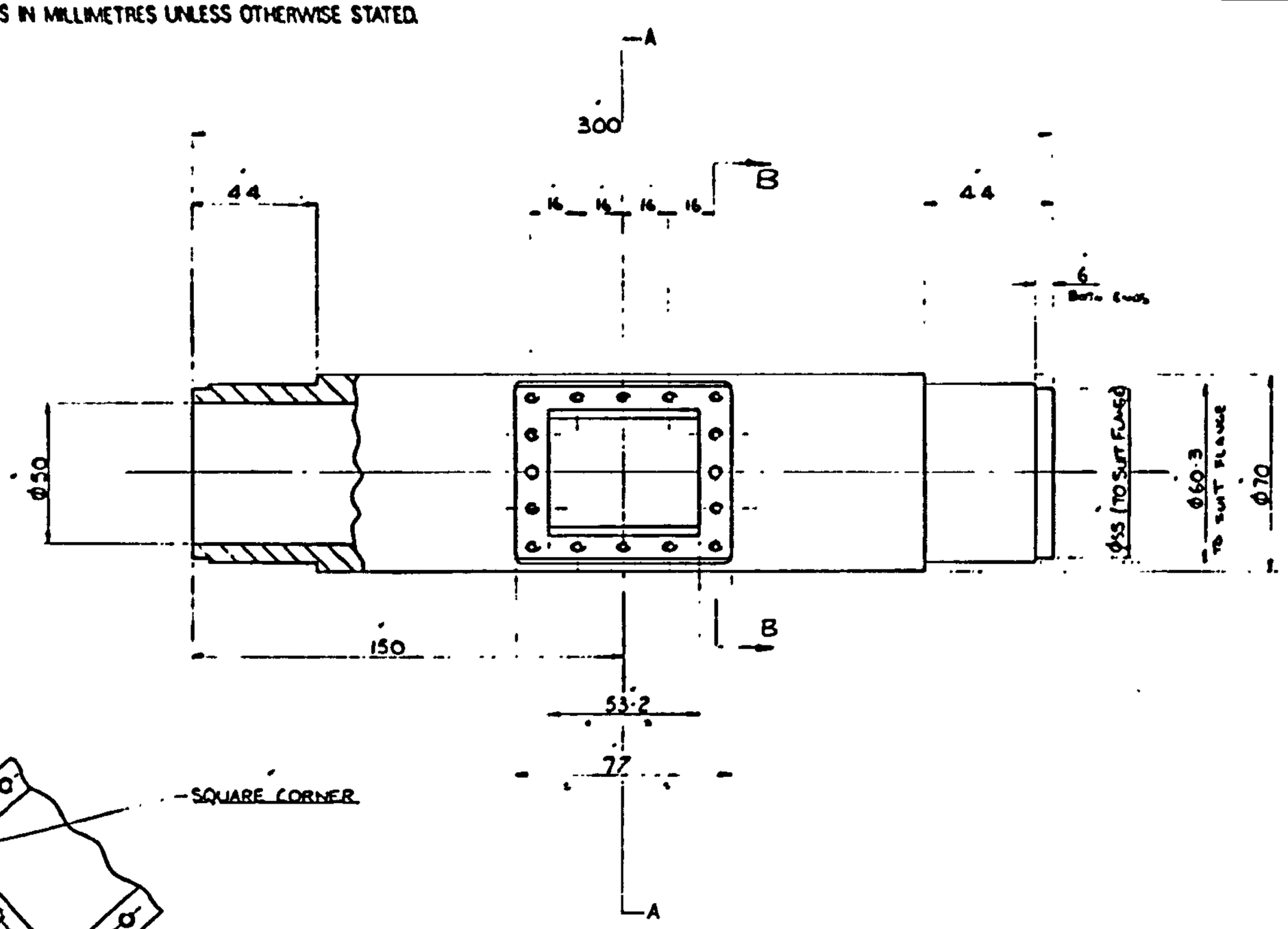

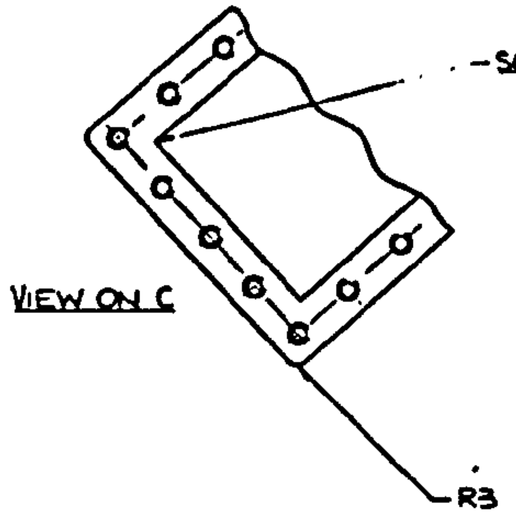

VIEW ON C

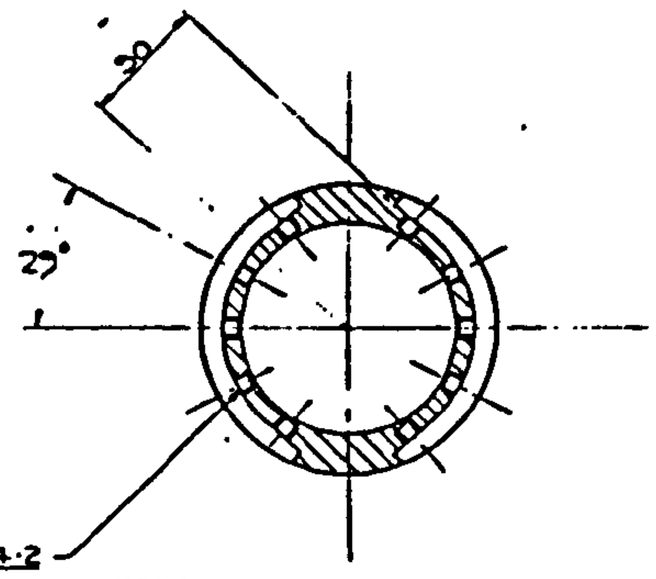

32 HOLES (16 PER SIDE) DRILL Ø4·2 THEN TAP M5 (FLAT BOTTOM) TO MAX DEPTH POSSIBLE, HOLES MUST NOT BREAK INTO FINAL BORE Ø50

SECTION BB

NOTES,

1. MACHINE ALL OVER.
2. REMOVE SHARP EDGES, UNLESS OTHERWISE STATED.
3. ALL DIAMETERS TO BE CONCENTRIC AND SQUARE TO ALL FACES.

THIRD ANGLE PROJECTION			SHEET SIZE A1	1	PB25876	CENTRE BODY	1	PVC		Ø75 x 320 lg.
				ITEM	PART No.	DESCRIPTION	No OFF	MATL	SPEC.	REMARKS
GENERAL TOLERANCE ON DIMENSIONS MACHINED ± 0·1 UNMACHINED — OTHER DIMENSIONS AS STATED	JOB No. B9005	No OF SETS REQ. 1	SCALE 1/1	DRAWN E. CLARK 19-1-93	CHKD R.W.D 27.1.93	APPVD	STRESS ANAL.	TITLE:- DFEI FLOWMETER CENTRE BODY		
WELD WHERE SHOWN THUS ⌐			FINISH SELF	SCHOOL OF MECHANICAL ENGINEERING CRANFIELD INSTITUTE OF TECHNOLOGY				DRAWING No. PB25876		
MACHINE WHERE SHOWN THUS ✓	USED ON DRG. PB25875							SHT. 1 OF 1 SHEETS		

170

DRAWING No. PB25877	
ISSUE	MODIFICATION
A	———

ALL DIMENSIONS IN MILLIMETRES UNLESS OTHERWISE STATED.

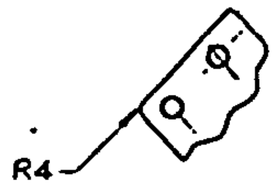

PART VIEW ON C
SHOWING CORNER RAD

-16 HOLES PER COVER PLATE DRILL Ø5·2
C'SINK TO SUIT M5 NYLON C'SUNK SCREW

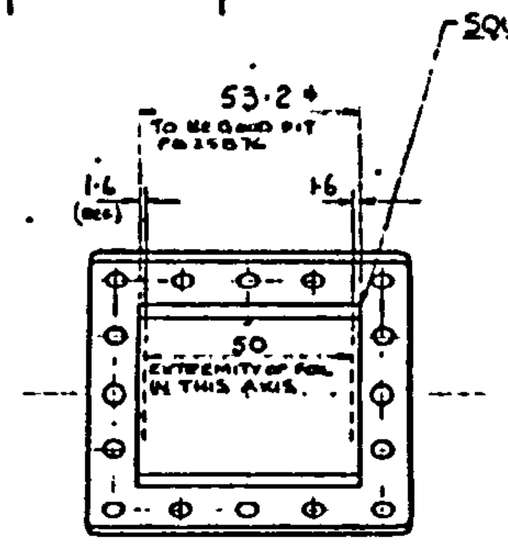

VIEW ON D

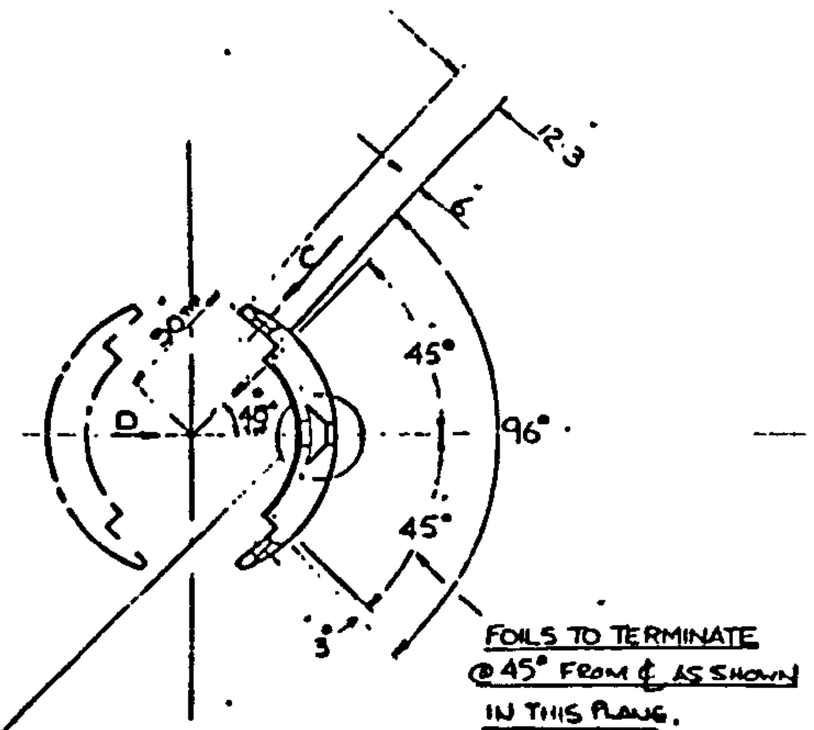

SECTION AA

FOILS TO TERMINATE @45° FROM ℄ AS SHOWN IN THIS PLANE.

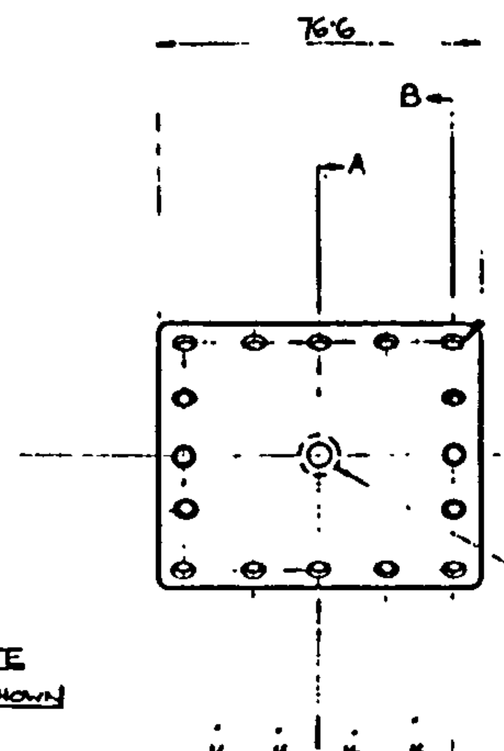

ONE HOLE DRILL Ø5
IN ITEM 1 ONLY
C'SUNK REVERSE FACE 2·0x45°

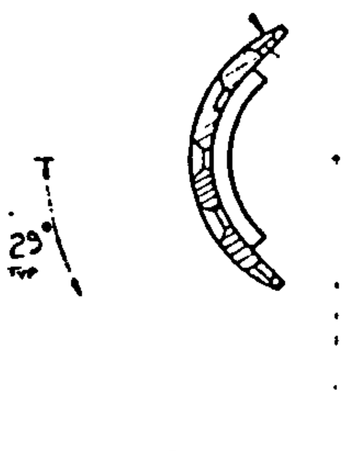

SECTION BB

DIMS MARKED * TO SUIT CENTRE BODY PB25876

0·08 THICK ALUMINIUM FOIL, SECURED WITH SUITABLE ADHESIVE

* NOT INCLUDING ADHESIVE THICKNESS

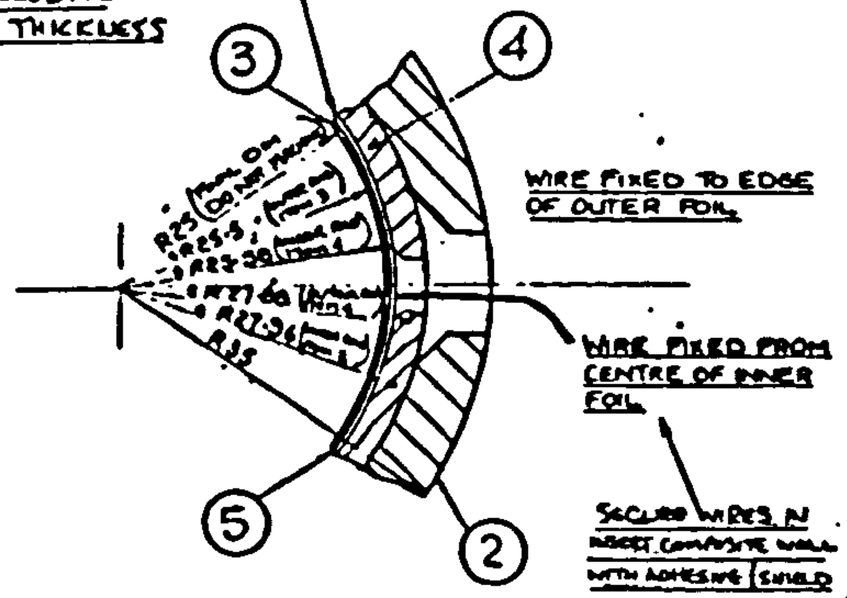

ENLARGEMENT SHOWING LAMINAR BUILD UP OF INSERT WALL. SCALE 5/1

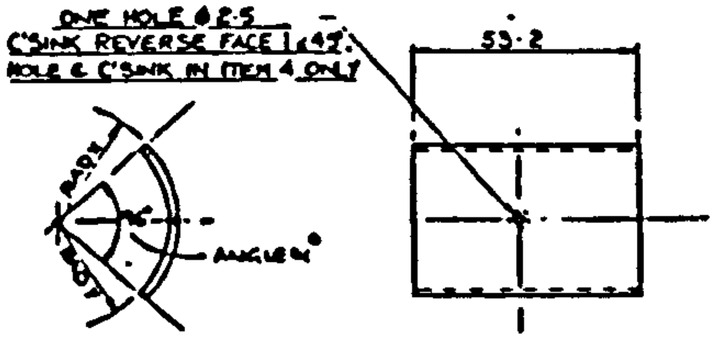

CONSTRUCTION DETAILS	ITEM Nº	RAD X	RAD Y	ANGLE α°	NO OFF
TURN FROM Ø75 BAR	(4)	27·08	25·58	96°	2

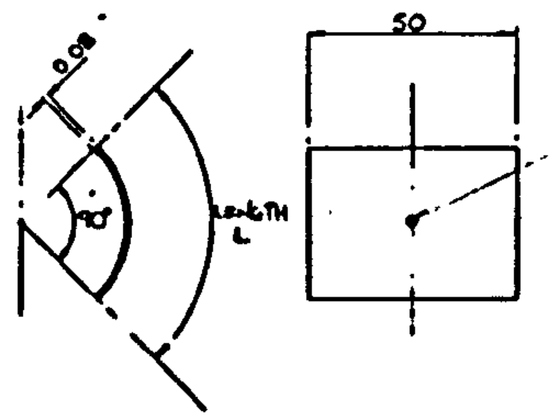

DESCRIPTION / ITEM Nº	RADIUS R (MEAN)	LENGTH L	Nº OFF
INNER FOIL 5	25·58	40·12	2

DETAIL OF FOILS
SCALE 1/1
MATERIAL:- ALUMINIUM FOIL

ITEM	PART No.	DESCRIPTION	No OFF	MAT'L	SPEC.	REMARKS
5		INNER FOIL	1	ALUM		0·08 TK
4		INTERMEDIATE SKIN	1	PVC		0·08 TK
3		INNER SKIN	1	PVC		TURN FROM BAR
2		INSERT SHELL	1	PVC		0·5 TK SHEET
1	PB25877	INSERT ASSY	1			TURN FROM BAR

NOTES.
1. MANUFACTURE ITEM 2 (2 OFF) FROM TUBE AS SHOWN ABOVE (MACHINE Ø75 BAR TO FORM TUBE)
2. MACHINE ALL OVER (EXCEPT ITEM 3)
3. REMOVE SHARP EDGES (LOS)
4. MANUFACTURE JIGS AS NECESSARY
5. SECURE ITEMS 5,3,4 & 2 TOGETHER WITH ADHESIVE

THIRD ANGLE PROJECTION

GENERAL TOLERANCE ON DIMENSIONS
MACHINED ±0·1
UNMACHINED —
OTHER DIMENSIONS AS STATED
WELD WHERE SHOWN THUS ⌒
MACHINE WHERE SHOWN THUS ✓

JOB No. 89005 | No OF SETS REQ. 1 | USED ON DRG. PB25875

SHEET SIZE A1 | SCALE 1/1 | FINISH SELF

DRAWN E CLARK 25-1-93 | CHKD 2ND 27-1-93 | APPVD | MFG ACTG

TITLE:- DFE1 FLOWMETER INSERT ASSEMBLY

SCHOOL OF MECHANICAL ENGINEERING
CRANFIELD INSTITUTE OF TECHNOLOGY

DRAWING No. PB25877

SHT 1 OF 1 SHEETS